PACIFIC EARTHQUAKE ENGINEERING RESEARCH CENTER

Preliminary Studies on the Dynamic Response of a Seismically Isolated Prototype Gen-IV Sodium-Cooled Fast Reactor (PGSFR)

Benshun Shao

Andreas H. Schellenberg

Matthew J. Schoettler

Stephen A. Mahin

Department of Civil and Environmental Engineering
University of California, Berkeley

PEER Report No. 2017/11
Pacific Earthquake Engineering Research Center
Headquarters at the University of California, Berkeley

December 2017

PEER 2017/11
December 2017

Disclaimer

The opinions, findings, and conclusions or recommendations expressed in this publication are those of the author(s) and do not necessarily reflect the views of the study sponsor(s), the Pacific Earthquake Engineering Research Center, or the Regents of the University of California.

Preliminary Studies on the Dynamic Response of a Seismically Isolated Prototype Gen-IV Sodium-Cooled Fast Reactor (PGSFR)

Benshun Shao

Andreas H. Schellenberg

Matthew J. Schoettler

Stephen A. Mahin

Department of Civil and Environmental Engineering
University of California, Berkeley

PEER Report No. 2017/11
Pacific Earthquake Engineering Research Center
Headquarters at the University of California, Berkeley

December 2017

ABSTRACT

The KEPCO Engineering and Construction Company, Inc. (KEPCO E&C) is developing a Prototype Gen-IV Sodium-Cooled Fast Reactor (PGSFR). Preliminary evaluations of the behavior of the isolated PGSFR when subjected to seismic and aircraft impact loading conditions were conducted to support design efforts by KEPCO E&C. Results and key findings of these analyses are as follows: (i) because isolator deformations are typically quite small for the considered seismic excitation levels, the benefit of seismic isolation could be enhanced with revised isolator designs that reduce the apparent yield strength and permit greater displacement demands; (ii) the amplitudes of acceleration and displacement responses resulting from the impact of a large aircraft are similar to or exceed the demands imposed by a seismic event based on the NRC hazard with a peak ground acceleration of 0.3*g*, and (iii) as provided, the isolator initial stiffness is poorly conditioned since it leads to fundamental isolation frequencies that are not well separated from the plant's superstructure frequencies, and triggers some resonance that significantly increases floor acceleration response spectra.

ACKNOWLEDGMENTS

This report summarizes results, observations, and findings developed as part of the initial phase of a research project entitled "Prototype Gen-IV Sodium-cooled Fast Reactor (PGSFR) with Seismic Isolation Adaptation (Phase 1)." This research was supported by Contract No. KCN04-15-46 from KEPCO Engineering and Construction Company, Inc. (KEPCO E&C) to the Pacific Earthquake Engineering Research Center (PEER). The authors are grateful for this opportunity to collaborate and financial support.

In addition, the PEER research team appreciates the advice and technical support provided by the engineering staff of KEPCO E&C, with special thanks to Drs. Sang-Hoon Lee and Young-Suk Lee. Their interest in and promotion of this research was exceptional.

The authors are grateful to those whose expertise helped improve the quality and outcome of the research. Ground motions provided by Professor Jack Baker at Stanford University provided the basis for developing the ground motions used in these studies. Dr. Frank McKenna provided support on developing the OpenSees structural analysis models used in the numerical studies described in this report.

The authors are especially indebted to the project's internal and external advisory committee for the numerous useful comments and suggestions. The expert committee participants during this phase included: Professors Ehud Greenspan, James Kelly, and Per Peterson from the University of California at Berkeley, and Charles Boardman (Consultant), Dr. Robert Budnitz (LBNL), Dr. Annie Kammerer (PEER/Consultant), Robert Kassawara (EPRI), Dr. Robert Kennedy (RPK Structural Mechanics), Joseph Maffei (Maffei Structural Engineering), Fred Tajirian (Chevron), and Dr. Wen Tseng (ECWST Consultants).

The opinions, findings, and conclusions or recommendations expressed in this publication are those of the author(s) and do not necessarily reflect the views of the KEPCO Engineering and Construction Company, Inc., the Regents of the University of California, or the Pacific Earthquake Engineering Research Center.

CONTENTS

LIST OF TABLES

LIST OF FIGURES

1 INTRODUCTION

1.1 INTRODUCTION

In the search for safe, economical, and environmentally friendly sources of electric power, many energy providers are turning to new technologies. These include advanced sodium-cooled fast reactors, which offer significant benefits in terms of safety, efficiency, and sustainability, and seismic isolation, which can substantially reduce demands and improve the performance of structures and their mechanical systems and components.

This report does not discuss any particular advantages and disadvantages of fast reactors. It presents the results of a preliminary study aimed at assessing the feasibility of using seismic isolation to help safeguard sodium-cooled fast reactors from hazards posed by strong earthquake ground shaking and aircraft impact. To focus this report, simplified numerical models were examined that are representative in general terms of a Prototype Gen-IV Sodium-Cooled Fast Reactor (PGSFR) being considered by the KEPCO Engineering and Construction Company, Inc. (KEPCO E&C). Since the details of the plant design and the required seismic and aircraft impact hazards are not yet known, the results are preliminary. However, they are useful in the conceptual design process of a PGSFR and the possible use of seismic isolation.

1.2 SCOPE OF REPORT

This report is divided into 6 chapters as follows:

- Chapter 1. Introduction
- Chapter 2. Literature Survey Related to Seismically Isolated Fast Breeder Reactors
- Chapter 3. Parametric study of a Seismically Isolated Rigid Mass
- Chapter 4. Dynamic Analysis of a Seismically Isolated PGSFR Subjected to Earthquake Excitation
- Chapter 5. Dynamic Analysis of a Seismically Isolated PGSFR Subjected to Aircraft Impact
- Chapter 6. Summary and Recommendations for Future Research

2 LITERATURE SURVEY RELATED TO SEISMICALLY ISOLATED FAST BREEDER REACTORS

2.1 INTRODUCTION

Currently, no fast reactor has been constructed using seismic isolation. However, the increased safety and sustainability of fast reactors suggests that a comparable effort to increase seismic safety margins would be useful. This is consistent with the overall stringent performance goals stipulated for Gen-IV reactors. It is thought that seismic loading is more important for fast reactors than for conventional commercial nuclear power plants (NPPs) due to the systems, components, and equipment used, which are characterized as being heavy and flexible.

This chapter presents a brief review of previous studies on the application of seismic isolation to fast breeder reactors. Included are a detailed introduction of each project and a discussion on several key points relevant to the seismic isolation of fast breeder reactors. A list of projects reviewed in this chapter is summarized in Table 2.1 below.

Table 2.1 List of previous projects on the study of seismic isolation for use in fast breeder reactors.

Country	Project Name	Full name	Approximate time line
USA	PRISM	**P**ower **R**eactor **I**nnovative **S**mall **M**odule	1984–1994
	SAFR	The **S**odium **A**dvanced **F**ast **R**eactor	1988–1995
Japan	DFBR	**D**emonstration **F**ast **B**reeder **R**eactor	1989–2001
	JSFR	**J**apan **S**odium-cooled **F**ast **R**eactor	1995–2000
Korea	STAR-LM	The **S**ecure, **T**ransportable, **A**utonomous **R**eactor-**L**iquid **M**etal	2002–2005
	KALIMER	**K**orea **A**dvanced **Li**quid **Me**tal **R**eactor	2009–2012
Europe	SILER	**S**eismic **I**nitiated events risk Mitigation in **Le**ad-cooled **R**eactor	2012–present

2.2 POWER REACTOR INNOVATIVE SMALL MODULE (PRISM)

2.2.1 Project Description

In 1981, General Electric Company (GE) initiated a program to develop an innovative Liquid Metal Reactor (LMR) conceptual design, which resulted in the Power Reactor Inherently Safe Module (PRISM). The target commercial PRISM plant has nine reactor modules arranged in three identical 465 MW power blocks, for an overall plant net electrical rating of 1395 MW, with a thermal efficiency of 32.9% [Berglund et al. 1987]. An overview of the plant is shown in Figure 2.1, and a schematic of each power block is shown in Figure 2.2. The reactor vessel is 6.1 m (20 ft) in diameter, 18.9 m (62 ft) high, and is supported from the top [Kwant and Boardman 1992; Tajirian et al. 1990] as shown in Figure 2.3; see Table 2.2 for a general summary of specifications for the PRISM reactor.

Table 2.2 General summary of specifications for the PRISM reactor.

Reactor capacity:	465 MW per power block
Reactor containment building weight:	40 MN (9000 kip) for whole isolated structure
Dimension:	Reactor vessel diameter of 6.1 m (20 ft), height of 18.9 m (62 ft)
Design safe shutdown earthquake (SSE)	Horizontal: 0.3*g*, Vertical: 0.3*g*
Bearing type:	High shape factor laminated rubber bearing
Base isolation system:	Only horizontal isolation system with 20 bearings for each reactor

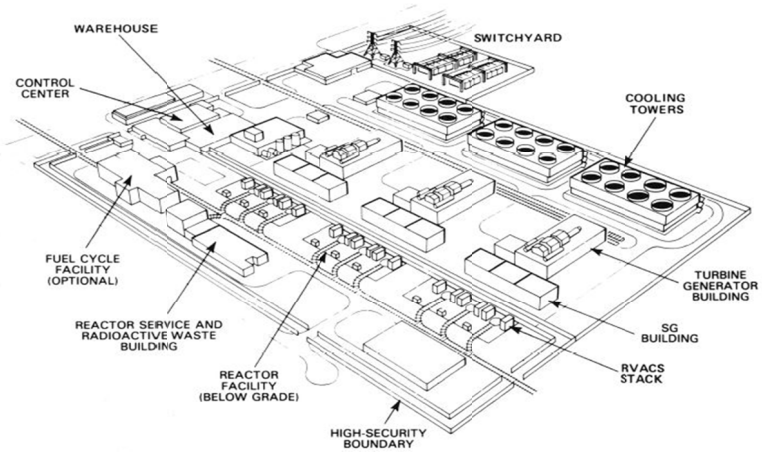

Figure 2.1 PRISM 1395 MW target commercial plant [Berglund et al. 1987].

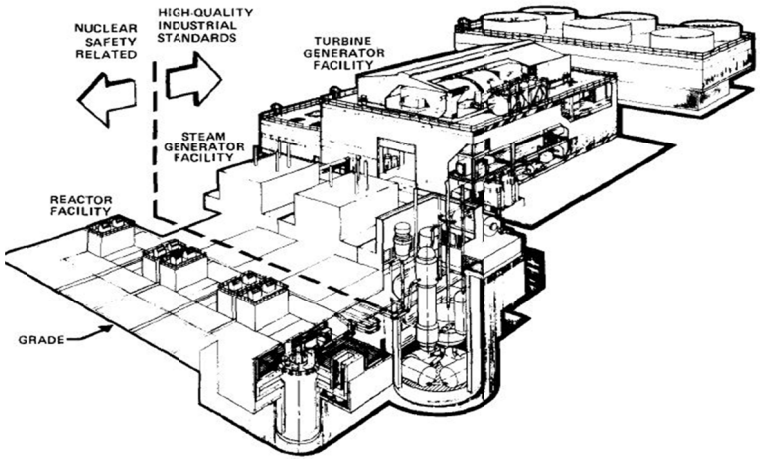

Figure 2.2 PRISM power block [Kwant and Boardman 1992].

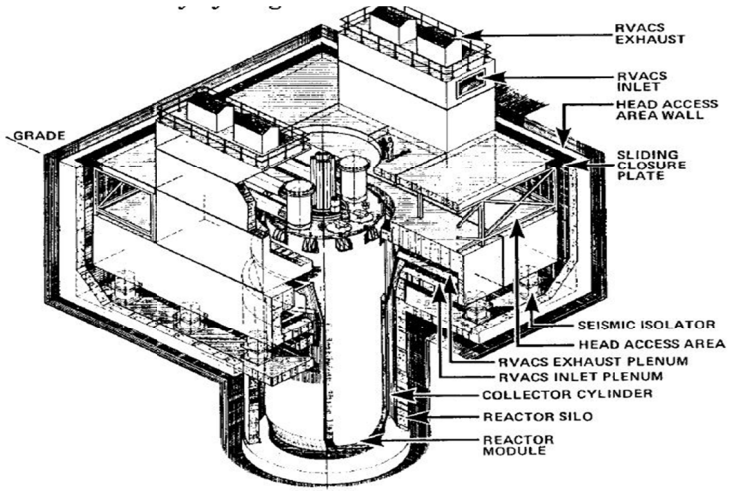

Figure 2.3 Schematic of reactor and base isolator [Tajirian et al. 1990].

The reactor module, RVACS, and head access area structures are seismically isolated in the horizontal direction with a fundamental frequency of 0.75 Hz. The isolated system responds to horizontal ground motion essentially as a rigid body with little amplification of ground acceleration. This limits the inertial loads and increases the structural design margins for the critical systems, components, and structures. Also, the reduction in the relative displacement between the components minimizes the forcing function for seismic interference between the control rod drives with their guide elements. The combined effect of decreased load transfer and decreased relative displacements is to increase the reactor capacity to sustain horizontal seismic loads by a factor of three. Another advantage of seismic isolation is that the nuclear island's response is insensitive to the soil properties at the site [Kwant and Boardman 1992].

The entire isolated structure weighs approximately 40 MN (9000 kip) and is supported on 20 large-diameter steel-laminated elastomeric bearings; it is housed in an underground silo as shown in Figure 2.3. The elastomeric compound used consists of a highly filled, high-damping natural rubber [Derham et al. 1985]. According to Tajirian et al. [1990], the relatively high shape factor (HSF) of the isolation bearings provides sufficient intrinsic stiffness in the vertical

direction to minimize amplifications due to vertical ground motions, making vertical isolation unnecessary. The seismic design basis was a design safe shutdown earthquake (SSE) with a maximum horizontal and vertical acceleration of 0.3*g*. Additional analysis has also been done to determine the cost of raising the SSE capability from the original 0.3*g* to 0.5*g* for zones of higher seismicity [Gyorey et al. 1992].

The main parameters governing the design of the bearings are the required horizontal and vertical stiffness and the allowable shear strains for different earthquake levels. The frequency goals are a horizontal frequency of 0.75 Hz and a vertical frequency of 20 Hz. The allowable shear strain during an SSE event was taken as 50%. The maximum horizontal displacement in the bearings for this condition is 190 mm (7.5 in.) [Tajirian et al. 1992]. The bearings are 1.3 m (52 in.) in diameter and (23.1 in.) high. Each bearing consists of thirty layers of 12.7-mm- (0.5-in.-) thick rubber bonded to 29 steel shims; see Figure 2.4. By using thin layers of rubber bonded to several steel shim plates, it was possible to achieve a high vertical stiffness. Such bearings are known as HSF bearings.

An extensive experimental program was undertaken at UC Berkeley to investigate the performance characteristics of the PRISM HSF bearings. Eight half-scale bearings were tested as well as several quarter-scale bearings. The series of tests included: vertical tests, horizontal tests, extreme horizontal tests, an ultimate vertical load test, and a buckling load test. To determine the preferred connection type for nuclear applications, two methods for connecting the bearing assembly to the adaptor plates were investigated: dowel type connections and bolted configurations [Tajirian and Kelly 1988; Mazda et al. 1989; and Kelly et al. 1990].

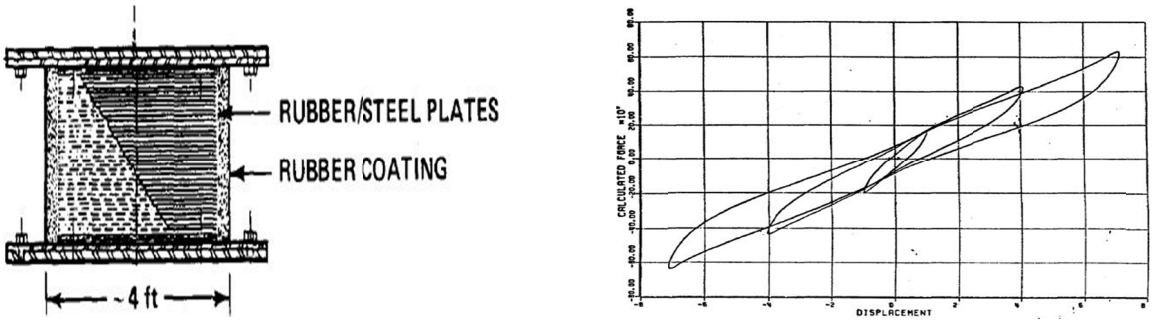

(a) Schematic of bearing **(b) Hysteresis loop for cyclic shear test**

Figure 2.4 Bearing used in the project [Tajirian et al. 1992].

2.3 THE SODIUM ADVANCED FAST REACTOR (SAFR)

2.3.1 Project Description

The Sodium Advanced Fast Reactor (SAFR) was designed by Rockwell International. SAFR utilizes LMR technology to provide an innovative power system, which is reportedly inherently safe, reliable, and cost competitive with alternate energy options [Johnson et al. 1988]. SAFR is a modular power system that uses a 900 MW (thermal) reactor to generate superheated steam, which drives a 350 MW turbine. The SAFR reactor assembly is shown in Figure 2.5. The vessel is 11.9 m (39 ft) in diameter, and 14.6 m (48 ft) high. The reactor assembly module is a standardized shop-fabricated unit housed in a building constructed above grade with plan dimensions of 37.8 m (124 ft) × 25 m (82 ft); see Figure 2.6. The entire SAFR building, which weighs 280 MN (63,000 kip) is supported on 100 seismic isolators; see Table 2.3 for a general summary of specifications for the SAFR reactor.

The SAFR design provides vertical as well as horizontal isolation. The design horizontal frequency is 0.5 Hz, and the vertical frequency is 3 Hz. This is achieved by using bearings with thicker rubber layers bonded to fewer steel shims, resulting in bearings that are flexible both vertically and horizontally [Tajirian et al. 1990]. The bearing is 1.08 m (42 in.) in diameter and 413 mm (16.25 in.) high. Each bearing consists of three layers of 101-mm- (4-in.-) thick rubber, resulting in a low shape factor (LSF) of 2.3. The seismic design basis was a SSE with a maximum horizontal and vertical acceleration of 0.3*g*. Additional analysis was performed to determine the cost of raising the SSE capability from the original 0.3*g* to 0.5*g* for zones of higher seismicity.

Dynamic analyses were performed by Tajirian et al. [1990] to compare the response of SAFR with and without isolation. Figure 2.7 compares the horizontal and vertical response spectra at the reactor supports. The isolated system resulted in substantial reductions in horizontal accelerations at all the equipment resonant frequencies. In the vertical direction, the response was amplified at the vertical isolation frequencies but was reduced at frequencies greater than 4 Hz, which is the vertical frequency of the range of equipment. The maximum SSE horizontal displacement of the bearings was 229 mm (9 in.). Small amounts of uplift due to rocking were computed in unanchored corner bearings.

The same tests done at UC Berkeley for the SAFR project were conducted for the PRISM project. The tests for the LSF bearings were performed to demonstrate the feasibility of using LSF bearings and to verify the validity of the design equations. Six quarter-scale bearings were tested. Two types of rubber compound (filled high-damping rubber versus unfilled rubber) and two types of end plate connection (dowelled versus bolted) were investigated [Aiken et al. 1989].

Table 2.3 General summary of specifications for the SAFR reactor.

Reactor capacity:	900 MW
Reactor containment building weight:	Reactor containment building weight: 280 MN (63,000 kip) for the whole isolated structure
Dimension:	Reactor vessel diameter of 11.9 m (39 ft.), height of 14.6 m (48 ft)
Design safe shutdown earthquake	Horizontal: 0.3*g*, Vertical: 0.3*g*
Bearing type:	Low shape factor laminated rubber bearing
Base isolation system:	Both horizontal and vertical isolation, 100 bearings

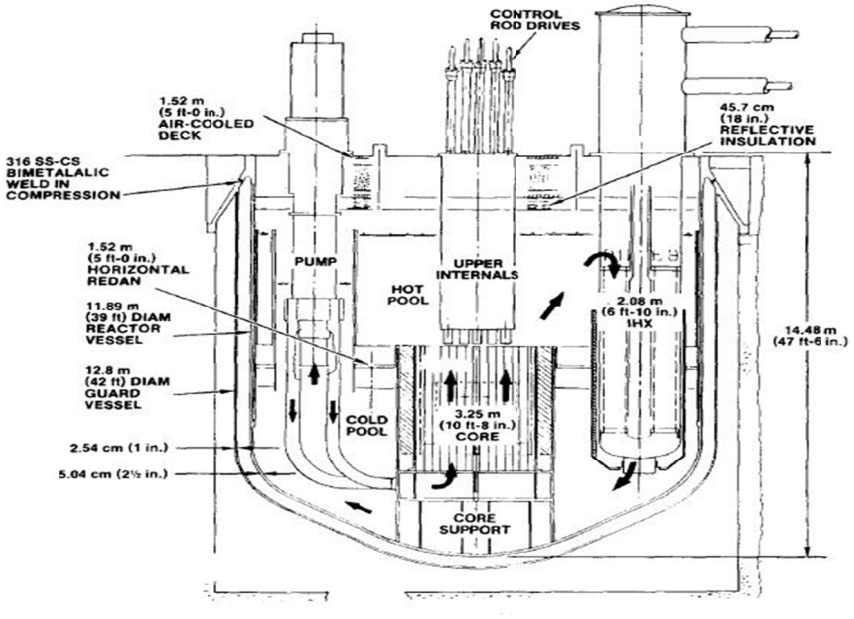

Figure 2.5 Schematic of SAFR reactor [Johnson et al. 1988].

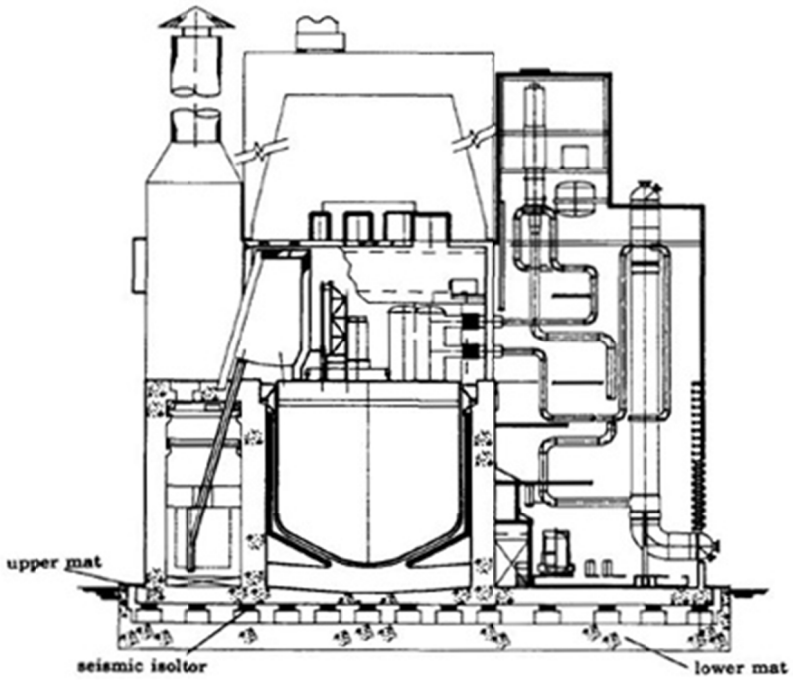

Figure 2.6 Schematic of isolated system for the SAFR design [Tajirian et al. 1990].

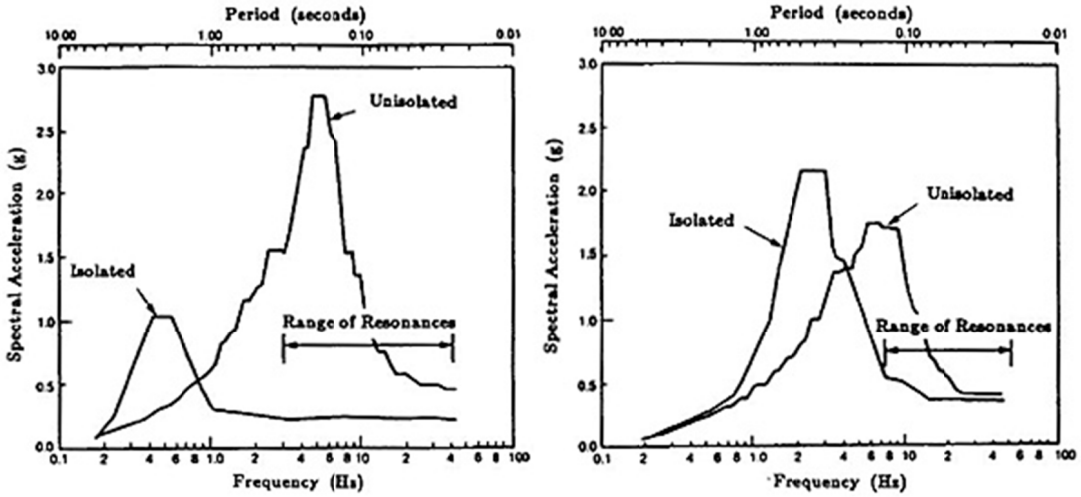

Figure 2.7 Comparison of horizontal and vertical response spectra for SAFR design [Tajirian et al. 1990].

2.4 ADVANCED DEMONSTRATION FAST BREEDER REACTOR PLANT (DFBR)

2.4.1 Project Description

In the course of developing a Japanese Fast Breeder Reactor (FBR), the experimental FBR "Joyo" has operated satisfactorily, and the prototype FBR "Monju" has achieved criticality. These successes have led Japanese utilities to consider construction of a demonstration fast breeder reactor "DFBR" with subsequent commercialization of the FBR design around the year

2030 [Ueta et al. 1995]; see Table 2.4 for a general summary of specifications for the DFBR reactor.

The design study for the DFBR was conducted by the Japan Atomic Power Co. (JAPC), which is the principal organization entrusted by nine electric power companies and the Electric Power Development Co. Ltd. to investigate construction of the DFBR. Construction of a FBR plant in a seismically vulnerable country like Japan must be very sensitive to seismic design requirements. Given Japan's seismicity, many consider base isolation as the optimum design approach for FBRs [Kato et al. 1991].

In 1987, a testing and research program was begun under contract with the Ministry of International Trade and Industry (MITI) to verify the reliability and effectiveness of seismic isolation for the FBR. It was intended to select appropriate seismic isolation concepts and then determine their effectiveness and feasibility, and finally to develop a rough draft of design technical guidelines [Sawada et al. 1989]. A schematic of the isolated system is shown in Figure 2.8.

In the conceptual design phase, several seismic isolation concepts were proposed and compared, including building isolation, component isolation, and combined isolation. From a preliminary study of construction costs, the horizontal building isolation requires the smallest number of bearings and was expected to result in ample cost-reduction savings. The project contained two phases discussed below.

Table 2.4 General summary of specifications for the DFBR reactor.

Reactor containment building weight:	10,000 kN (2248 kips) for whole isolated structure
Dimension:	Reactor vessel diameter of 11.9 m (39 ft.), height of 14.6 m (48 ft)
Design safe shutdown earthquake	Horizontal: 0.3*g*, Vertical: 0.3*g*
Bearing type:	Laminated rubber bearing
Base isolation system:	Horizontal only; 175 bearings

2.4.2 Phase 1: Horizontal Seismic Isolation System for the DFBR

Design and analysis studies have been completed on the seismically isolated reactor containment building (RCB). The arrangement of the bearings and a schematic of the isolated RCB are shown in Figure 2.9. The isolation system is composed of laminated rubber and steel bar dampers; see Figure 2.10.

The results of the analytical studies show the base-isolated FBR plant is capable of resisting very large seismic motions. The study reported that severe seismic loads were not transmitted to safety related components [Kato et al. 1991]. The ultimate state of the system was also investigated. Studies showed that the isolation layer has an appreciable seismic safety margin for the design-basis SSE considered. Torsional response of the plant was investigated using a special numerical model consistent with computational capabilities available at the time of the study. The analysis results show that torsion had insignificant influence on the total

response. However, the rocking response of the isolated DFBR building has a much larger influence on the ultimate behavior [Kato et al. 1995b].

Besides the preliminary analytical studies, an additional test and research program was begun in 1987 by the Central Research Institute of Electric Power Industry (CRIEPI) under contract with Ministry of International Trade and Industry (MITI). These studies supported development of the design of the demonstration reactor. The studies were intended to select appropriate seismic isolation concepts, to determine their effectiveness and feasibility, and to develop a rough draft of design technical guidelines [Shiojiri 1991].

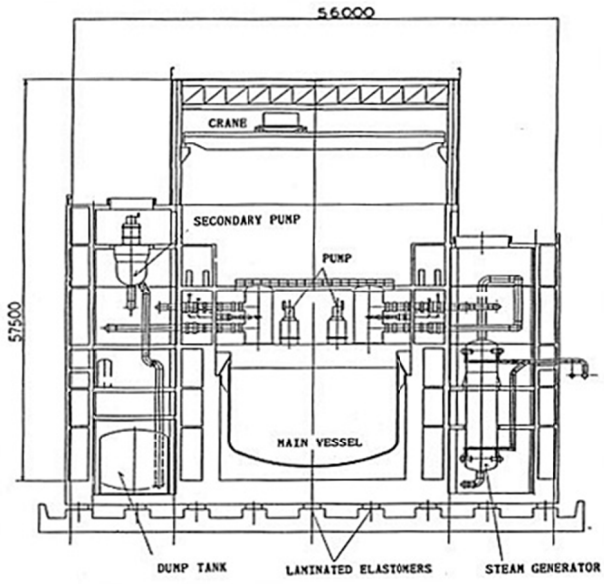

Figure 2.8 Schematic of seismic isolated system [Sawada et al. 1989].

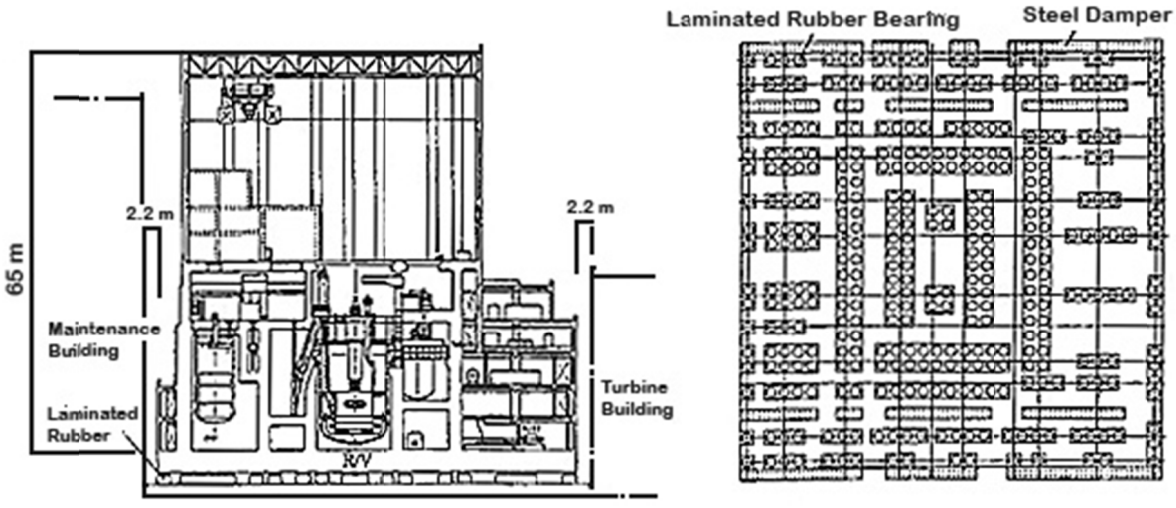

Figure 2.9 Layout of bearing and schematic of isolated reactor containment building for the DFBR [Kato et al. 1991].

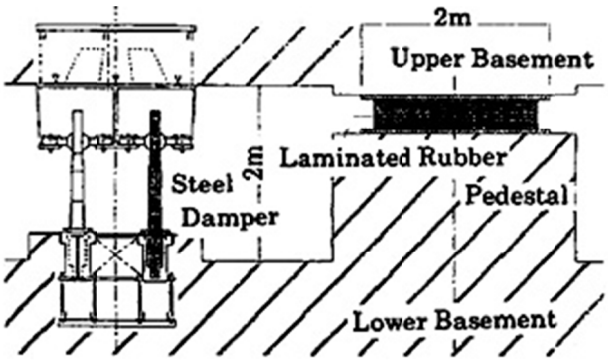

Figure 2.10 Rubber bearing with steel damper system for the DFBR [Kato et al. 1995a].

2.4.3 Phase 2: Development of 3D Isolation System for DFBR

The seismic isolation technology developed for the DFBR project in the horizontal direction occurred largely from 1987–1997. This resulted in the publication of a design guideline for the horizontal seismic isolation system [JEAG 2000]. However, a remaining challenge was to mitigate the seismic loads in the vertical direction. Therefore, a large-scale project on designing a three-dimensional seismic isolation system for FBR began in 2000 [Kato et al. 2003].

Two types of three-dimensional seismic isolation systems were selected for the DFBR based on practicality and cost-effectiveness. One approach was an integrated three-dimensional Seismic Isolation System (3D SIS); the other approach was a local vertical isolation system for the main components within a plant already outfitted with a horizontal base isolation system (V+2D SIS).

The development of the 3D isolation system was established by collecting ideas from major private companies in Japan involved in the development of FBRs. For the V+2D SIS, dish springs were selected as the vertical isolation device. The dish springs were thought to be efficient from the perspective of design, layout, maintenance, and economy. Both concepts required testing of large-scale specimens to verify the design concept and validate design and analysis methods.

The three-dimensional isolated systems studied included:

- A three-dimensional base isolation system incorporating a hydraulic mechanism [Kahiwazaki et al. 2000]; see Figure 2.11a.
- A three-dimensional seismic isolation system using a hydraulic cylinder [Kajii et al. 2000]; see Figure 2.11b.
- Double metal bellows air pressure springs with LRBs as an integrated three-dimensional seismic isolator [Nakamura et al. 2000]; see Figure 2.11(c).
- A cable reinforced three-dimensional base isolation air spring [Kageyama et al. 2000]; see Figure 2.11d.

- A three-dimensional seismic isolation device with laminated rubber bearings and rolling seal-type air springs [Suhara et al. 2000]; see Figure 2.11e.

For the DFBR project, extensive testing was conducted. Besides bearing tests, shaking table tests were also carried out to prove the effectiveness of base isolation and to study the behavior of the isolated system. To grasp the ultimate behavior of the seismically isolated DFBR plant under earthquakes at a level beyond the design ground motions and to establish ultimate strength design methods for the seismic isolators, a series of shaking table tests were conducted on a large seismically isolated test specimen using the "E-Defense" shaking table in Japan.

The test specimen consisted of concrete mass blocks and an isolation layer with six lead-plug laminated rubber bearings (LRBs). A superstructure consisting of reinforced concrete (RC) walls and additional concrete and steel plate masses was incorporated in the specimen design. The gross mass of upper structure of the test specimen was about 5.3 MN (1191 kip). The diameter of the 1/3-scale LRBs used was 505 mm (18.9 in.). The test configuration is shown in Figure 2.12, and the original reactor schematic considered in the test is shown in Figure 2.13.

Three behaviors were assumed as the ultimate behavior of the seismic isolation system: (1) loss of response reduction function of isolation system by hardening of rubber; (2) nonlinear response behavior by the cracking of the concrete wall; and (3) braking of the LRB. The test specimen was designed to show the ultimate behavior in the above-mentioned order.

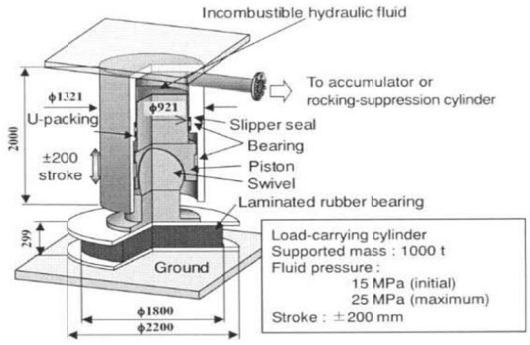

(a)

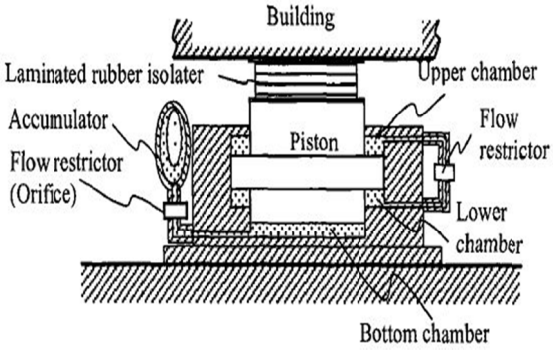

(b)

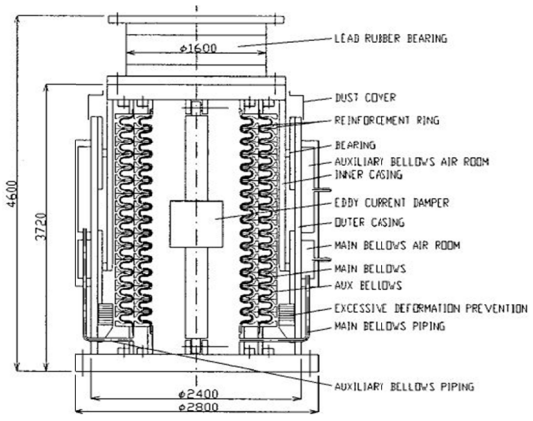

(c)

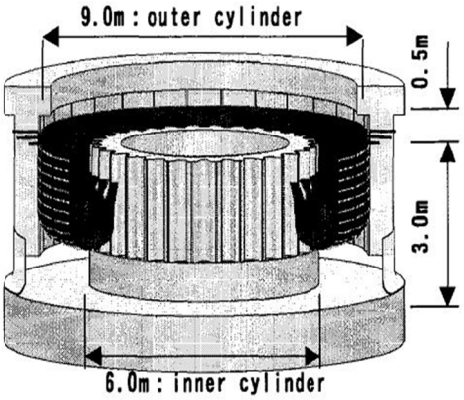

(d)

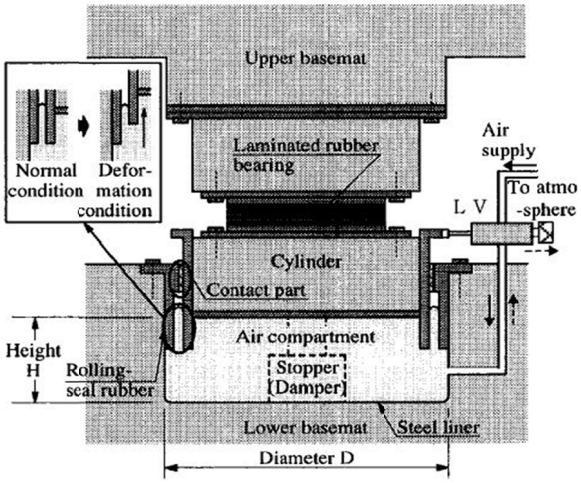

(e)

Figure 2.11 Schematic of five proposed types of three-dimensional isolation systems.

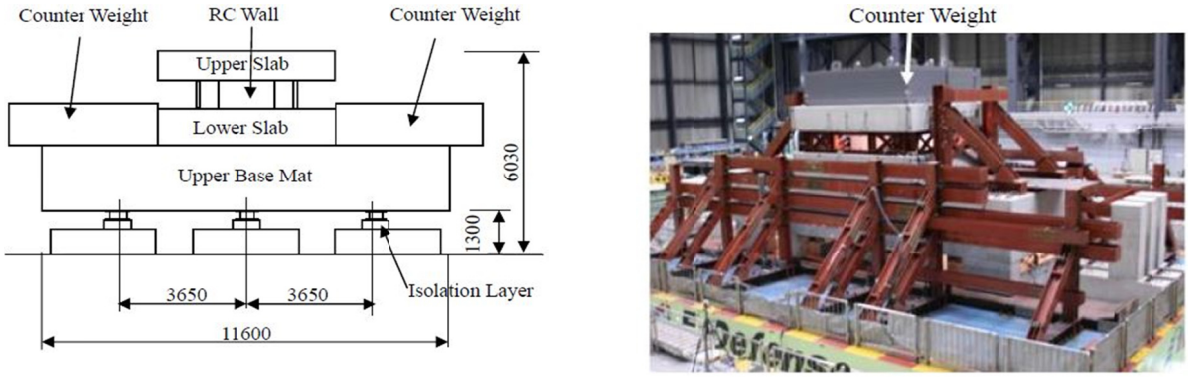

(a) Schematic of specimen **(b) Photo of test**

Figure 2.12 Setup of the shaking table test for the DBFR project [Kitamura 2009].

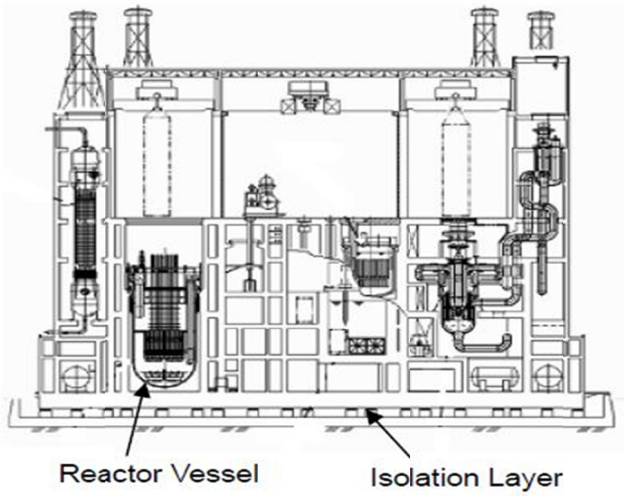

Figure 2.13 Original design of the DFBR considered as the basis of the test specimen shown in Figure 2.12 [Kitamura 2009].

2.4.4 Shaking Table Tests and Analysis Model with High-Damping Rubber Bearings for the DFBR

High-damping laminated rubber bearings (HDRB) were also considered as one of the three types of base isolation systems for the demonstration DFBR project. The seismic isolation specifications of these prototype devices were that the period associated with the initial loading (elastic) stiffness of the bearing should be T_1 = 1.0 sec, the effective period associated with the post-yield tangent stiffness of the bearing should be T_2 = 2.0 sec, and the yield strength ratio to the total building weight was 0.1. The design axial capacity of these devices was about 4.45 MN (1000 kip). A series of shaking table tests employing a scaled model were conducted for the purpose of verifying seismic safety and adequacy of analytical methods. Subsequently, simulation analyses of the shaking table tests were carried out considering several variations of the parameters used to characterize the seismic isolation system [Watanabe et al. 2000a; 2000b].

The shaking table test model is shown in Figure 2.14. The model represents the dynamic characteristics of the DFBR. The specimen was taken to be a 1/15.3 scale model of the prototype. Similitude was followed so that both acceleration and stress were equal in the model and prototype. The superstructure, for which the proportions are the same as for the DFBR, consisted of a three-story steel frame. The center of gravity was located on the second floor. The configuration of the specimen HDRB is shown in Figure 2.15. The bearing was 92 mm (3.6 in.) in diameter with a total rubber thickness equal to 16 mm (0.63 in.).

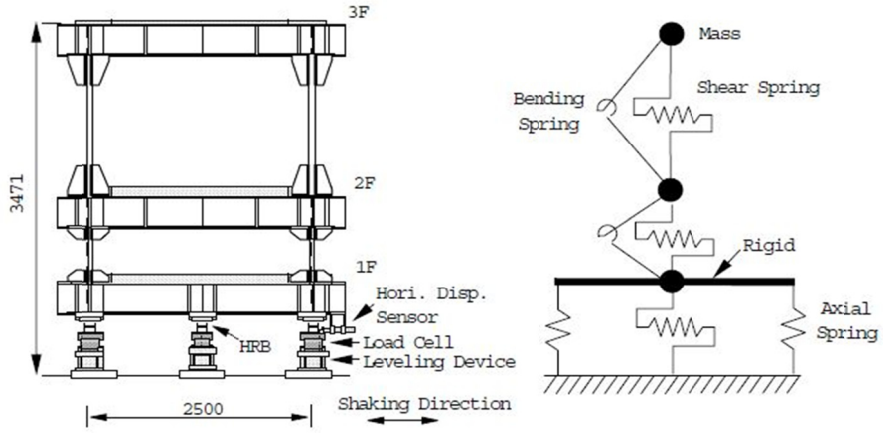

Figure 2.14 Test specimen and analysis model for DFBR with high-damping rubber bearings [Watanabe et al. 2000a].

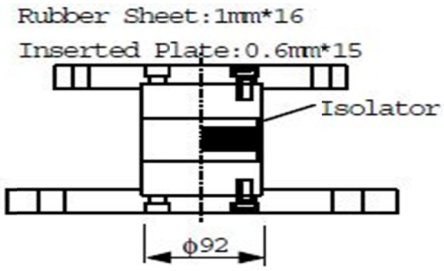

Figure 2.15 Schematic of high-damping rubber bearing used in the test ([Watanabe et al. 2000a].

2.5 FAST REACTOR CYCLE TECHNOLOGY DEVELOPMENT (FACT) PROJECT (JSFR)

2.5.1 Project Description

The Japan Atomic Energy Agency (JAEA) undertook a conceptual design study for the Japan Sodium Cooled Fast Reactor as part of the Fast Reactor Cycle Technology (FaCT) Research and Development project. The plant design aimed to achieve improved economic competitiveness, enhanced safety, and increased reliability. Commercialization of this plant concept is scheduled for ~2050. It is envisioned as a sodium-cooled fast reactor with a power output of 1500 MW and includes other innovative technologies; see Table 2.5 for a general summary of specifications for the FaCT reactor.

Due to the thin walled nature of many components of Japanese SFR designs, a seismic isolation system was employed to reduce the seismic forces. This was in large part due to the sensitivity of the systems, components, and equipment to severe ground motion [Okamura et al. 2010]. Following the Niigata-ken Chuetsu-oki earthquake in 2007, design criteria became more stringent and required that seismic forces acting on critical components be reduced to less than that of those considered in the development of previous seismic isolation systems. As such, a new advanced seismic isolation system was developed using laminated rubber bearings that were thicker than the previous ones in conjunction with oil dampers.

The RCB and the seismic isolation system of JSFR are shown in Figure 2.16. The seismic isolation system is installed between an upper base mat and a lower base mat. An isolation bearing and energy-dissipation device are shown in Figure 2.17.

Table 2.5 General summary of specifications for the FaCT reactor.

Reactor capacity:	1500 MW
Bearing:	Laminated rubber bearings

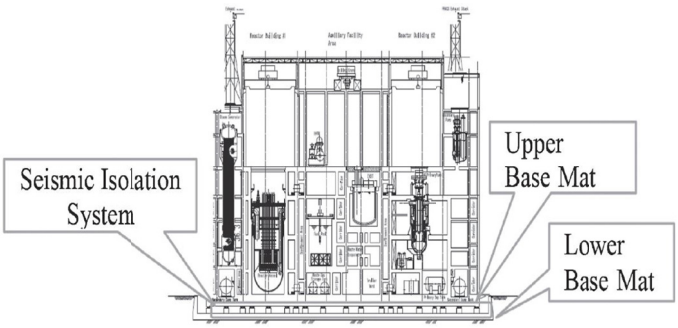

Figure 2.16 FAcT reactor containment building and seismic isolation systems [Okamura et al. 2011].

Figure 2.17 Thick laminated rubber bearings and oil dampers used in the FAcT reactor facility [Okamura et al. 2011].

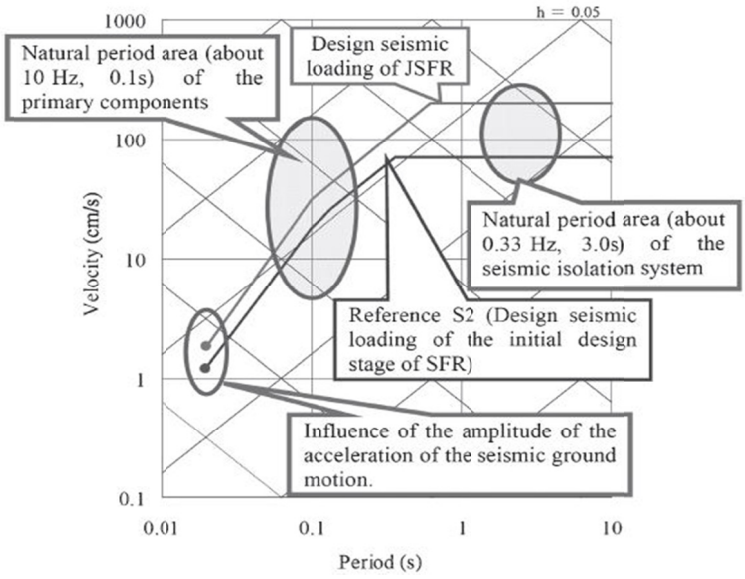

Figure 2.18 Design seismic loading of FAcT JSFR [Okamura et al. 2011].

The design seismic loadings of JSFR are shown in Figure 2.18. The Reference S2 wave was the preliminary design seismic loading of the initial design stage of SFR. To improve its seismic resistance, the design seismic loading was increased to be greater than for JSFR; see Figure 2.18. Vertical seismic loads were assumed two-thirds of the horizontal seismic loads.

The study shows that the advanced isolation system mitigates the horizontal seismic force through the thicker laminated rubber bearings with a longer period; the adoption of oil dampers in lieu of steel bar dampers improved damping performance. Moreover, the thicker rubber laminations of the bearings mitigated the vertical seismic force, resulting in a longer period. The margin of safety in design was reportedly increased by using bearings and viscous dampers in tandem. The natural period of the system in the horizontal direction was 3.4 sec and 0.125 sec in the vertical direction. The diameter of the bearing was set at 1600 mm (63 in.).

2.6 SECURE, TRANSPORTABLE, AUTONOMOUS REACTOR-LIQUID METAL (STAR-LM)

2.6.1 Project Description

The Secure, Transportable, Autonomous Reactor–Liquid Metal (STAR-LM) is a small reactor module for 300-MW steam supply of using lead-bismuth as a heavy liquid-metal coolant. The reactor structure for STAR-LM includes a reactor module, four steam generators, a coolant module, and a guard vessel. It is shown schematically in Figure 2.19. The outside diameter and thickness of the module is assumed to be 12.65 m (41.5 ft) and 5.0 cm (2 in.), respectively. The coolant vessel, which is a welded structure of stainless steel, has an outside diameter of 5.5 m (18 ft) and is 14 m (45.9 ft) high and 5 cm (2 in.) thick. The coolant vessel is contained in a guard vessel has an outside diameter of 5.85 m (19.2 ft.), is 14.2 m (46.6 ft.) long and 25 mm (1 in.) thick. The total weight of the reactor structure without and with the coolant inside of the coolant

module are about 3.56 MN (800 kip) and 27.6 MN (6200 kip), respectively; see Table 2.6 for a general summary of specifications for the STAR-LM reactor.

The nuclear island in which the reactor structure is contained is designed to be a seismically base-isolated RCB with an SSE of 0.3*g* in horizontal direction and 0.2*g* in the vertical direction. Two isolation systems were studied: a two-dimensional seismic isolation system and a three-dimensional seismic isolation system.

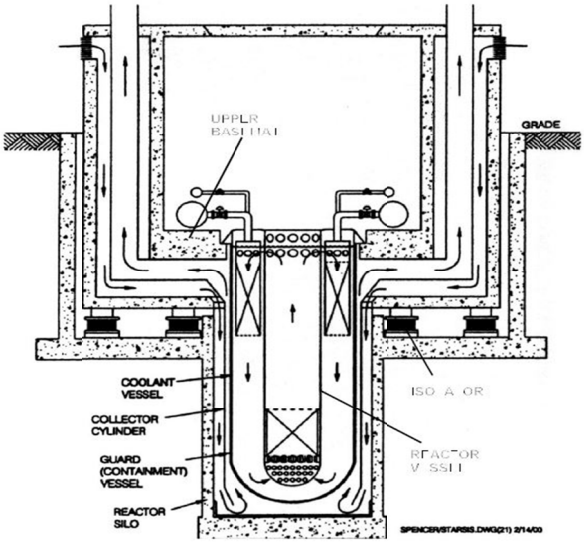

Figure 2.19 Schematic of STAR-LM reactor [Yoo et al. 2002].

Table 2.6 General summary of specifications for the STAR-LM reactor.

Reactor containment building weight:	27.6 MN (6200 kip) for whole isolated structure
Dimension:	Reactor vessel diameter of 5.5 m (18 ft), height of 16.9 m (55.4 ft.) Thickness 0.05 m (2 in.)
Design safe shutdown earthquake (SSE)	Horizontal: 0.3*g*, Vertical: 0.2*g*
Bearing type:	Laminated rubber bearings
Base isolation system:	Both two dimensional and three dimensional

2.6.2 Two-Dimensional Isolation System for STAR-LM Reactor

High-damping laminated rubber bearings were used. The vertical design load was selected to be 2.85 MN (640 kip) and the horizontal isolation frequency and the vertical frequency were set to be 0.5 Hz and 21 Hz, respectively. Design displacement in the horizontal direction was 27.8 cm (10.9 in.). The isolators had an outside diameter of 120 cm (47.2 in.) and were 50 cm (19.7 in.) high with 29 rubber layers alternating with 28 layers of steel for a total height of 27.8 cm (10.9 in.). The design targets for the isolators were a damping coefficient of 12% and 300% maximum shear strain.

2.6.3 Three-Dimensional Isolation System for STAR-LM Reactor

A three-dimensional isolator was developed whereby HDRBs were designed to isolate horizontal seismic loadings, working in tandem with independent vertical isolation device that employed a series of disc springs oriented in the vertical direction. The resulting isolator assembly was effective in reducing both vertical and horizontal seismic loadings. The vertical design load and horizontal isolation frequency was 2.85 MN (640 kip) and 0.5 Hz, respectively. These values are the same as that for the two-dimensional isolator case.

When compared with the conventional fixed-base design, the two- and three-dimensional isolation systems reduced the floor accelerations in the horizontal direction by a factor of 4 at the upper basement and a factor of 20 at the bottom of the coolant vessel. Compared to the fixed-base system, the three-dimensional isolation system reduced the floor accelerations in the vertical direction by a factor of 2.4 at the upper base mat, and by a factor of 7.4 at the bottom of the coolant vessel.

The maximum shear displacement for the two- and the three-dimensional systems is calculated as 19.97 cm (7.9 in.), equivalent to 109% shear strain, which is well within the maximum shear failure limit of 300%. The maximum relative displacement in the vertical direction for the three-dimensional isolation system was 4.4 cm (1.7 in.).

2.7 KOREA ADVANCED LIQUID METAL REACTOR (KALIMER)

2.7.1 Project Description

The research and development program on the seismic base isolation system for the KALIMER NPP began in 1993 as a project by the Korean Atomic Energy Research Institute (KAERI) as a national long-term R&D program. The objective of this program is as follows: to enhance the seismic safety, produce an economic design, and standardize plant design through the development of technologies based on seismic base isolation for liquid metal reactors [Yoo. et al. 2000]; see Table 2.7 for a general summary of specifications for the KALIMER project. The original KALIMER design is shown in Figure 2.20. It produces 333 MW per reactor module. Subsequent designs are capable of generating significantly more power.

The design of the seismically isolated RCB of KALIMER is based on a 0.3*g* SSE. Laminated rubber bearings were proposed for the project. In order to understand the mechanical behavior of the proposed bearings, extensive tests on reduced-scale LRB specimens were performed [Yoo et al. 1995, 1997; Kelly et al. 1997]. Quarter-scale high-damping LRBs and 1/8-scale low-damping LRBs were tested. Several of the bearing specimens are shown in Figure 2.21(a). To investigate the seismic isolation capability and verify the seismic analysis methodology, shaking table tests were carried out with a test model designed to simulate the KALIMER RCB and structures [Yoo et al. 2000]; Figure 2.21(b).

Besides these tests, analysis methodologies using finite element (FE) methods were developed to predict the behavior of the LRB proposed for isolating KALIMER; the analysis results were compared with the test results. Once they were verified, numerical simulation models were then used to analyze the response of the seismic isolated KALIMER structure and critical systems and components.

The seismic design loads used in analyses are the operating basis earthquake (OBE) (0.15*g*) and SSE (0.3*g*). Seismic input motions were imposed in both the horizontal and vertical directions. The seismic responses of reactor structures were reduced significantly for acceleration and relative displacements in the horizontal direction: 0.11*g* for the OBE and 0.22*g* for the SSE. The responses are reduced around 14 times in IHX, nine times in EMP, and eight times in the reactor vessel liner, support barrel, and core compared to the non-isolated case. Note that in the vertical direction, significant response amplifications occurred in whole structure, which was due to the vertical structural frequency of 8.1 Hz located in the dominate excitation frequency band of the input motion.

Table 2.7 General summary of specifications for the KALIMER reactor.

Reactor capacity:	333 MW
Bearing:	Laminated rubber bearings

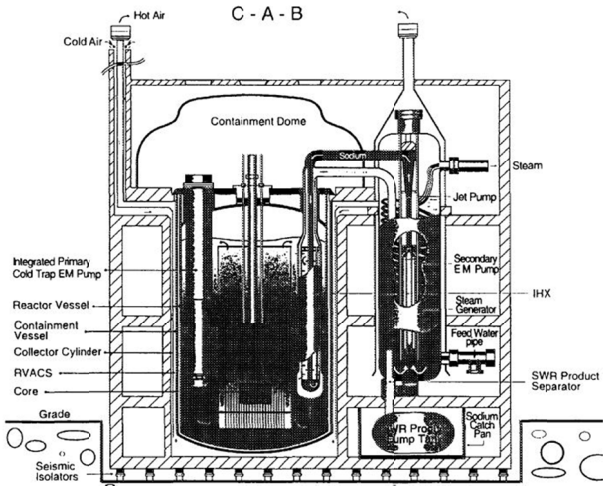

Figure 2.20 KALIMER reactor module and steam generator [Hahn et al 1995].

(a) Test LRB specimen

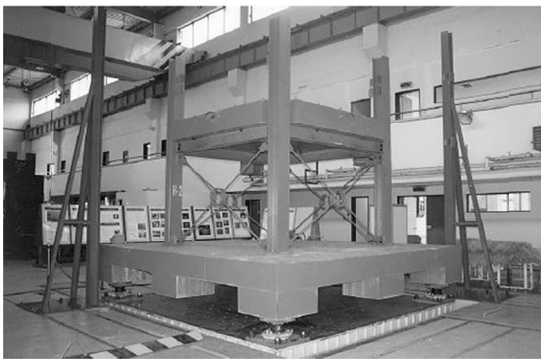

(b) Shaking table test for KALIMER

Figure 2.21 Set up of the shaking table test of the KALIMER [Yoo et al. 2000].

2.7.2 KALIMER-600

In recent years, KAERI has extended the development of KALIMER to include the mid-sized SFR called the KALIMER-600. Its design was intended to satisfy Generation-IV reactor design goals. Its conceptual design was completed in 2007. The main features of the structural design of KALIMER-600 were the seismically isolated RCB [Hahn et al. 2007]. The reactor vessel is 18 m (59 ft) high and 50 mm (2 in.) thick, with an outer diameter of 11.41 m (37.4 ft). The total reactor weight is nearly 24.9 MN (5600 kip). Seismic isolation between the ground and lower base mat in the KALIMER-600 uses 164 seismic isolators that are 1.2 m (47.25 in.) in diameter.

A total of 164 HDRBs are to be installed between ground and the lower base mat in the KALIMER-600 reactor and fuel-handling buildings. The seismic gap between the isolated RCB and the non-isolated wall is about 1.2 m (47 in.), which is sufficient to avoid contact even when the plant is subjected to a beyond-design earthquake with a peak ground acceleration (PGA) of 1.0*g* [Forni et al. 2012].

2.8 SEISMIC-INITIATED EVENTS RISK MITIGATION IN LEAD-COOLED REACTOR (SILER)

2.8.1 Project Description

SILER is a project partially funded by the European Commission aimed at studying and controlling the risk associated with Generation-IV Heavy Liquid Metal reactors subjected to seismic events and developing adequate protection measures in the event of such shaking. Attention is focused on evaluating the effects of earthquakes on the structures and most critical components, with particular regards to unexpected (beyond-design) events and the identification of mitigation strategies [Forni et al. 2012]; see Table 2.8 for a general summary of specifications for the SILER reactor.

Table 2.8 General summary of specifications for the SILER reactor.

Reactor capacity	600 MW (ELSY)
Reactor containment building weight:	2800 tons for whole isolated structure
Dimension:	Reactor vessel diameter of 11.4 m (37.3 ft.), height of 18 m (59 ft.), thickness 0.05 m (2 in.).
Design safe shutdown earthquake (SSE)	Horizontal: 0.3*g*, Vertical: 0.3*g*
Bearing type:	Laminated rubber bearings

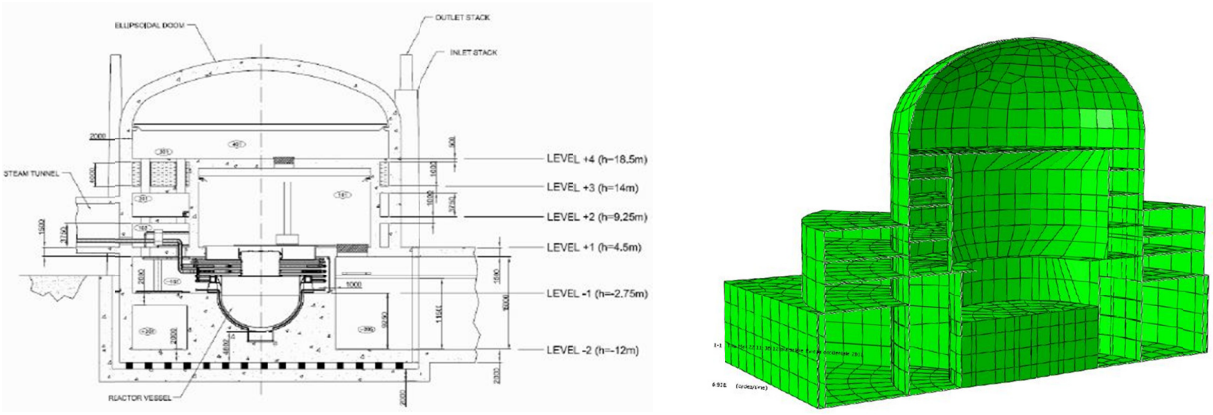

(a) Schematic of reactor containment building **(b) Finite-element node**

Figure 2.22 Schematic images of ELSY.

Two types of reactors were selected for this study:

1. **ELSY** (European Lead-Cooled System): The European Lead Fast Reactor began development in September 2006. The ELSY project is sponsored by the Sixth Framework Program of EURATOM. The ELSY reference design is a 600 MW pool-type reactor, cooled by pure lead, see Figure 2.22. As part of the framework of SILER, a complete seismic analysis of ELSY was carried out for both the isolated and fixed-base configurations.

2. **MYRRHA** (Multi-Purpose Hybrid Research Reactor for High-tech Application): MYRRHA is a flexible experimental accelerator-driven system being developed at the Belgium Nuclear Research Center, SCK.CEN. MYRRHA is intended as a replacement for its material-testing reactor, BR2. A sketch of the plant is shown in Figure 2.23. In the framework of SILER, a complete seismic analysis of MYRRHA in both isolated and fixed-base conditions will be carried out.

Two types of isolators are being considered in the SILER project: a HDRB [Figure 2.24(a)] and a LRB [Figure 2.24(b)]. The isolators developed in the SILER Project are expected to be tested in full-scale and realistic three-directional dynamic conditions up to failure, with the aim of carefully evaluating the safety margins in event of beyond-design earthquakes. Preliminary design of the seismic isolation system made up of HDRBs has been completed for both ELSY and MYRRHA using FE models. In both cases, seismic isolation was applied to the whole nuclear island.

The seismic gap is to be covered with a weatherproof joint capable of absorbing bi-directional horizontal displacements and to avoid infiltration of water into the vault where the isolators are installed. In addition, an expansion joint for the pipes crossing the seismic gap has been tested; see Figure 2.25. Additional tests of umbilical cords are expected to be carried out in the near future. In addition, a restraining mechanism using rubber bumpers to limit isolator

displacement was considered as shown in Figure 2.26. This “soft stop” is intended to protect the isolator from failure under larger-than-expected excitations. It limits the isolator deformation and softens the hammering between the isolated building and the foundation when lateral displacements exceed design values.

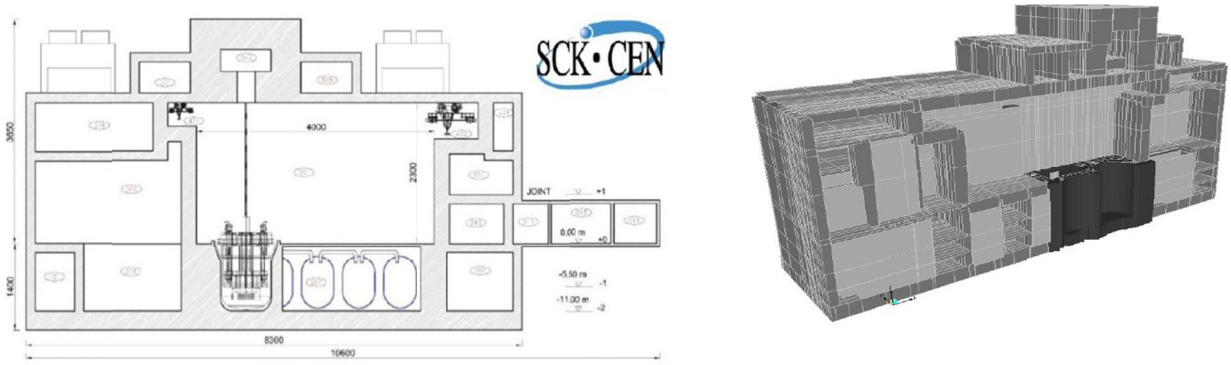

(a) Schematic of reactor containment building (b) Finite-element node

Figure 2.23 General layout of MYRRHA.

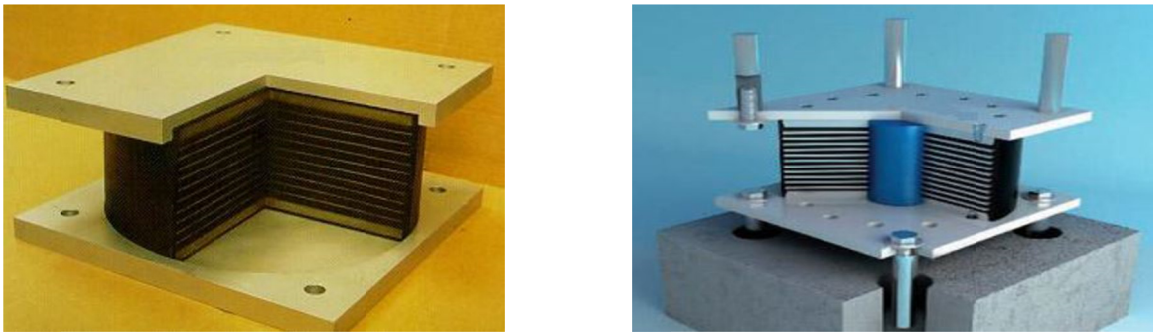

(a) Sample of high-damping rubber bearing (b) Sample of lead-rubber bearing

Figure 2.24 Schematic of bearings used for SILER.

Figure 2.25 Pipeline expansion joints being tested for SILER.

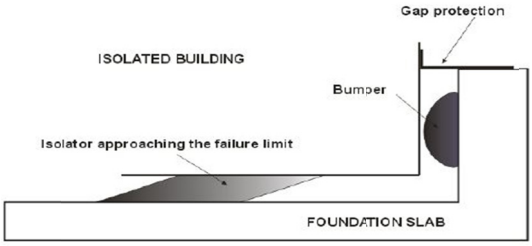

Figure 2.26 Schematic of bumper mechanism.

2.9 DISCUSSION OF CRITICAL ISSUES

Because fast reactor systems operate at virtually atmospheric pressure at high temperatures, the fast reactor vessels, piping, and other components tend to be very thin-walled and flexible. For most commercial NPPs, the high pressure of the system results in thick-wall pressure vessels and piping that are well suited to provide the strength, stiffness, and buckling resistance needed to resist seismic loads. However, the thin-wall components and piping and the heavy coolant used in fast reactors make conventional seismic design approaches for traditional NPPs insufficient in the event of strong ground shaking.

While it may be possible to increase the seismic capacity of the system, it may be more economical and reliable to reduce demands through the appropriate application of seismic isolation. This use of a robust, passive technology to improve the seismic safety of the plant is consistent with the passive approach to improving the operating safety of a Gen-IV Sodium-Cooled Fast Reactor. Seismic isolation technology has been extensively researched and investigated around the world for buildings, bridges, and industrial structures. As noted earlier, most fast reactor development programs have considered using one form of seismic isolation or another.

2.9.1 Isolation Strategy

In the design of any isolation system, the location of the isolators, the direction of the seismic input, and the type and mechanical characteristics of the isolation system must be selected. Most of the projects summarized above place the isolators between a base mat supporting the whole RCB and a mat foundation supported on the ground. It is not necessary to place the isolation plane at the base of a structure, and cases where the isolation plane is provided above this level or at multiple levels are not uncommon. Some isolation designs provide seismic isolation in the horizontal direction only, but some provide isolation in both the horizontal and vertical directions. Furthermore, some isolate the complete structure in the horizontal direction, but provide additional localized isolation of selected regions of the building or of components in the vertical direction. As outlined in studies of the very earliest DFBR project [Shiojiri et al. 1989], several isolation concepts are possible.

As illustrated in Figure 2.27, the most commonly used strategy in previous fast reactor studies is whole-building isolation, i.e., the isolation system is set under the whole RCB. This approach is versatile as it can provide isolation in the horizontal direction only or in both the horizontal and vertical directions. In the former case, the isolators might either transmit the

vertical components unreduced to the superstructure, or actually amplify the effects of vertical excitations. This may be a problem for many critical components and systems used in a fast reactor. Vertical isolation may solve some of these problems, but the system is susceptible to large vertical and rocking motions. The rocking motion can amplify long-period horizontal motions at the top of the structure. Zhou et al. [2013] sought to mitigate rocking motions by carefully selecting the vertical stiffness of the bearings, modifying the configuration of the plant so that the isolation plane is located near the center-of-mass of the supported structure, or by providing a mechanical or hydraulic anti-rocking mechanism.

Another isolation concept is to isolate the specific components inside the RCB that are particularly sensitive to horizontal and/or vertical vibrations. This approach is shown in Figure 2.28 where the reactor vessel is isolated at its top. This is the same approach used in the prior studies for the PRISM and STAR-LM plants. In this configuration, the RCB is not isolated; however, the internal primary component is.

In the case shown in Figure 2.28, the center-of-mass of the vessel is significantly below the isolation plane. Since the reactor vessel is a very heavy component within the whole system, the bearings supporting the vessel in this configuration will likely have higher axial loads than in the case of the whole-building isolation schematic. This helps the bearings resist possible tension loads due to vertical input motions and rocking response. Further reductions in rocking motions can be achieved by locating the bearing plane near the elevation of the reactor vessel's center-of-mass. Note that more than one local part of the plant could be isolated. There may be a practical limit to this approach due the increasing costs of providing multiple seismic gaps, umbilical cords, etc.

Any of the approaches using localized component or region isolation should expect relative displacement inside the building due to the relative movement of the piping system between the reactor vessel and generators, or other umbilical connecting the isolated and non-isolated portions of the plant. Special devices or expansion joints for the piping system or other umbilical cords to accommodate these relative movements may need to be developed and validated.

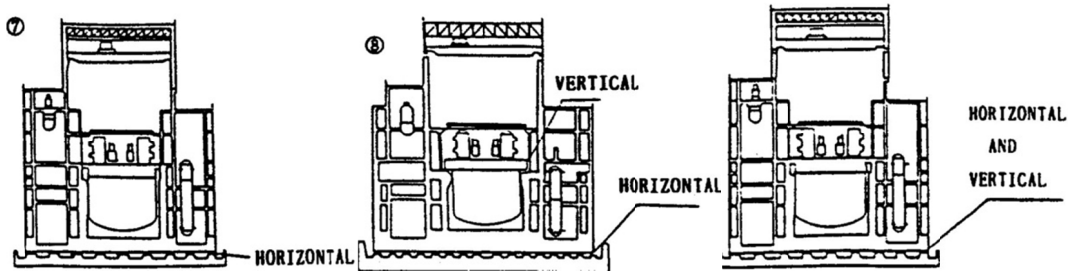

Figure 2.27 Different building isolation strategies [Shiojiri et al. 1989].

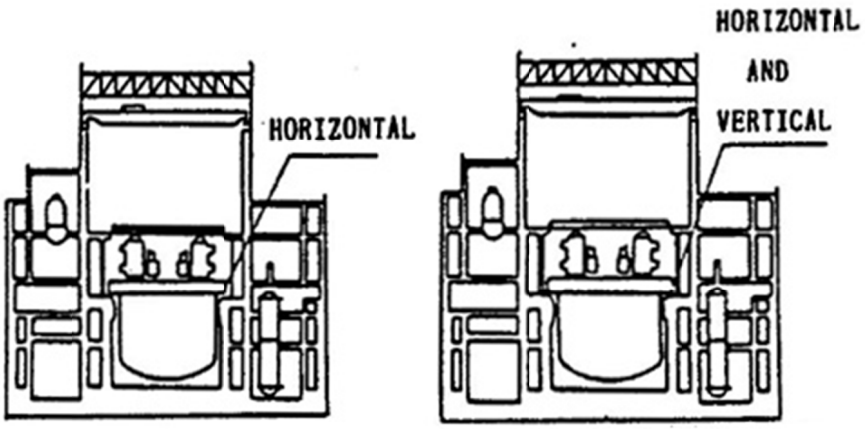

Figure 2.28 Primary component isolation strategy [Shiojiri et al. 1989].

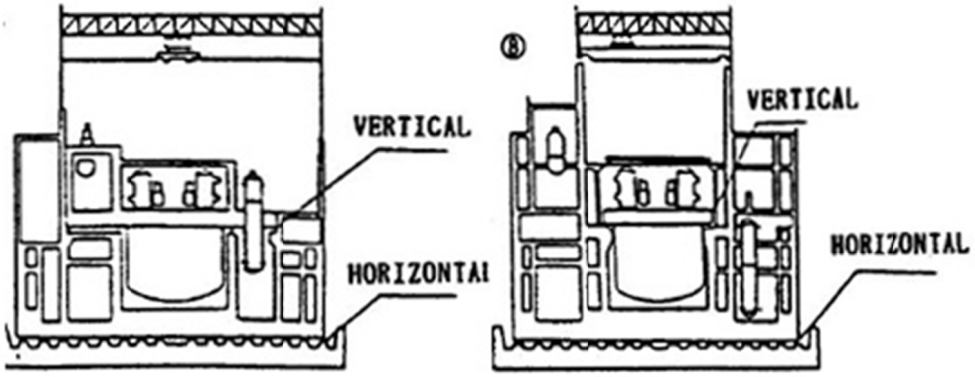

Figure 2.29 Combined isolation strategy [Shiojiri et al. 1989].

Another possibility is to combine the two strategies. A typical example is to isolate the whole building in horizontal direction and provide isolation for the internal equipment in the vertical direction; see Figure 2.29. A special application of this concept would be to provide horizontal and vertical isolation in a single plane, but to design the vertical isolation to have only limited effectiveness in reducing the rocking response. Supplemental vertical isolation can then be provided for those special components where extra protection in the vertical direction is needed.

For the horizontal direction, the isolation for the whole RCB and localized isolation of specific components provide similar response reduction effects; essentially, the wider the range of isolation, the better seismic response. The rocking response of the whole reactor needs to be determined and investigated if the whole RCB is isolated. In the case where the primary system is isolated, the relative displacement must be accommodated by deformation of the piping systems. Detailed investigation of methods for accommodating the displacement is needed.

For the vertical direction, it is generally difficult to obtain the optimal horizontal and vertical isolators properties. Separating the horizontal and vertical isolation is a promising strategy and will be discussed in more detail below. Ultimately, the selection of the isolation strategy should be based on the layout of the plant and the specific requirements of the project.

2.9.2 Vertical Isolation

Vertical isolation was considered in most of the projects reviewed above. There are two general approaches:

- Locally adding vertical isolation systems for individual components of the structure, which are already globally isolated against horizontal ground shaking.
- Using a complete three-dimensional seismic isolation solution.

As shown in Figure 2.30, Shojiri et al. [1989] studied implementing localized vertical isolation as a supplement to the horizontal isolation system. Localized vertical isolation requires a device to lower the vertical natural frequency and damp vibrations, as well as bear vertical loads due to gravity, vertical excitations, and overturning forces. For the project shown in Figure 2.30, coil springs were selected as the vertical load-bearing device. In other cases, metal disk springs or air springs have been used. Such springs are generally supplemented with oil dampers or other supplemental viscous dampers to provide damping in the vertical direction of vibration.

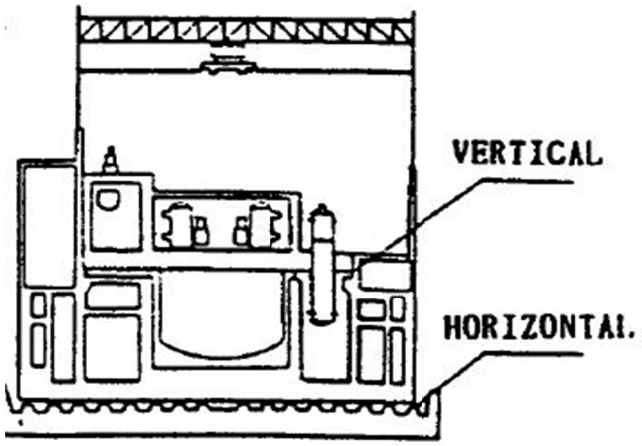

Figure 2.30 Localized vertical isolation [Shiojiri et al. 1989].

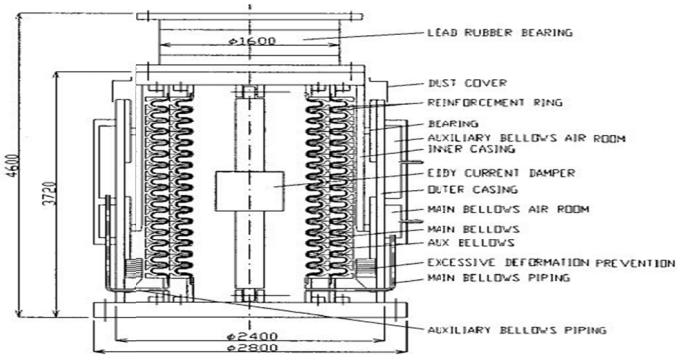

Figure 2.31 Schematic of one of the proposed 3D isolation system for DFBR.

Most fast reactor projects that consider vertical isolation use devices capable of providing three-dimensional isolation. Several approaches are available to incorporate the vertical isolation as part of a larger, comprehensive isolation assembly. One approach has been called partial three-dimensional approach as it is achieved by reducing the vertical stiffness of the original horizontal isolation system. This is most easily and commonly achieved using laminated elastomeric bearings. This was done for the SFAR project, which used LSF rubber bearings whereby thicker rubber layers are laminated to fewer steel shims. As a result, the bearings are more flexible vertically as well as horizontally [Tajirian et al. 1990]; bearings can be manufactured with a vertical design frequency of 3 Hz.

A number of studies have been carried out in Japan where the overall bearing subassembly incorporates a separate horizontal and vertical isolation mechanism. This approach was followed for Phase 2 of the DFBR project. Laminated rubber bearings that provide horizontal isolation for the superstructure are each supported on vertically oriented metallic, hydraulic or air springs (combined with vertical viscous dampers). Shown in Figure 2.31, this approach can provide isolation in both the horizontal and vertical direction. As pointed out earlier, however, the use of three-dimensional isolation system has the potential to introduce an additional rocking movement to the superstructure. Therefore, a detailed investigation is needed when considering a three-dimensional isolation system, and supplemental dampers and other mechanisms may be needed to suppress the rocking motion introduced. These mechanisms may reduce the effectiveness of the horizontal isolation and increase costs.

2.9.3 Seismic Gap Size and Hard or Soft Stops

Designers of isolation systems are required to provide a seismic gap to accommodate the relative displacements of the isolators; however, the size of the seismic gap is not well established. As noted previously, the U.S. NRC is developing guidelines that suggest that a NPP should have more than a 90% confidence of not exceeding the deformation capacity of the isolation system or contacting a hard stop for a large beyond-design-basis event. This can result in the need for a very large isolator capacity. In previous studies, the base isolation system has been sized for the design-level SSE. When analyzing the safety evaluation of the whole system, the margin of safety in beyond-design-level earthquakes requires providing both a reasonable seismic gap size and a suitable “stopping” mechanism.

Usually, the seismic gap size is selected according to the displacements expected at the design event plus some margin of safety. However, if a larger than expected event occurs, the resulting displacements may be larger than the size of the seismic gap. In such a case, contact between the lower mat of the RCB and the surrounding moat wall may induce large impact loads at the base of the isolated structure. This impact will propagate large forces and accelerations up the RCB.

The draft U.S. NRC guidelines for seismic isolated NPPs [Kammerer et al. 2012] require a hard stop; many researchers are exploring mechanisms to soften this stop to avoid intense impact loads. A solution to this critical problem is still under development. For the reviewed SILER project, a rubber bumper stopping mechanism was developed in order to absorb the impact energy. In other cases, the deformation hardening characteristics of recrystallizing rubber

bearings, HDRBs, and some types of friction bearings are being explored as a soft-stop mechanism.

Several investigations, including the E-Defense tests that were undertaken for the DFBR project in Japan, have examined approaches that exploit the behavior of the bearings themselves. However, the amount of energy absorbed by these soft-stop mechanisms may not be enough to limit the displacements and avoid the hard stop; additionally, the forces developed by the bearings may be large enough to still transmit unacceptably large forces and accelerations to critical structures, systems and components (SSCs). Therefore, to ensure an appropriate safety margin, seismic gap sizes need to be determined according to detailed analysis on the ultimate behavior of the isolation system.

3 PARAMETRIC STUDY OF A SEISMICALLY ISOLATED RIGID MASS

3.1 INTRODUCTION

Before investigating multi-degree-of-freedom analysis models, a parametric study was conducted using a simplified analysis model to generate nonlinear response spectra of the isolated NPP superstructure. This study assumed that the NPP superstructure consists of a rigid mass block with one isolator element representing all isolators in the isolation layer. Key design parameters of the isolator were studied through bi-directional response history analysis. The purpose of this simplified parametric study was to obtain a general sense of how the response of the isolated PGSFR will be affected by isolator properties. Furthermore, the parametric study illustrates how changing a design parameter of the isolation system influences the seismic response of the NPP and also provides guidance on isolation parameters that lead to improved response.

3.2 ANALYSIS MODEL

In this phase of the study, a rigid mass representing the reactor facility and one isolator bearing representing the whole isolation system, which can capture the bi-directional behavior, are defined. Initial isolator parameters were chosen to best capture the dynamic characteristics of the original isolation system as provided by KEPCO E&C. The MATLAB programming language for technical computing was used for modeling and numerical analysis.

3.2.1 Reactor Containment building Model

The RCB was simplified as a rigid mass with a total weight of 152,000 tonf (335,000 kip). Since the RCB is typically very stiff in both horizontal directions as well as in the vertical direction, it is reasonable to assume for the purposes of this preliminary study that it is a perfectly rigid mass block. No supplemental viscous damping was introduced, so the damping of the whole system was provided by the hysteretic behavior of the isolator only, which is an ideal case for a base-isolated structure. The two components of the simulation model are shown in Figure 3.1.

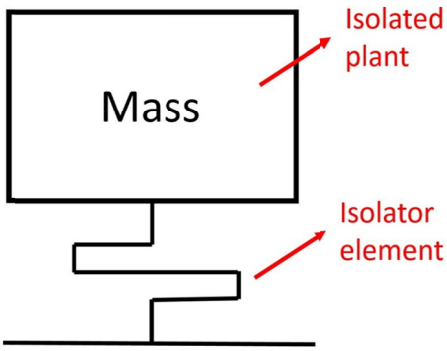

Figure 3.1 Simplified rigid-mass model for analysis.

3.2.2 Isolator Model

The type of isolator considered in these analyses was a LRB. Both a bilinear and a Bouc–Wen model were used to model the LRB, and results from the two modeling approaches were compared. Bi-directional numerical response-history analyses were conducted using dispersion-appropriate ground-motion sets, which are described in the next section. The hysteresis loops of the two bearing models are shown in Figure 3.2. The bilinear model is characterized by three parameters: Q_d, which is the characteristic strength or approximately the apparent yield force of the bearing, the initial stiffness K_0, and the post-yield stiffness αK_0 or the post-yield stiffness ratio α. For the Bouc–Wen model, the corners of the hysteresis loop were rounded instead of sharp as compared to the bilinear model. To characterize the sharpness of the hysteresis loop corners, the Bouc–Wen model utilizes an additional parameter η (η = 0.5 to 20), where smaller values produce more rounded corners and larger values produce sharper corners. The bearing moves in both horizontal directions simultaneously and captures the bi-directional behavior with a circular yield surface under two-component earthquake input conditions. No vertical–horizontal coupling—neither in terms of force or kinematic coupling—were considered in this rigid mass parametric study.

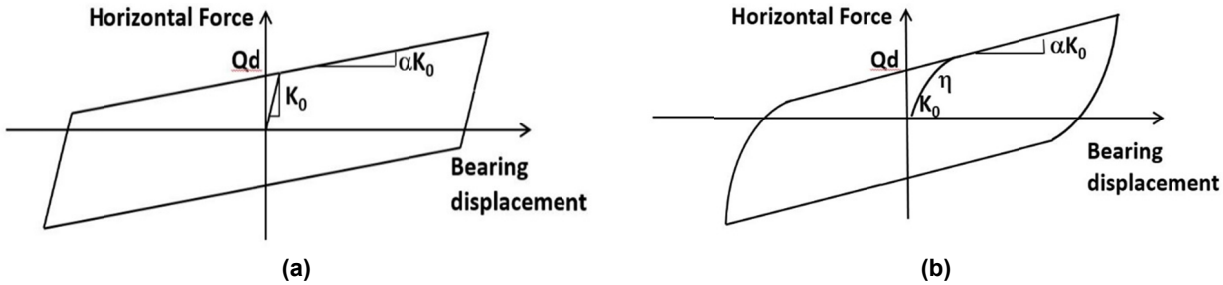

Figure 3.2 Hysteresis loops of the two bearing models used in the rigid mass analysis: (a) bilinear isolator model and (b) Bouc–Wen isolator model.

3.3 GROUND-MOTION SELECTION FOR ANALYSIS

To assess the performance of a seismically isolated NPP, it is important to select appropriate input ground acceleration histories in order to obtain unbiased estimates of the structural response of the isolation system and the plant superstructure. To perform the parameter studies described herein, ground-motion ensembles with a fairly large number of records were used. Such ground-motion ensembles are essential in performing meaningful studies of the behavior of seismically isolated NPPs and to develop a better understanding of the effect of seismic isolation on plant performance.

Regulatory Guidelines issued by the U.S. Nuclear Regulatory Commission (NRC) [NRC 2014] and European Utility Requirements (EUR) [EU 2012] were used to define target response spectra in the horizontal and vertical directions. Based on these target spectra, six different ground-motion sets were developed previously for a study on seismic isolation technology applied to the APR 1400 NPP, which PEER conducted for KEPCO E&C. For this previous study, PEER generated dispersion-appropriate, single-damping spectral-matched and multi-damping spectral-matched ground-motions sets for both the NRC and the EUR target response spectra scaled to a PGA of 0.5*g*.

No specific construction sites were given for this preliminary study, and the properties of the seismic isolation systems vary widely; therefore, to investigate their effectiveness in the application to PGSFR power plants, unconditional (structure- and site-independent) ground-motion records need to be utilized. Furthermore, in light of the USNRC draft NUREG on Technical Considerations for Seismic Isolation of Nuclear Facilities [Kammerer et al. 2013], which requires the assessment of probabilistic performance measures and confidence levels, it is essential to correctly characterize the dispersion of the ground motions and the dispersion of the caused structural response for design as well as beyond-design-level shaking intensities. Hence, this work used two of the earlier developed ground-motion sets, namely, the dispersion-appropriate sets based on the NRC and EUR target spectra. Both of these sets consist of 20 three-component ground motions; their development is described in detail in Schellenberg et al. [2014].

For this study, the design-level target spectra for the isolated NPP is set at a PGA of 0.3*g*, and the design-level target spectra for the fixed-base NPP is set at a PGA of 0.1*g*. It was therefore necessary to amplitude scale the ground motions from the previous study by 0.6 for the isolated plant analyses and by 0.2 for the fixed-base plant analyses. In addition, the high-frequency enrichment, which is added to the USNRC RG1.60 target spectrum, was left unmodified at 50 Hz instead of reducing it to 40 Hz, so that the NRC ground-motion set did not have to be regenerated but could simply be scaled to the required PGA levels.

The individual and mean pseudo-acceleration spectra and displacement spectra for the USNRC RG1.60 set of 20 dispersion-appropriate records scaled to a PGA of 0.3*g* are plotted in Figure 3.3 and Figure 3.4. The individual and mean pseudo-acceleration spectra and displacement spectra for the EUR 2.4.6 set of 20 dispersion-appropriate records scaled to a PGA of 0.3*g* are shown in Figure 3.5 and Figure 3.6. For the targeted effective isolation period of 2 sec, the expected mean isolator displacement demand from the EUR motion set is around 7.6 cm (3 in.) and around 25.4 cm (10 in.) for the NRC motion set, which is a factor of 3.3 larger than the demands produced by the EUR-motion set.

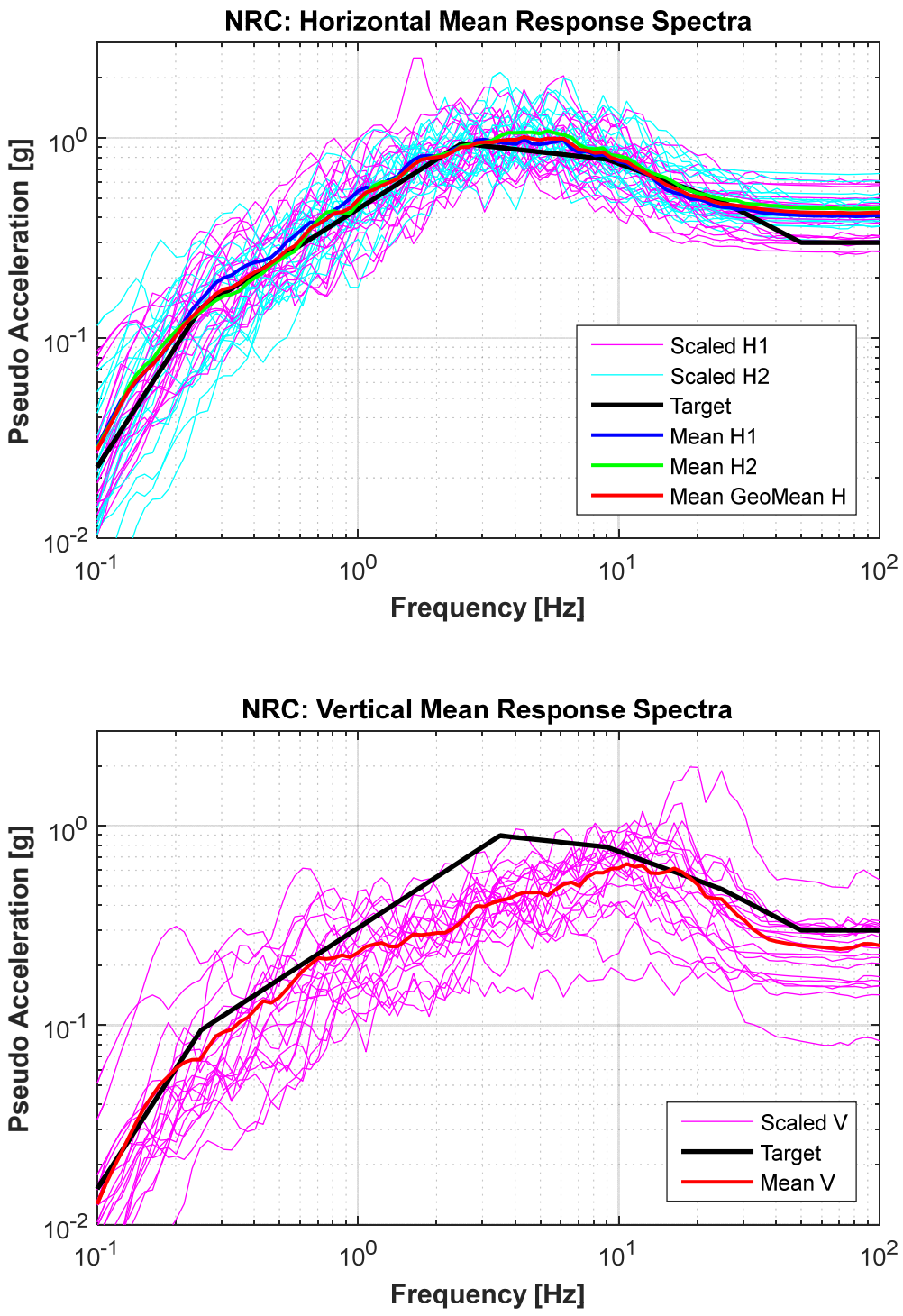

Figure 3.3 **Horizontal (top) and vertical (bottom) pseudo acceleration response spectra for the set of 20 dispersion-appropriate motions selected to match the 5% damped USNRC RG1.60 target spectrum with a PGA = 0.3*g* in an average sense over the frequency range from 0.25 Hz–20 Hz.**

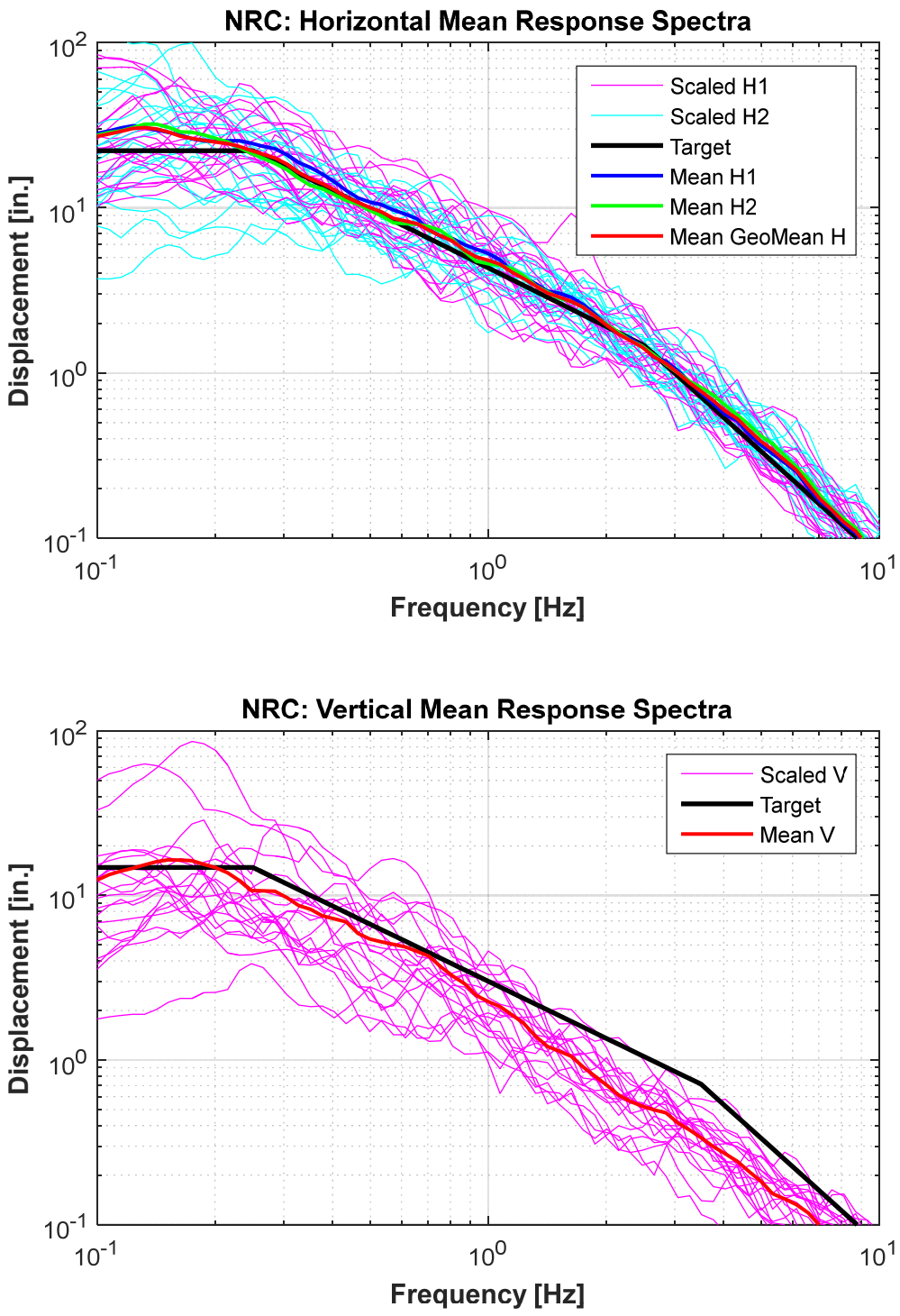

Figure 3.4 **Horizontal (top) and vertical (bottom) displacement response spectra for the set of 20 dispersion-appropriate motions selected to match the 5% damped USNRC RG1.60 target spectrum with a PGA = 0.3*g* in an average sense over the frequency range from 0.25 Hz–20 Hz.**

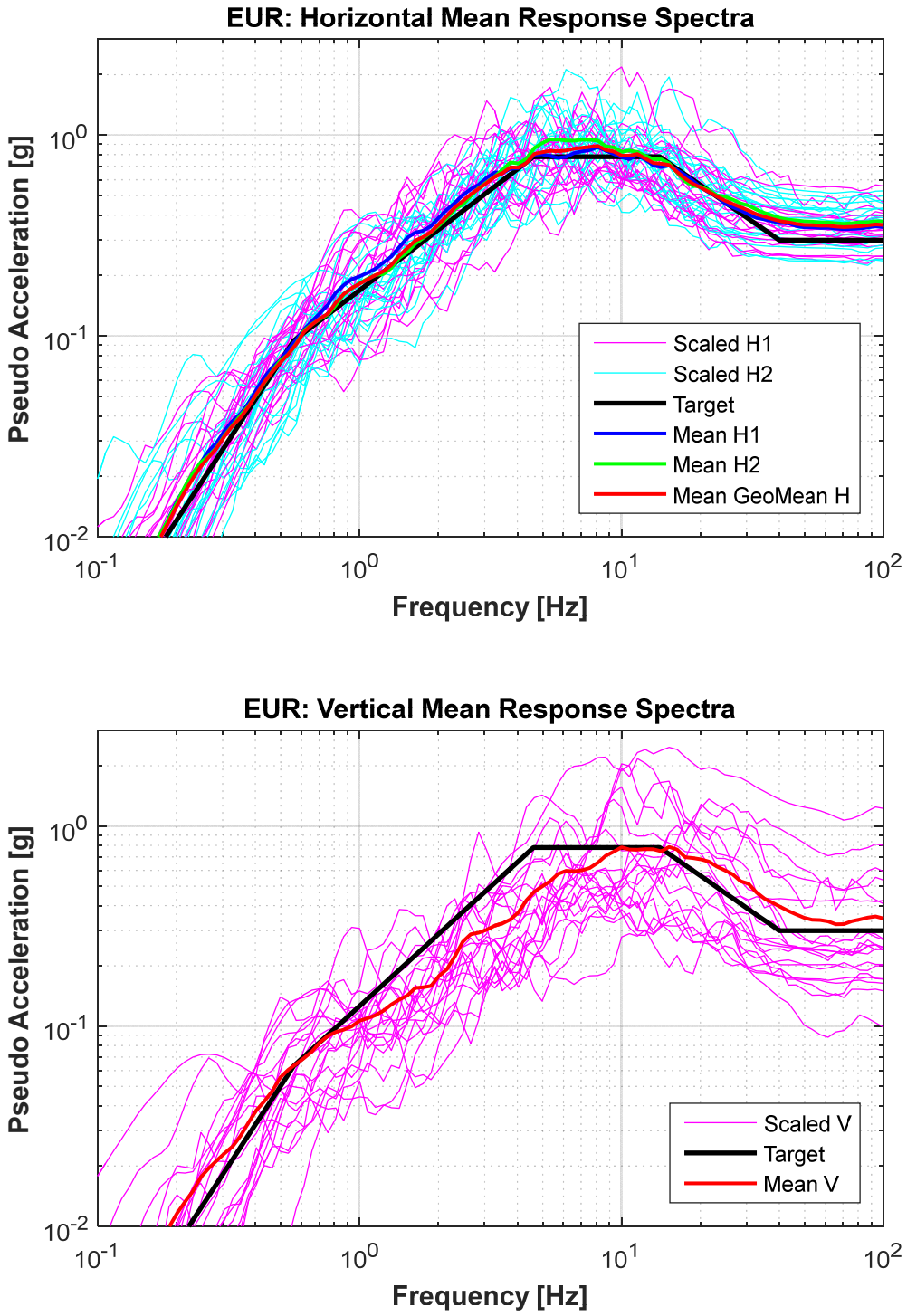

Figure 3.5 **Horizontal (top) and vertical (bottom) pseudo acceleration response spectra for the set of 20 dispersion-appropriate motions selected to match the 5% damped EUR 2.4.6 target spectrum with a PGA = 0.3*g* in an average sense over the frequency range from 0.25 Hz–20 Hz.**

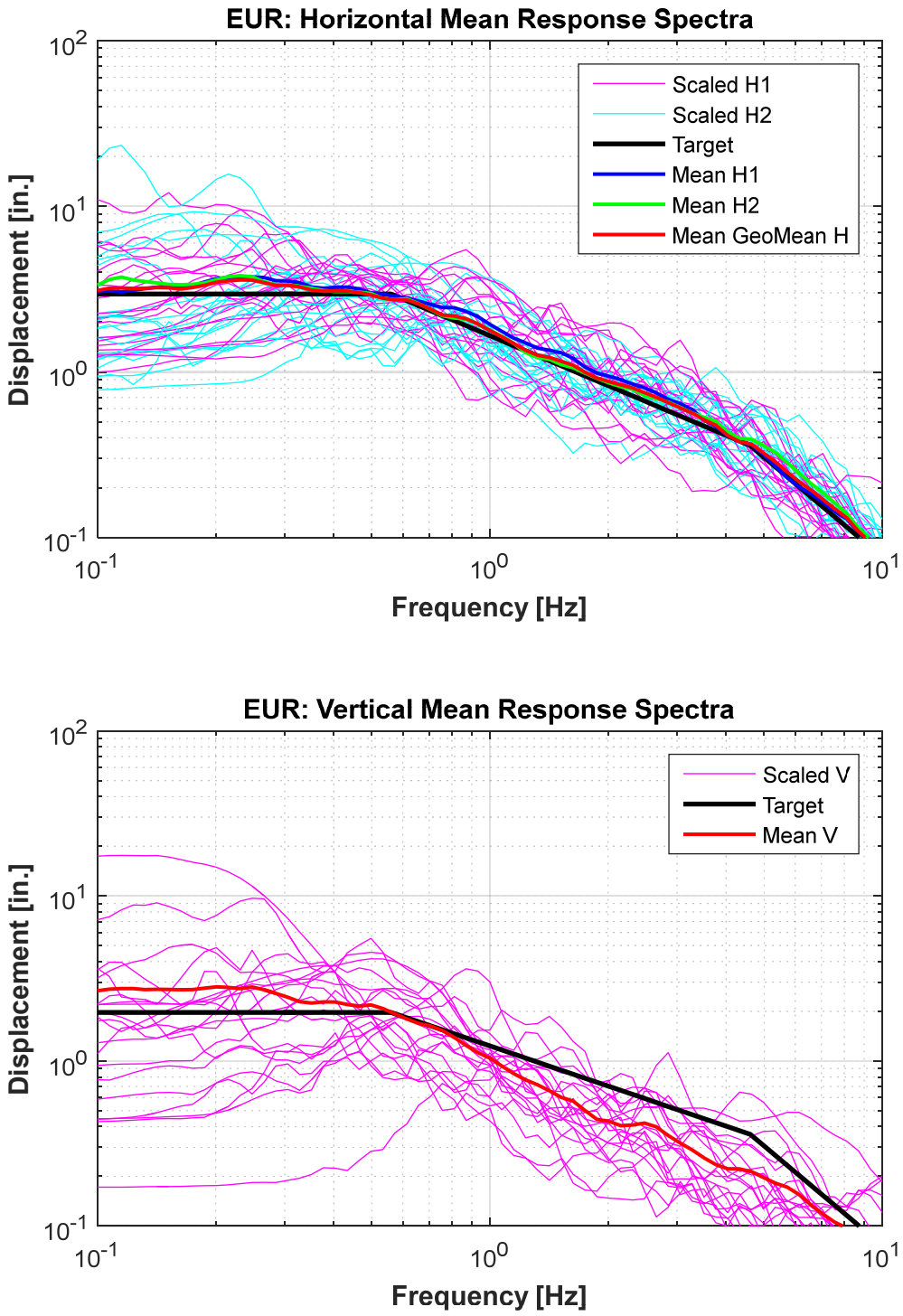

Figure 3.6 **Horizontal (top) and vertical (bottom) displacement response spectra for the set of 20 dispersion-appropriate motions selected to match the 5% damped EUR 2.4.6 target spectrum with a PGA = 0.3*g* in an average sense over the frequency range from 0.25 Hz–20 Hz.**

3.4 SUMMARY OF PARAMETERS CONSIDERED

The parametric study aims to look at the effect of the key bearing design parameters on the response of the isolated structure. Different combinations of parameter values were studied, and general trends were assessed based on the numerical analysis results. For each of the analysis cases with a certain combination of parameters values, the isolation post-yield period was set from 0.001 sec to 6 sec—corresponding to the horizontal axis in the nonlinear spectra plots—and peak responses were recorded for each of the period values. The wide range of periods investigated helped generate useful nonlinear response spectra. Details on each of the cases or parameter combinations are shown in Table 3.1.

Table 3.1 Summary of individual cases considered in the rigid mass parametric study and parameter values used for each case.

	Bearing model	Q_d/W	Post-yield stiffness ratio	η	Post-yield period
Bouc–Wen vs. bilinear	Bouc-Wen	10%	1%	1.0	0.001 to 6
	Bilinear	10%	1%	NA	
Different Q_d	Bilinear	5%	1%	NA	
	Bilinear	7.5%	1%	NA	
	Bilinear	10%	1%	NA	
	Bilinear	12%	1%	NA	
Different K_0	Bilinear	7.5%	0.1%	NA	
	Bilinear	7.5%	1%	NA	
	Bilinear	7.5%	5%	NA	
	Bilinear	7.5%	10%	NA	

3.4.1 Comparison of Bouc–Wen and Bilinear Models

First, the bilinear model and the rounded Bouc–Wen model are compared. The purpose of this preliminary comparison is to investigate the effect on the response due to the roundness of the analytical hysteresis loops. The comparison can also be interpreted as a comparison of a LRB and a single friction-pendulum bearing since the latter gives exact bilinear behavior, while the former will bring rounded hysteretic behavior. To compare the two models, the characteristic force, Q_d, was kept at 10%, and the post-yield ratio was kept at 1%. Different isolation periods in terms of post-yield period from 0.001 to 6 sec were considered, and comparisons were made based on the peak response for each of the two bearing models.

3.4.2 Different Bearing Characteristic Strength, Q_d

An important design parameter is the characteristic strength of the bearing. Since the initial stiffness is always large, the yielding force of the bearing is almost the same as Q_d. Therefore, the study can also be considered as a parametric study on yielding force, which indicates the threshold needed to begin the movement of the isolation system. In this parameter analysis, Q_d of

5% W, 7% W, 10% W, and 12% W were considered and compared, where W indicates the total gravity force compressing the bearing. Although, the vertical force will change due to vertical ground motion and rocking response during the time-history analysis, the assumption was made that it remains constant for the simplified model investigated here. For this comparison, the post-yield stiffness ratio was kept at 1%. For each value of Q_d, different isolation periods were considered from 0.001–6 sec.

3.4.3 Different Initial Stiffness K_0

The comparison for this part of the study aims to investigate the effect of the initial stiffness of the isolation system on the response. The design-level seismic event of 0.3g PGA for NPPs means that the movement of the isolation system is relatively small, and large numbers of cycles occur within the elastic range of the bearing. Therefore, the initial stiffness of the bearing is an important parameter. To construct the nonlinear response spectra, for each case the study investigated the response of the system through a wide range of isolation periods (0.001–6 sec); therefore, this part of the analysis used the post-yield stiffness ratio, α, to represent the initial stiffness. For the same isolation period that results in the same post-yield stiffness, different α values ranging from 0.1%–10% were investigated to represent equivalently different initial stiffnesses.

3.5 ANALYSIS RESULTS AND DISCUSSION

The responses considered in this parametric study are isolator displacement and rigid mass total acceleration. Since the model contains a perfectly rigid mass on top of an isolator element, the total acceleration times the mass is equal to the shear force in the isolator. Therefore, the response of the total acceleration can be interpreted as approximately the total base shear the isolated reactor will experience. Peak response in each parametric study case is plotted against a wide range of isolation post-yield periods to generate the nonlinear response spectra for all 20 ground motions used in these analyses. Median as well as 84th-percentile responses (one standard deviation above median) are presented. Since each time-history analysis is a bi-directional analysis, the peak response was taken as the norm of the values of the two directions.

3.5.1 Response Values Determined by Bouc–Wen and Bilinear Models

Results are compared first in terms of the peak isolator displacement; see Figure 3.7. The nonlinear bearing displacement spectrum of the median response under the NRC and EUR motion sets were plotted together with the 84th-percentile response spectrum. Results show that the total displacement demand of the isolator is around 15.24 cm (6 in.) for the NRC motion set if using the isolator post-yield period of 2.1 sec, which is the targeted isolation period used in the seismic isolation design of many fast breeder reactors from previous projects. The 84th-percentile demand is around 0.25 m (10 in.) under the NRC motion set, which is approximately 1.5 times the median response. Considering the dispersion of earthquake loading and uncertainty of ground motion, 1.5 seems a reasonable number to move from median response to one standard deviation above.

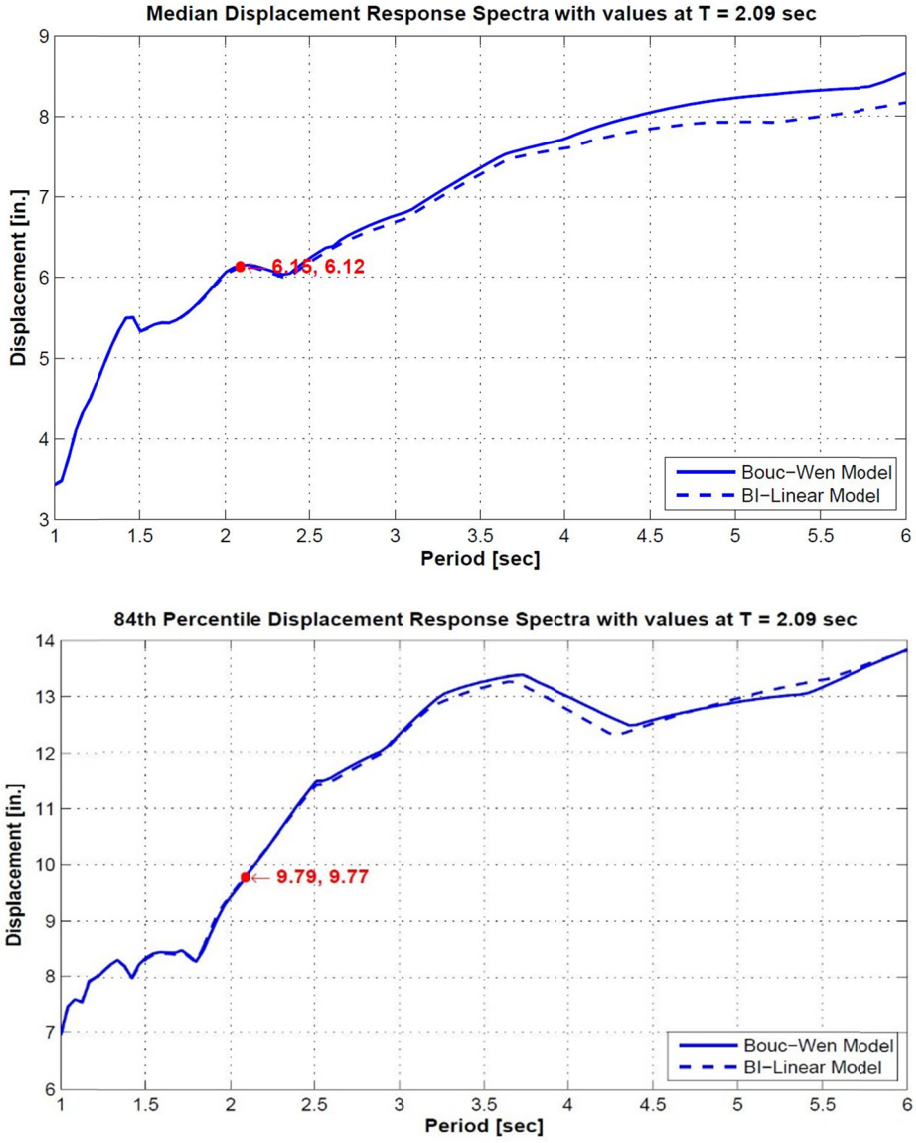

Figure 3.7 **Median and 84th-percentile isolator displacement spectra under the NRC hazard. Response values using bilinear and Bouc–Wen models are plotted together for comparison. Values at the isolator period of 2.1 sec are marked in the plot.**

In comparing the response for different periods along the horizontal axis, it is obvious that a larger isolation period will result in larger bearing displacement demands. This is intuitive since the lower post-yield stiffness will have less constraint on the displacement of bearing. However, the isolator displacement demand does not increase exponentially with an increase of the isolation period because of the relative small ground-motion intensity. Increase of isolation period beyond about 4 sec does not make much difference on the displacement demand of the isolator. From the plot, the slope of the displacement spectrum tends to decrease with increasing periods.

A comparison of the bilinear model and the Bouc–Wen model, which are indicated in the plots by the solid line and the dashed line, respectively, demonstrates that the difference of the

response is negligible in terms of peak displacement response. The minor difference may be due to the initial assumption of a rigid superstructure. The two bearing models are expected to have somewhat larger difference in response when the superstructure above the isolation system is flexible.

The responses shown in Figure 3.7, for the NRC dispersion-appropriate ground-motion set scaled to 0.3*g* PGA indicate the anticipated response under the SSE level considered in the design. However, another commonly used ground-motion target spectrum, the EUR hazard, was also investigated, and the isolator displacement response is shown in Figure 3.8.

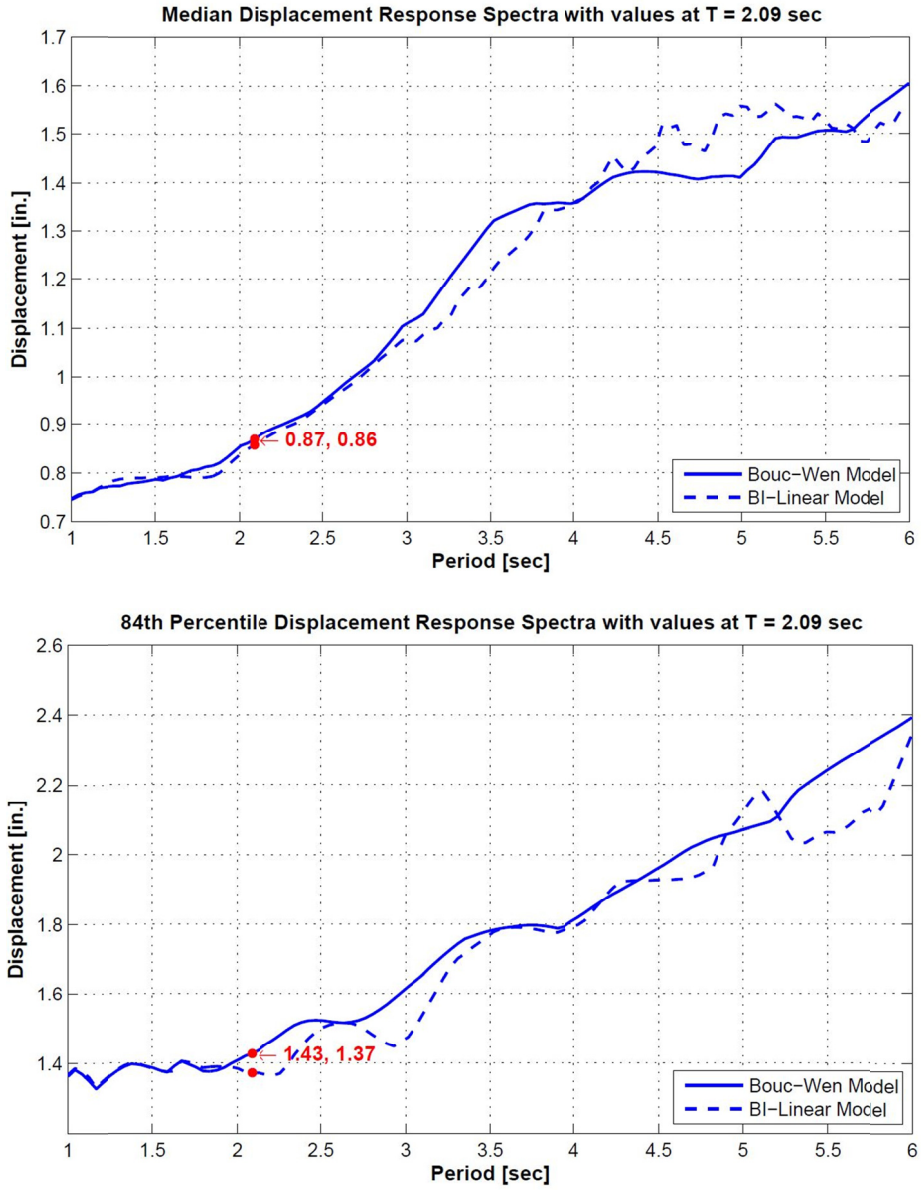

Figure 3.8 **Median and 84th-percentile isolator displacement spectra under the EUR hazard. Response values using bilinear and Bouc–Wen models are plotted together for comparison. Values at the isolator period of 2.1 sec are marked in the plot.**

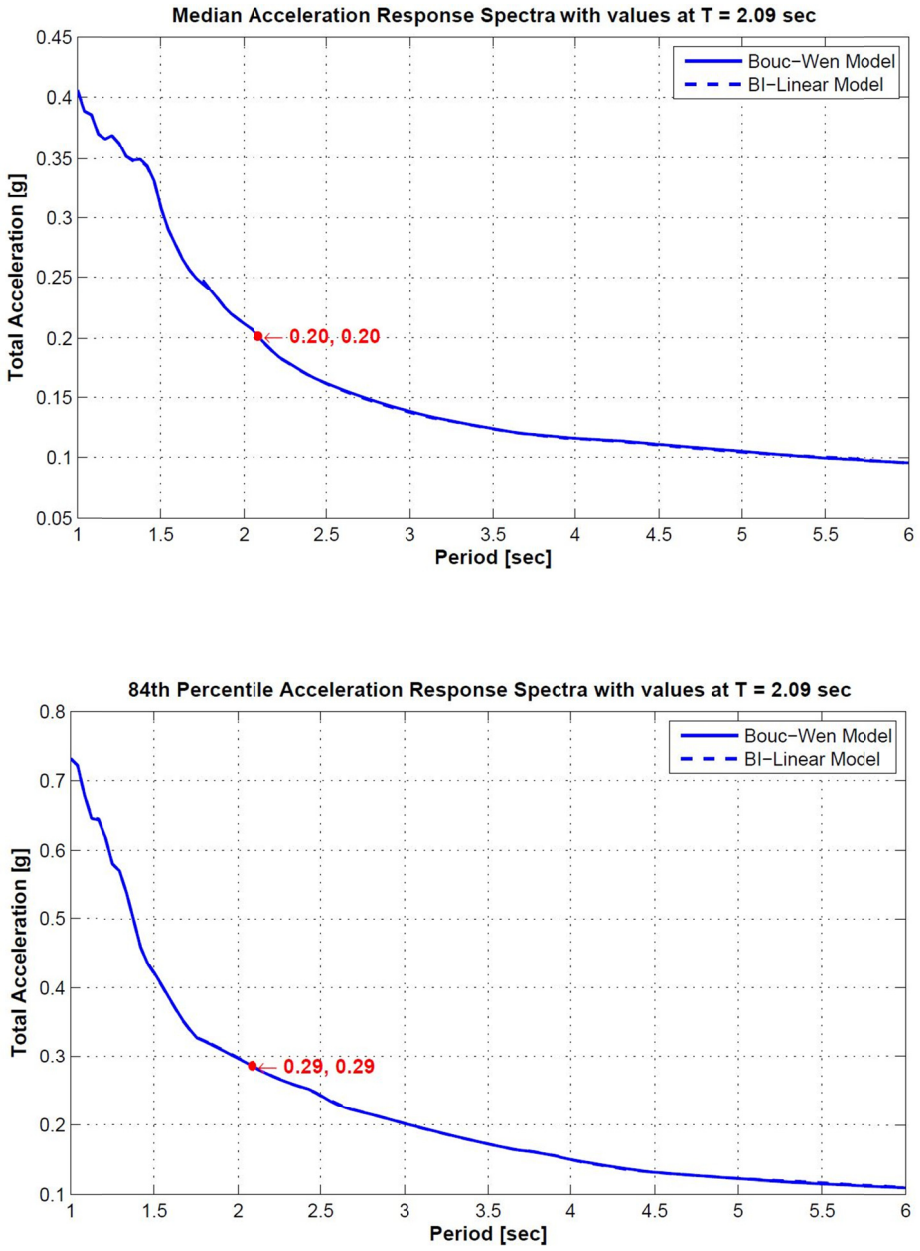

Figure 3.9 **Median and 84th-percentile isolated mass total acceleration spectra under the NRC hazard. Response values using bilinear and Bouc–Wen models are plotted together for comparison. Values at the isolator period of 2.1 sec are marked in the plot.**

Comparing the response amplitude in Figure 3.8 and Figure 3.7 for the same system with isolation period of 2.1 sec, the median response under EUR motion is around 25 mm (1 in.) compared to 15.24 cm (6 in.) under NRC motion, although the target spectra were both scaled to 0.3*g* PGA. The 84th-percentile response under EUR hazard is around 35.6 mm (1.4 in.), while the NRC hazard resulted in around 254 mm (10 in.). As pointed out earlier, although the two target spectra have the same PGA, their frequency contents are very different. The NRC target spectrum has much higher values compared to the EUR target, especially in the long-period

range relevant to the isolation system. Because of the large difference in response amplitude, subsequent studies will all be carried out with the NRC hazard only.

From results shown in Figure 3.9 of the peak total acceleration response, 0.2*g* total acceleration or 0.2 *W* base shear is expected in the isolated RCB when using a seismic isolation system with a 2.1-sec post-yield period under the NRC hazard with 0.3*g* PGA. An additional increase of the isolation period will reduce the force demand. The increase of the isolation period from 2 to 4 sec will reduce the force demand by 50% but only increase the displacement demand by 30%. The difference between the bearing models is negligible with respect to the acceleration response. The 84th-percentile force demand is around 0.3*g*, which is 1.5 times the median response; the ratio is consistent with the scale obtained in the isolator displacement demand. The force reduction ratio, which is defined as the ratio between the total acceleration in the isolated mass and the peak ground acceleration, is shown in Figure 3.10. Derived from the trend in Figure 3.9, it is easy to conclude that the effectiveness of the isolation system will increase when the isolation period increases. The force reduction factor is around 2.5 for an isolation system with 2.1-sec post-yield period when compared to the fixed-base case.

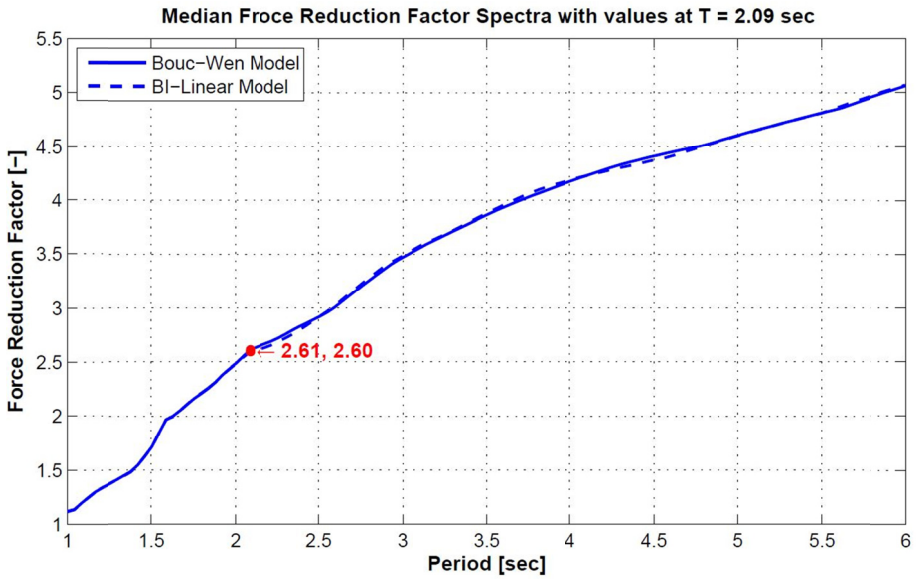

Figure 3.10 **Median force (total acceleration) reduction ratio under the NRC hazard. Response values using bilinear and Bouc–Wen models are plotted together for comparison. Values at the isolator period of 2.1 sec are marked in the plot.**

3.5.2 Comparison of Responses for Different Q_d

Characteristic strength is an important parameter in the design of isolation systems, which indicates the threshold needed for initiation of post yield movement of the isolator. Four cases are compared with Q_d equal to 5%, 7.5%, 10%, and 12% of the weight on the bearing. Since the comparison in Section 3.5.1 showed there is almost no difference in response using a bilinear bearing model or a Bouc–Wen bearing model in this simplified rigid mass case, the subsequent parametric study in this section will use the perfect bilinear bearing model. Because of the large

initial stiffness, Q_d and F_y values are nearly the same for the bilinear model. Therefore, the value of Q_d can also be interpreted as the yield force of the bearing.

First, peak bearing displacement response was investigated as shown in Figure 3.11 with median and 84th-percentile level responses. The dependence of isolator displacement on isolator period is pronounced in this plot, but the dependence decreases with the increase of the isolation period beyond around 3 sec because of the small displacement of the isolator under this level of ground-motion excitation.

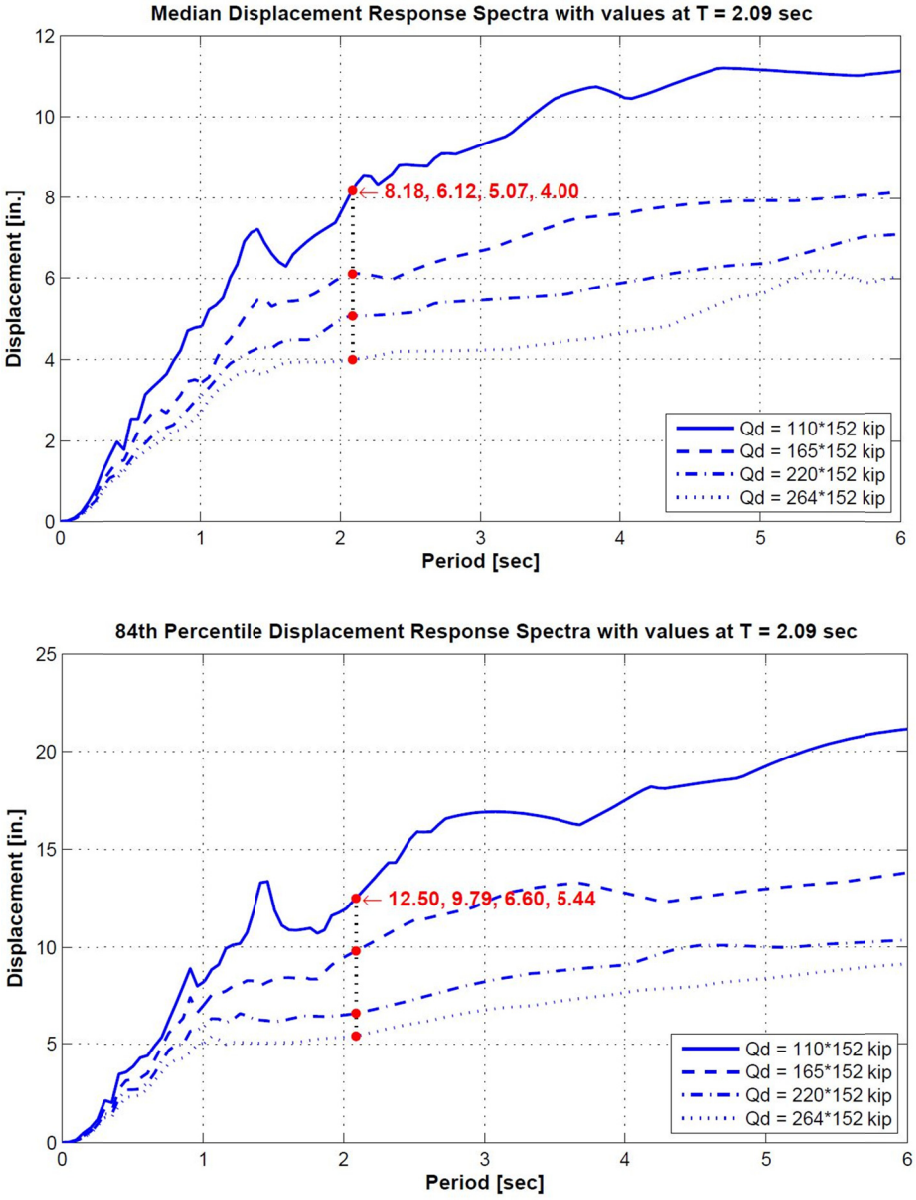

Figure 3.11 **Median and 84th-percentile isolator displacement spectra under the NRC hazard. Response values using a bilinear model with different Q_d (5% *W*, 7.5% *W*, 10% *W*, and 12% *W*) are plotted together for comparison. Values at the isolator period of 2.1 sec are marked in the plot.**

The dependence of the response on yield force F_y or characteristic strength Q_d is also noticeable as indicated by different lines in Figure 3.11. Larger Q_d results in smaller isolator displacement demand. Comparing between a Q_d of 5% W and 10% W, which is around twice the yield force, the displacement demand drops from around 0.20 m (8.2 in.) to 0.13 m (5 in.) at the 2.1-sec isolation period. With the increase of the isolation period, the dependence of the results on Q_d is similar. Since larger isolator displacements result with differences in Q_d, the resulting effective period of the system can be obtained as shown in Figure 3.12. The effective period is defined based on the secant stiffness from the origin.

The peak total acceleration response is shown in Figure 3.13. The dependence of the responses on different Q_d is not as significant as might be expected. The parameter values, 5% W–12% W, represent a wide range of practical values, but the resulting acceleration responses have little deviation as observed in the figure. Interestingly, for low isolator periods, the larger displacement demands imposed by a small Q_d produce larger force demands due to the post-yield stiffness. Therefore, although Q_d is smaller, the total horizontal shear force might be larger. The effect is reversed at larger isolator periods where the lower Q_d produces lower force demands. Since force and total acceleration are equivalent in the simplified rigid mass system, the term "force demand" is used subsequently in this section to represent the total acceleration response. Comparing the median and 84th-percentile responses, a factor of 1.5 is still a reasonable ratio to account for the scatter of the responses due to the uncertainty in the input excitation.

The force reduction factor was computed by comparing these results with a fixed-base mass; this factor is shown in Figure 3.14. From this plot, it can be seen that below a period of around 3 sec, a larger Q_d will produce a larger force reduction factor. When the period of the isolation system is larger, the larger Q_d has a smaller force reduction factor than a lower Q_d.

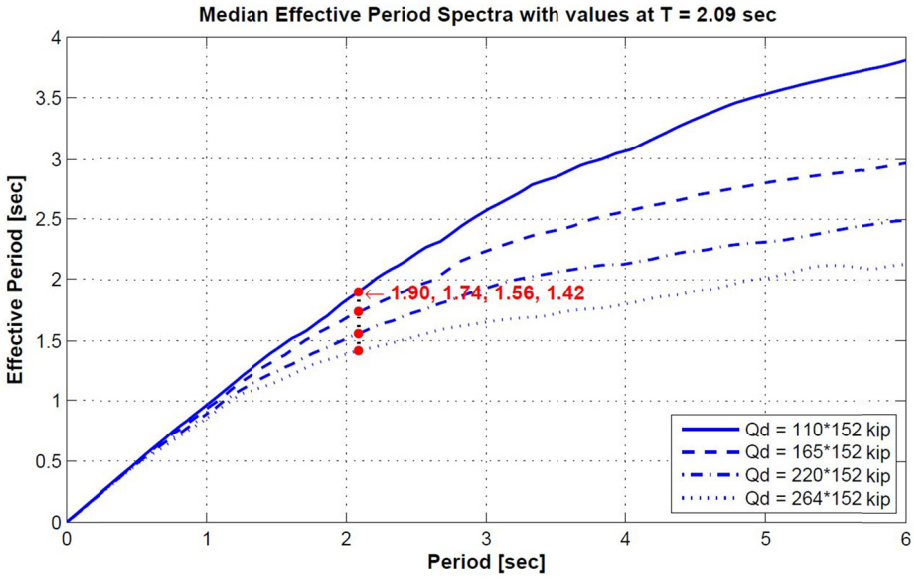

Figure 3.12 Median effective period spectra under the NRC hazard. Response values using a bilinear model with different Q_d (5% W, 7.5% W, 10% W, and 12% W) are plotted together for comparison. Values at the isolator period of 2.1 sec are marked in the plot.

As demonstrated above, a force and displacement tradeoff must be balanced in terms of isolator design. This balance is achieved through design parameters like isolation period and Q_d. A larger Q_d may produce smaller displacement demands, but it may bring larger force demands even if the effect is not predominant. However, if Q_d is too large, the design objective may already exceed the design force limit. The relation between force demand and bearing displacement demand is shown in Figure 3.15 to better understand the relationship.

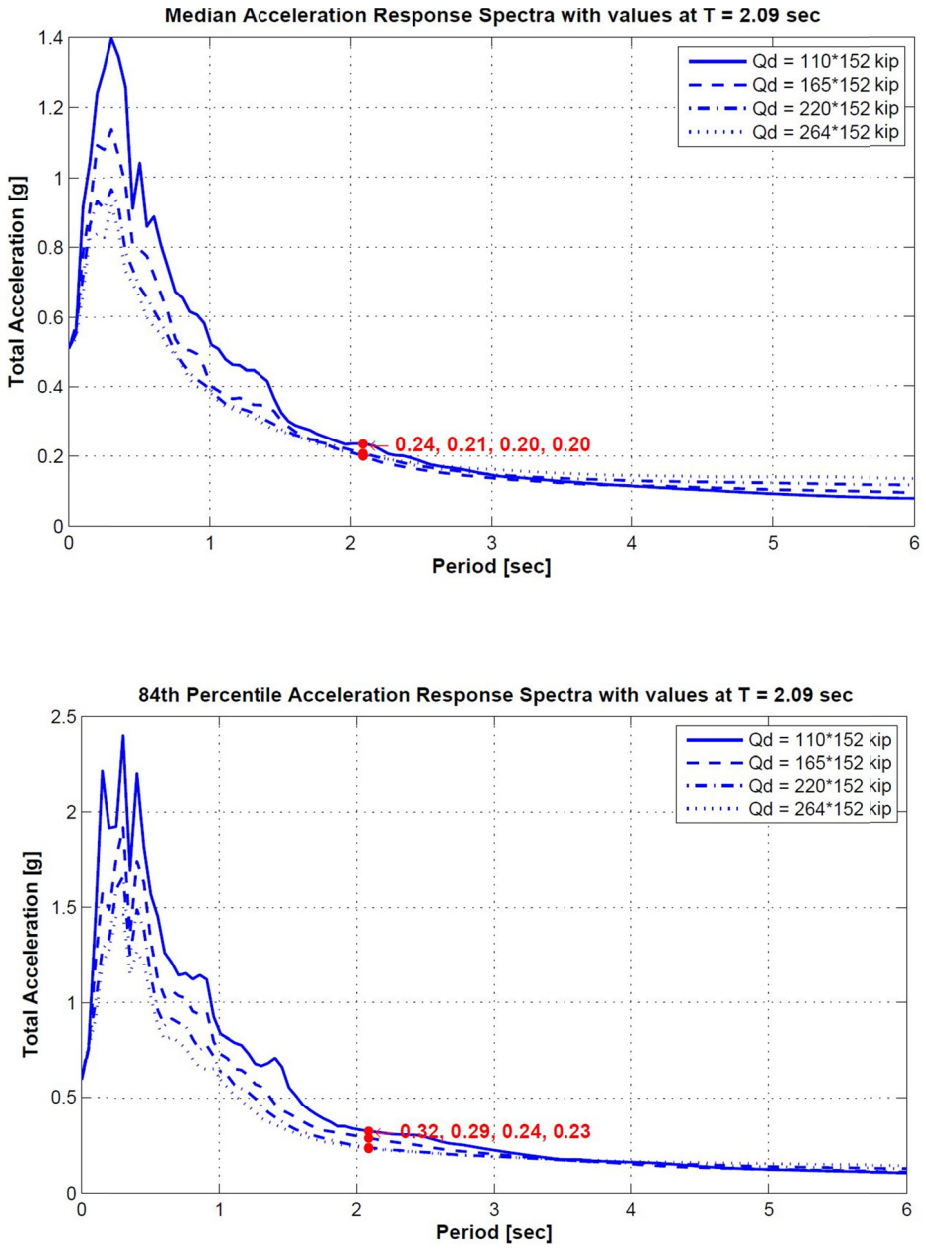

Figure 3.13 **Median and 84th-percentile isolated mass total acceleration spectra under the NRC hazard. Response values using a bilinear model with different Q_d (5% *W*, 7.5% *W*, 10% *W*, and 12% *W*) are plotted together for comparison. Values at the isolator period of 2.1 sec are marked in the plot.**

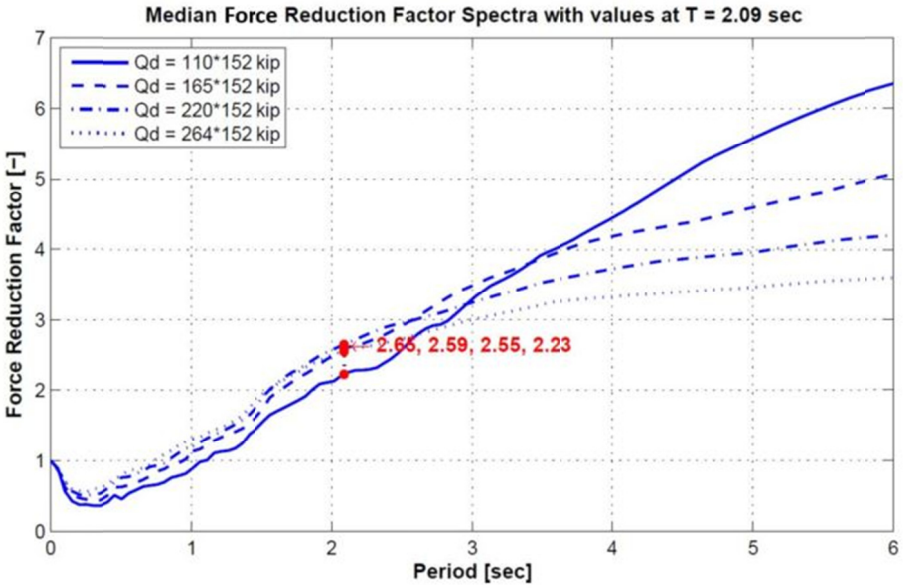

Figure 3.14 **Median force (acceleration) reduction ratio using isolation system under the NRC hazard. Response values using a bilinear model with different Q_d (5% W, 7.5% W, 10% W, and 12% W) are plotted together for comparison. Values at the isolator period of 2.1 sec are marked in the plot.**

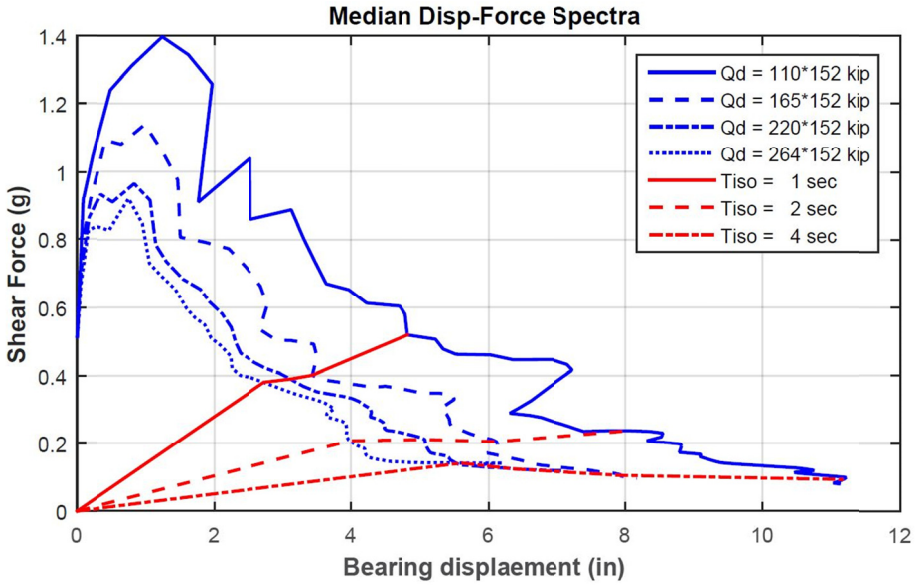

Figure 3.15 **Force (acceleration) versus bearing displacement relation under the NRC hazard. Response values using a bilinear model with different Q_d (5% *W*, 7.5% *W*, 10% *W*, and 12% *W*) are plotted together for comparison.**

When considering the force demand for design purposes, Figure 3.15 is useful in identifying appropriate design parameters such as isolator period and Q_d. The influence of these parameters is visually apparent. Subsequently, the bearing displacement demands are easily identified to determine if they are within an acceptable range. For example, the line that represents Q_d = 264 × 152 kips in Figure 3.15 will never reach the force level below 0.1*g*.

Alternatively, the line for an isolator period of 2.0 sec indicates that a force demand of 0.2g is anticipated for any Q_d value selected, but the selected Q_d will significantly influence the bearing displacement demand.

3.5.3 Comparison of Responses for Different K_0

The parameter used to study the initial isolator stiffness was the post-yield stiffness ratio, α. This ratio can capture the intended parameter since at the same post-yield stiffness or isolation period, different post-yield ratios produce different initial stiffness. Four values were considered in this comparison study: 0.1%, 1%, 5% and 10%. For each post-yield stiffness ratio, Q_d was kept constant at 7.5% of the weight on the bearing.

The displacement spectra are shown in Figure 3.16. The amplitude of the peak displacement demand is the same as the results presented in Section 3.5.2. A 2.1-sec isolation period results in a median displacement demand around 15.24 cm (6 in.), and the 84th-percentile demand is around 0.25 m (10 in.). The influence of initial stiffness on peak displacement demand is negligible when the isolation period is small. A small isolation period is due to a large post-yield stiffness, which in turn produces a relatively large initial stiffness for all values of α considered. This produced indistinguishable results for low isolation periods. When the isolation period is larger, observable differences on the displacement demand occur; see Figure 3.16. Larger initial stiffness results in smaller displacement demands. However, in the isolation period range of interest—namely the 2-sec range—no significant difference was observed.

There is negligible difference in terms of force demands among isolators with different initial stiffness, see the force spectrum in Figure 3.17. The force demand is dependent on the isolation period. Since Q_d in this comparison was the same for all four cases, the difference of force demand comes from the post-yield stiffness and displacement demand. However, at a given isolator period, the post-yield stiffness is identical, and any increase in force demand is a consequence of the variation in displacement demand produced by the initial stiffness. Therefore, insignificant influence by α is expected—and observed—in terms of force demand.

The force reduction factor was produced by comparing these results with a fixed-base case. The results are shown in Figure 3.18. The impact of α on the force reduction factor had only modest influence for isolator periods greater than 3 sec. The force-displacement demand relationship is shown in Figure 3.19. From this figure, the initial stiffness only has an effect on the displacement demand and almost no influence on force demand, as was observed in Figure 3.17. For a given displacement demand, a different initial stiffness will not produce different force responses. However, for a given force demand, a different initial stiffness will produce different bearing displacement demands.

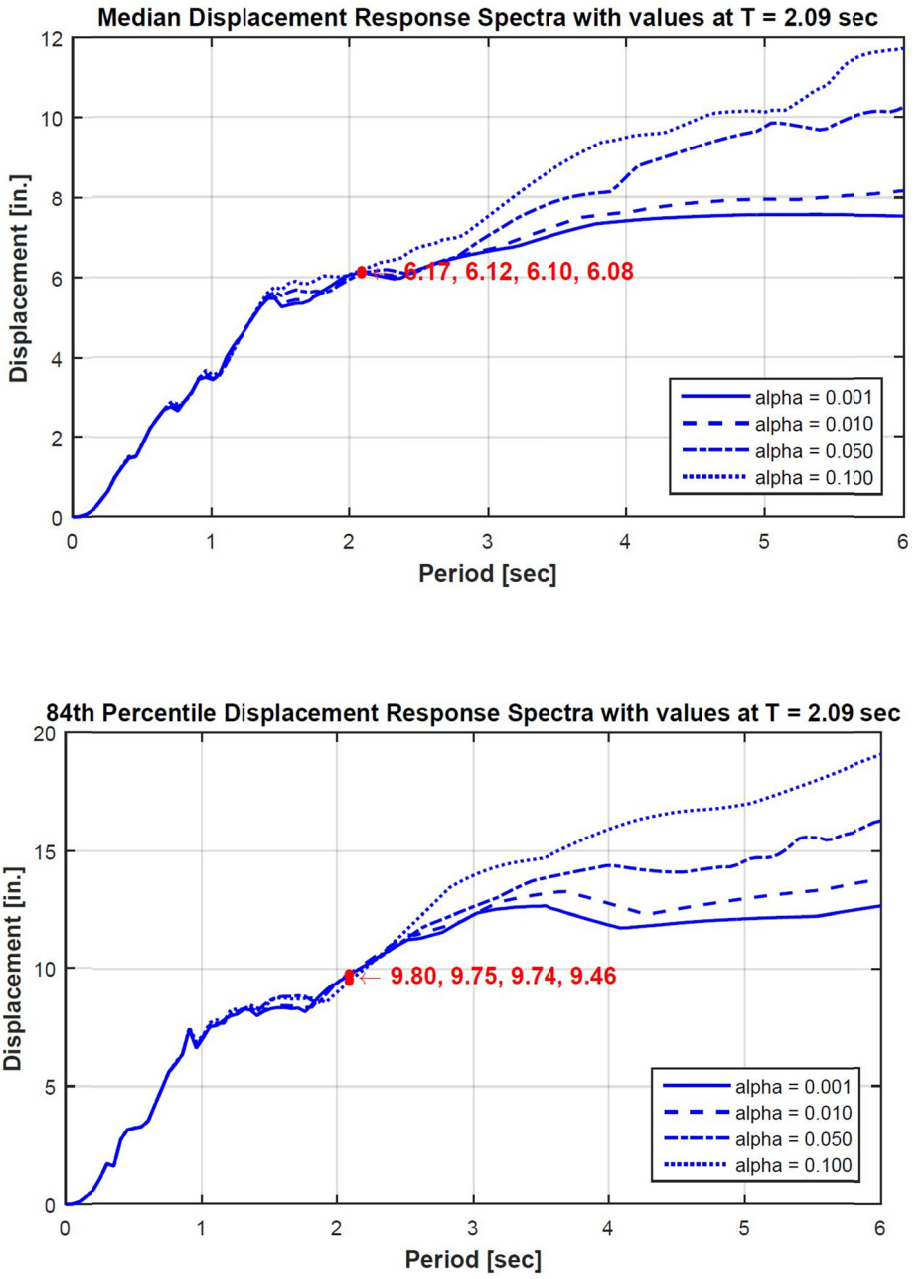

Figure 3.16 **Median and 84th-percentile isolator displacement spectra under the NRC hazard. Response values using a bilinear model with different α (0.1%, 1%, 5%, and 10%) are plotted together for comparison. Values at the isolator period of 2.1 sec are marked in the plot.**

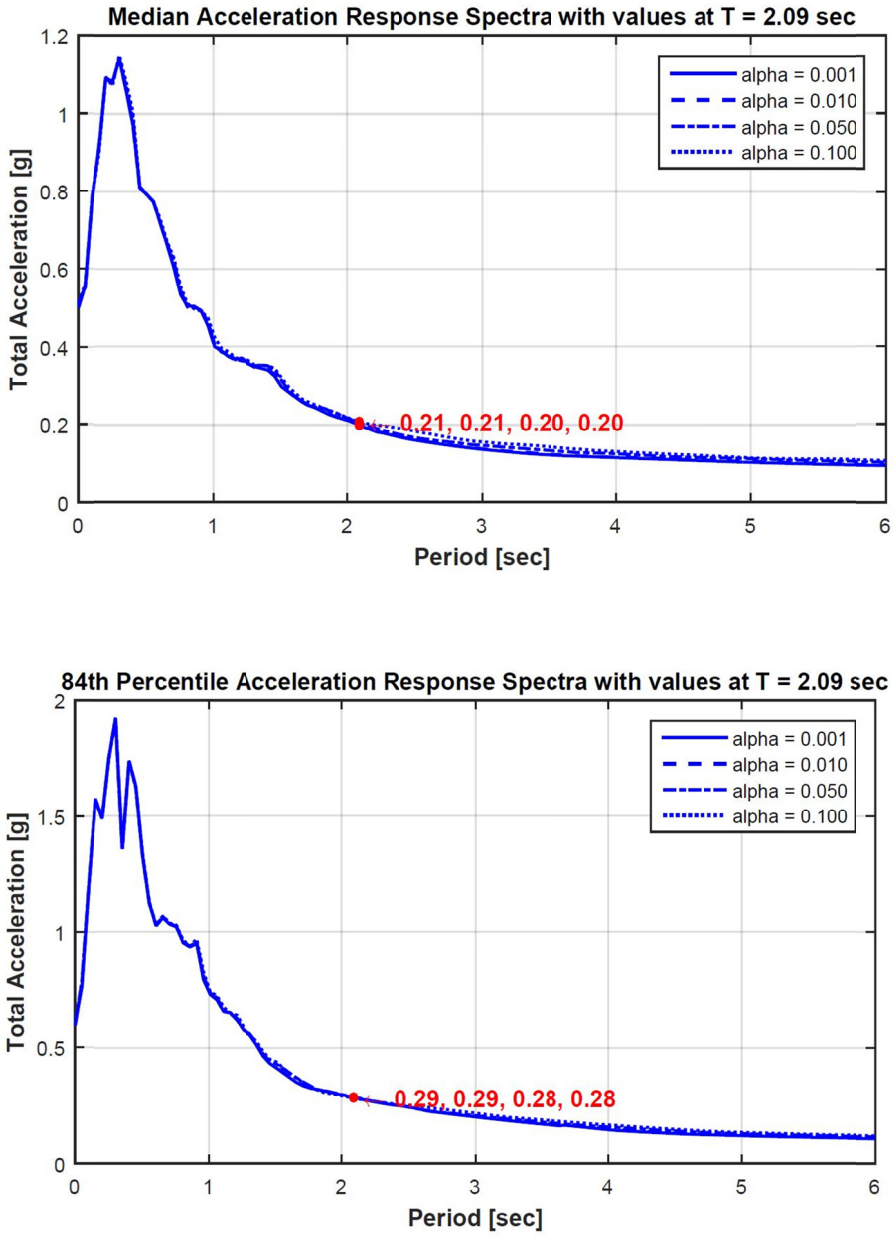

Figure 3.17 **Median and 84th-percentile isolated mass acceleration spectra under the NRC hazard. Response values using a bilinear model with different α (0.1%, 1%, 5%, and 10%) are plotted together for comparison. Values at the isolator period of 2.1 sec are marked in the plot.**

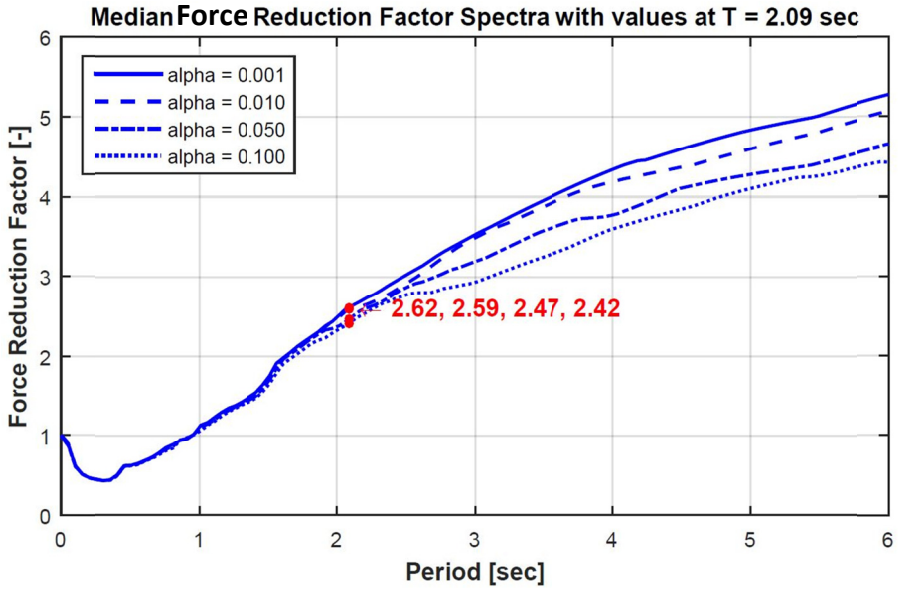

Figure 3.18 **Median force (acceleration) reduction ratio using the NRC hazard. Response values using a bilinear model with different α (0.1%, 1%, 5%, and 10%) are plotted together for comparison. Values at the isolator period of 2.1 sec are marked in the plot.**

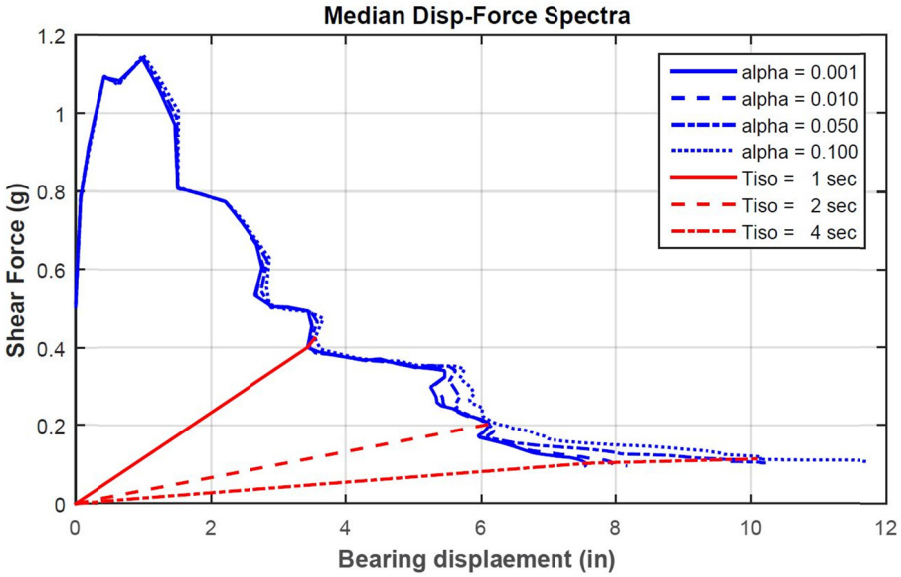

Figure 3.19 **Median force (acceleration) versus bearing displacement relation under the NRC hazard. Response values using a bilinear model with different α (0.1%, 1%, 5%, and 10%) are plotted together for comparison.**

3.6 CONCLUSION AND SUMMARY

This section presented the results of a parametric study conducted using a simplified analysis model with a rigid mass representing the superstructure of the PGSFR NPP. The effect of key isolator design parameters on the peak response of the supported mass was investigated. Bi-directional time-history analyses were conducted using NRC and EUR hazards. With this preliminary analysis, some key conclusions have been drawn:

- The two bearing models considered, a bilinear model and a Bouc–Wen model, have almost identical responses for the rigid mass superstructure model. The roundedness of the Bouc–Wen model did not impact peak displacement or acceleration demands.
- Regarding the two hazards considered, the NRC response was around six times larger than the EUR in terms of displacement demand and twice as large in terms of force demand. While the two hazards were scaled to the same 0.3*g* PGA, these results reflect the larger demands imposed by the NRC hazard spectra.
- Under the NRC hazard scaled to 0.3*g* PGA, the median bearing displacement demand was approximately 15.24 cm (6 in.), with force demands around 0.2*g*. The force reduction factor when compared to a fixed-base case is around 2.5 for a 2.1-sec isolation system.
- The response of the isolated structure is mainly influenced by the isolation period (post-yield stiffness). A large isolation period (smaller post-yield stiffness) will reduce force demands but induce larger displacement demands as a tradeoff. The initial stiffness of the bearing had little effect on the response in this simplified rigid-mass model.
- Larger characteristic strength Q_d, or equivalently larger bearing yield force F_y, will decrease the isolator displacement demand but not significantly affect the force demand.
- The initial stiffness of the bearing did not produce significant variation in the force demands or the displacement demands in the likely period range of interest.

4 DYNAMIC ANALYSIS OF A SEISMICALLY ISOLATED PGSFR SUBJECTED TO EARTHQUAKE EXCITATION

4.1 INTRODUCTION

Chapter 3 presented the results of parametric analyses carried out using a rigid-mass model that represented the upper reactor and auxiliary building. That simplified model restrained rocking of the plant about any horizontal axis and rotation about a vertical axis. As such, it was possible to model the plant as being supported on a single isolator unit that represents the whole isolation system. Although some key conclusions were drawn from parametric study on the simplified model, a more refined model of the PGSFR is needed to capture fully the three-dimensional dynamic response characteristics of the facility.

In this section, a more refined model representing the PGSFR RCB, auxiliary building (AUX), and base mat is considered. While the model is more refined than the rigid block model used in Chapter 3, it was still based on a simplified lumped-mass "stick" representation when modeling upper plant buildings. Given the lack of current details regarding the plant design, and the evolving configuration and properties of the superstructure, this model is believed to be appropriate for the type of preliminary investigations being carried at this stage of the study. The superstructure is supported on an isolation system consisting of 152 LRBs. The overall model was developed in OpenSees. In addition to a model of the isolated PGSFR, a fixed-base model was developed and analyzed for comparison purposes. Parametric studies were conducted using time-history analysis methods considering three components of earthquake excitation. The results of these parametric studies are described in this chapter.

4.2 DEVELOPMENT OF A REFINED 3D MODEL IN OPENSEES

A more refined lumped-mass stick model was developed in OpenSees to study the dynamic behavior of the plant superstructure in terms of isolator displacements and floor response spectra, as well as to assess overturning response including possible tension and uplift of the bearings, and torsional effects in the isolation system associated with the stiffness and mass eccentricity of the current design. The same stick model with some minor modifications is also being used for aircraft impact analyses discussed in Chapter 5.

4.2.1 Plant General Description and Geometry

The refined model consists of two sticks with lumped masses at major floor elevations connected to a common base mat, which is supported by 152 LRBs. Soil under the plant was not considered in these analyses, and the bearings are connected to a fixed base.

The first stick in the superstructure model represents the AUX and the second stick represents the RCB. The model geometry was developed based on dimensions from preliminary general arrangement drawings provided by KEPCO E&C; see Figure 4.1. The plan view of the PGSFR is shown in Figure 4.2, and the elevation view is shown in Figure 4.3. As can be seen from the drawings, the AUX wraps around the RCB; the perimeter of the AUX is almost rectangular in plan with a maximum dimension of 77 m (252 ft) × 59.5 m (195 ft). The north–west and south–west corners have small cutouts of 7.5 m (24.6 ft) × 7.5 m (24.6 ft). The center of the RCB is located 26.25 m (86.1 ft) from the outside of the east wall of the AUX, and the outside diameter of the RCB is 30 m (98.4 ft).

Other general data of the preliminary PGSFR plant design that was provided by KEPCO E&C is the overall plant weight of 151,897 tonf (334,875 kip), the targeted effective isolation period of 2.1 sec, and a range of estimated superstructure fundamental frequencies for the RCB and AUX between 3.5–5 Hz. Despite the limited amount of data, the analysis model was developed, and its dynamic behavior tuned to match the provided weight and frequency characteristics.

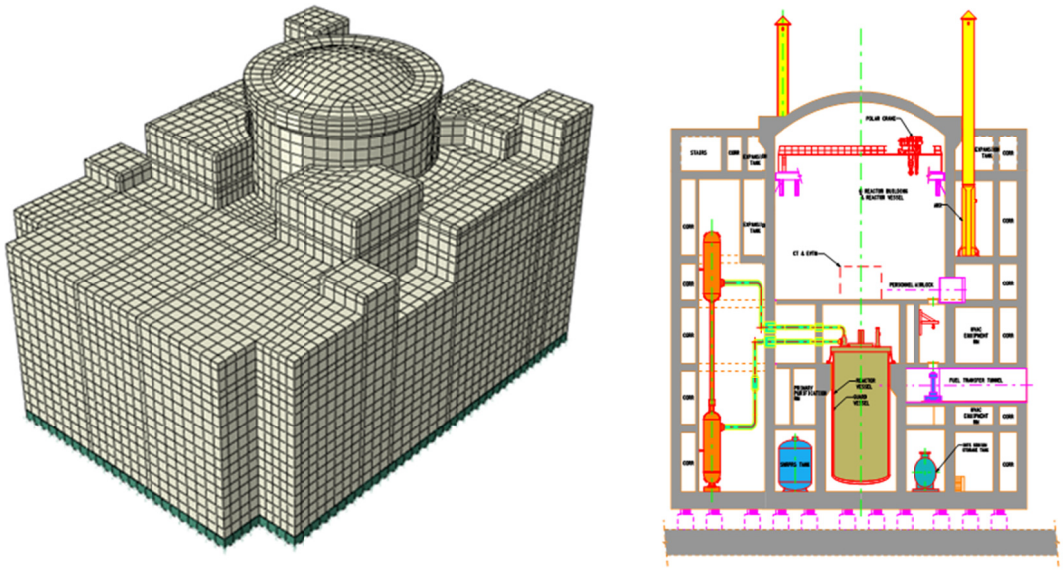

Figure 4.1 Perspective and schematic view of PGSFR power plant.

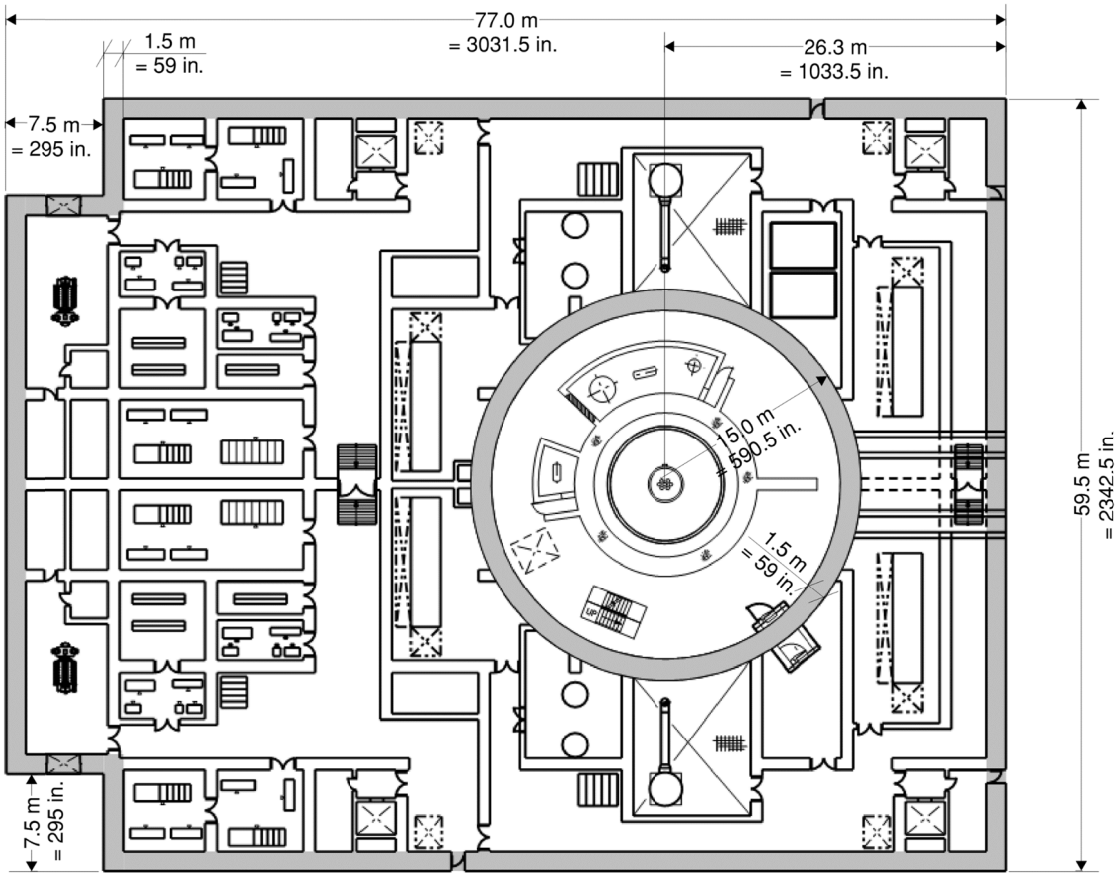

Figure 4.2 Plan view of preliminary PGSFR general arrangement with dimensions.

The geometry of the plant is such that the overall layout is symmetric in north–south direction but asymmetric in east–west direction. This is an important consideration for the aircraft impact analysis (AIA) discussed in Chapter 5. It may also have an effect on torsional response during seismic excitation. The RC wall thickness for both the AUX and the RCB is 1.5 m (59 in.). A gap of unknown size separates the RCB from the AUX. For modeling and analysis purposes, it was assumed that the gap is sufficiently large such that no impact and/or pounding will occur between the two plant superstructures during ground shaking and aircraft impact. Therefore, the two sticks that represent the RCB and AUX are only connected through the common base mat; thus, dynamic interaction between the two superstructures is only possible in the seismically isolated models but not the fixed-base models.

Elevations of major floors are called out in Figure 4.3. The top of the common base mat is embedded and located 8 m (26.25 ft) below ground. The thickness of the RC base mat is 2 m (78.74 in.). For modeling purposes, it was assumed that the roof of the AUX is located at 30 m (98.43 ft). The RCB sticks out of the AUX and is 39.4 m (129.22 ft) tall.

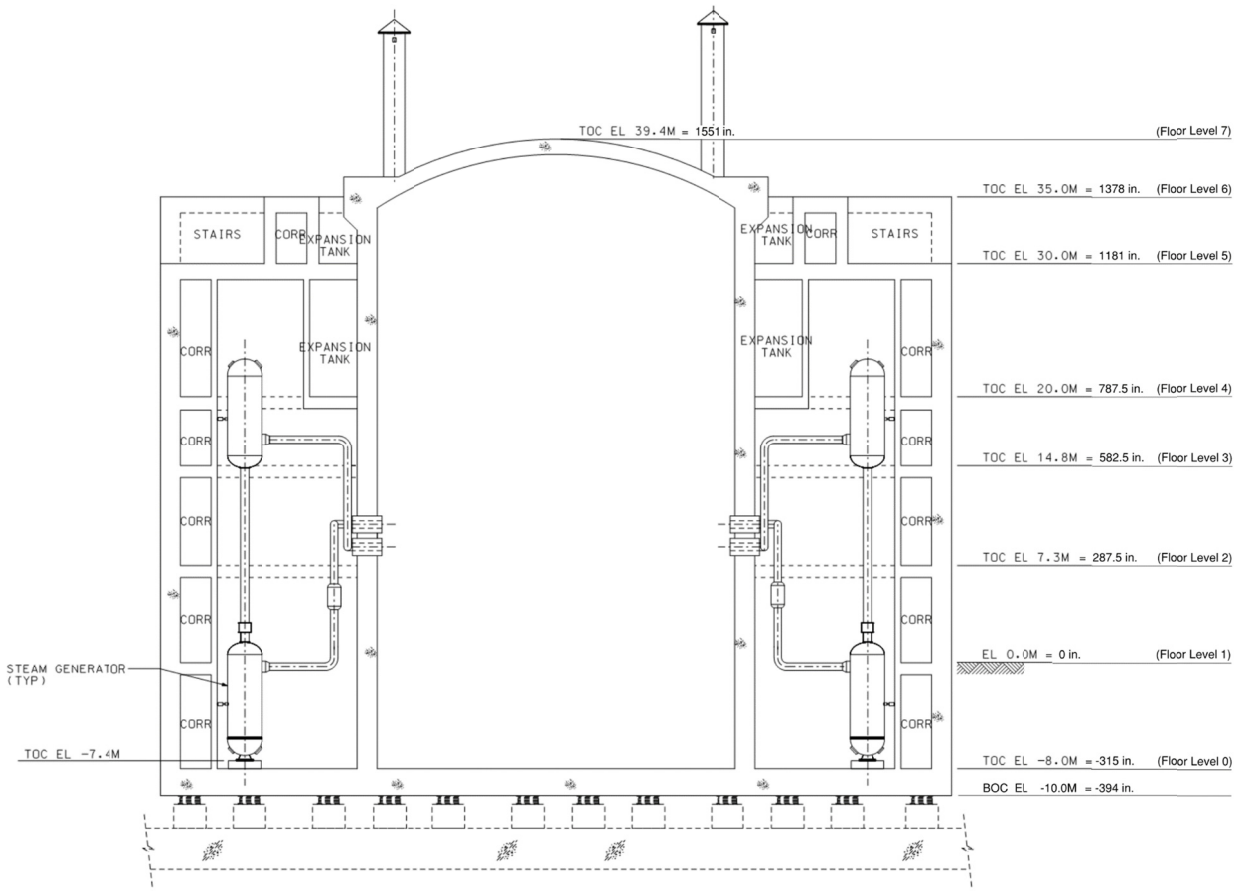

Figure 4.3 Elevation view of preliminary PGSFR general arrangement with dimensions.

4.2.2 Material and Damping Properties

The strength, stiffness, and weight density of the RC used to model the RCB, AUX, and the common base mat was selected with the following properties:

RC material:

- Strength: 27.6 MPa (4 ksi)
- Elastic Modulus: 24,856 MPa (3605 ksi)
- Shear Modulus: 10,356 MPa (1502 ksi)
- Poisson's Ratio: 0.2
- Weight Density: 23.56 kN/m^3 (150 pcf)

Rigid material:

- Strength: 27.6 MPa (4 ksi)
- Elastic Modulus: 24,856 GPa (3,604,997 ksi)
- Shear Modulus: 10,356 GPa (1,502,082 ksi)

- Poisson's Ratio: 0.2
- Weight Density: 0.0 kN/m^3 (0 pcf)

Damping was assigned as stiffness proportional damping with the following values:

- RCB: 5% anchored at 4.3 Hz
- AUX: 7 % anchored at 5.4 Hz
- Base Mat: 7 % anchored at 7.0 Hz

Less damping was assigned to the RCB than the AUX because it was assumed that the RCB is a prestressed RC structure, while the AUX is assumed to be constructed from regular RC.

4.2.3 Analysis Model

In the analysis model shown in Figure 4.4, the left shorter stick represents the AUX and the right taller stick represents the RCB. The origin of the coordinate system for the analysis model is located at the center of the RCB at ground elevation. Beam–column frame elements were used to model the two portions of the lumped-mass plant superstructure. The common base slab was modeled using shell elements; therefore, it had distributed weight and mass properties. Beneath the base mat, 152 elastomeric bearing elements were defined to model the isolation system. The FE mesh of the base mat was created in such a way that it consisted of 152 nodes and isolator elements that were connected to each one of these nodes. The other end of the isolator elements was fixed directly to the ground, which means that isolator pedestals and soil were not included in the analysis model and possible soil–structure interaction (SSI) effects were not considered in this preliminary study.

In order to connect the two lumped-mass sticks to the base mat and to correctly transfer axial forces, shear forces, and overturning moments, several additional frame elements were created and assigned to the analysis model. For the RCB, a weightless frame element was defined with stiffness properties that corresponded to the walls of the RCB, which was assigned along the circumference of the RCB. These RCB-wall elements were then connected to the base mat, and rigid elements were then used to radially connect the RCB stick to the RCB-wall elements. Similarly, for the AUX, a weightless AUX-wall element was defined and assigned to the perimeter of the AUX. Diagonal rigid elements were then defined to connect the AUX stick to the AUX-wall elements, which were connected to the base mat. Hence, the weightless wall elements, which act as imbedded beams in the shell element base mat, provided a means to accurately connect the simplified superstructure sticks to the mat; they also accounted for the stiffening effect of the base mat along wall lines. The numbering of nodes and elements for the two lumped-mass sticks is shown in the bottom subfigure of Figure 4.4. Vertical node locations correspond to the elevations called out in the elevation view of Figure 4.3.

Frame-element section properties are summarized in Table 4.1. As shown in Figure 4.5, the RCB section was assigned over the entire height of the RCB stick; similarly, the AUX section was assigned over the entire height of the AUX stick; therefore, stiffness properties were uniform along the height. RCB-wall elements were assigned at the base mat elevation around the circumference of the RCB superstructure, and AUX-wall elements were assigned at the base mat

elevation around the perimeter of the AUX superstructure. The remaining frame elements that connect together the different parts of the model were assigned *RIGID* section properties using the rigid material definition, which is 1000 times stiffer than the typical RC material.

The shell elements used to model the base mat had an assigned thickness of 2 m (78.74 in.) and used the *RC material* to determine their distributed weight and mass properties.

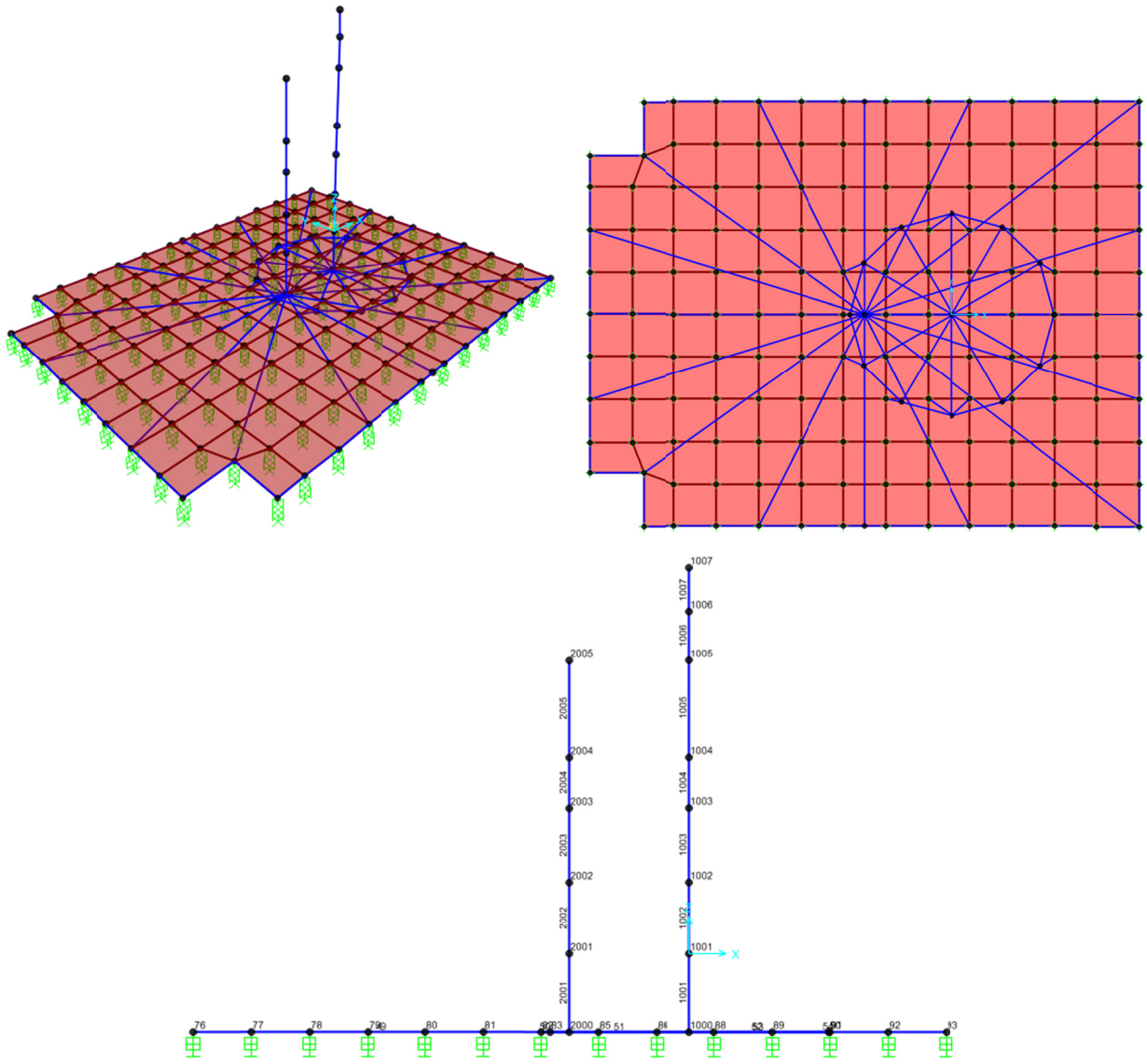

Figure 4.4 3D view, plan view, and elevation view of analysis model.

Table 4.1 Frame element section properties (in.).

Section	A (in.^{2})	I_z (in.^{4})	I_y (in.^{4})	A_y (in.^{2})	A_z (in.^{2})	J (in.^{4})
RCB	208,169	3.2851E10	3.2851E10	104,276	104,276	6.5702E10
AUX	620,773	8.5460E11	5.7516E11	358,050	276,672	1.0353E12
RCB-Wall	103,368	2.6440E10	2.9985E07	86,140	86,140	1.1740E08
AUX-Wall	76,641	1.0780E10	2.2232E07	63,868	63,868	8.6384E07
RIGID	100,000	1.0000E10	1.0000E10	100,000	100,000	1.0000E10

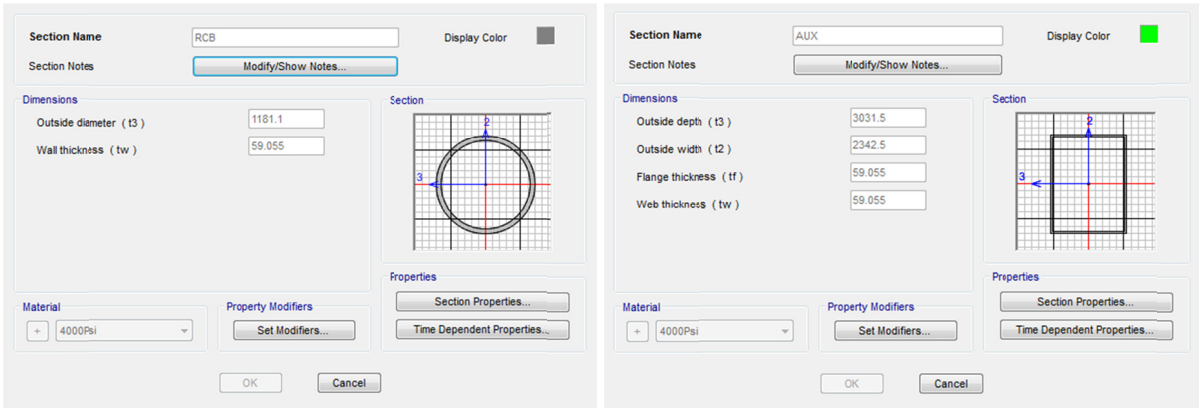

Figure 4.5 Section property definitions for the reactor containment building and auxiliary building frame elements (kip, in.)

The initial properties of the LRB isolators before they were modified for the parametric study are given in Table 4.2. The weight of the 2 m (78.74 in.) thick base mat is 21,477 tonf (47,348 kip). It is not possible in OpenSees to assign distributed weight to shell elements; therefore, the weight of the base mat was assigned as vertical forces to the 152 nodes. On the other hand, masses and mass moments of inertia of the base mat were directly calculated from the mass density (ρ = 2.2483e-07 kip sec^2/in.^{4}) assigned to the shell elements. The weights and masses assigned to the nodes of the two superstructure sticks are summarized in Table 4.3. In the absence of any more detailed data about building and component weights, it was assumed that the slab self-weight plus additional dead load of all major floors was 31.41 kN/m^3 (200 pcf). It was then assumed that the reactor makes up the difference to reach the total plant weight of 151,897 tonf (334,875 kip). Based on this assumption, the estimated weight of the reactor is 7492 tonf (16,516 kip), which was assigned to node 1002.2 at elevation 7.3 m (287.5 in.).

Finally, the weight and the mass contributions of the RCB and AUX containment walls were accounted for as distributed frame-element properties on the two superstructure sticks. For the RCB elements, the distributed weight per length was 18.07 kip/in. and the distributed mass per length was 0.0468 kip sec^2/in.^{2}. For the AUX elements, the distributed weight per length was 53.89 kip/in. and the distributed mass per length was 0.1396 kip sec^2/in.^{2}.

Table 4.2 Initial lead-rubber bearing element properties (kip, in.).

Direction	Linear		Nonlinear		
	Stiffness	Damping	Stiffness	Yield strength	Post-yield stiffness ratio
X	73,656.00	90.70	-	-	-
Y	51.24	11.27	3070.36	226.98	7.82E-03
Z	51.24	11.27	3070.36	226.98	7.82E-03
XX	1.00	0.00	-	-	-
YY	1.00	0.00	-	-	-
ZZ	1.00	0.00	-	-	-

Table 4.3 Nodal weight and mass assignments (kip, in.).

Node	W	m_x	m_y	m_z	m_{xx}	m_{yy}	m_{zz}
1001	4,993	12.931	12.931	12.931	0	0	2,254,900
1002.1	4,993	12.931	12.931	12.931	0	0	2,254,900
1002.2	16,516	42.778	42.778	42.778	6,151,200	6,151,200	701,510
1003	4,993	12.931	12.931	12.931	0	0	2,254,900
1007	4,868	12.608	12.608	12.608	0	0	2,198,500
2001	27,366	70.880	70.880	70.880	0	0	86,694,000
2002	27,366	70.880	70.880	70.880	0	0	86,694,000
2003	27,366	70.880	70.880	70.880	0	0	86,694,000
2004	27,366	70.880	70.880	70.880	0	0	86,694,000
2005	27,366	70.880	70.880	70.880	0	0	86,694,000

4.2.4 Dead Load and Eigenvalue Analysis Results

Figure 4.6 depicts the plan distribution of vertical reactions. The distribution due to dead load is concentrated around the perimeter and around the RCB. This distribution is not ideal and likely a consequence of rigid elements used to distribute loads from the building into the base mat. The independence of lateral and axial forces in analytical bearing models used means this distribution does not invalidate analysis results.

Eigen-frequencies and mode shapes of the fixed-base model are provided in Table 4.4 and Figure 4.7, respectively. The primary mode corresponds to translation of the RCB at a

frequency of 4.3 Hz. This frequency shifts to 3.6 Hz in the isolated model; see Table 4.5. The primary mode in the isolated model corresponds to translation at the isolation layer; see Figure 4.8. The frequency of this mode is 0.47 Hz or a 2.1-sec period, and coincides with the translational mode in the perpendicular direction. The third mode of the isolated model is rotation about the vertical axis with a frequency of 0.67 Hz or a 1.5-sec period.

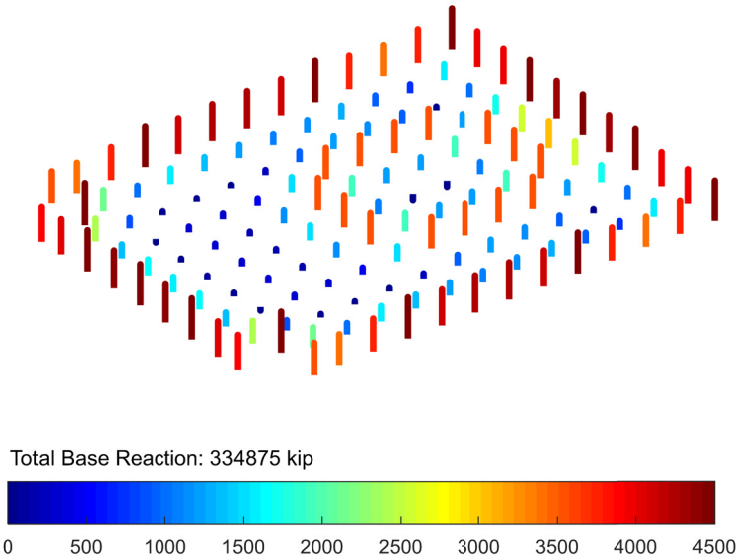

Figure 4.6 Axial load distribution in isolators under dead-load case.

Table 4.4 Eigen-frequencies of fixed-base model.

Mode	*F* (Hz)	Bldg. Comp.	Direction
1	4.284	RCB	H2 translation
2	4.284	RCB	H1 translation
3	5.010	AUX	H2 translation
4	5.732	AUX	H1 translation
5	10.599	RCB	H2 translation
6	10.599	RCB	H1 translation
7	11.188	AUX	V rotation
8	12.103	AUX	V translation
9	12.635	RCB	V translation
10	14.646	AUX	H2 translation
11	16.744	AUX	H1 translation
12	19.493	RCB	V rotation

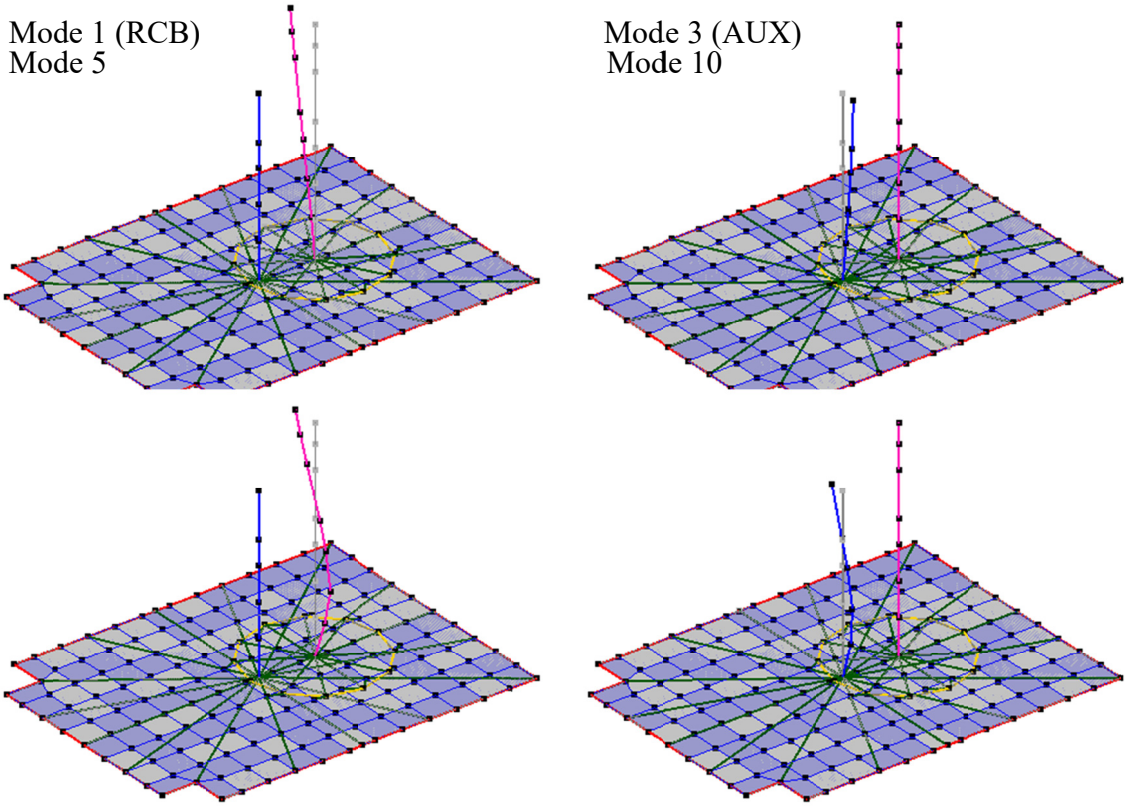

Figure 4.7 **Selected mode shapes of fixed-base model.**

Table 4.5 **Eigen-frequencies of the seismically isolated model.**

Mode	*F* (Hz)	Bldg. Comp.	Direction
1	0.472	ISO	H2 translation
2	0.475	ISO	H1 translation
3	0.668	ISO	V rotation
4	3.580	RCB	H2 translation
5	3.695	RCB	H1 translation
6	7.384	RCB/AUX	H2 translation
7	8.197	RCB/AUX	H1 translation
8	8.836	ISO	V translation
9	9.729	RCB	V translation
10	11.145	RCB/AUX	H2 translation
11	11.636	RCB/AUX	H1 translation
12	16.245	RCB/AUX	V rotation

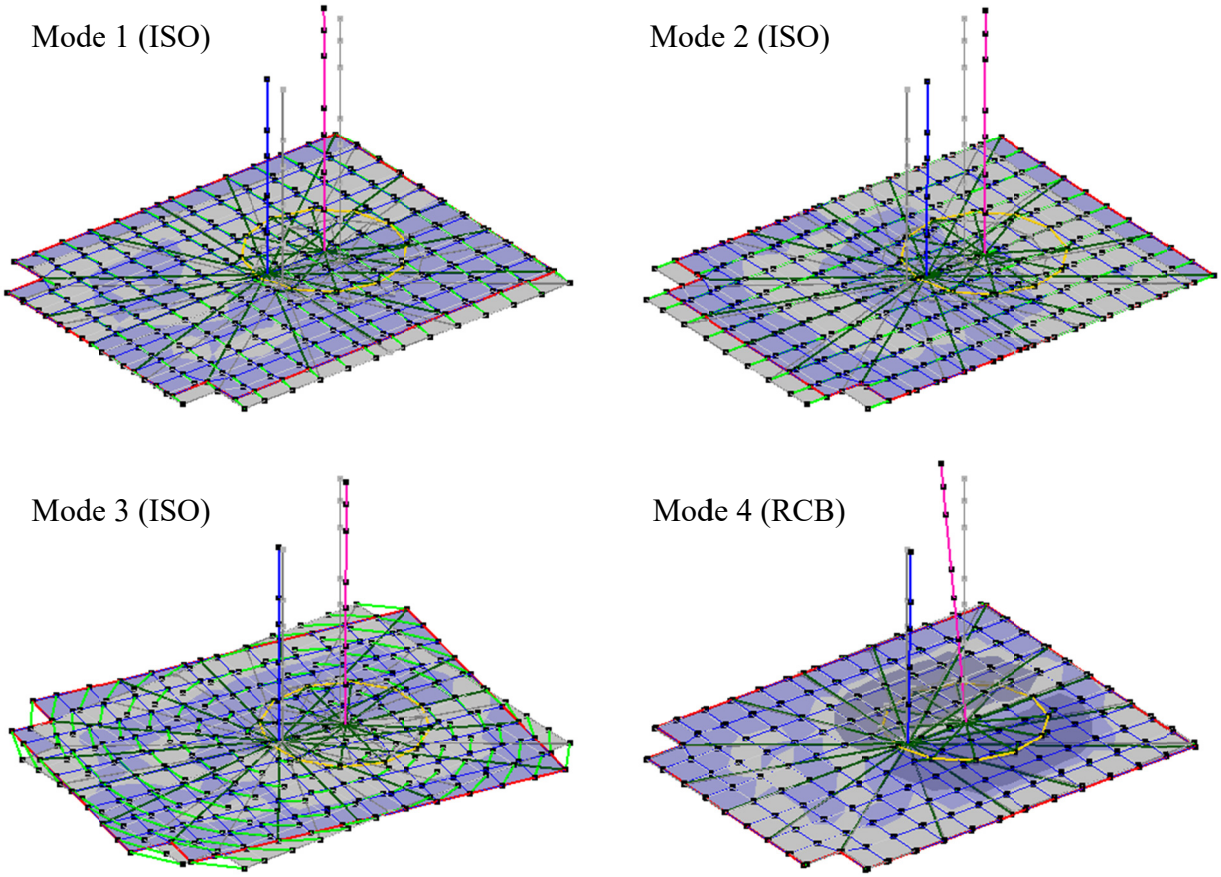

Figure 4.8 Selected mode shapes of the seismically isolated model.

4.3 GROUND MOTIONS CONSIDERED IN THE ANALYSES

Ground motions used for the analyses in this chapter were the same as those used in the simplified rigid-mass model presented in Chapter 3. The original ground-motion set contains 20 ground motions scaled to the NRC target spectrum with a target PGA of 0.5*g*. In this chapter, each ground motion contains three components (Horizontal 1, Horizontal 2, and Vertical), which are used in the three-component time-history analyses with the refined model in OpenSees. The ground-motion set used in the analyses was scaled to a PGA of 0.3*g* and a PGA of 0.1*g* by scaling the amplitudes of all time histories with scale factors of 0.6 and 0.2, respectively. The following section will use a ground-motion set of 0.3*g* PGA and a ground-motion set of PGA 0.1*g*.

The ground-motion set of 0.3*g* PGA was considered as the general design-level ground motion for the isolated NPP. The responses of the isolated model and the fixed-base model subjected to the 0.3*g* PGA design-level ground motion set is compared first to investigate the benefit of using seismic isolation for the PGSFR power plant. The other ground-motion set, which was scaled to 0.1*g* PGA, was used for analysis of the fixed-base PGSFR model. The 0.1*g* PGA level ground motion was viewed as the design-level ground motion for a fixed-base design of the PGSFR. Therefore, another comparison will be made between the isolated 0.3*g* PGA case and the fixed-base 0.1*g* PGA case to see how much of an increase in the seismic hazard can be

achieved for the design-level ground motion by using seismic isolation; see Section 3.3 for additional information on selecting ground-motion time histories and the construction of the NRC RG1.60 target spectra.

4.4 PARAMETRIC STUDY SUMMARY

The study compares the seismic response of the fixed-base PGSFR and the base-isolated PGSFR. Per Section 4.3, two seismic conditions were used in the comparison. The two comparisons are performed for different reasons. The purpose of comparing the base-isolated case subjected to the 0.3*g* PGA ground-motion set with the fixed-base case subjected to the same ground-motion set is to investigate the benefits obtained from seismic isolation. The purpose of comparing the base-isolated case with 0.3*g* PGA and the fixed-base case with 0.1*g* PGA is to examine how much the seismic hazard can be increased by using isolation while maintaining acceptable plant superstructure response levels and safety margins. Similar to the previous chapter, different parameters of the isolators are being studied in this chapter but are applied to the refined model in OpenSees instead of the rigid-mass model.

The parameters considered here for the isolators are the initial stiffness ($K_{initial}$), the post-yield stiffness or the post-yield period (T_{iso}), and the yield force (F_y) or the characteristic strength of the bearing. The detailed summary of each case considered in this parametric study is shown in Table 4.6.

Table 4.6 Summary of analysis cases used in the parametric study.

	Seismic Input	Initial stiffness ($K_{initial}$)	Isolation period (T_{iso})	Bearing yield force (F_y)	Parameter considered
Fixed-base	NRC set with PGA of 0.1*g*	NA	NA	NA	
	NRC set with PGA of 0.3*g*	NA	NA	NA	
Base-Isolated	NRC set with PGA of 0.3*g*	**5 $K_{postyield}$**	3 sec	10% *W*	Different $K_{initial}$
		10 $K_{postyield}$	3 sec	10% *W*	
		100 $K_{postyield}$	3 sec	10% *W*	
		10 $K_{postyield}$	**2 sec**	10% *W*	Different T_{iso}
		10 $K_{postyield}$	**3 sec**	10% *W*	
		10 $K_{postyield}$	**4 sec**	10% *W*	
		10 $K_{postyield}$	3 sec	**5% *W***	Different F_y
		10 $K_{postyield}$	3 sec	**10% *W***	
		10 $K_{postyield}$	3 sec	**15% *W***	
		10 $K_{postyield}$	3 sec	**20% *W***	

4.4.1 Comparison of Different $K_{initial}$

Because of the relatively low value of PGA selected for the design-basis earthquake (SSE), the isolator deformations are expected to be small. In a preliminary run using the refined model and a representative 0.3*g* record, the peak bearing response amplitude is around 50 mm (2 in.) for T_{iso} = 3 sec, F_y = 0.1 W, and $K_{initial}$ = 10 $K_{postyield}$. During this response, the bearing deformed into the post-yield range only a few times; in most of the cycles, and the bearing remained in the elastic range; therefore, the isolator and structural response may depend significantly on the initial stiffness of the isolator. Thus, in the first part of this parametric study, the post-yield stiffness of the isolator is fixed at T_{iso} equals 3 sec, and F_y is fixed at 10% W. To show the importance of this parameter, three different initial stiffness values were considered and the responses compared. The initial stiffnesses used here are characterized by the ratio of the post-yield stiffness. The post-yield stiffness was held constant, and the initial stiffness was assumed to be 5, 10, and 100 times stiffer. The reason to choose the ratio of $K_{initial}$ to post-yield stiffness instead of a real value of the initial stiffness (which is mainly based on the area of a particular lead plug), is to obtain a more intuitive sense on the value of the initial stiffness used. The post-yield stiffness is a common design-oriented parameter considered in bearing design. The most common ratio used in practice is around 10%. The actual values of the initial stiffness are 827, 1655, and 16,550 MPa (120, 240, and 2400 kips/in.) for each bearing.

4.4.2 Comparison of Different T_{iso}

As discussed in Chapter 3, the isolation period T_{iso}, which is based on the post-yield stiffness of the isolator, is the most important parameter considered in the design of a seismic isolation system since it influences both the displacement demands of the isolators and the forces transferred to the superstructure. However, because of the small deformations that the isolators in the refined model underwent when subjected to the SSE, the effectiveness of T_{iso} on the response may not be as large as for the simplified rigid-mass model discussed in Chapter 3.

In this part of the parametric study, a T_{iso} of 2 sec, 3 sec, and 4 sec were evaluated and compared, while the isolator yield force F_y was kept at 10% of weight on bearing, and the initial stiffness was kept at 10 times the post-yield stiffness. When studying different post-yield stiffnesses, the initial stiffness values need to be kept unchanged. Therefore, by changing the post-yield stiffness ratio, different post-yield periods can be achieved for the same initial stiffness.

4.4.3 Comparison of Different F_y

The yield force of the isolator is another parameter considered in this series of parameter studies. Per Chapter 3, it was found that F_y has a fairly large influence on the displacement demand but has only a minor effect on the force demand for the simplified isolated rigid-mass case. However, because of the overall smaller bearing deformations, F_y has a more pronounced effect on the superstructure response in this case. The total shear force that propagates up into the superstructure from the bearing is the yield force plus the increase of force due to the post-yield stiffness of the bearing. Since the isolator deformation is small, the contribution from the second part is negligible; therefore, any change of the force demand in the superstructure is directly

related to F_y. More detailed results and a discussion of this behavior will follow later in this chapter.

In this section, different isolator yield forces were considered and compared, with F_y equal to 5%, 10%, 15%, and 20% of the initial gravity load on the bearing. As mentioned earlier, the LRB isolator elements used in these studies do not account for any vertical–horizontal coupling effects in terms of forces and bearing kinematics. Hence, changes in the vertical force in the isolators due to vertical excitation and rocking during the response history analyses do not affect the shear behavior of the isolators. The other two parameters are kept unchanged. The post-yield period was kept at 3 sec, and the initial stiffness was kept at 10 times the post-yield stiffness, which is 1655 MPa (240 kips/in.).

4.5 ANALYSIS RESULTS AND DISCUSSION

Selected results will be shown below and accompanied by an in-depth discussion. With the refined analysis model, horizontal floor response spectra and vertical floor response spectra of each floor level for both the RCB and AUX were generated and compared. Drift response of the RCB and AUX along their height were also analyzed. Isolator hysteresis loops and displacement orbits were captured for all of the 152 bearings supporting the plant superstructure. The corner bearing and center bearing are shown and compared in detail.

The described response quantities were analyzed and discussed for the NRC ground-motion set, which contains 20 ground motion histories either scaled to 0.3*g* PGA or 0.1*g* PGA. The results shown in this section for the RCB and the AUX are median response quantities as well as 84th-percentile response quantities (which are one standard deviation above the median).

For each of the plots showing response results, peak absolute values over the entire response history are reported; however, plots illustrating isolator responses show the entire response history. Since the ground-motion input is three-directional, horizontal response quantities were calculated by taking the norm of the response values of the two horizontal directions at each time step.

For each of the plots, fixed-base cases for a PGA of 0.1*g* are represented by black dashed lines, fixed-base cases for a PGA of 0.3*g* are shown as black solid lines, and different base-isolated cases for a PGA of 0.3*g* are represents by colored lines.

4.5.1 Results for Different $K_{initial}$

A comparison of different $K_{initial}$ values was carried out since a reasonable initial stiffness value for the isolators is needed for subsequent parameter studies. As an insightful response quantity for the design of NPPs, floor acceleration spectra are compared first. The horizontal floor spectra of the RCB are shown in Figure 4.9. The RCB model has seven floors, and the floor acceleration spectra in the horizontal direction for the first floor, fourth floor, and the roof are shown in Figure 4.9. As previously noted, the spectral acceleration value corresponds to the norm of the two horizontal directions; therefore, for the spectral acceleration at the largest frequency in the graph, the fixed-base peak floor acceleration is not 0.3*g* because the norm of the two scaled components is larger than 0.3*g*.

Comparing the floor spectra of each floor, from the ground floor to the top floor, a pronounced amplification of the spectral accelerations can be observed as the floor level increases. The largest peak in each spectrum corresponds to the fundamental mode of the RCB of the fixed-base model at 4.3 Hz. The peak spectral acceleration at the fixed-base fundamental frequency is amplified from 1.2*g* to almost 5*g*, whereas the peak floor acceleration at large frequencies increases less from 0.5*g* for the ground level to 1*g* for the roof level. These large amplifications are reasonable around the fundamental frequency of the fixed-base case since the fundamental mode shape increases with height and is largest at the top. However, when considering the fundamental isolation mode, which is represented by the small spectral acceleration peak at around 0.6 Hz, the peak is not amplified much from the ground floor to the roof. This is due to the fundamental isolation mode shape being nearly constant along the height.

In a comparison between the base-isolated cases and the fixed-base cases for the horizontal floor acceleration spectra of the RCB, the base-isolated case for the 0.3*g* PGA design-level ground motion set generates similar spectral acceleration amplitudes as the fixed-base design subjected to the 0.1*g* PGA ground-motion set. Hence, the isolated PGSFR NPP can sustain design-hazard levels that are approximately three times larger than what is possible for the fixed-base plant. However, even though the overall spectral acceleration amplitudes are similar, the frequency content of the floor spectra is changed. The response for the isolated plant is larger for certain parts of the frequency range as compared to the 0.1*g* PGA fixed-base case, especially around the fundamental isolation frequency. Note that most of the equipment will not be sensitive to long-period motion except for possible sloshing of free-liquid surfaces. This difference may not influence much the design of the plant superstructure and equipment, but it needs further investigation. A comparison of the same 0.3*g* PGA fixed-base case with the base-isolated case clearly demonstrates the great benefit obtained by using seismic isolation technology as can be seen by comparing the colored lines with the black solid line in Figure 4.9 for each floor level. The reduction in spectral accelerations is approximately by a factor of 3 for the base floor and slightly smaller as the floor level increases.

When comparing floor spectra for each of the base-isolated cases with different bearing initial stiffnesses, it is clear that a small initial stiffness produces better results than a large initial stiffness. A distinct change of the spectral acceleration peak at the fundamental isolation frequency can be seen in the acceleration spectra for all floor levels. For a smaller initial stiffness of the isolator, the effective stiffness of the isolator is also reduced, and the spectral acceleration peaks corresponding to the effective isolator frequencies are shifted to lower frequencies. For higher floor levels, significant amplification of the spectral acceleration peaks occurred around the fundamental frequency of the RCB for cases with large isolator initial stiffness. Higher-mode peaks in the floor response spectra were also more amplified for cases with the larger isolator initial stiffness.

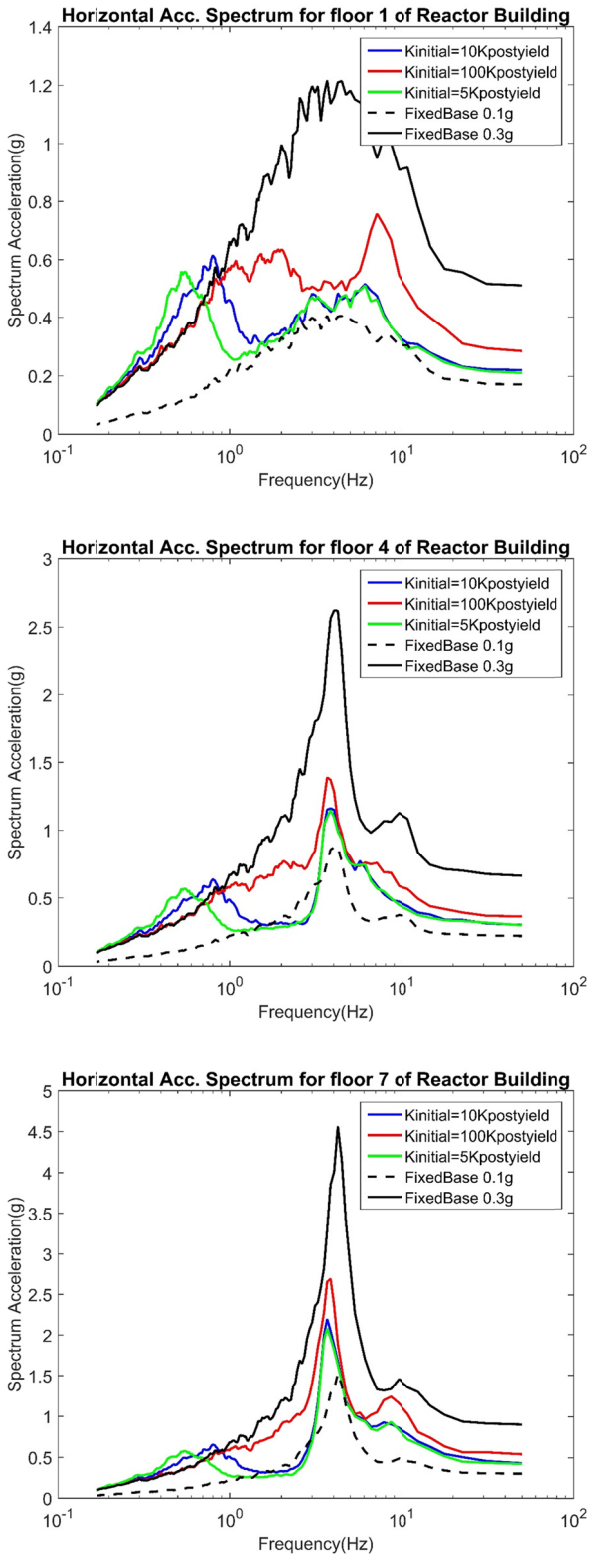

Figure 4.9 **Median horizontal floor acceleration spectra for first floor, fourth floor, and roof of the reactor containment building. Base-isolated cases with different initial stiffness and fixed-base cases with different PGA are compared.**

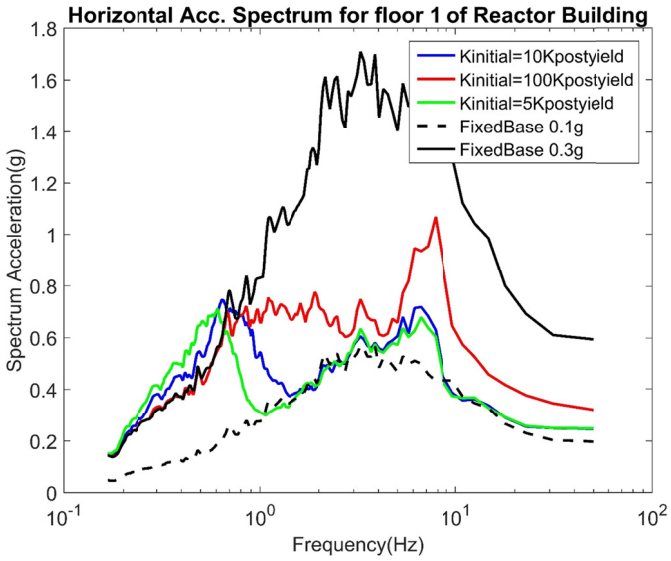

Figure 4.10 **84th-percentile horizontal floor acceleration spectra for first floor of the reactor containment building. Base-isolated cases with different initial stiffness and fixed-base cases with different PGA are compared.**

As demonstrated, for large bearing initial stiffness the spectral acceleration peak at the effective isolator frequency shifted to larger frequencies and eventually approached the fundamental frequency of the RCB. This lack of frequency separation caused significant amplification of the floor acceleration spectra around the fundamental frequency of the RCB. The relatively small bearing deformations seen at the given hazard level intensified the effect the isolator initial stiffness had on the floor acceleration spectra.

For subsequent studies, the initial stiffness of the bearing was selected to be 10 times the post-yield stiffness instead of the much larger initial stiffness initially considered. Because the isolation system underwent fairly small deformations at the 0.3*g* PGA hazard level, it is desirable to use a smaller, more typical isolator initial stiffness to better separate the fundamental frequency of the isolation system from the lowest frequency of the superstructures to avoid resonance effects.

Figure 4.10 shows the 84th-percentile horizontal floor acceleration spectra at the first-floor level of the RCB. Comparing the spectral acceleration amplitudes between the 84th-percentile response and the median response, the amplification factor is around 1.25, which is less than the 1.5 factor obtained from the simplified analyses using the rigid-mass model. The difference between the median and the 84th-perentile values is smaller because typical bearing deformations are smaller, i.e., the bearing responded more often in its elastic range, thus the variability of the response was smaller.

The AUX horizontal floor acceleration spectra are shown in Figure 4.11. Large amplifications of the response along the height were observed, similar to the behavior of the RCB. The benefit of using isolators with small initial stiffness is demonstrated once again as spectral acceleration amplitudes are higher for the case with a large isolator initial stiffness. Compared to the floor acceleration spectra of the RCB, spectral acceleration amplitudes for the AUX are generally smaller, especially at the fundamental frequency for the fixed-base case.

Unlike the spectral accelerations of the RCB, the peak around the fundamental frequency of the AUX is suppressed instead of amplified.

This is due to the change of modal characteristics of the isolated structure from the original fixed-base structure. For the fixed-base case, the first vibration mode frequency corresponding to the deformation of the RCB is around 4 Hz. This is consistent with the results shown in Figure 4.9 and Figure 4.10, where the fixed-base response spectra peak is around 4 Hz, which is the fundamental frequency of the RCB. When isolated, the vibration mode frequency corresponding to the deformation of the RCB is also around 4 Hz; therefore, in Figure 4.9 and Figure 4.10, for the floor spectra of the isolated model, the second peak is still predominant, which is also around 4 Hz as fixed-base case.

Because the mode corresponding to the movement of the AUX is around 5 Hz, the peak of floor acceleration spectra for the fixed base is around 5 Hz. However, given the interaction between the base mat and the two sticks in the model, the mode corresponding to the movement of the AUX in the isolated model has shifted; Therefore, the floor spectra response of the isolated AUX has a shifted peak compared to the fixed-base model.

In terms of the peak floor acceleration response value, the PGA of 0.5*g* for ground level can be reduced to around 0.2*g* by choosing smaller initial stiffness of bearings, and a response reduction factor around 2.5 can be achieved. Overall, considering floor spectra for frequencies larger than 1 Hz (which we are considering critical in the design of a NPP), the response reduction using seismic isolation is more pronounced for the AUX comparing to the RCB.

In addition to the horizontal spectra, the vertical floor acceleration spectra were also investigated; see Figure 4.12. A comparison between different floors demonstrates that the amplification effect of the vertical ground motion is not as large as the horizontal ground motion. The peak value of the acceleration spectrum increased from 1.0*g* at the base up to 1.8*g* at the roof, which is approximately double.

In terms of the amplitude of vertical acceleration compared to the horizontal acceleration, the vertical acceleration is around one-half. Comparing the base-isolated case and the fixed-base case, amplification is expected for the base-isolated case because the vertical stiffness of the bearing is included. Based on modal analysis of the fixed-base model, the original vertical mode frequency of the RCB was around 12 Hz. Including the isolation plane and the vertical stiffness of the isolation system, the new vertical mode frequency becomes around 9.7 Hz; note the shift in peak in Figure 4.12. The amplitude of the new peak is larger than the original peak, around 50% higher in amplitude.

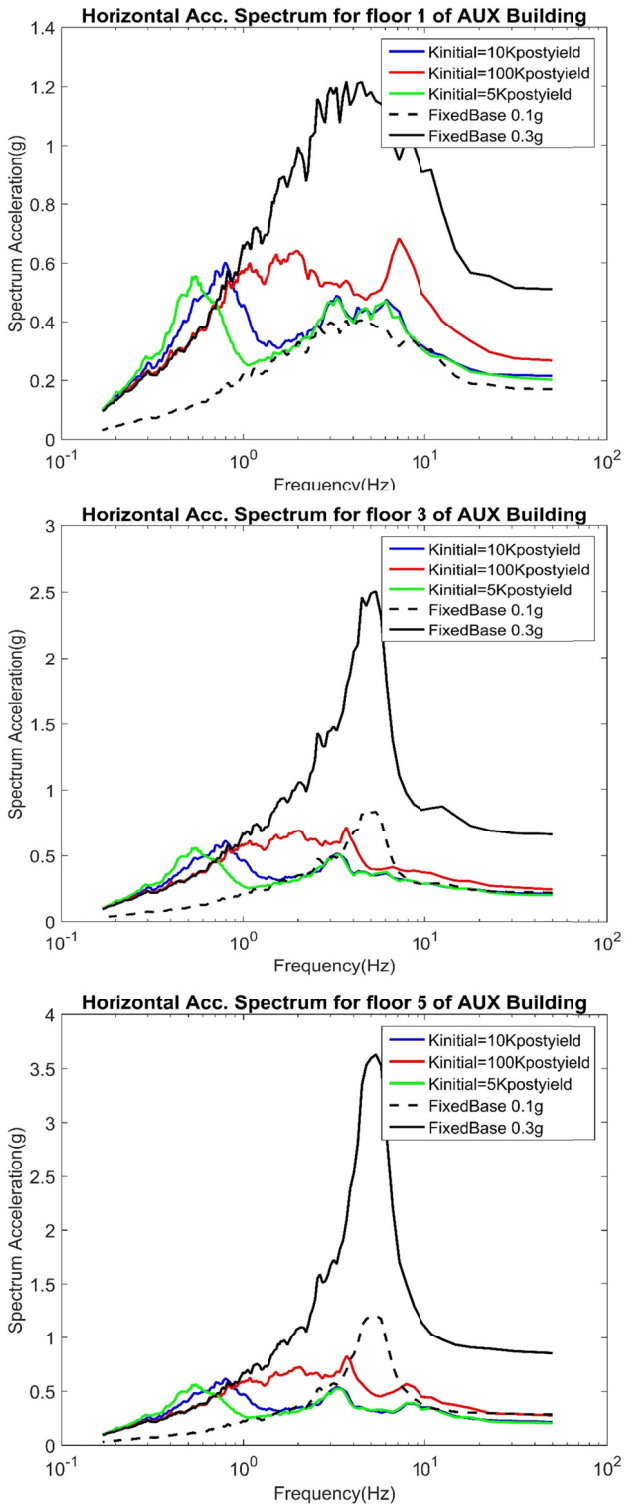

Figure 4.11 **Median horizontal floor acceleration spectra for first floor, third floor, and roof of the AUX. Base-isolated cases with different initial stiffness and fixed-base cases with different PGA are compared.**

The response is identical if we compare the vertical acceleration responses of the bearings with the different initial stiffness. Since the different parameters used in the bearing model only affect the horizontal behavior of bearing, the vertical characteristics of bearing are not affected by the horizontal parameters; therefore, the response is not influenced. The response of vertical floor spectrum for the AUX is similar and is not shown here.

Besides the response of floor spectrum, the force or drift demands were evaluated for the RCB and the AUX. The maximum story drift value of each floor during the time history was recorded, and the median response for each story is shown in Figure 4.13. The floor level or the story level is defined based on the discretization of the model representing the RCB and AUX. The story may not represent the real story of the facility especially for the RCB, but it will give a general view on the distribution of drift deformation along height for both buildings.

For the RCB, comparing the drift responses of the isolated model and fixed-base model for the 0.3*g* PGA hazard the response is almost the same, with the isolated reactor drift demand slightly smaller. Comparing the isolated model to the fixed-base case evaluated at the 0.1*g* PGA hazard, drift demands of the latter are much smaller. Since the isolator deformation is fairly small, the benefits of using base isolation are not quite obvious in terms of the force or drift demands. Since the seismic load is small, the force demand at the base of the superstructure is almost the same as the fixed base.

When investigating the drift response of the AUX, which is shown in the second subplot in Figure 4.13, the drift demand of the base-isolated case is much smaller than the fixed base for the 0.3*g* PGA hazard; the response is almost the same compared to a fixed-base case for the 0.1*g* PGA hazard. This difference in the drift response between the isolated RCB and AUX is consistent with the results shown in the floor spectra. The response reduction effect by using seismic isolation is not very evident because of the small deformation imposed on the isolator. However, the effect of dominate vibration frequency shift due to interaction of AUX, RCB and base mat suppressed the original peak response in the fixed-base AUX. Therefore, compared to the RCB which only obtains response reduction from the effect of base isolation, the response is much smaller for both drift scenarios for AUX.

A comparison between the drift responses of isolated systems with different initial stiffness demonstrates that the larger initial stiffness will result in a larger drift demand. For the system with bearing initial stiffness—5 and 10 times the post-yield stiffness—the responses are identical since the difference between the two stiffness (120 kips/in. and 240 kips/in., respectively) is relatively small. For the other case, corresponding to an initial bearing stiffness of 2400 kips/in., the drift is much larger. Overall, however, the drift demand, on the order of 0.02%, is fairly small. Even though the response may show some minor trends or differences between different isolator parameter values considered or even between the fixed-base case and base-isolated case, drift response might not control the design of this stiff upper structure. The 84^{th}-percentile drift response is shown in Figure 4.14. From the plot, the maximum drift response is in the order of 0.03%; therefore, even for one standard deviation above the median-level design ground motion, drift response is still very small since upper-structure is fairly stiff this case.

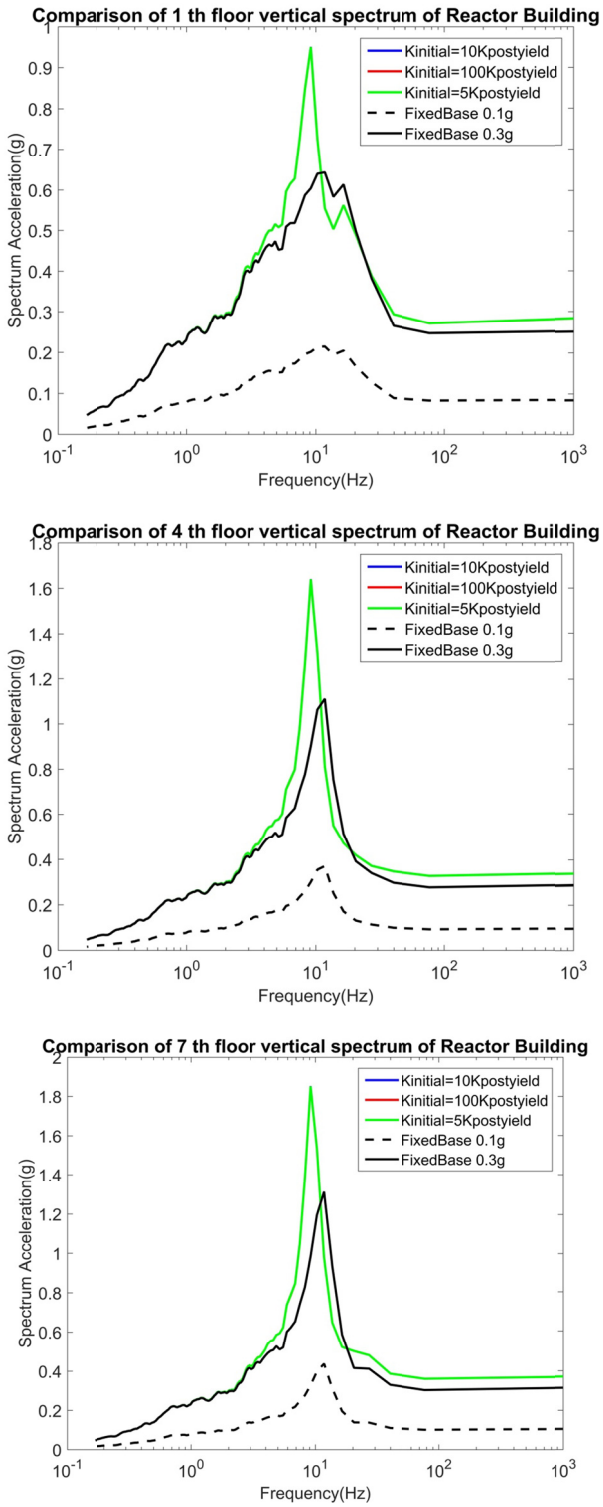

Figure 4.12 **Median vertical floor acceleration spectra for first floor, fourth floor, and roof of the reactor containment building. Base-isolated cases with different initial stiffness and fixed-base cases with different PGA are compared.**

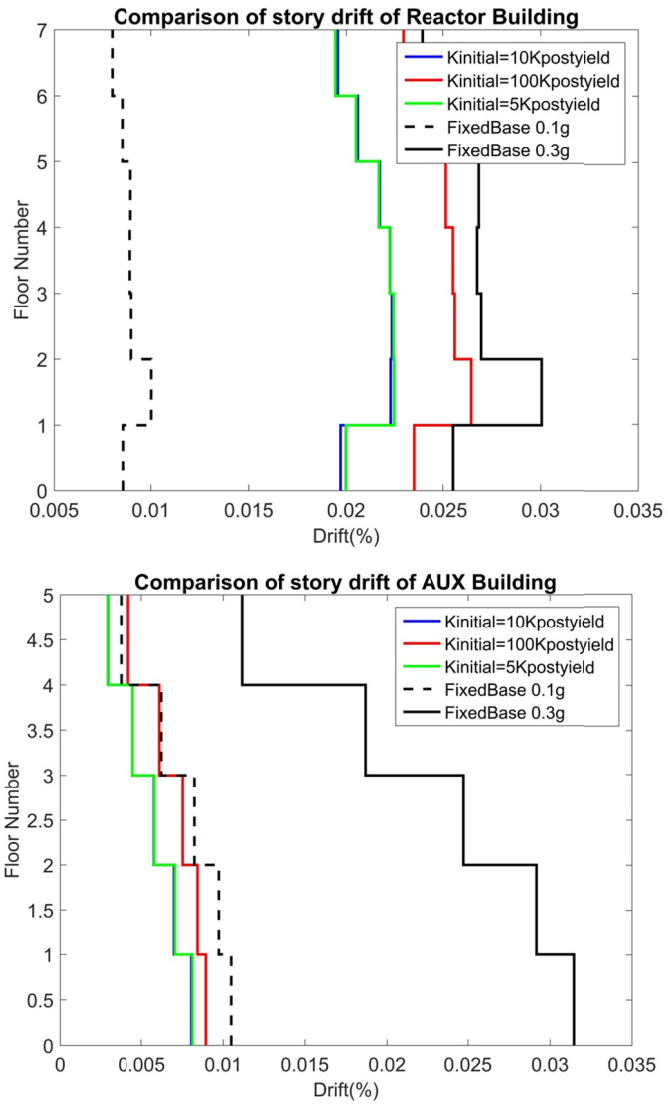

Figure 4.13 **Median maximum story drifts for reactor containment and auxiliary buildings. Base-isolated cases with different initial stiffness and fixed-base cases with different PGA are compared.**

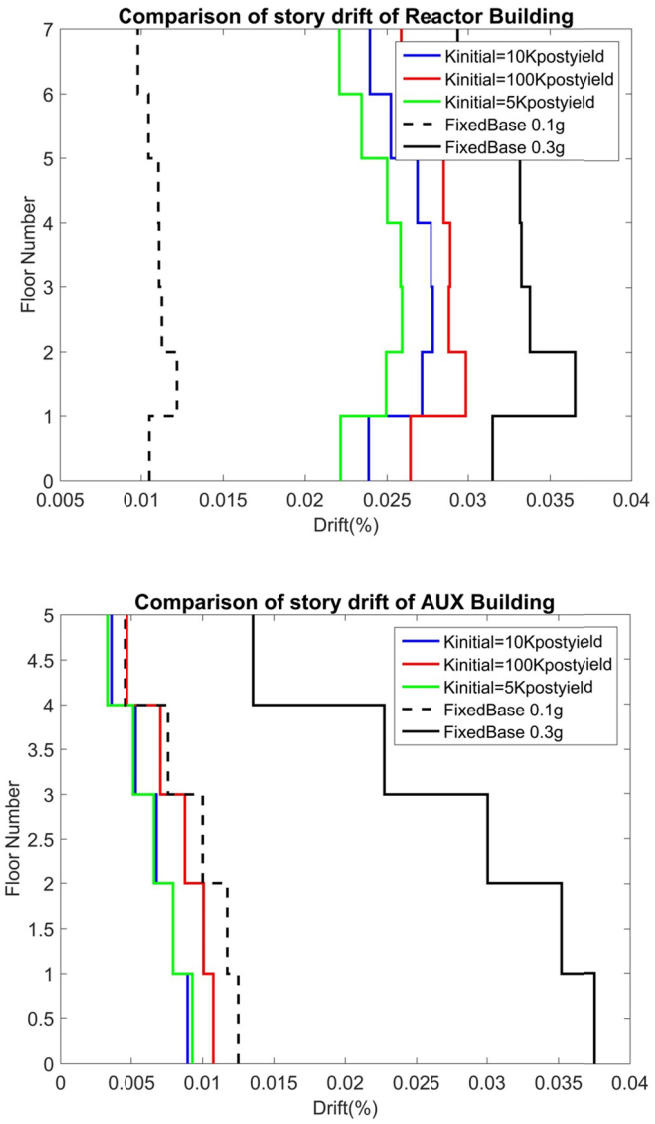

Figure 4.14 **84th-percentile maximum story drifts for reactor containment and auxiliary buildings. Base-isolated cases with different initial stiffness and fixed-base cases with different PGA are compared.**

As discussed previously, the isolation plan consisted of 152 isolators beneath the base mat. The difference in the responses for the bearings at different locations may be due to torsion of the base mat, but not due to axial load differentials induced by overturning because of the lack of vertical-horizontal coupling of isolator analytical models. The two bearings, one located at the northwest corner and the other located at the center of the base mat, will be investigated. Bearing hysteresis response and displacement orbit in horizontal direction are shown in Figure 4.15 and Figure 4.16, respectively.

Note that for this part of parametric study, the post-yielding stiffness and the yielding strength of bearings are kept the same for the different initial horizontal stiffnesses considered Although they are kept the same for different initial stiffnesses as shown in Figure 4.15, the bearing yielding strength is used instead of the bearing characteristic force as a comparison

parameter; therefore, the bearing hysteresis characteristic strength or the loop thicknesses for different cases are actually different. Because the thickness of hysteresis loop of a bearing is determined by the characteristic force instead of the yielding force, a lower initial stiffness will result in a lower characteristic force. As shown in Figure 4.15, the hysteresis loop of bearing with an initial stiffness five times the post-yielding stiffness is slightly thinner compared to the other two cases. The same issue is relevant when discussing the results of Chapter 5 for aircraft impact with bearings of different initial stiffnesses.

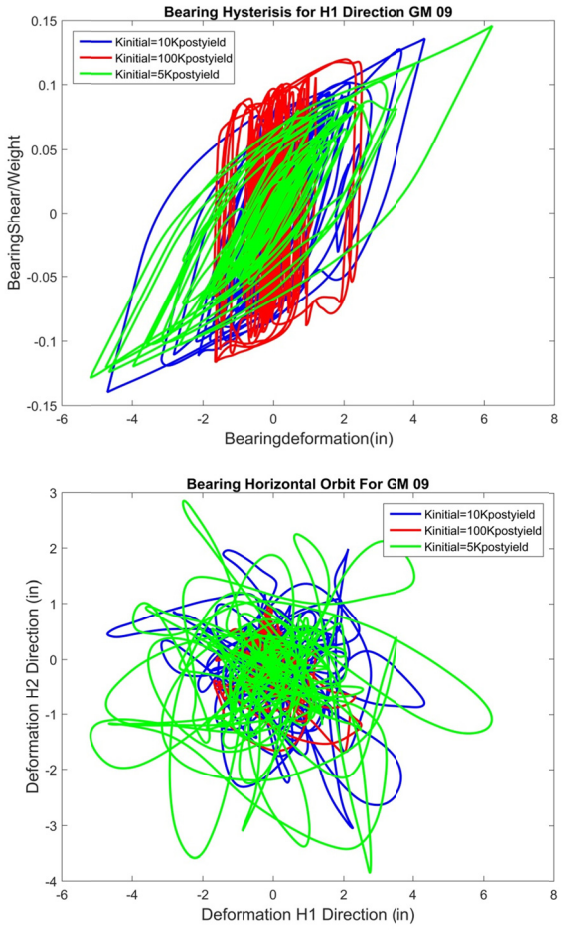

Figure 4.15 Southwest Bearing H1 direction hysteresis loop and displacement orbit under NRC PGA 0.3*g* ground-motion time-history number 9. The isolation system with different initial stiffnesses are shown together.

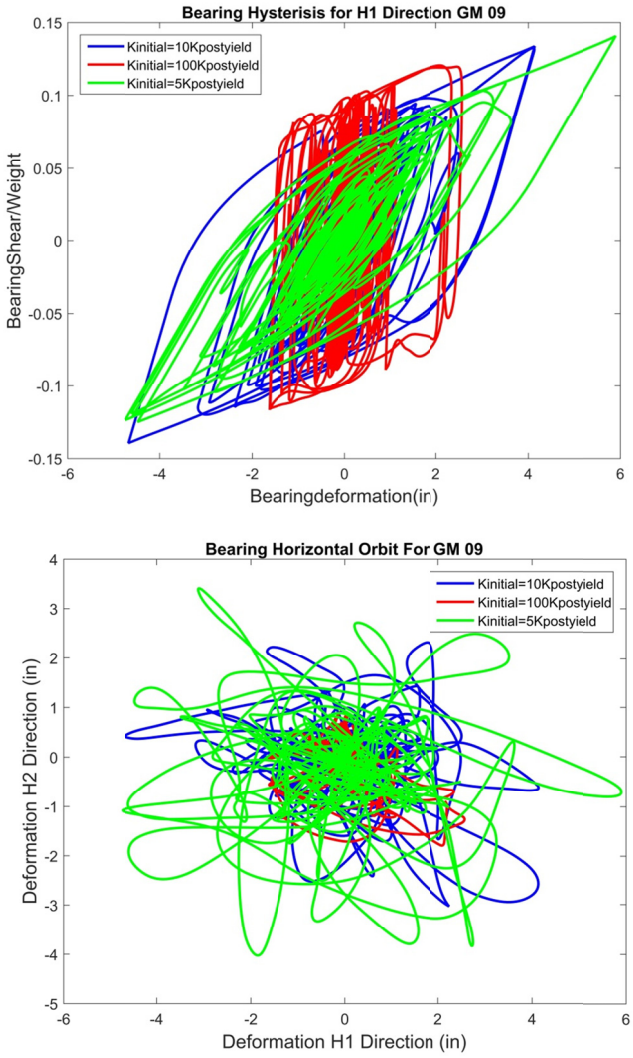

Figure 4.16 Center Bearing H1 direction hysteresis loop and displacement orbit under NRC PGA 0.3g ground-motion time-history number 9. The isolation system with different initial stiffnesses are shown together.

From the bearing horizontal hysteresis itself, the displacement of the isolator is rather small, on the order of 10.2 cm (4 in). The response of isolator subjected to ground-motion 9 is around the median response among all the 20-ground-motions. The force developed in the isolation systems is almost the same for the three cases considered: around 0.15*g*. Clearly, for isolators with different initial stiffnesses, the hysteresis behavior is not the same; the bearing with smaller initial stiffness has a larger displacement response as shown in the displacement orbit. The one with large initial stiffness has an isolator displacement around 5.1 cm (2 in.), which is approximately half of the displacement of the other two cases considered.

Compared to the center bearing, the corner bearing had a slightly larger displacement response, but, in general the responses were almost the same. The displacement orbits were almost identical. Therefore, no significant torsion effect is expected, and it can be assumed that the response of the isolators in the whole isolation plane are similar. The isolators moved in the

same direction and in phase. Since the distribution of the gravity load was assumed uniform for the whole isolation plane, the effect of different vertical loads on the bearings was not considered.

Based on results of the refined model developed in OpenSees to determine the effect of initial bearing stiffnesses on seismic response, some preliminary conclusions can be drawn. Some of the conclusions and findings associated with general effect of seismic isolation are not only for this specific comparison; they pertain to all the parameter studies conducted in this chapter and are summarized below:

1. Under design-level seismic loading considered, the isolator displacement is small for the archetype isolated PGSFR, and the effectiveness of seismic isolation is not pronounced, especially for the RCB.
2. The response of horizontal floor spectrum of the base-isolated case under the 0.3*g* PGA hazard is almost the same as the fixed-base case under 0.1*g* PGA hazard.
3. Horizontal floor spectra were largely reduced when using seismic isolation, especially for the high-frequency range compared to fixed-base case under 0.3g PGA hazard, even though the isolator deformation was small.
4. Vertical floor spectra responses were not reduced by using seismic isolation, and the response is not affected by the initial stiffness of the isolator.
5. The initial stiffness of the isolation affected the response of the isolated structure; a larger initial stiffness produced large floor response spectra and drift demand, but smaller bearing displacement demand.
6. The response reduction with base-isolation was much more significant for the AUX than for the RCB. The change of modal frequency of AUX further separated the upper plant frequency and isolation frequency. The change is due to the interaction of the RCB and base mat with the AUX.
7. Isolators at different locations behaved almost identically, and no torsion effect was observed in the base mat.

4.5.3 Results for Different T_{iso}

Based on the general conclusions outlined in the previous section regarding initial isolator stiffness, this section will focus on the difference in response when comparing the post-yield stiffness or period of the isolator. The three isolator periods considered were 2, 3, and 4 sec.

Responses of horizontal floor spectrum are shown in Figure 4.17. The amplitude of response is consistent with that obtained under different initial stiffnesses. First, as shown in Figure 4.17 for the first peak at around 2.5 sec on the spectrum, there is no shift of the location of the peak response among the different cases with different isolation periods; therefore, the effective period of the isolation system is not influenced by the post-yield stiffness and is dependent on the different initial stiffness. This conclusion is intuitive since the displacement of the isolator is small the initial stiffness contributes more to the response. Slight differences can be seen for the amplitude of the peak response, whereby a smaller post-yield period results in a larger response; however, the difference in the response of the floor spectrum is negligible,

especially for the high-frequency response. The different isolation period only affects the floor spectrum of the first peak and has no effect on the high-frequency response.

As demonstrated earlier regarding the amplification of the response from the base to the top, the scale comparing the fixed-base case and base-isolated case is similar for different isolation periods. The floor spectrum for the AUX when using seismic isolation resulted in an almost five-fold reduction; see Figure 4.18. It is clear in this figure that the peak response on the original fixed-base floor spectrum is suppressed using base isolation. This is especially true for the top floor response, where the isolated response is better than the fixed-base response under 0.1*g* PGA hazard; the performance in response to design-level ground motion is far superior when using seismic isolation. Despite the larger response in smaller frequency ranges because of the isolation period, most of the equipment is in the range larger than 1 Hz. Thus, the effectiveness of using base isolation is fairly good.

Because the vertical response spectrum is not dependent on the horizontal property of the bearing, it will not be discussed. This parametric study considered the properties for the horizontal behavior of the bearings; therefore, the vertical response acceleration spectrum is the same for all cases. Due to the vertical stiffness of the isolators, the floor spectrum was amplified slightly when using seismic isolation compared to the original fixed-base case.

The drift response is shown in Figure 4.19, which is almost identical to the drift response shown in Figure 4.13; thus, similar conclusions can be drawn. The effectiveness on reducing drift demand or shear demand (since the relation of shear and drift are the same in elastic range) is small for the RCB. The drift is almost the same when comparing the base-isolated case and fixed-base case for the RCB. For the AUX, the effect is much improved. The base-isolated cases under PGA 0.3*g* ground motion have drift demands even smaller than the fixed-base case under the 0.1*g* ground motion.

A comparison between the drift response of different post-yield stiffnesses or isolation period does not show much difference. The separation for different cases on the plot indicates larger isolation period results in a smaller drift response. The 3- and 4-sec responses are almost the same, which differs from the 2-sec case.

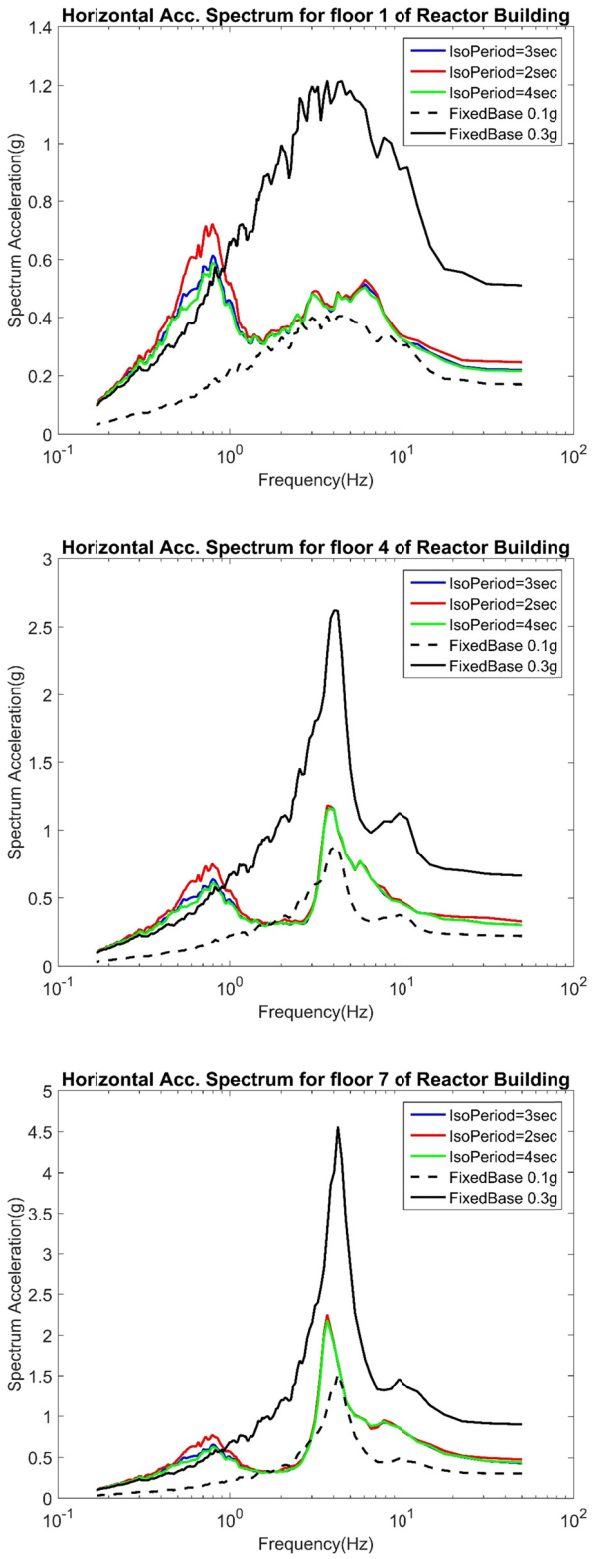

Figure 4.17 **Median horizontal floor acceleration spectrum for first floor, fourth floor, and top floors of the reactor containment building. Base-isolated cases with different isolation period and fixed-base case under PGA 0.3*g* NRC motion set and fixed-base under PGA 0.1*g* motion set are compared.**

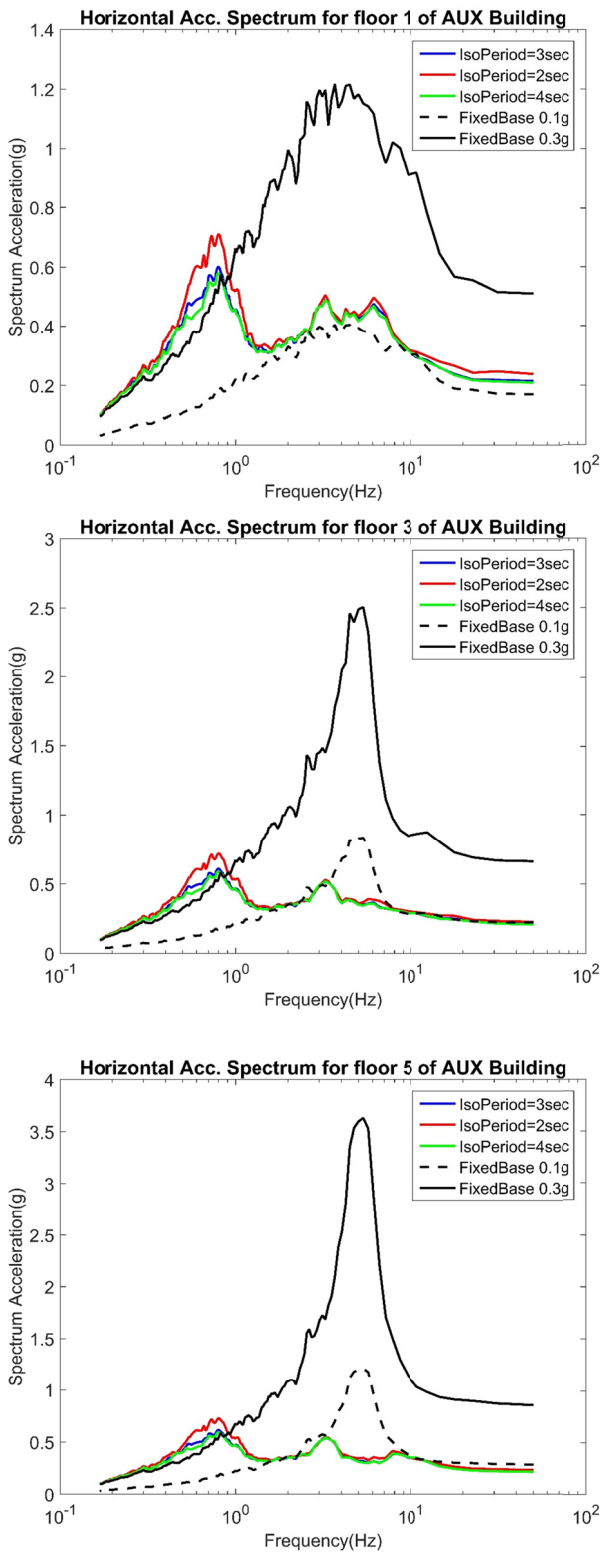

Figure 4.18 **Median horizontal floor acceleration spectrum for first, third, and top floors of the auxiliary building. Base-isolated cases with different isolation period and fixed-base case under PGA 0.3*g* NRC motion set and fixed-base under PGA 0.1*g* motion set are compared.**

Next, bearing response is considered with respect to ground-motion 4, which is the largest ground motion considered in the set. The bearing hysteresis and displacement orbit is shown in Figure 4.20 and Figure 4.21. For ground-motion 4, bearing displacement around 25.4 cm (10 in.) is expected.

A comparison between the bearing response of different isolation periods demonstrates that the displacement demand is similar; however, the force demand is quite different. The isolator with 2-sec isolation period exhibited up to a 0.25*g* maximum horizontal force while the 3- and 4-sec isolation periods had around a 0.15*g* peak value, which is consistent with the drift responses for these three cases. Note that for the isolator with a 2-sec period, there was a large cycle recorded in the positive H1 direction. This may due to the interaction of bi-directional motions or the change of previous cycle response. A comparison between the corner bearing and the center bearing shows that the responses are identical; therefore, the movement of the whole floor mat is almost purely translational, with all the isolators moving together in the same phase.

Figure 4.22, which shows the top floor spectrum of the RCB subjected to ground-motion 4, indicates that the difference in isolator responses due to different post-yield stiffness is obvious when the isolator displacement is large. Comparing with Figure 4.17, where there is almost no difference in responses for different isolation periods, since the isolator displacement is fairly small. In Figure 4.22 the red line which indicates the response with isolation period as 2 secs is more separated from the other two cases. This indicates the larger displacement the bearing undergoes the more important the post-yield stiffness is on the response.

From simplified analysis results in chapter 3, the post-yield stiffness is an important parameter considered in design. However, in this case, the effect of isolation period has an unexpectedly small influence on the response because isolator displacement is small. Some key conclusions obtained from this section are summarized below:

1. In terms of the floor spectrum, the post-yield stiffness will affect the amplitude of the peak response at the isolation period. Larger periods will result in smaller responses. Variations between the post-yield stiffness did not influence the horizontal floor spectrum responses at high frequency.
2. The larger the isolator displacement, the greater the dependence will be on different isolation periods. With the small isolator displacement in this study, the dependence is weak.
3. In terms of AUX and RCB drift responses, smaller isolation periods will result in smaller drift responses. But since the overall drift demand is fairly small, the difference can be negligible.

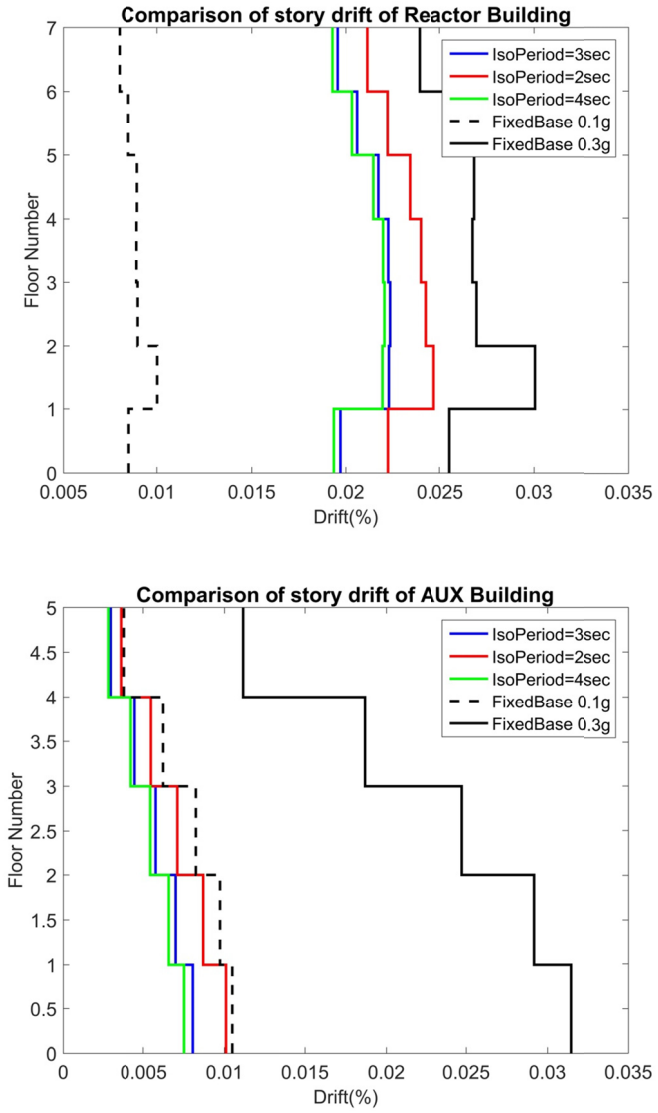

Figure 4.19 **Median maximum drift responses for the reactor containment building and auxiliary building. Base-isolated cases with different isolation period and fixed-base case under PGA 0.3*g* NRC motion set and fixed-base under PGA 0.1*g* motion set are compared.**

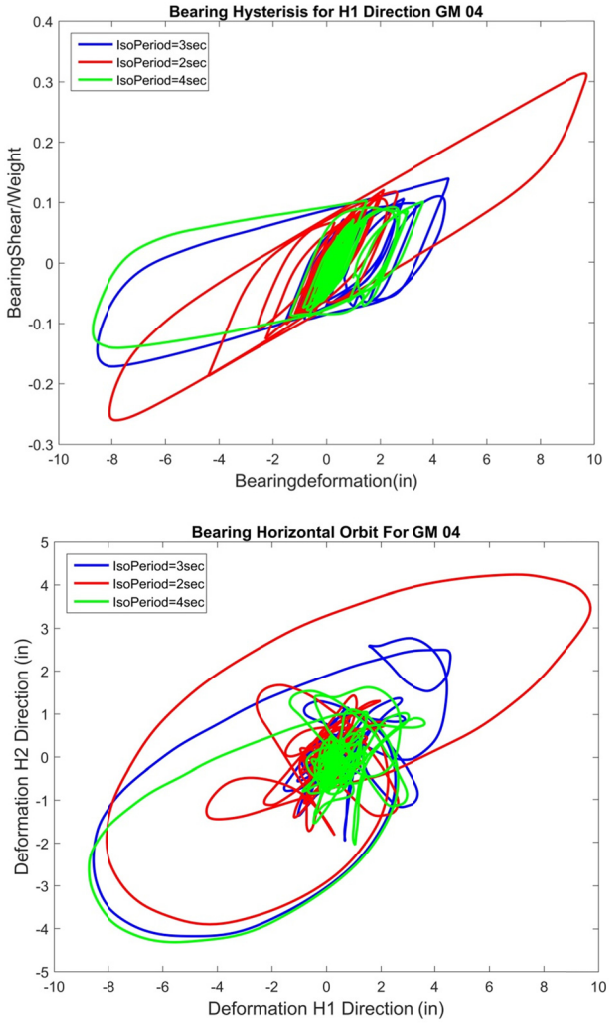

Figure 4.20 **Southwest Bearing H1 direction hysteresis loop and displacement orbit under NRC PGA 0.3*g* ground-motion time-history number 4. The isolation system with different isolation periods are shown together.**

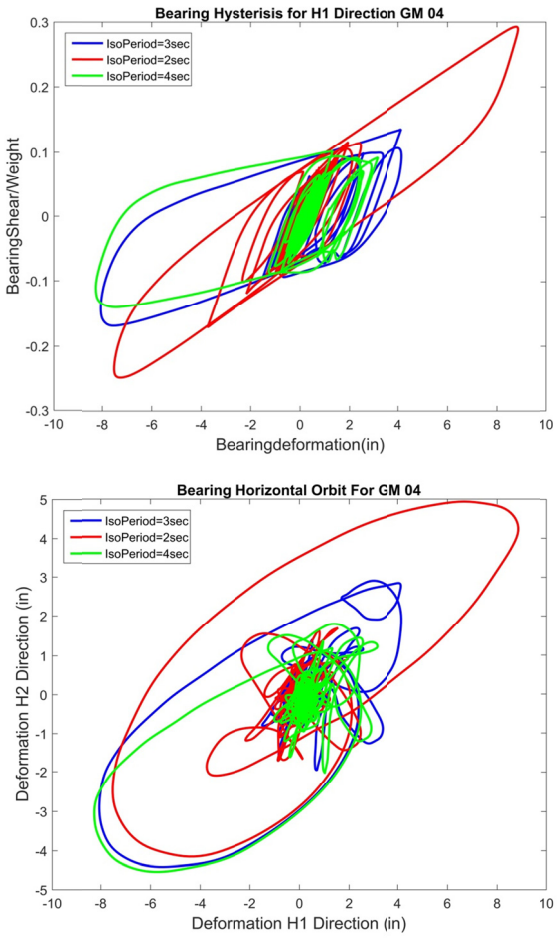

Figure 4.21 **Southwest Bearing H1 direction hysteresis loop and displacement orbit under NRC PGA 0.3*g* ground motion time-history number 4. The isolation system with different isolation periods are shown together.**

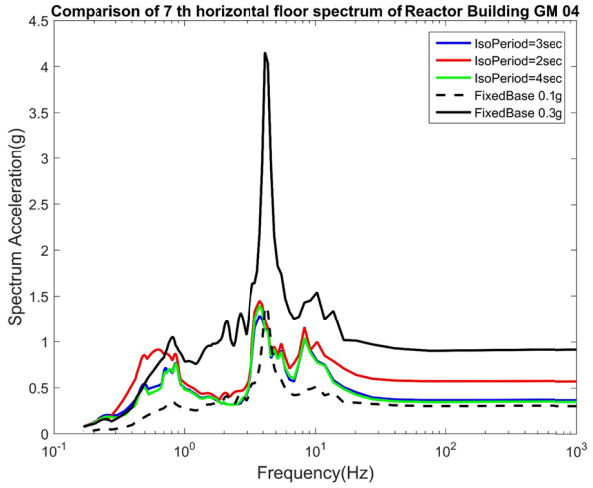

Figure 4.22 **Horizontal floor acceleration spectrum for top floor of the reactor containment building is shown. Base-isolated cases with different isolation period and fixed-base case under 0.3*g* NRC motion set and fixed base under 0.1*g* is compared. The response is for ground-motion 4.**

4.5.4 Results for Different F_y

Finally, we investigate the effect of different yield forces on bearing performance. The yield forces are set as 5%, 10%, 15%, and 20% of the weight on the bearing. Since the displacement of bearing is small, F_y is expected to be the most important parameter influencing response. Note that the conclusions reached in Chapter 3 determined that that F_y has only a minor effect on displacement demand of the bearing and almost no effect on force demand.

First, we study the floor spectrum shown in Figure 4.23. Note the great difference in the first peak of the floor spectrum for different yielding forces of the bearing. Since the different yielding forces affect the behavior of the isolator significantly in the small displacement range, the peak of the isolation mode is well separated. If the yield force is equal to 20% weight on the bearing, the peak is a factor of 3 higher than the case for a yield force equal to 5%.

When the yield forces become larger, the amplitude of the first peak response corresponds to the isolation mode on floor spectrum increases. However, responses at higher frequency remain unchanged. The second peak on the response spectrum collapses together for different yield force cases. The effect is similar to the response of different isolation periods discussed previously and is different from the responses of different initial stiffness of bearing.

In previous section, when comparing responses under different isolator initial stiffness, amplitudes of higher frequency contents on the floor spectrum are affected rather than lower frequency content. While there is a shift of dominant frequency of the low frequency peak, no amplitude difference is observed. For the two cases considering different T_{iso} and F_y, the change of these two parameters has little effect on the stiffness of the system but does affect the isolator force. Therefore, without changing the stiffness, the peak location is not changed for the isolation mode, but the response differs significantly in the peak amplitude in contrast to the response with different initial stiffnesses, which can be seen in Figure 4.23 and Figure 4.17.

An investigation of second peak responses on the floor spectrum reveals that for all cases, the second peak location (corresponding to the model frequency of the RCB in the isolated system) remained unchanged. However, since a different initial stiffness shifts the location of the first peak, with a larger initial stiffness, the distance between the first peak and second peak is closer, i.e., the isolation period is not well separated for the original fixed-base period. This causes base isolation to be ineffective, and the response of the original fixed-base mode remains higher. The amplitude of floor spectrum for those cases with different initial stiffnesses for the second peak is much larger for a larger initial stiffness compared to smaller one.

Variations of T_{iso} and F_y did not affect the original RCB mode, nor did they shift the isolation period. Therefore, the response other than the isolation mode remained unchanged. The only differences for these cases are the amplitude in the floor response spectra at the isolation mode. For the AUX, the response is shown in Figure 4.24 and similar conclusions can be drawn.

Because the peak of the fixed-base AUX mode on floor spectrums is suppressed, the peak response of the floor spectrum is controlled by the isolation mode. For the RCB, the peak response of floor spectrum is controlled by the peak of the RCB mode, which lies in the frequency range of most of the equipment. In the case of increasing floor levels, responses at higher frequency range is increasing since the upper-structure modes starts to contribute to responses. The vertical floor acceleration spectrum will not be discussed again since changing isolator horizontal design parameters do not affect vertical responses.

The drift response along the height of the RCB and the AUX is shown in Figure 4.25. In general, the amplitude of drift response is similar for different cases regardless of the initial stiffness, post-yield period, or the yield force of the bearing. The relative amplitude relation between the base-isolated cases and the two fixed-base cases are similar.

For different yield forces of the bearing, a smaller F_y results in smaller drifts since drift is mostly affected by the isolator force. When the displacement is small, the bearing yield force is the most effective way to change the isolator force. Considering the small amplitude of the drift responses, the response may already be controlled through other design considerations.

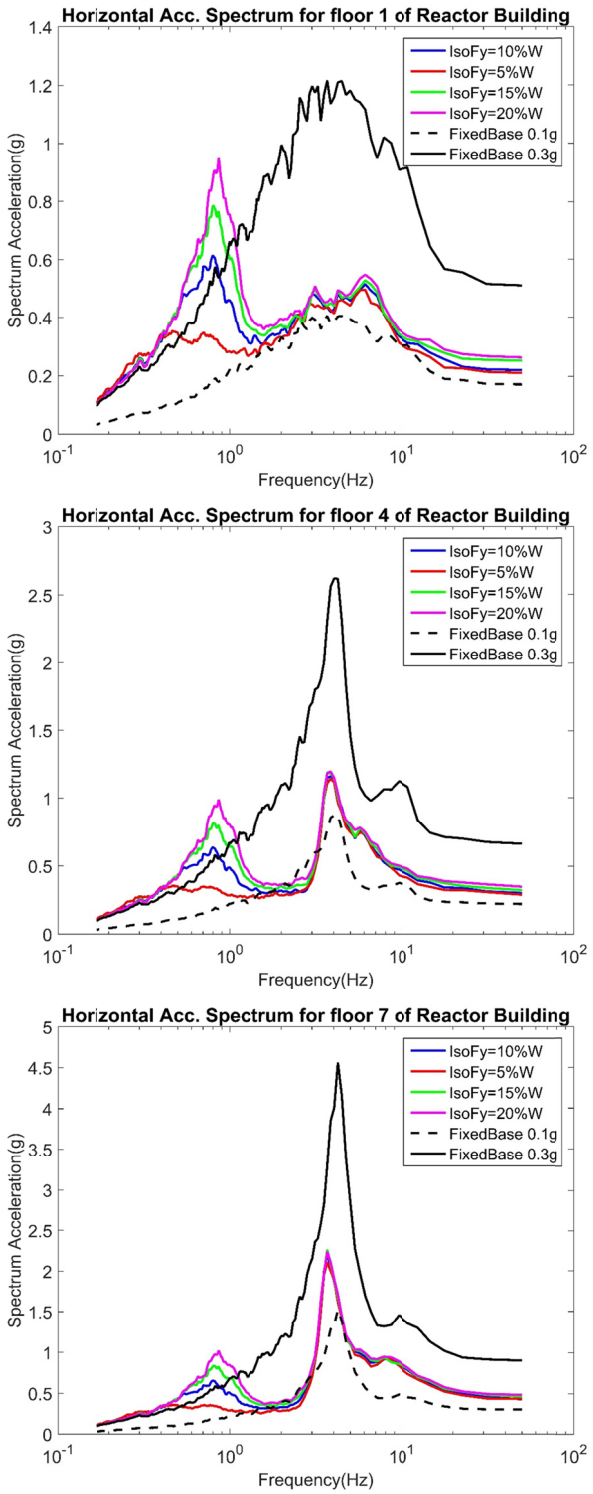

Figure 4.23 **Median horizontal floor acceleration spectrum for first floor, fourth floor, and top floors of the reactor containment building. Base-isolated cases with different bearing yield forces and fixed-base cases under PGA 0.3*g* NRC motion set and fixed-base case under PGA 0.1*g* motion set are compared.**

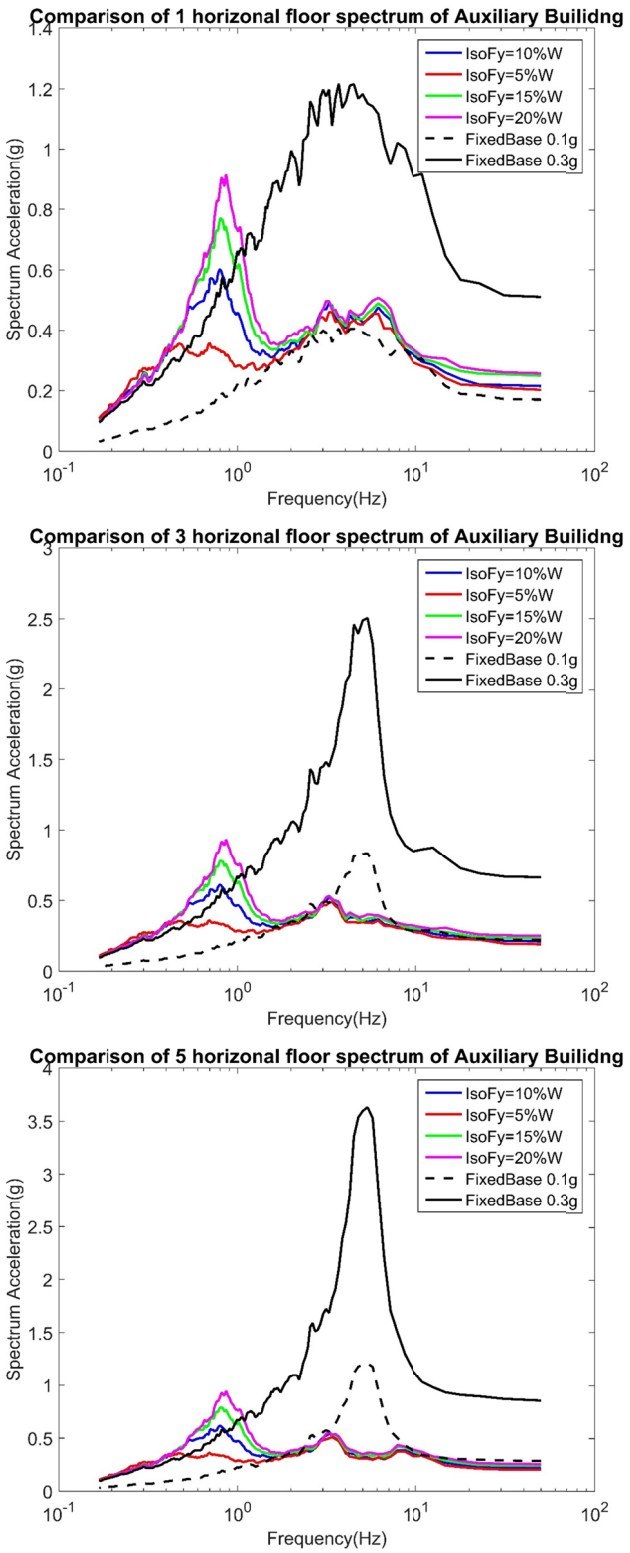

Figure 4.24 **Median horizontal floor acceleration spectrum for first floor, third floor, and top floors of the auxiliary building. Base-isolated cases with different bearing yield forces and the fixed-base case under PGA 0.3*g* NRC motion set and fixed base under PGA 0.1*g* motion set are compared.**

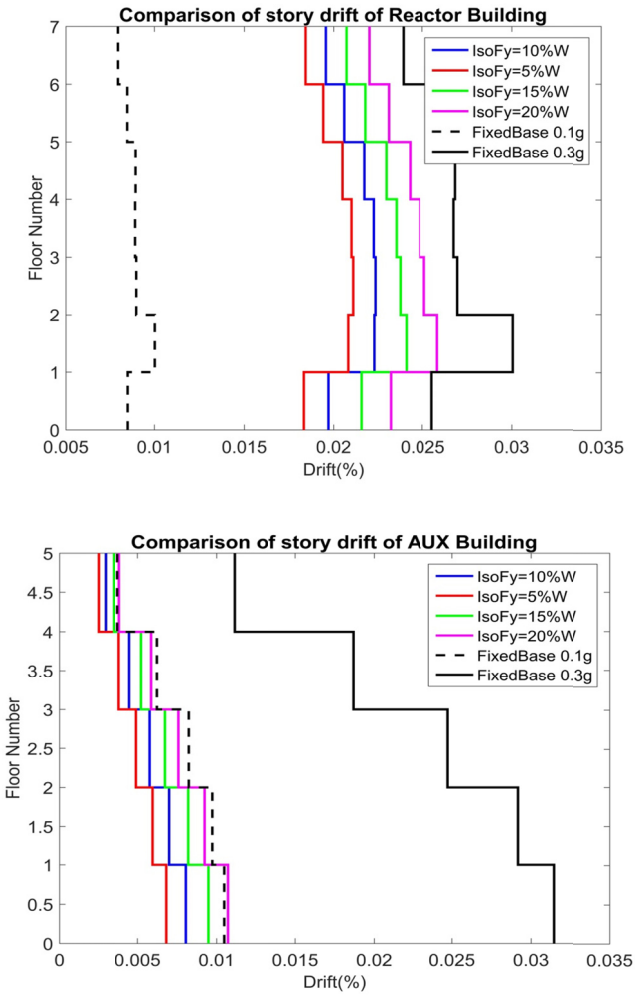

Figure 4.25 **Median maximum drift responses for reactor containment building and auxiliary building. Base-isolated cases with different bearing yield forces and fixed-base case under PGA 0.3*g* NRC motion set and fixed-base case under PGA 0.1*g* motion set are compared.**

The response of the corner bearing and the center bearings are shown in Figure 4.26 and Figure 4.27 together with the displacement orbit. The ground motion used for the response in these figures is ground-motion 19. Clearly, from the hysteresis responses, the smaller yield force will result in a larger displacement response of the bearing. For this particular ground-motion time history, the three bearings with the largest yield forces had much smaller displacements, and the bearing remained elastic under several cycles. The bearing corresponding to a 5% weight underwent a large displacement for one cycle, which may correspond to the pulse in the ground-motion time history.

From the displacement orbit of the bearing, the orbit is almost 45°, indicating that the two horizontal responses are similar. The difference between the corner bearing and the center bearing is not obvious, but slightly larger displacements are observed in the corner bearing, see Figure 4.26 and Figure 4.27. Although the post-yield stiffness is kept the same for different yielding strengths of the bearing, those cases with higher bearing yielding forces (indicated by

the blue, purple, and green lines) show a much higher secant stiffness comparing to the case with a lower yielding force (indicated by the red line). Those bearings with large yielding forces experienced such small deformations that they lie in the transition range from initial stiffness to post-yielding stiffness. Although this part of the parametric study aimed at investigating the effect of different bearing strengths with the same initial and post-yielding stiffness, because of the Bouc-Wen model used, the secant stiffness will be different under small displacements. Interestingly, those bearings actually show a horizontal stiffness behavior between the initial and post-yielding stiffness. This phenomenon also occurs in the aircraft-impact analysis in Chapter 5.

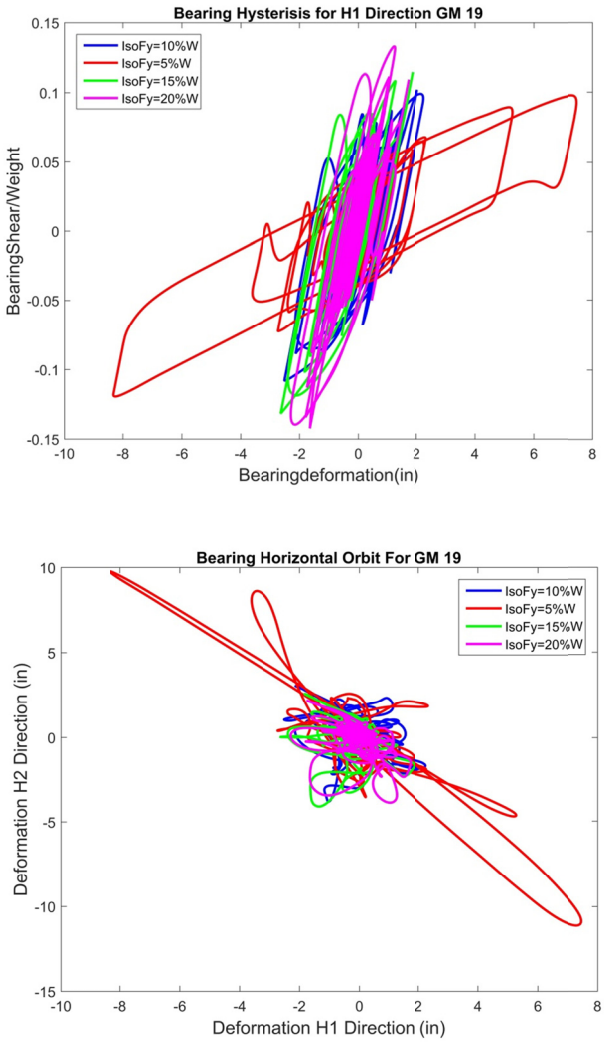

Figure 4.26 **Center Bearing H1 direction hysteresis loop and displacement orbit under NRC PGA 0.3*g* ground-motion time-history number 19. The isolation system with different yield strengths are shown together.**

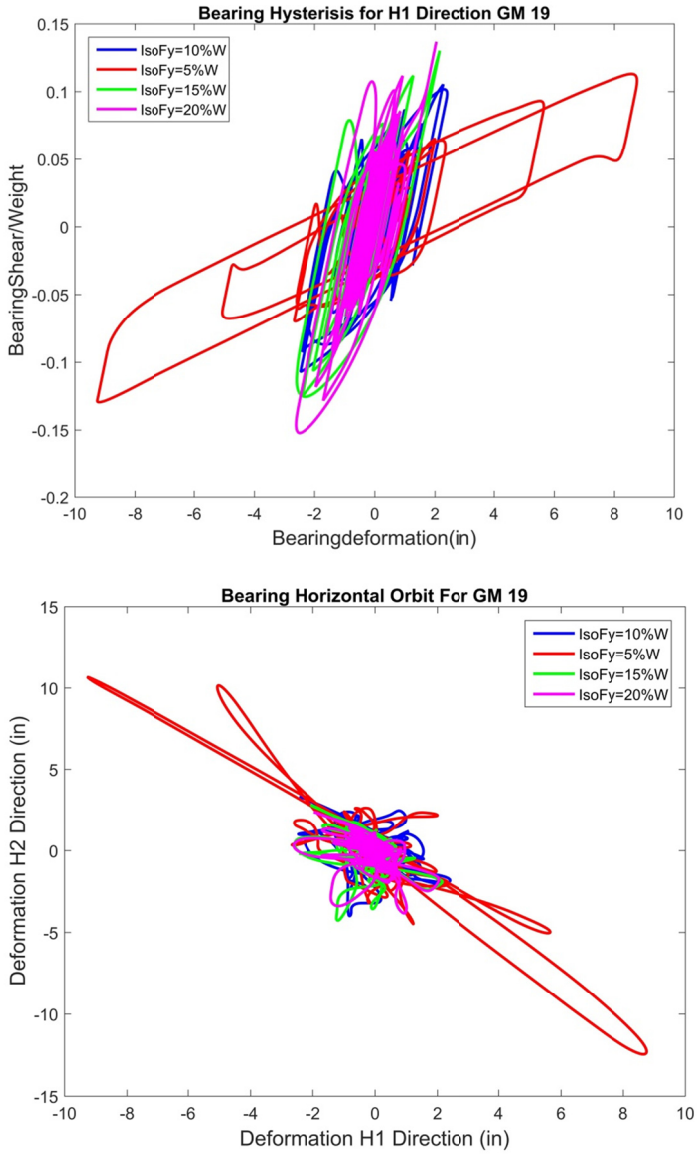

Figure 4.27 Southwest Bearing H1 direction hysteresis loop and displacement orbit under NRC PGA 0.3*g* ground-motion time-history number 19. The isolation system with different yield strengths are shown together.

Observations and conclusions drawn from the parametric study on different yielding forces of bearing are as follows:

- For the response of horizontal floor pseudo-acceleration spectrum, different bearing yielding forces will only affect the response amplitude at the isolation mode. A larger yield force results in a larger response. The affect is larger than the other two parametric study cases when comparing different initial stiffness and isolation periods.

- Different bearing yield forces will not affect the high-frequency responses on the horizontal floor spectrum.
- The drift response is similar when using isolators with different F_y. With a larger F_y, the drift response will be slightly larger.
- The bearing displacement demand will be much smaller when a larger F_y is used.

4.6 CONCLUSION AND SUMMARY

This chapter described the results of a parametric study for different bearing properties including initial stiffness, post-yield period, and yielding force using the refined model developed in OpenSees. Floor acceleration spectrum, drift response, and bearing response were investigated to determine the sensitivity of the response to each of the parameters and the efficiency of the isolation system. Some key conclusions were drawn:

Under the ground-motion level of 0.1*g* PGA, the fixed-base model response was similar to an isolated model evaluated under the ground-motion level of 0.3*g* PGA. This means the design-level ground motion can be increased by a factor of 3 using the isolation system investigated. However, the isolation system requires a site-specific design, and an isolated NPP designed for a higher PGA cannot be indiscriminately relocated since the isolation system must be appropriately tailored.

The AUX received the most significant benefit from seismic isolation as observed through floor response spectra. The peak value was reduced by a factor of 2 on the top of the upper mat for both the RCB and AUX. On the top of the AUX, the floor spectrum peak was reduced by a factor of 8, and the RCB response was reduced by a factor of 5.

Vertical acceleration responses were amplified when seismic isolation was used as compared to the fixed-base model because of the introduced vertical flexibility of the bearing. Once isolated, the original fixed-base mode of the AUX was shifted by interaction with the RCB and isolation system. The original peak in the floor spectrum of the fixed-base AUX was suppressed as the isolated mode became predominant. Initial stiffness of the bearing had an impact on the horizontal floor spectrum. Larger initial stiffness produced a larger response and excited the RCB response in the upper floor. Slightly larger drift and smaller bearing displacement response was expected for bearings with a larger initial stiffness.

The post-yield period has less influence on the response than other parameters. Bearing yield force had a significant impact on the floor response spectrum; a larger yield force resulted in a larger response but much smaller bearing displacement demand. The drift response for both the RCB and AUX were small, which should benefit the elastic design of these structures.

Overall, a seismically isolated structure will perform much better compared to a fixed-base structure. For the isolated PGSFR considered in this study, because the displacement demand was small under the design-level earthquake, the effectiveness of seismic isolation was not as beneficial as a seismic isolation system with reduced yield force and larger displacement demand.

5 DYNAMIC ANALYSIS OF A SEISMICALLY ISOLATED PGSFR SUBJECTED TO AIRCRAFT IMPACT

5.1 INTRODUCTION

It is now generally accepted that the effects of deliberate crashes of large commercial aircraft should be considered in the design of critical facilities such as NPPs. Most of the current regulatory guides for the design of NPPs now incorporate analysis and design requirements to assess or mitigate the effects of a large commercial aircraft impact.

For instance, the U.S. NRC stipulates in Title 10 CFR Part 50.150 that an applicant for a license to construct and operate a NPP

"…shall perform a design-specific assessment of the effects on the facility of the impact of a large, commercial aircraft. Using realistic analyses, the applicant shall identify and incorporate into the design those design features and functional capabilities to show that, with reduced use of operator actions:

- The reactor core remains cooled, or the containment remains intact
- Spent fuel cooling or spent fuel pool integrity is maintained"

The U.S. NRC further stipulates that the assessment "must be based on the beyond-design-basis impact of a large, commercial aircraft used for long-distance flights in the United States, with aviation fuel loading typically used in such flights, and an impact speed and angle of impact considering the ability of both experienced and inexperienced pilots to control a large, commercial aircraft at the low altitude representative of a NPP's low profile."

The Nuclear Energy Institute has also published a methodology for evaluation of aircraft impact on new NPPs [NIE 2009]. Its recommendations differ, and, in some cases, are less conservative than mandated by the U.S. NRC.

For a traditional fixed-base design, considerable research and development has been done to strengthen and detail the containment structure and other critical structural features of the nuclear island necessary to achieve these goals [Riera 1968, Riera 1980, Riera 1982, Chadmail 1985; Sugano et al. 1993, Arros and Doumbalski 2007, Wilt and Chowdhury 2011, Lee et al. 2013, and Sadique et al. 2013]. These have had an effect on plant design, including strengthening and toughening of the containment structure and other portions of the nuclear island to prevent

local penetration or perforation, separation of safety critical internal systems and components from structural elements that might undergo large deformations during aircraft impact, and the protection of systems and components from the high accelerations that might be associated with impact. Other recent studies have focused on special issues of analysis including the accelerations imposed on components due to impact [Andronov et al. 2010], and the effect of different refinements to the numerical modeling of the response to aircraft impact [Bignon and Riera 1980; Abbas et al. 1996; and Siefert and Henkel 2014]. A recent comprehensive review of analyses and tests related to aircraft impact, and computer programs used in such analyses is available [Jiang and Chorzepa 2014].

With the consideration of seismic isolation for nuclear facilities, attention has begun to focus on the effect of aircraft impact on isolated facilities [Kulak and Yoo 2003; Blandford et al. 2009; and Noh and Kim 2012]. Kulak and Yoo [2003] considered a simple single-degree-of-freedom model of a supported rigid mass on HDRBs intended to be representative of the horizontal isolation systems used for the STAR-LM or KALIMER fast reactors. The dampers were modeled as equivalent linear springs, giving the plant a frequency of 0.5 Hz and an equivalent viscous damping ratio of 12%. Aircraft impacts included a Boeing-720 traveling at 100 m/sec and a Boeing-747 traveling at 150 m/sec. The impact loading on the plant was obtained by simplifying results derived using the methodology suggested by Riera [1968]. The results showed that even for the heavier and faster Boeing-747, the bearing displacements were limited to about 29 cm (11.4 in.), which corresponds to a shear strain of about 90% for the isolation bearings considered. This was very similar to the shear strains expected during the SSE and well within the deformation capacity of the bearing (about 300%).

Blandford et al. [2009] investigated the case of a simplified elastic two-degree-of-freedom lumped mass stick model supported on a base-isolated raft foundation. The facility was intended to be representative of a relatively light small modular reactor. The frequency of the plant in its fixed-base configuration was set to 3 Hz. Total isolated weights ranging from 20,000 to 100,000 metric tons (44,000 to 220,000 kips) were considered. The properties of the bearings were held fixed in a way that a plant having a total weight of 50,000 metric tons (110,000 kips) would have an effective isolated frequency of 0.5 sec. Considering the variation of plant weights, the overall effective frequencies of the plant were 0.3, 0.5 and 0.75 Hz. The bearings in this study were assumed to have an effective viscous damping ratio of 10%. The superstructure was assumed to have 5% viscous damping. Aircrafts considered included a Boeing-747-400 weighing 397 metric tons (875 kips) with an impact velocity of 201 m/sec and a Boeing-737-900 weighing 85.3 metric tons (188 kips) with a velocity of 180 m/sec. Principles of dynamic similitude were used to modify a force loading history for these planes based on histories developed by Riera [1968] for a smaller and lighter Boeing-707-320. The findings of this study indicated that high accelerations, large internal forces, and high bearing lateral displacements would develop for light plants. For heavier plants, the accelerations and bearing displacements were more reasonable even for the faster and heavier Boeing-747. Since this study focused on light-weight small modular reactors, the study then focused on the design of external latticed frames that were uncoupled from the main plant as a means of avoiding aircraft impact.

Noh and Kim [2012] analyzed a detailed FE model of a fictitious pressurized water RCB considering fixed-base and isolated conditions, subjected to an impact by a Boeing-767-400. They also utilized the force response-history analysis method developed by Riera. The FE model incorporated yielding of the concrete containment. For conservatism, the authors assumed that

the 400 isolation bearings had no damping and had a stiffness that resulted in a fundamental frequency for the isolated NPP of 0.5 Hz. They indicated that the local effect (strains) of the aircraft impact on the wall at the impact location was nearly the same for the cases with and without the isolation system.

Thus, it appears that although for heavier NPPs, the global dynamic response may be of a similar order of magnitude as considered in seismic analysis, the studies to date that consider aircraft impact have been limited in scope. The structural models have been complex, but the superstructure has been represented by very simple rigid body or reduced degree-of-freedom elastic stick models. In addition, aircraft impact where the direction of impact does not go through the center-of-mass of the structure may induce torsional response of the isolated plant that can increase isolator displacement demands at the corners of the raft foundation.

This chapter modifies the refined 3D lumped-mass stick model of the PGSFR developed for seismic response analysis in Chapter 4 to simulate behavior under aircraft impact. The response for two modern commercial planes impacting the PGSFR at different locations are investigated for fixed-base and isolated plant conditions. A parametric study is undertaken to assess the effect of effective isolation period, initial isolator stiffness and isolator strength on bearing displacements, hysteresis loops, floor accelerations, floor response spectra, story drifts, and floor rotations. The response is examined for the AUX as well as the RCB, considering different aircraft types and impact locations. In all cases, the structures above the isolation plane are assumed to remain elastic, and the flexibility and energy-dissipation capabilities of the supporting soil are not considered.

5.2 STUDY BACKGROUND

5.2.1 Force Loading Function for Aircraft Impact

The impulse load due to an aircraft impacting a structure is a complicated function of (a) the mass, stiffness, and strength distribution along the aircraft, its velocity at impact; (b) the material, strength, and detailing of the structure at the point of impact. The global stiffness of the structure and its dynamic interaction with the aircraft during impact are also expected to influence response. Analyses to account for these and other factors are possible but time consuming to model and execute, and require detailed information about the plane and structure that are typically not yet available during the schematic design process. Thus, for these preliminary studies, a simplified force loading function initially proposed by Riera [1968] will be used.

The loading function proposed by Riera is widely used in the analysis of aircraft impact; however, the loading function developed by Riera only considers the impact of a Boeing-707-320, which was the largest commercial plane at the time of publication. Current planes, such as a Boeing-747, 767, or 777, are heavier, wider, and longer than the Boeing-707-320 that Riera considered. Furthermore, Riera's loading function is based on an impact velocity corresponding to a controlled takeoff or landing condition, rather than a malicious high-speed collision. As a result, velocities corresponding to cruising or higher speeds should be considered. Blandford et al. [2009] demonstrated that concepts of dynamic similitude could be used to adjust Riera's linearized force loading functions to correspond to planes of different length and mass, and traveling at different velocities.

Considering the scaling method proposed by Blandford et al. [2009], force loading time histories for a Boeing-737-900 and Boeing-747-400 were developed. It is assumed that the Boeing-737-900 is cruising at 180 m/sec and that the Boeing-747-400 is cruising at 201 m/sec when impact occurs. The resulting force time histories are shown along with the original loading function for a Boeing-707-320 in Figure 5.1 (from Blandford et al. [2009]). By comparing the relative amplitudes of loading in this figure, it can be observed that the peak force and impulse exerted by the Boeing-747 is much larger than those for the Boeing-737 or Boeing-707. Thus, the 747-400 represents an upper bound of impacts considered in this study, and the Boeing-737 represents a lower bound. Higher and lower impact forces can be imagined for heavier (or lighter) planes traveling faster (or slower). However, for the purpose of this preliminary investigation, these impact force loading functions allow for investigation of the basic aspects of the response of an isolated PGSFR and provide insight into the need for more refined analyses considering other aircraft types.

The analysis model used here is identical to that developed in Chapter 4, except for the addition of rigid links extending from the lumped mass stick models to the location on the perimeter of the buildings where the planes will be assumed to impact, and the addition of additional recorders to help study the dynamic response of the PGSFR during aircraft impact.

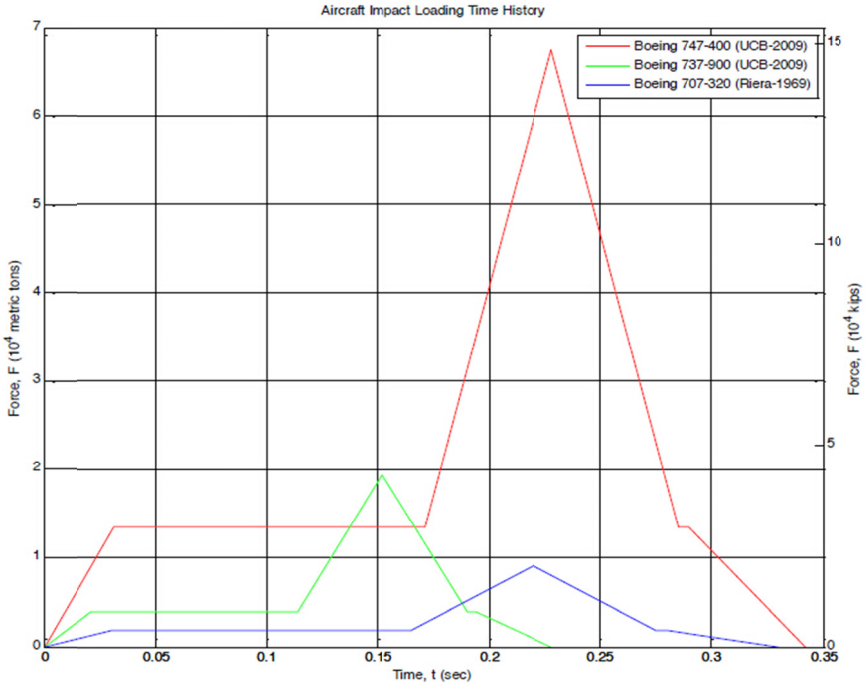

Figure 5.1 **Force loading functions for aircraft impact analysis. Impact loading histories for a Boeing-747-400 and Boeing-737-900 are used in this study. The forcing function for a Boeing-707-320 is shown for reference (after Blandford et al. [2009]).**

5.3 AIRCRAFT IMPACT CASES

The study conducted in this chapter considers the following aircraft impact loading scenarios:

- Two different aircrafts
- Three different locations of impact

For each loading scenario, the fixed-base and seismically isolated structures were analyzed. For the isolated PGSFR, the study includes nine different isolator characteristics, due to variation of the following bearing parameters:

- Initial isolator stiffness
- Post-yield isolator tangent stiffness
- Isolator strength at initial yield

More information on these variations is presented below. In the following discussion, "scenario" is used to describe the aircraft loading condition, and "case" is used to represent a specific structure with specific parameters subjected to a specific loading scenario.

5.3.1 Impact Force Loading Scenarios

As discussed above, the two loading functions considered in this report are shown in Figure 5.1. In principle, the location of impact can be anywhere on the periphery of the plant. Furthermore, impact need not occur with a path perpendicular to the contacting surface. For these studies, it was assumed that impact occurred perpendicular to the surface on which impact occurs. This is consistent with the assumptions used by Riera to derive the force functions.

Three locations were selected for the aircraft-impact analysis; all of them occurring on the AUX as it has a greater exposed surface. Because of the layout and geometry of the different building components of the PGSFR, it is very difficult for an airplane to impact the RCB directly. For the fixed-base models, the perfect rigidity of the supporting soil means that the reactor containment structure will not vibrate as a result of the impact: only the auxiliary structure will move in this scenario. Both will move in the base-isolated case, as they are supported on the common raft foundation on top of the isolation system.

The three impact locations selected were at mid-height of the AUX, i.e., about 25 m (82 ft) above ground. The impact sites are shown in Figure 5.2. In the traverse direction, the structure is relatively symmetric; therefore, impact along longitudinal direction (H1) is imposed along the central axis of the building. This condition is not expected to induce significant torsional response. Two additional impacts are oriented in the H2 (traverse) direction. The RCB is not symmetrically placed within the building in longitudinal direction. As such, an impact by a plane flying in the global H2 (traverse) direction is likely to induce torsion about a vertical axis. To investigate this, two impact locations were considered; see Figure 5.2 These are roughly at the one-third point of the building.

For all three impact-loading locations, both planes were considered. Therefore, six different aircraft impact loading scenarios were analyzed in this study. For these six scenarios,

several variations of bearing properties were considered for the isolated PGSFR as described next.

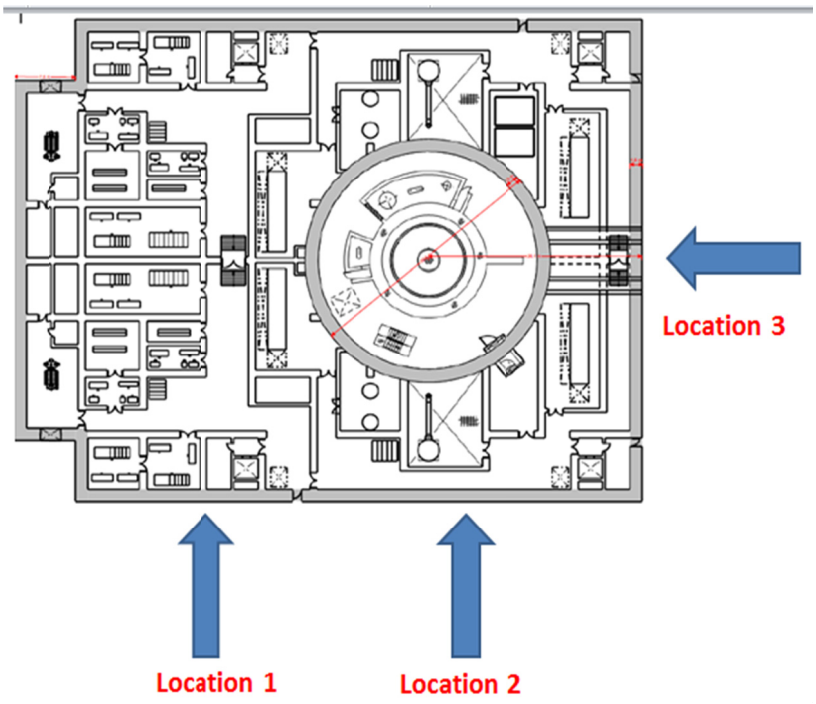

Figure 5.2 **Location and direction considered for the impact loading in this study. Two types of aircraft were considered for each location. The H1 direction is along the longitudinal axis of the structure, and the H2 direction is along the transverse axis.**

5.3.2 Parametric Study Cases

For each of the basic impact loading scenarios described above, the fixed-base structure and seismically isolated structure were analyzed. For the seismically isolated PGSFR, a range of isolator characteristics was considered. Similar to the analyses discussed in Chapters 3 and 4, the bearing initial stiffness, post-yield tangent stiffness, and initial yield force levels were systematically varied for each impact scenario. The six combinations of plane and impact location are listed below:

- Impact Scenario 1: Loading location 1 for Boeing-737
- Impact Scenario 2: Loading location 2 for Boeing-737
- Impact Scenario 3: Loading location 3 for Boeing-737
- Impact Scenario 4: Loading location 1 for Boeing-747
- Impact Scenario 5: Loading location 2 for Boeing-747
- Impact Scenario 5: Loading location 3 for Boeing-747

The details of the parametric study cases are shown in Table 5.1. The values used for each of the bearing properties are the same as previously used in Chapters 3 and 4 for the seismic evaluation of the PGSFR.

Table 5.1 Summary of analysis cases and loading scenarios considered in the parametric study.

Structures	AIA loading scenarios	Initial stiffness ($K_{initial}$)	Isolation period (T_{iso})	Bearing yield force (F_y)	Primary isolator parameter considered
Fixed Base	3 locations, 2 planes each	NA	NA	NA	NA
Base Isolated	3 locations, 2 planes each	**5 $K_{postyield}$**	3 sec	10% W	$K_{initial}$
		10 $K_{postyield}$	3 sec	10% W	
		100 $K_{postyield}$	3 sec	10% W	
		10 $K_{postyield}$	**2 sec**	10% W	T_{iso}
		10 $K_{postyield}$	**3 sec**	10% W	
		10 $K_{postyield}$	**4 sec**	10% W	
		10 $K_{postyield}$	3 sec	**5% W**	F_y
		10 $K_{postyield}$	3 sec	**10% W**	
		10 $K_{postyield}$	3 sec	**15% W**	
		10 $K_{postyield}$	3 sec	**20% W**	

5.4 ANALYSIS RESULTS AND DISCUSSION

Similar to the analysis results presented in Chapter 4, results in terms of the three parameters ($K_{initial}$, T_{iso}, and F_y) are presented. For each key bearing parameter, results are discussed for the various loading scenarios as well as for the fixed-base cases. Since the aircraft impacts are either in the H1 or H2 directions, the response results are evaluated separately in the H1 and H2 directions. Response quantities presented include:

1. Floor accelerations and floor response spectra in the AUX and RCB
2. Maximum drift demands in the AUX and RCB
3. The peak angle of rotation about a vertical axis for each floor for the AUX and RCB
4. Bearing displacement demands
5. Bearing hysteresis loops for individual bearings at the corners of the base mat.

5.4.1 Responses Considering Different $K_{initial}$

Responses of the study on different bearing initial stiffness are discussed next. The values considered for initial stiffness are summarized in Table 5.1. T_{iso} and F_y were kept constant for all of the cases presented in this section.

Note that the displacement demands on the isolation system were quite small for this scenario (see Section 5.4.4.1); none of the bearings reached a shear force equal to the nominal F_y value, and some only reached half or less of this value. Nonetheless, the use of Bouc–Wen hysteretic models for the bearings resulted in signification nonlinear hysteretic behavior even for low-amplitude excursions. However, for these low levels of response, the behavior was dominated by the initial "elastic" loading stiffness of the bearings. Thus, the value of $K_{initial}$ had a significant influence on the behavior of the PGSFR (and other loading scenarios); note that the behavior of the Bouc–Wen hysteretic models may not be well calibrated to actual bearing properties for this level of excitation, and the model has several well-known difficulties (e.g., ratcheting under asymmetric loading conditions) in simulating cyclic behavior in the nominally elastic range.

5.4.1.1 Response of Auxiliary Building: Scenario 1

The first loading scenario considered was for the Boeing-737 impacting the AUX at location 1, on the left side of the building in the H2 direction; see Figure 5.2. Because the loading direction was in the H2 direction, torsional response was expected. Results show that the acceleration response in the H1 direction was insignificant. The peak pseudo-acceleration in the horizontal floor spectrum at the fifth floor of the AUX, which is the floor level at which impact occurred, was only $4 \times 10^{-5} g$; see Figure 5.3. Similar results were observed for all other Scenario 1 loading cases. As a result, only results parallel to the loading direction will be presented below.

The corresponding floor spectra for the AUX in the H2 direction is shown in Figure 5.4 for the second, fifth, and sixth (top) floors. Comparing the response spectra in Figure 5.4 and the peak total acceleration responses over the height in Figure 5.5, the fixed-base case had total accelerations that tended to increase linearly with elevation. For the base-isolated case, the peak total accelerations were similar to the fixed-base case. Figure 5.5 shows that the case with a very stiff initial stiffness resulted in somewhat lower floor accelerations in the upper levels. Since the isolation system moved during the impact, the lower floors had higher accelerations than did the fixed-base case.

The portion of the plant above the isolation plane responded nearly as a rigid body, and all floors had nearly the same peak floor total acceleration. Again, the case with a very stiff initial stiffness had somewhat lower accelerations; for the isolated model, the response was almost uniform along the height.

From Figure 5.4, it can be seen that pseudo-accelerations in the high-frequency range followed the trend shown by the peak floor total acceleration. Between 5–10 Hz, the isolated systems had higher pseudo-accelerations at the second floor than the fixed-base structure, especially in the case of the bearings with very high initial stiffness values. This is again likely due to the nearly rigid body movement of the isolated structure; it is expected that the lower floors will move more than in the fixed-base case. At the fifth and sixth floors, the isolated systems all tended to have similar spectral pseudo-acceleration values between 5–10 Hz; these

were significantly less than those for the fixed-base structure. For frequencies below 3–5 Hz, the spectral accelerations at all floor levels were significantly above those for the fixed-base structure.

Since there is no vertical input, vertical acceleration would most likely result from bending motion of the super structure and axial elongation and shortening of bearings. The vertical floor spectrum of the impact floor is shown in Figure 5.6. The vertical pseudo-acceleration values were very small, and thus were disregarded in subsequent discussions in this chapter.

When comparing the responses of base-isolated case and fixed-base case, note that the response of peak floor acceleration for the fixed-base case was almost the same as the base-isolated case in the upper floor for the AUX; for the lower part of the AUX, the acceleration was much smaller for the fixed-base case. The benefit of isolation on acceleration response considering aircraft impact is that it doesn't lower the peak floor acceleration amplitude but changes the frequency content of the floor spectrum. Isolation lowers the peak on the fixed-base spectrum but results in higher pseudo-accelerations in the lower frequency range. Most but not all of the equipment in a plant is likely to be sensitive to the frequency range of the original peak. In a comparison between different bearing initial stiffnesses, the one with larger initial stiffness will result in moderately better peak pseudo-acceleration response.

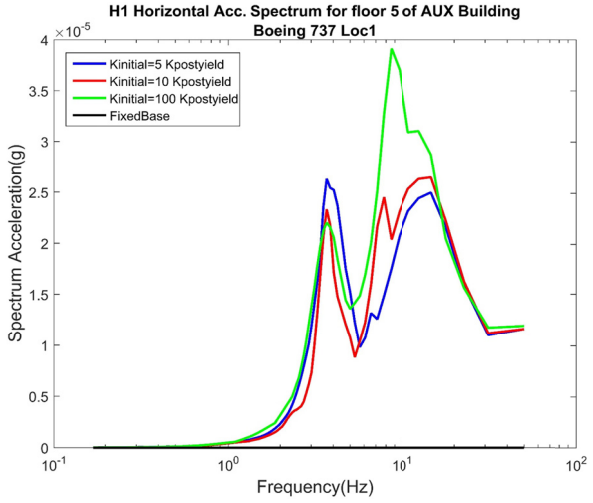

Figure 5.3 **Floor acceleration spectra in the H1 direction for the auxiliary building. Impact Scenario 1 (Boeing-737 at location 1); fixed-base and base-isolated cases with different $K_{initial}$ (T_{iso} = 3 sec and F_y = 0.1 W).**

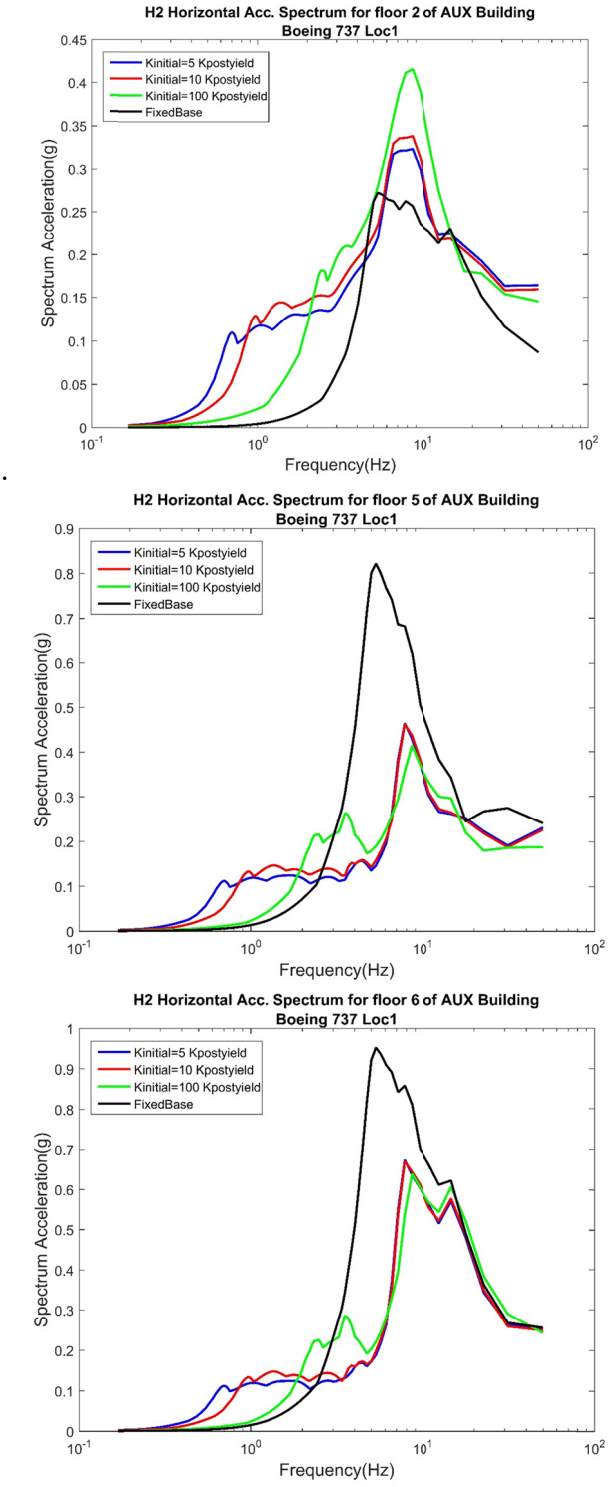

Figure 5.4 **Floor acceleration spectra in the H2 direction for the auxiliary building. Impact Scenario 1 (Boeing-737 at location 1); fixed-base and base-isolated cases with different $K_{initial}$ (T_{iso} = 3 sec and F_y = 0.1 W).**

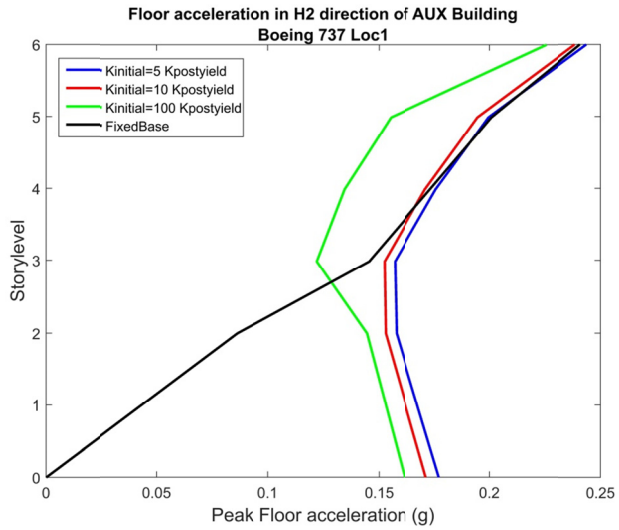

Figure 5.5 **Peak floor accelerations along height. Impact Scenario 1 (Boeing-737 at location 1); fixed-base and base-isolated cases with different $K_{initial}$ (T_{iso} = 3 sec and F_y = 0.1 W).**

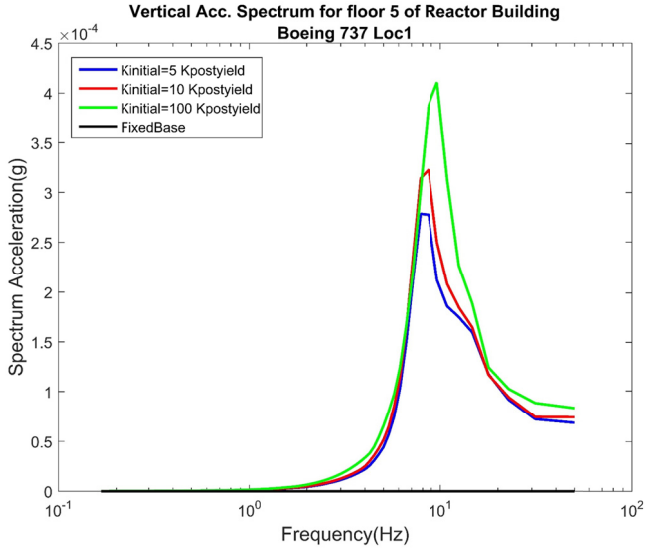

Figure 5.6 **Vertical floor acceleration spectra for auxiliary building. Impact Scenario 1 (Boeing-737 at location 1); fixed-base and base-isolated cases with different $K_{initial}$ (T_{iso} = 3 sec and F_y = 0.1 W).**

The peak story drift response for Impact Scenario 1 is shown in Figure 5.7. As shown in the plot, the amplitude of the maximum drift response is very small: on the order of 0.01% for all cases considered. In a comparison between the base-isolated case and the fixed-base case, the base-isolated case had significantly smaller drift, especially in the lower stories. Note that drift response of the fixed-base case was larger at the lower part of the building and smaller on the top, whereas for the base-isolated cases, the lower part of the building had smaller drift responses. The difference of the drift shape was due to the movement of the base mat. A smaller initial stiffness had a better drift response when comparing different base-isolated cases. This trend is different compared to floor accelerations and floor response spectra, where the isolated systems respond more severely in the lower stories.

Since the loading for this scenario is eccentric with respect to the center-of- stiffness of the structure, the rotation of each floor and the twist within the AUX were investigated. The total rotation angle of each floor is shown in Figure 5.8. The rotation of each floor increased continuously with elevation for the fixed-base building, i.e., the floor rotation was larger on the top; however, the amplitude of twisting was small, with the maximum rotation at the top being less than 0.002°.

In comparison, the base-isolated cases had much higher floor rotation, e.g., the total rotation of the roof for the bearings with the smallest $K_{initial}$ value was nearly 0.05°; however, the rotation of the base mat was nearly the same as that at the top floor for the base-isolated cases. This is because of the significant rotation of base mat about the vertical axis. Because the fixed-base model cannot rotate at the base and the buildings are torsionally stiff, only small twisting occurs. For the base-isolated cases, all the floors above the base have nearly the same rotation; Figure 5.8. Thus, the AUX and the base mat rotate as a nearly rigid block. As a result, the relative twist that occurred within the elevated portion of the AUX was smaller than that experienced by the fixed-base structure.

The rotation reached 0.03° for the baseline model with $K_{initial} = 10\ K_{postyield}$ and was uniformly distributed along the height. Note that the twist that occurred between floors was smaller for all of the isolated structures shown than for the fixed-base structure. In all cases, the twist that developed as a result of Impact Scenario 1 was rather small. A comparison between bearings with different initial stiffness showed a large difference of the floor rotation about the vertical axis. Because the vertical rotation is governed by the torsional resistance of the isolation plane, this is mainly influenced by the shear stiffness of the isolator. Therefore, a larger bearing initial stiffness will result in smaller rotations of the base mat and thus of the supported super-structure.

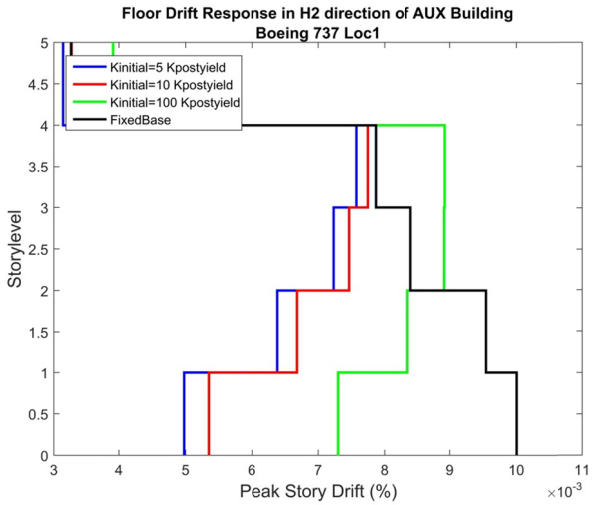

Figure 5.7 **Peak story drifts along height. Impact Scenario 1 (Boeing-737 at location 1); fixed-base and base-isolated cases with different $K_{initial}$ (T_{iso} = 3 sec and F_y = 0.1 W).**

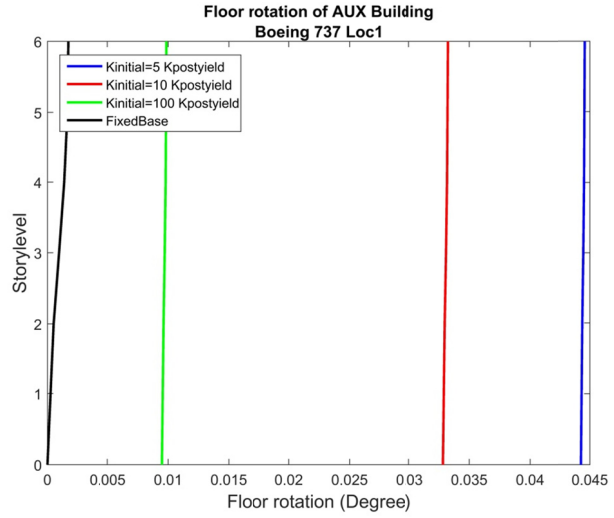

Figure 5.8 **Maximum floor rotations along height. Impact Scenario 1 (Boeing-737 at location 1); fixed-base and base-isolated cases with different $K_{initial}$ (T_{iso} = 3 sec and F_y = 0.1 W).**

5.4.1.2 Response of Reactor Containment Building: Scenario 1

The RCB is separated from the AUX above the base mat by a gap. Therefore, for the fixed-base model, assuming the gap between the AUX and the RCB is sufficient to avoid pounding as a result of aircraft impact, theoretically, the RCB will be undisturbed. However, in a real structure, vibration of the ground will transmit forces to the RCB. For the base-isolated case, because the RCB and the AUX share a common isolated base mat, the movement and the rotation of the base mat result in movement of the RCB. Consequently, the isolated RCB will also vibrate when an aircraft impacts the AUX.

The floor spectra for the RCB are shown in Figure 5.9. Floor spectra in the H2 direction are shown for the first floor, fourth floor, and top floor of the RCB. The peak absolute floor accelerations for the RCB along the height are shown in Figure 5.10.

The acceleration response at the base is the same as the base response of the AUX since they sit on the same base mat. The peak acceleration response is nearly constant up until the fifth floor, at which point the accelerations increase sharply with height. In fact, the peak accelerations are larger for the RCB than for the AUX. The peak pseudo-acceleration in the floor spectra for the upper-most floor is nearly 1*g*, which is about 40% larger than the peak spectral acceleration in the AUX that bears the brunt of the impact. This behavior is different than the anticipated rigid body response of the structure. It is likely that modes in the RCB and AUX interact through the isolated mat, and that the impulsive excitation caused by the yielding/unloading of the isolators triggers response of certain modes in the RCB. Note: although the isolators considered in this scenario all have T_{iso} = 3 sec, the low level of response in the isolators means that behavior is dominated entirely by the value of $K_{initial}$. Thus, the bearings in this scenario are likely to transmit more high-frequency vibrations into the supported superstructure than what is typically associated with relatively long-period isolators. This can be seen by the localized peaks in the floor spectra near 2.5 Hz and 8 Hz, where the bearing model with higher initial stiffness resulted in higher floor response spectra for all frequencies above about 2 Hz. However, the initially stiff bearing had lower spectral accelerations for frequencies less than 2 Hz.

The drift response is shown in Figure 5.11. In general, the amplitude of the peak story drift is small, on the order of 0.01%. The drift response of the RCB is uniform along the height, and the amplitude is larger than the drift of the AUX. As noted for the AUX, the bearings with large initial stiffness resulted in larger drift; see the green line in Figure 5.11. This is because the bearings with higher initial stiffness develop greater shear forces, which are transmitted upward into the superstructures, which in turn, develop larger drifts.

Since some torsion occurred about a vertical axis in the base mat, the isolators that were located on the four corners of the base mat responded differently; see plots in Figure 5.12 where they are plotted in the same relative location as their placement shown in Figure 5.2. In Figure 5.12, both the hysteresis loops and the horizontal displacement orbits of the four bearings are shown and compared for the different isolator initial stiffnesses. The peak lateral displacements of the bearings were relatively small; for the most flexible bearing, the displacement was less than 50 mm (2 in.), and for the bearings with the highest initial stiffness, it was less than about 10 mm (0.4 in.).

From the first two sets of hysteresis loop plots, it can be seen that none of the bearings reached the nominal yield strength of 0.1 W. Thus, their behavior was dominated by K_{initial}. Note that the Bouc–Wen model results in some nonlinearity for the bearings that absorbs energy during the impact. The bearings with larger initial stiffness developed smaller lateral displacements and higher shear forces. The bearing displacement was on the order of 25.4–51.8 mm (1–2 in.), which is a similar value as the demand under seismic loading.

The loading of location 1 is in the H2 direction; however, because of rotation of the base mat, isolators not only moved in the H2 direction, but in the H1 direction as well. The bearing displacement amplitude in the H1 direction was nearly half of the amplitude in the H2 direction for the corner bearings shown. As illustrated in the displacement orbit plots in Figure 5.12, it can be imagined from the orientation of the orbits at each corner that the movement of the bearings was heavily influenced by the clockwise rotation of the base mat.

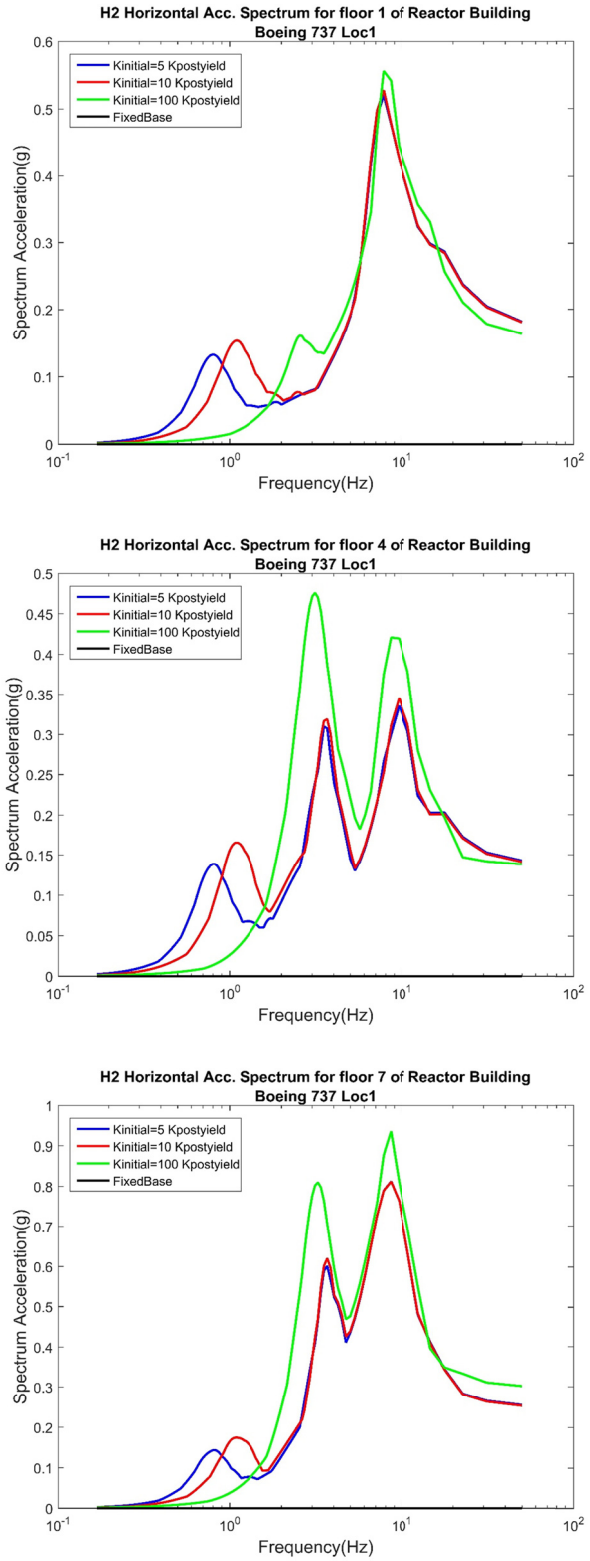

Figure 5.9 **Floor acceleration spectra for reactor containment building in the H2 direction. Impact Scenario 1 (Boeing-737 at location 1): fixed-base and base-isolated cases with different $K_{initial}$ (T_{iso} = 3 sec and F_y = 0.1 W).**

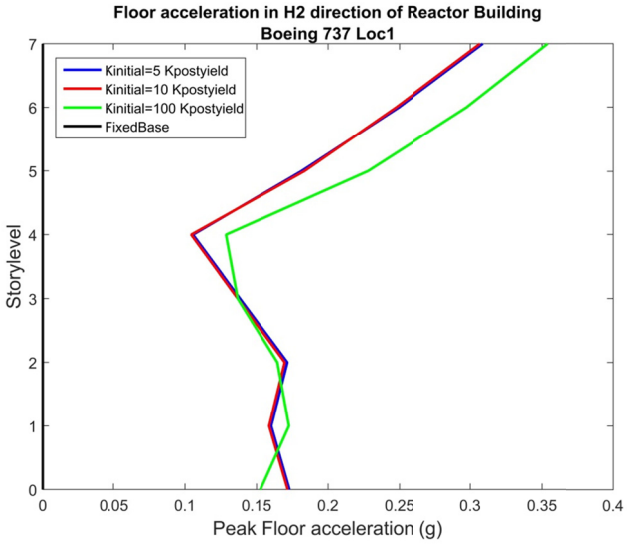

Figure 5.10 **Peak floor accelerations along height of the reactor containment building. Impact Scenario 1 (Boeing-737 at location 1): fixed-base and base-isolated cases with different $K_{initial}$ (T_{iso} = 3 sec and F_y = 0.1 W).**

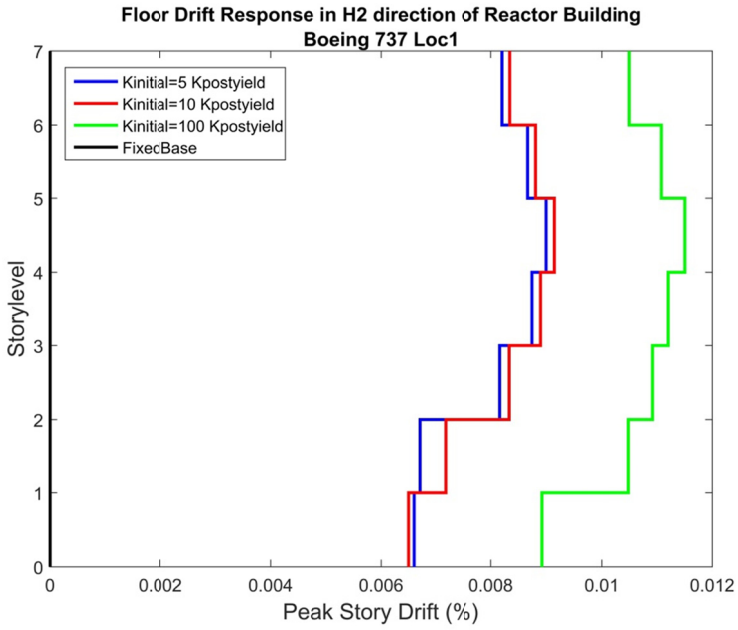

Figure 5.11 **Peak story drifts along height for the reactor containment building. Impact Scenario 1 (Boeing-737 at location 1): fixed-base and base-isolated cases with different $K_{initial}$ (T_{iso} = 3 sec and F_y = 0.1 W).**

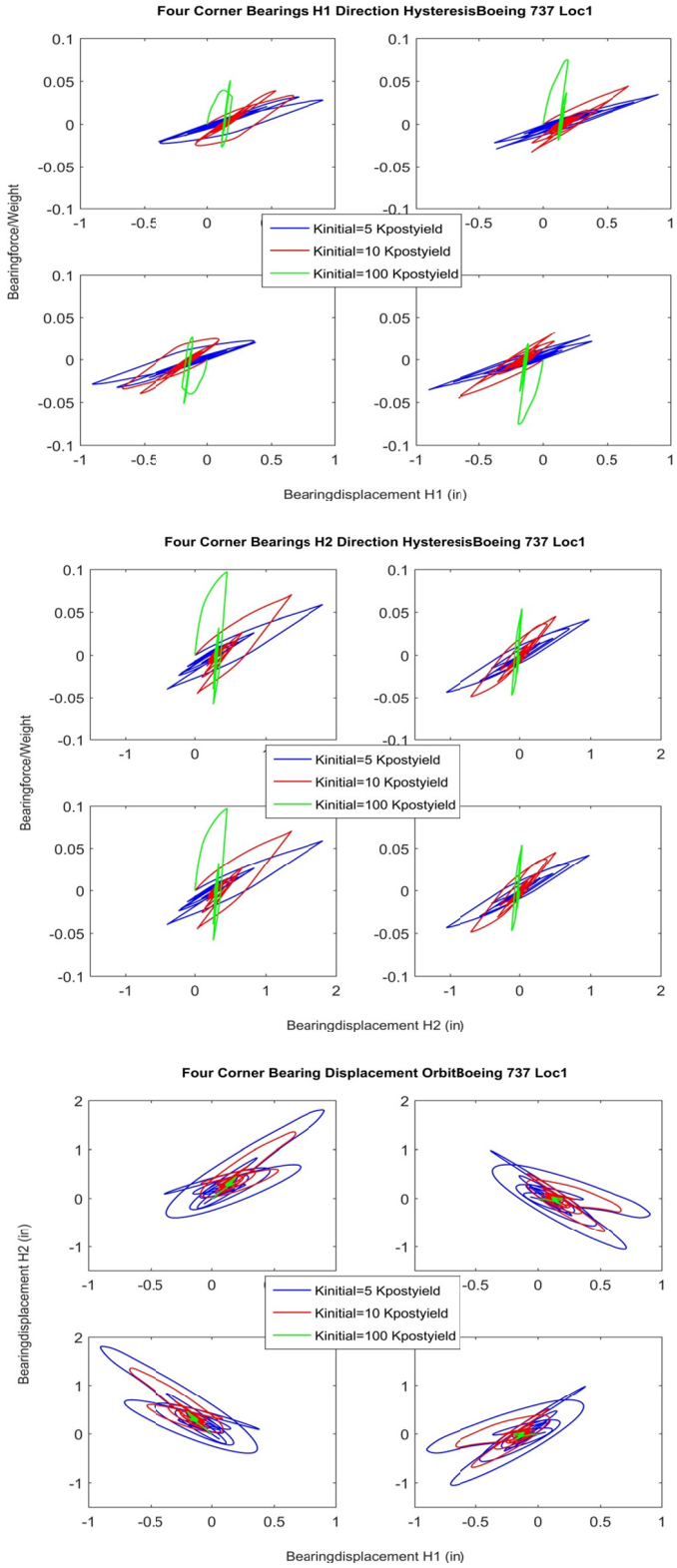

Figure 5.12 **Hysteresis loops and displacement orbits for bearings at the four corners of the base mat. Impact Scenario 1 (Boeing-737 at location 1): base-isolated cases with different $K_{initial}$ (T_{iso} = 3 sec and F_y = 0.1 W).**

5.4.1.3 Response of Auxiliary Building: Scenario 4

Impact Scenario 4 was the same as Scenario 1, but the impact was due to the heavier and faster-moving Boeing-747 (instead of the Boeing-737). A comparison between the two scenarios will provide insight regarding the effect of the amplitude of the impulse loads on the dynamic response. Some of the results for this case are similar to those already noted for Scenario 1, and thus they will not be discussed again. This section focuses on the differences of response between Impact Scenarios 1 and 4. Here, the bearings will have much larger displacement demands, reaching more than 30 cm (12 in.) in the H2 direction for the bearings with the smallest K_{initial}. All of the bearings developed shear demands in excess of F_y.

Floor response spectra for the AUX are shown in Figure 5.13. The peak total floor accelerations over the height of the AUX are shown in Figure 5.14. These figures can be compared to Figure 5.4 and Figure 5.5 for Impact Scenario 1. Note that the peak floor total accelerations (Figure 5.14) increased linearly with height for the fixed-base building as they did for Impact Scenario 1, but the peak accelerations increased from about 0.24*g* to nearly 1*g*. The trends for the base-isolated case differ significantly. Rather than being similar to the fixed-base case near the top of the building and higher than the fixed-base case near the bottom of the structure (as was the case for Impact Scenario 1), the total accelerations were nearly constant for the full height. This is consistent with an almost rigid structure on flexible seismic isolators. The accelerations decreased by nearly a factor of two at the top of the structure. As a result of the rigid-body-like motion of the isolated PGSFR, the accelerations increased at the base to about 0.6*g* for all of the K_{initial} values. Thus, once the impact loading becomes severe enough, the sensitivity to K_{initial} decreases. As shown in Figure 5.14, the case with the highest initial stiffness tended to develop floor accelerations that are consistently slightly smaller than those for softer bearings.

The floor response spectra for levels 5 and 6 for all base-isolated cases (near the impact location) show substantially reduced pseudo-accelerations for frequencies higher than about 2.5 Hz; see Figure 5.13. For floor 5, where the impact occurred, the peak pseudo-acceleration was reduced by a factor of nearly 5 when employing seismic isolation; the spectral accelerations became greater than for the fixed-base case at lower frequencies that approached the frequency of the isolation system. These trends are similar to what might be expected in a traditional isolated structure.

For the response spectra for the first floor shown in Figure 5.13, the pseudo-accelerations for the base-isolated case were higher as compared to the fixed-base case for nearly all frequencies. For a building subjected to large earthquake ground accelerations, the in-structure floor accelerations would be expected to be smaller than the ground acceleration. But for the impact loading case, the ground does not accelerate (based on the assumptions made in this study); therefore, the rigid body motion of the isolated superstructure tended to amplify the accelerations in the lower stories compared to a fixed-base structure. At the peak in the spectra between 5–6 Hz, isolation was still effective in reducing the worst of the pseudo-acceleration peaks. Even though the spectral accelerations were not reduced significantly when compared to the fixed-base case, they were comparable to the spectra at other levels for the isolated structure. Thus, demands on components and equipment in the isolated building were nearly uniform over the height of the AUX.

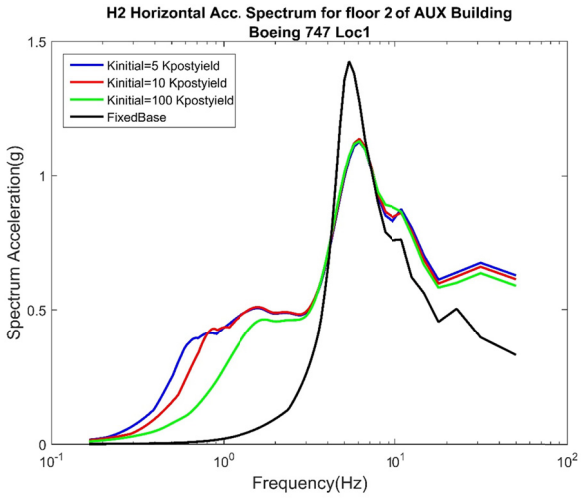

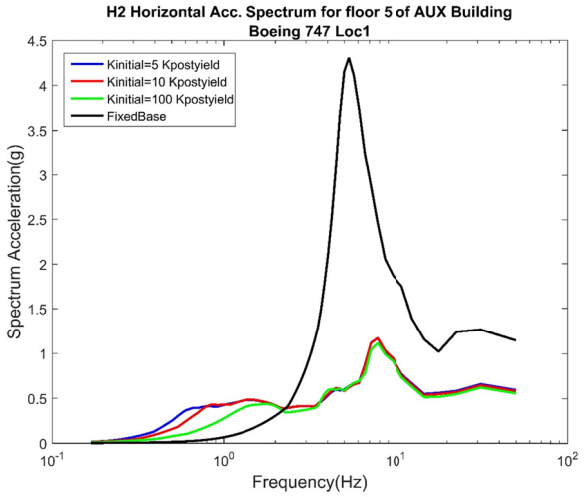

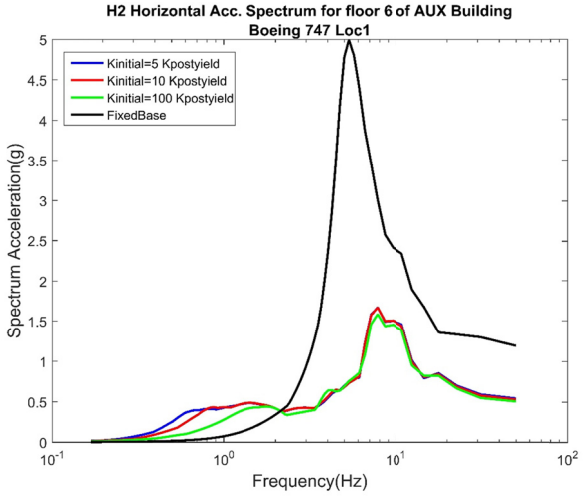

Figure 5.13 **Floor acceleration spectra in the auxiliary building in the H2 direction. Impact Scenario 4 (Boeing-747 at location 1): fixed-base and base-isolated cases with different $K_{initial}$ (T_{iso} = 3 sec; F_y = 0.1 W).**

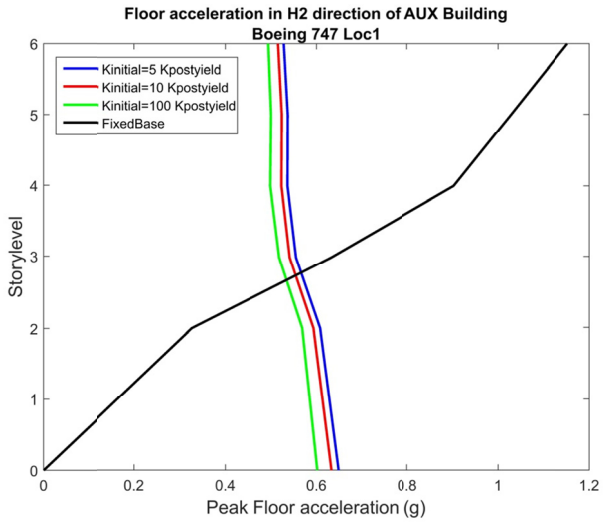

Figure 5.14 Peak floor accelerations along height of the auxiliary building. Impact Scenario 4 (Boeing-747 at location 1): fixed-base and base-isolated cases with different $K_{initial}$ (T_{iso} = 3 sec and F_y = 0.1 W).

Interestingly, the value of $K_{initial}$ has a significant influence on floor spectra for only those frequencies lower than about 2.5 Hz. A larger initial stiffness produced smaller spectral values in this low-frequency range. In the higher frequency range, the response was almost identical regardless of the value of $K_{initial}$.

A comparison between the results in Figure 5.13 and Figure 5.4 demonstrate that the acceleration-related response of the isolated PGSFR is complex, largely because the response is dominated by the $K_{initial}$ selected and the modeling of the hysteretic behavior of the bearings at very low response levels. More work is needed to improve bearing models in this range of response and under high rates of loading. Note that for the fixed-base case, accelerations increased disproportionately as the impulse increased with heavier and faster moving planes; the accelerations in the isolated systems are far less sensitive to increases in impulse magnitudes.

The drift response of the AUX is shown in Figure 5.15. The drift response under the impact of a Boeing-747 versus a Boeing-737 (Figure 5.7) is almost 5 times larger. The shape of the floor response and the relative response amplitude between different base-isolated cases and fixed-base cases remained unchanged. Drift responses remained small for all cases. For the base-isolated cases, they were all on the order of 0.03% and less than 0.02% at the base. Story drifts were larger for the fixed-base case, especially away from the impacted floor level. For example, at the bottom story, the drifts in the fixed-base structure were 2.5 times larger than for the base-isolated cases. As noted for Impact Scenario 1, the bearings with the highest initial stiffness tended to have slightly larger in-structure story drifts. As can be seen by comparing Figure 5.7 and Figure 5.15, as the impulse associated with aircraft impact increases, the effectiveness of base isolation becomes more apparent, and the sensitivity of the response to $K_{initial}$ substantially decreases.

Rotation of each floor due to Impact Scenario 4 is shown in Figure 5.16 for the AUX. As discussed for Scenario 1, the rotation of the floors was highly uniform along the height of the AUX for the base-isolated cases. On the other hand, the rotation for the fixed-base case increased

from the bottom to the top; however, the amplitude of rotation of the fixed-base case was much smaller. Recall that the superstructure was assumed to remain elastic and checks of yielding of the superstructures were not conducted. For the three base-isolated cases, the floor rotation was between 0.15–0.3°, which is not insignificant. However, as noted previously, nearly all of this rotation occurred at the isolation plane, and hence the in-structure twisting of the AUX was quite small.

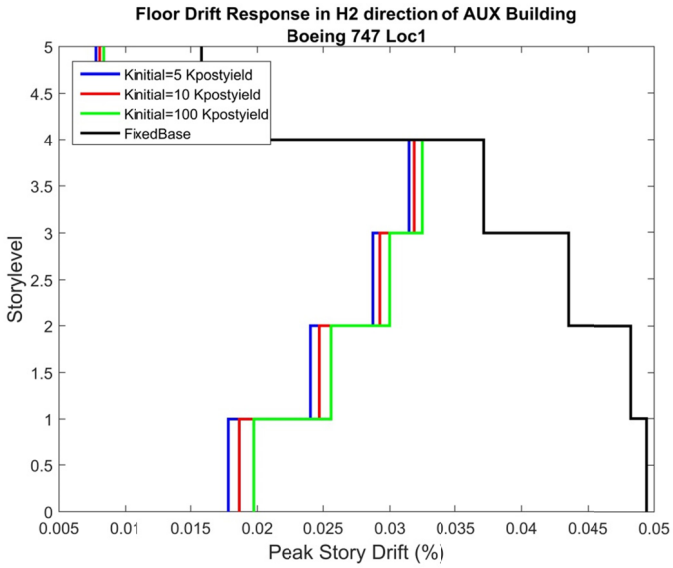

Figure 5.15 **Peak story drifts along height. Impact Scenario 4 (Boeing-747 at location 1): fixed-base and base-isolated cases with different $K_{initial}$ (T_{iso} = 3 sec and F_y = 0.1 W).**

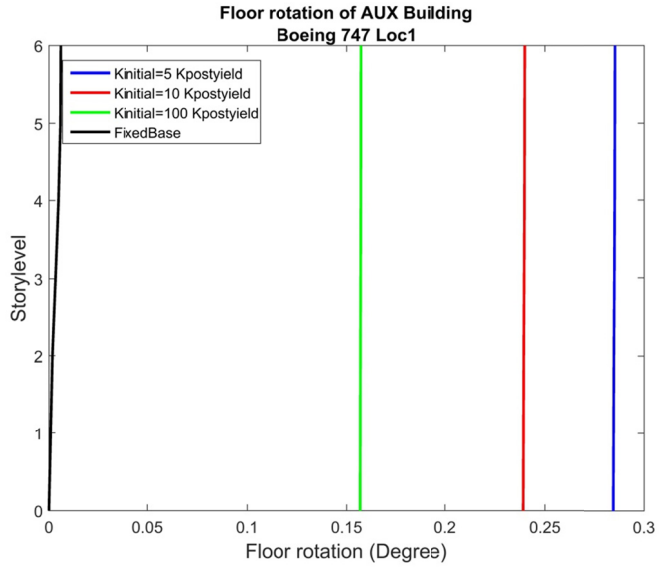

Figure 5.16 **Maximum floor rotations along height. Impact Scenario 4 (Boeing-747 at location 1): fixed-base and base-isolated cases with different $K_{initial}$ (T_{iso} = 3 sec and F_y = 0.1 W).**

In a comparison between different base-isolated cases, larger initial bearing stiffness will result in a small rotation response. The amplitude of floor rotations was almost 8 times larger for the base-isolated cases under impact of a Boeing-747 compared to a Boeing-737. Thus, additional work may be useful in identifying different distributions of bearing types and properties to help mitigate torsional response. Also, the efficacy of adding supplement energy-dissipation devices to help resist torsion, or the use of bearing systems that may be more resistant to torsion, should be investigated.

5.4.1.4 Response of Reactor Containment Building: Scenario 4

The response of the RCB under the Aircraft Impact Scenario 4 is described below. Given previous discussions, the behavior trends examined earlier will not be revisited. Plots of the floor response spectra and floor total accelerations for Impact Scenario 4 are shown in Figure 5.17 and Figure 5.18. These may be compared to Figure 5.9 and Figure 5.10 for Impact Scenario 1. As was the case with Impact Scenario 1, the isolated RCB vibrated significantly, unlike the idealized fixed-base power plant. The total accelerations at the base increased from about 0.16g for the smaller Boeing-737 to about 0.5*g* for the larger Boeing-747. In both cases, accelerations in the upper three levels increased substantially. For the top floor level accelerations increased from about 0.35g for the Boeing-737 to about 1*g* for the Boing-747 .

Considering the floor response spectra, there was very little variation among the floor spectra for different values of K_{initial} for frequencies greater than about 2 Hz. Below that frequency, there was a systematic increase of spectral amplitudes relative to the fixed-base case. Spectra for each K_{initial} were higher than others at a particular frequency. Again, as seen for other response quantities (except for base rotation), the increase in the peak of the pseudo-acceleration floor spectra was only on the order of 2, even though it was on the order of a factor of 5 for the fixed-base AUX when considering the heavier and faster Boeing-747.

The trends regarding floor rotation of the RCB were the same as shown for the AUX. The magnitude of rotation was highly amplified due to the rotation of the isolation plane. The rotation of floors increased significantly for the Boeing-747 compared to the Boeing-737. The floor rotation of the RCB was almost the same compared to the floor rotation of the AUX. Both rotations were nearly constant over the height, indicating a nearly rigid body motion of the upper part of the structure.

The hysteresis loops and displacement orbits for isolators at the four corners of the PGSFR under Impact Scenario 4 are shown in Figure 5.20. The bearing displacement demand in the impact direction was about 30 cm (12 in). For the perpendicular direction, the peak bearing displacement demand was about half that value. These displacements are about 5 to 6 times those for Impact Scenario 1. The hysteresis loops for the heavier and faster Boeing-747 appear more like those expected for an isolation bearing. This was not the case for Impact Scenario 1, where the bearings did not reach their nominal yield value.

The effect of torsion on the bearing behavior was far more pronounced for Impact Scenario 4 than for Scenario 1. This can be seen in the displacement orbits shown in Figure 5.20. The two bearings on the left side of the plot, corresponding to the side of the building hit by the aircraft, were displaced far more than those on the right side. The direction of principal movement of the bearings was again skewed relative to the H2 impact direction. This is suggestive of an initial clockwise torsional movement of the plant. The bearings on the left side

of the model moved more in the H2 direction than in the H1 direction, but the opposite was true for the two bearings on the right side of the building; see Figure 5.2.

The displacement demand of the isolator reached 30.5 cm (12 in.) for the smallest value of $K_{initial}$. Peak displacements were about 60% of these values for the stiffest values of $K_{initial}$ considered. For the SSE level seismic events considered in Chapters 3 and 4, isolator demands were smaller. The seismic displacement demands on the bearings will be larger if recommendations currently being developed in the U.S. NRC regulatory guideline for seismically isolated structures will be followed in the future. In this case, the bearing capacities might be expected to be on the order of 1.67 × 1.6 (or 2.67 times) larger than the median SSE displacement demands. This increased displacement capacity for seismic design considering beyond-design-basis earthquake events will help the PGSFR mitigate beyond-design basis aircraft impacts.

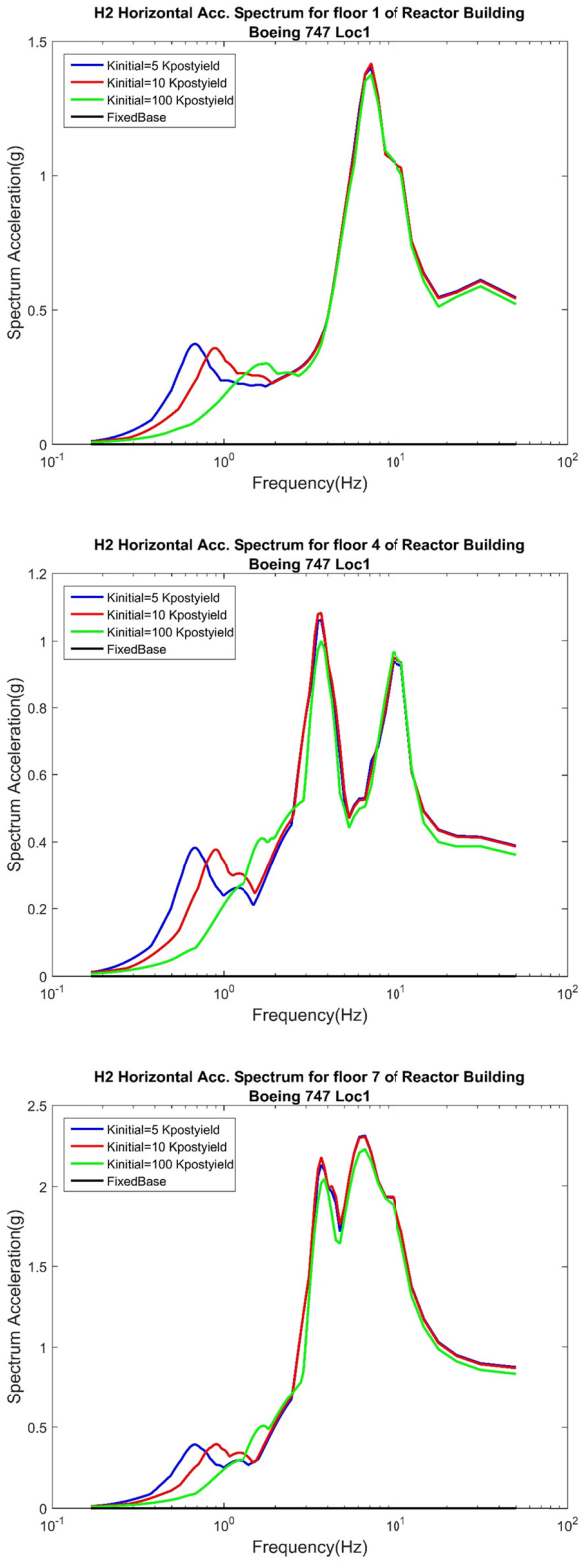

Figure 5.17 **Floor acceleration spectra for the reactor containment building in the H2 direction. Impact Scenario 4 (Boeing-747 at location 1): fixed-base and base-isolated cases with different $K_{initial}$ (T_{iso} = 3 sec and F_y = 0.1 W).**

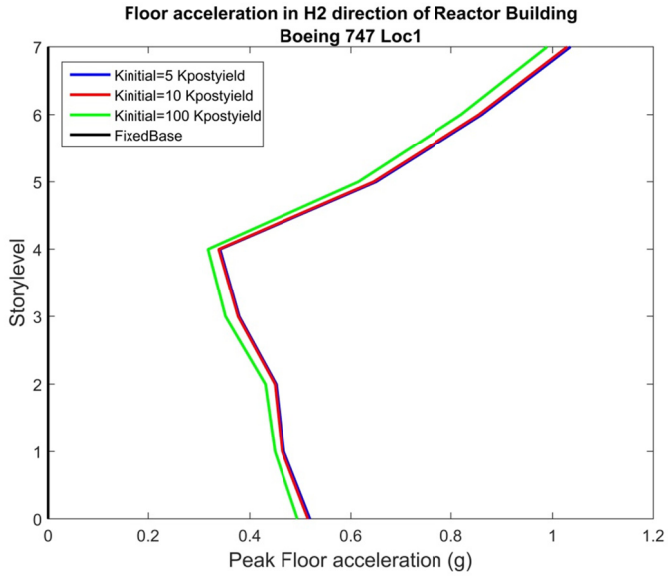

Figure 5.18 **Peak floor accelerations along height. Impact Scenario 4 (Boeing-747 at location 1): fixed-base and base-isolated cases with different $K_{initial}$ (T_{iso} = 3 sec and F_y = 0.1 W).**

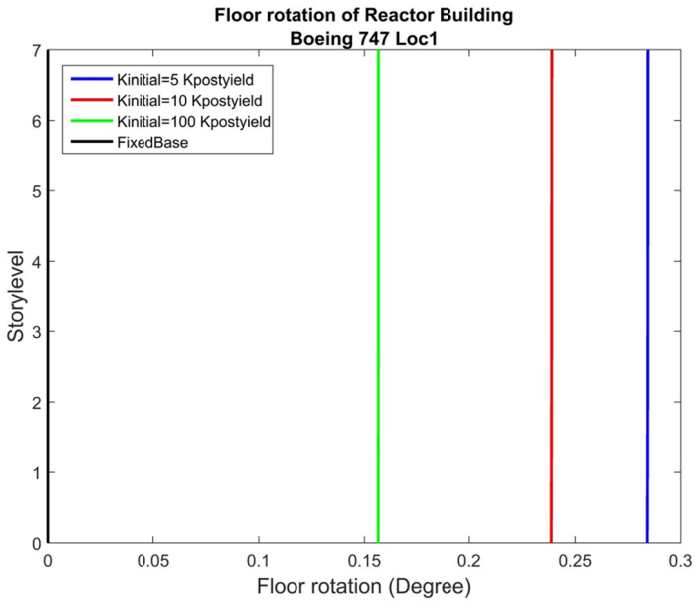

Figure 5.19 **Peak floor rotations along height for the reactor containment building. Impact Scenario 4 (Boeing-747 at location 1): fixed-base and base-isolated cases with different $K_{initial}$ (T_{iso} = 3 sec and F_y = 0.1 W).**

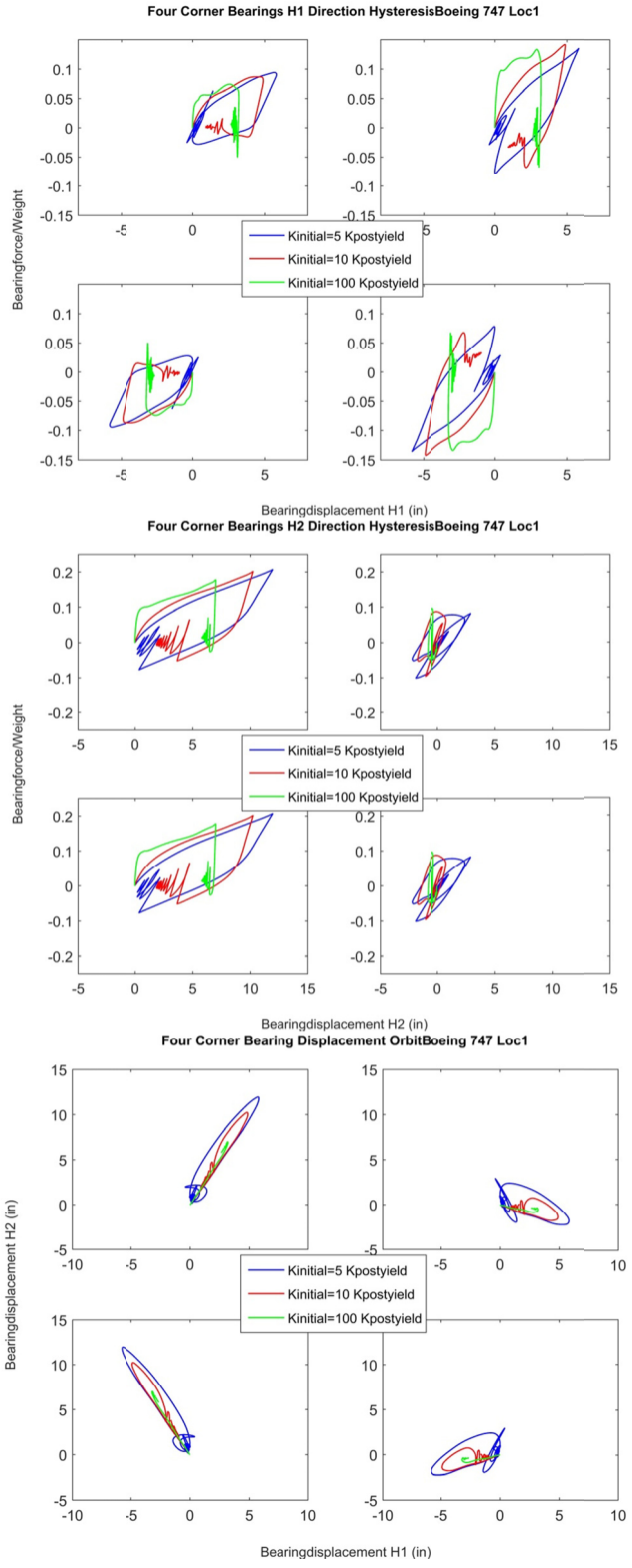

Figure 5.20 **Hysteresis loops and displacement orbits for bearings at the four corners of the base mat. Impact Scenario 4 (Boeing-747 at location 1): base-isolated cases with different $K_{initial}$ (T_{iso} = 3 sec and F_y = 0.1 W).**

5.4.1.5 Conclusions Regarding the Effect of Different $K_{initial}$

In terms of acceleration and drift, the primary response appears to have occurred in the direction of the impact loading. However, given the significant torsional response of the structure, some reduced response perpendicular to the direction of impact may occur locally. Further study is needed to better assess this response, considering likely locations of critical equipment and components.

For the AUX, the floor acceleration spectra due to aircraft impact were larger at the top of the building and smaller at the lower part for the fixed-base case, but almost uniform for the base-isolated case. This is mostly true for large impulses that represent stiff structures above the isolation plane moving as a nearly rigid body. The value of $K_{initial}$ had a small or secondary importance on the horizontal accelerations that developed due to impact, especially for the heavier and faster Boeing-747.

The reduction of floor spectrum amplitudes for cases using base isolation was more pronounced for larger impact loading scenarios. The reduction of the peak value in the floor spectrum was around 5 considering the larger impact of the Boeing-747.

In-structure story drift values were generally small. This study assumed the structure above the isolation plane remained elastic.

Because of the eccentricity of the loading for Impact Scenarios 1 and 4, it was expected that rotation of the building and the base mat would occur. For the fixed-base model, minor torsion was observed with the twist of the AUX from the base to the top. For the base-isolated case, rotation of the whole AUX occurred as a result of rotation of the isolated base mat about a vertical axis. Rotations as large as 0.2° were computed for Impact Scenario 4, with the lowest of the $K_{initial}$ values considered. Larger values of $K_{initial}$ effectively reduced the rotations.

Since the RCB is not attached to the AUX, for the fixed-base case, no response was observed due to impact loading on the AUX. However, for the base-isolated case, the RCB shares the same isolated mat foundation as the AUX, and the RCB vibrated considerably as a result of aircraft impact. For the base-isolated case, the RCB had greater floor response spectra in comparison to the AUX. There was a large amplification of accelerations above floor 4 in the RCB. This was assumed to be associated with the relatively light and flexible structure used in this region of the plant.

The rotation of the RCB appears to be primarily a result of the rotation of the underlying isolated mat foundation. It is assumed that when the aircraft impact occurs eccentrically, the isolated mat foundation will rotate significantly, and the bearings will move not only in the direction of the aircraft impact but also in the orthogonal direction. In reality, the principal direction of motion is skewed to the principal directions of the building, corresponding to the relative significance of the torsional and translational movement of the isolation plane. For the cases studied herein, the bearing displacement perpendicular to the direction of impact was around 50% of that occurring in the direction of the impact.

For the smaller impact loading, the isolator displacement demand was around 5 cm (2 in.), which is similar to the demand for the design-level earthquake (SSE) loading. For larger impact loading due to the faster and heavier Boeing-747, the displacement demand reached about 30 cm (12 in.). This is much larger than the displacement demand at the SSE; therefore, the design of

the isolator should take into account the response under aircraft impact. With a larger $K_{initial}$, the bearing displacement demand can be cut in half. Other methods to reduce the torsional and translational response of the PGSFR were mentioned and should be investigated in future studies.

5.4.2 Responses Considering Different T_{iso}

Selected results comparing the effect of different isolation periods T_{iso} on the response to aircraft impact are discussed below. Impact Scenarios 2 and 5 are considered as follows:

Impact scenario 2: Loading location 2 for a Boeing-737

Impact scenario 5: Loading location 2 for a Boeing-747

The discussion in this section focuses on the response differences due to three isolation periods (T_{iso} = 2, 3, and 4 sec) and the difference of responses because of the change of loading location. For these case studies, $K_{initial}$ = 10 $K_{postyield}$ and F_y = 0.10 W remain constant. Observations determined in previous sections will not be repeated.

The second loading case is similar to the first loading case; however, the second loading location is closer to the centroid of the RCB, thereby nearer to the overall center-of-mass of the PGSFR. This scenario considers the smaller of the two aircrafts. As presented earlier, the bearing response is relatively small, with the peak forces not exceeding about 70% of the nominal yield strength, and the peak displacement being less than 3.5 cm (1.5 in). When compared to scenario 1, there was far less torsional response for impact location 2.

5.4.2.1 Response of Auxiliary Building: Scenario 2

The general trends in the floor response spectra for Impact Scenario 2 are similar to those for Impact Scenario 1, as can be seen by comparing Figure 5.4 and Figure 5.21. The peak total accelerations developed at each floor are similar, as can be seen by comparing Figure 5.5 and Figure 5.22. The amplitude and trends for the total acceleration response is very similar. A comparison of the response spectra for different T_{iso} shows little difference. The three base-isolated cases have almost identical responses. The reason that T_{iso} does not have more influence on the plant and bearing behavior is that the responses for this impact scenario are not sufficient to raise the forces in the bearings to F_y or above. As such, changing the slope of the post-yield force-displacement relationship has little (essentially no) effect on response.

- Unlike seismic loading, the aircraft impact loading does not have many loading cycles. The isolator will stay in the initial stiffness range for most of the cycles. Therefore, the responses of bearings with different post-yield stiffness are almost the same since the behavior is mainly influenced by the initial stiffness. Because of the use of the Bouc-–Wen isolator model, the value of F_y has only a very small effect on the shape of the hysteresis loops prior to reaching F_y.
- The peak accelerations for impact Scenarios 1 and 2 were nearly identical. The primary difference between these two scenarios was that the eccentricity of Scenario 2 was much smaller, and its sign was opposite to that of Scenario 1.

- The drift responses shown in Figure 5.23 were very small as before for the Boeing-737. In these cases drift does not depend on the post-yield stiffness of the bearing. The amplitude of drift was about the same as for impact Scenario 1.

Rotation of the AUX is shown in Figure 5.24. The trends are very similar to those for Impact Scenario 1, except that the rotations were slightly less for Impact Scenario 2. For example, for Impact Scenario 1, a representative rotation was about 0.033° but only about 0.025° for Impact Scenario 2. Since the impact force history is the same for both cases, the difference is due to the reduced eccentricity of impact location 2. A comparison of Figure 5.8 and Figure 5.24 shows that the torsional response is much less sensitive to T_{iso} than to the initial elastic stiffness.

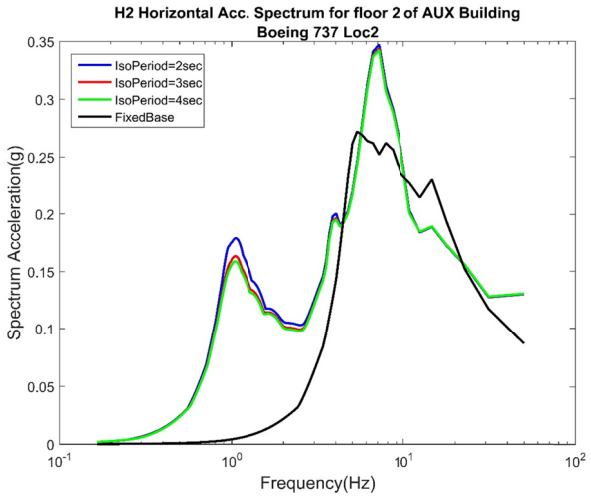

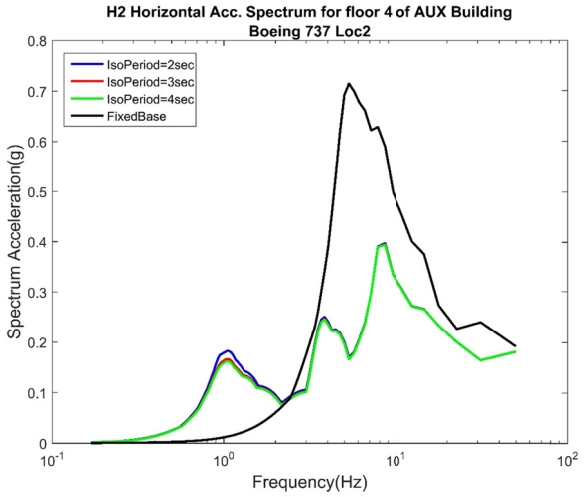

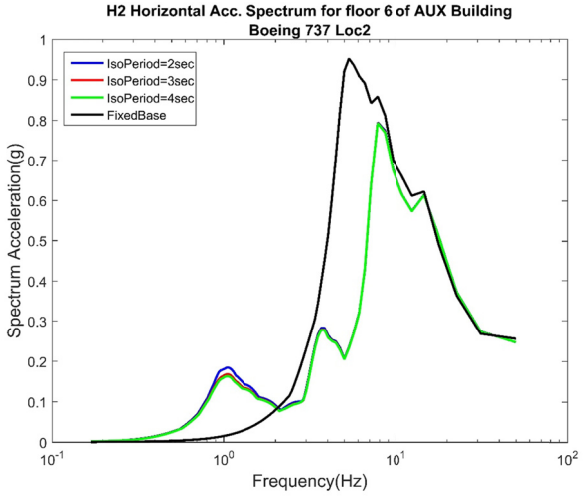

Figure 5.21 **Floor acceleration spectra for the auxiliary building in the H2 direction. Impact Scenario 2 (Boeing-737 at location 2): fixed-base and base-isolated cases with different T_{iso} ($K_{initial}$ = 10 $K_{postyield}$ and F_y = 0.1 W).**

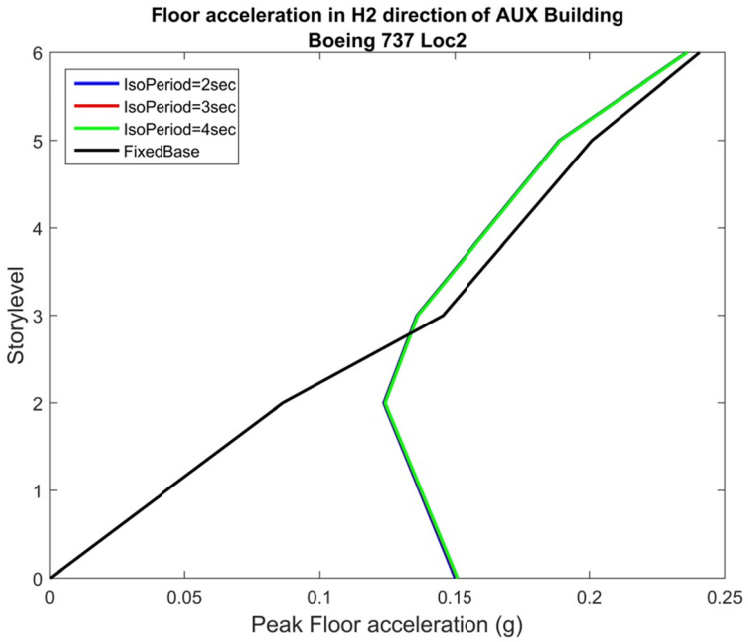

.

Figure 5.22 **Peak floor accelerations along height for the auxiliary building. Impact Scenario 2 (Boeing-737 at location 2): fixed-base and base-isolated cases with different T_{iso} ($K_{initial}$ = 10 $K_{postyield}$ and F_y = 0.1 W).**

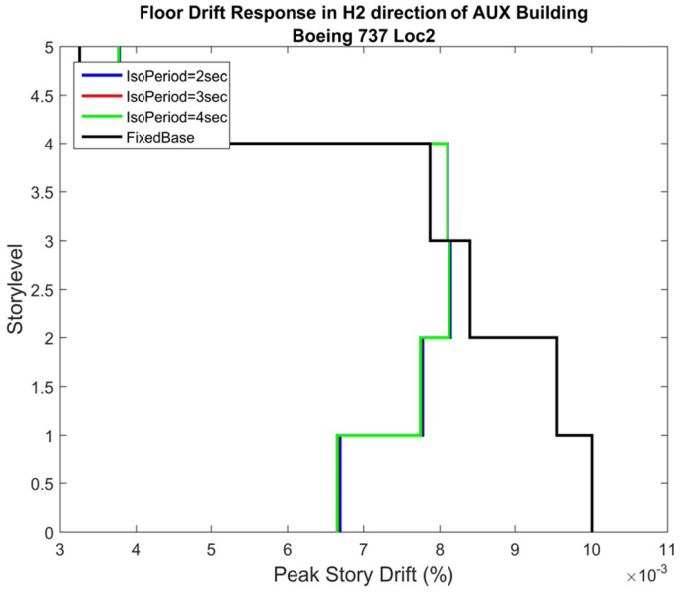

Figure 5.23 **Peak story drifts along height for the auxiliary building. Impact Scenario 2 (Boeing-737 at location 2): fixed-base and base-isolated cases with different T_{iso} ($K_{initial}$ = 10 $K_{postyield}$ and F_y = 0.1 W).**

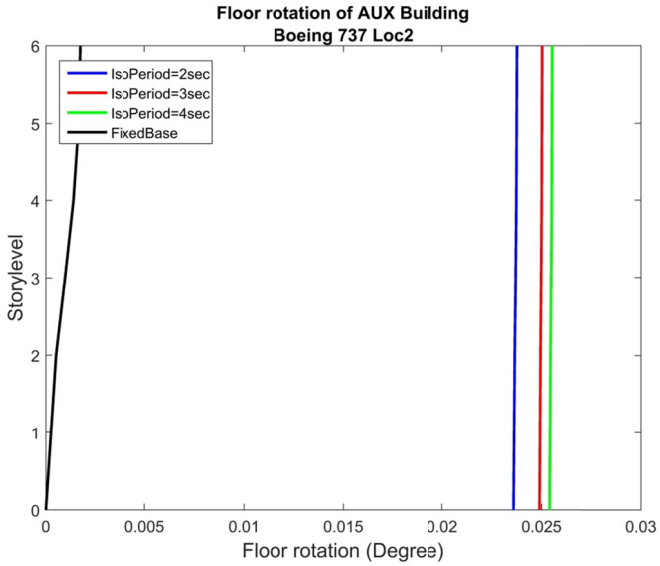

Figure 5.24 **Maximum floor rotations along height for the auxiliary building. Impact Scenario 2 (Boeing-737 at location 2): fixed-base and base-isolated cases with different T_{iso} ($K_{initial}$ = 10 $K_{postyield}$ and F_y = 0.1 W).**

5.4.2.2 Response of Reactor Containment Building: Scenario 2

Floor response spectra for the RCB are shown in Figure 5.25, and the distribution of total accelerations is shown in Figure 5.25. The difference of acceleration responses in the RCB in the H2 direction due to different T_{iso} is negligible for Impact Scenario 2. Compared to the response of the AUX for Impact Scenario 2, floor accelerations in the RCB are larger; see Figure 5.22. The peak acceleration at the top of the AUX is about 0.22g, while the acceleration at the same location in the RCB is almost 0.5g. There may be a "penthouse" type of phenomena occurring in the upper levels of the RCB.

Consistent with the previous results for this impact scenario, there was very little difference between the responses for the RCB supported on bearings having different $T_{iso.}$ The drift was small and nearly constant for the full height of the RCB (in spite of there being a sudden change in accelerations above level 4).

The isolator responses for the four corner bearings are shown in Figure 5.28. For the hysteretic behavior of the isolators during impact loading, there was very little difference between different bearings with different post-yield periods. The isolators behaved similarly since the isolator remained in the initial stiffness range for most of the cycles. Even the most heavily loaded bearing did not exceed a lateral shear greater than about 70% of F_y. There is some difference in the hysteretic behavior because the Bouc–Wen model was constructed to be asymptotic to the initial and second slope of a bilinear backbone curve. By changing T_{iso}, there was a small change in the shape of the curves even if F_y was not reached.

The displacement demand for the isolator in the direction of loading was around 25 mm (1 in.), and the displacement demand for the orthogonal direction was around 12 mm (0.5 in.) due to torsion of the base mat. It is clear that compared to Impact Scenario 1, the two bearings at the corners on the right side of Figure 5.2 for Impact Scenario 2 experienced larger

displacements compared to the two bearings on the left side. This differs from the trend observed under Impact Scenario 1. Because the loading is to the right side of the AUX, the displacements in the right-hand side bearings were larger since they are nearer to the impact on the side where torsion tended to increase displacement demands.

The rotation direction under Loading Case 2 was opposite to that of Loading Case 1, as illustrated by the displacement orbits of the bearings. The rotation was counter-clockwise instead of clockwise like in Loading Case 1 since the loading location was to the right of the center of rotation. This resulted in the skewed direction of the principle direction of motion of the bearing displacement orbits. The skew is consistent with a rotation of the plant about a vertical axis.

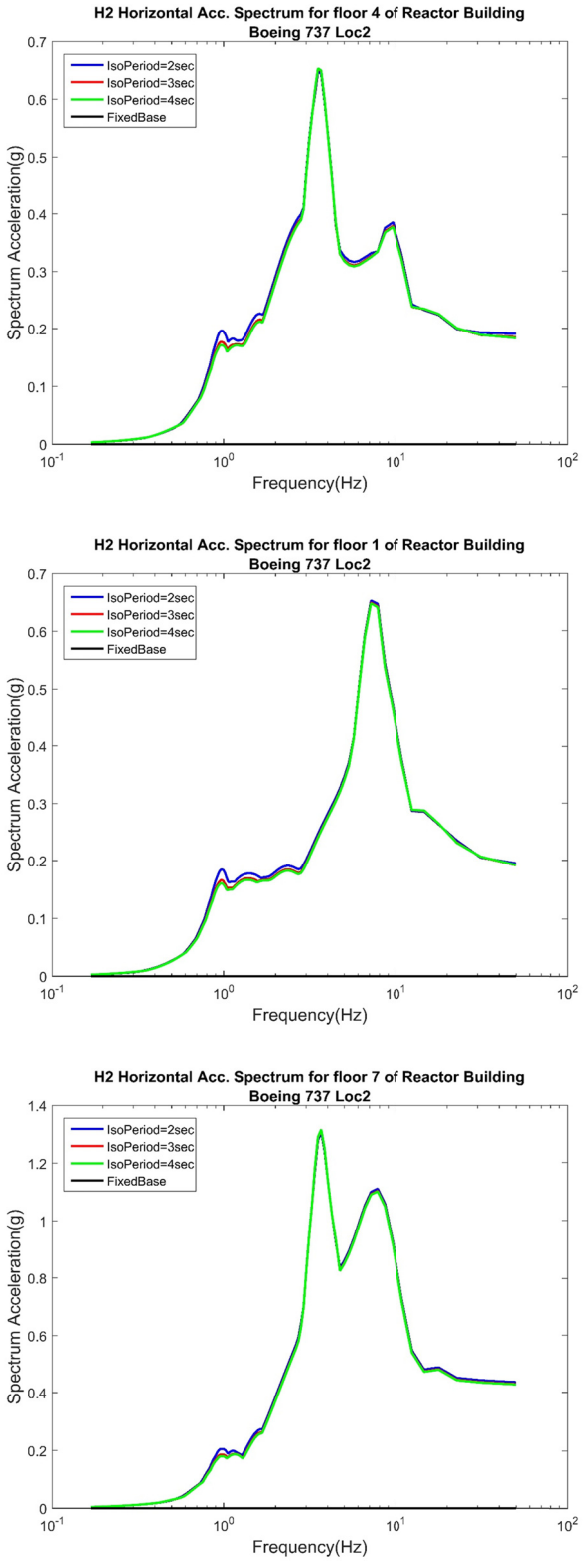

Figure 5.25 **Floor acceleration response spectra for the reactor containment building in the H2 direction. Impact Scenario 2 (Boeing-737 at location 2): fixed-base and base-isolated cases with different T_{iso} ($K_{initial}$ = 10 $K_{postyield}$ and F_y = 0.1 W).**

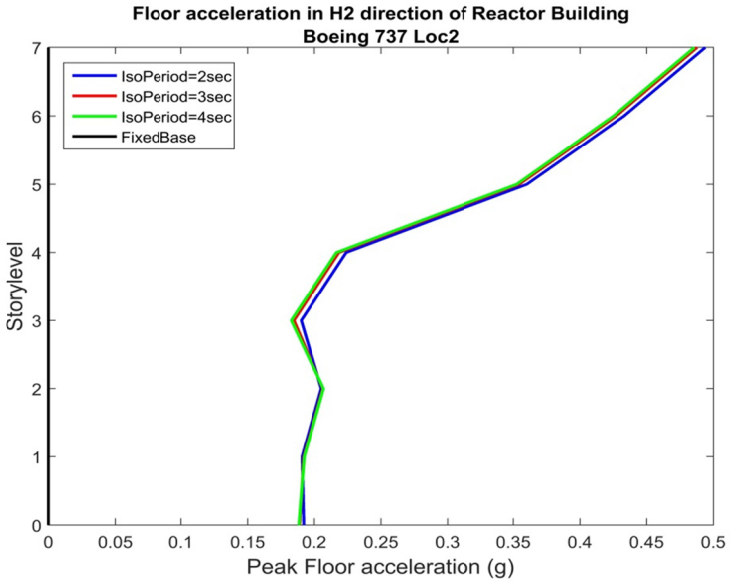

Figure 5.26 **Peak floor accelerations along height for the reactor containment building. Impact Scenario 2 (Boeing-737 at location 2): fixed-base and base-isolated cases with different T_{iso} ($K_{initial}$ = 10 $K_{postyield}$ and F_y = 0.1 W).**

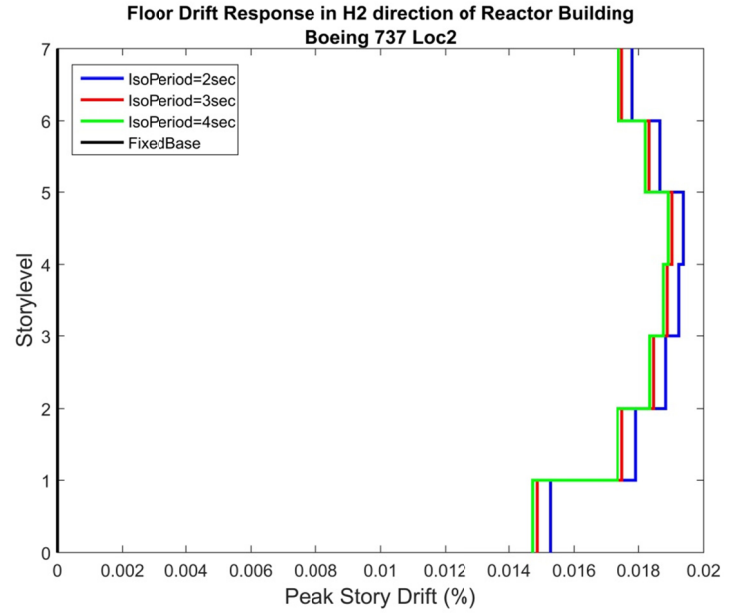

Figure 5.27 **Peak story drifts along height for the reactor containment building. Impact Scenario 2 (Boeing-737 at location 2): fixed-base and base-isolated cases with different T_{iso} ($K_{initial}$ = 10 $K_{postyield}$ and F_y = 0.1 W).**

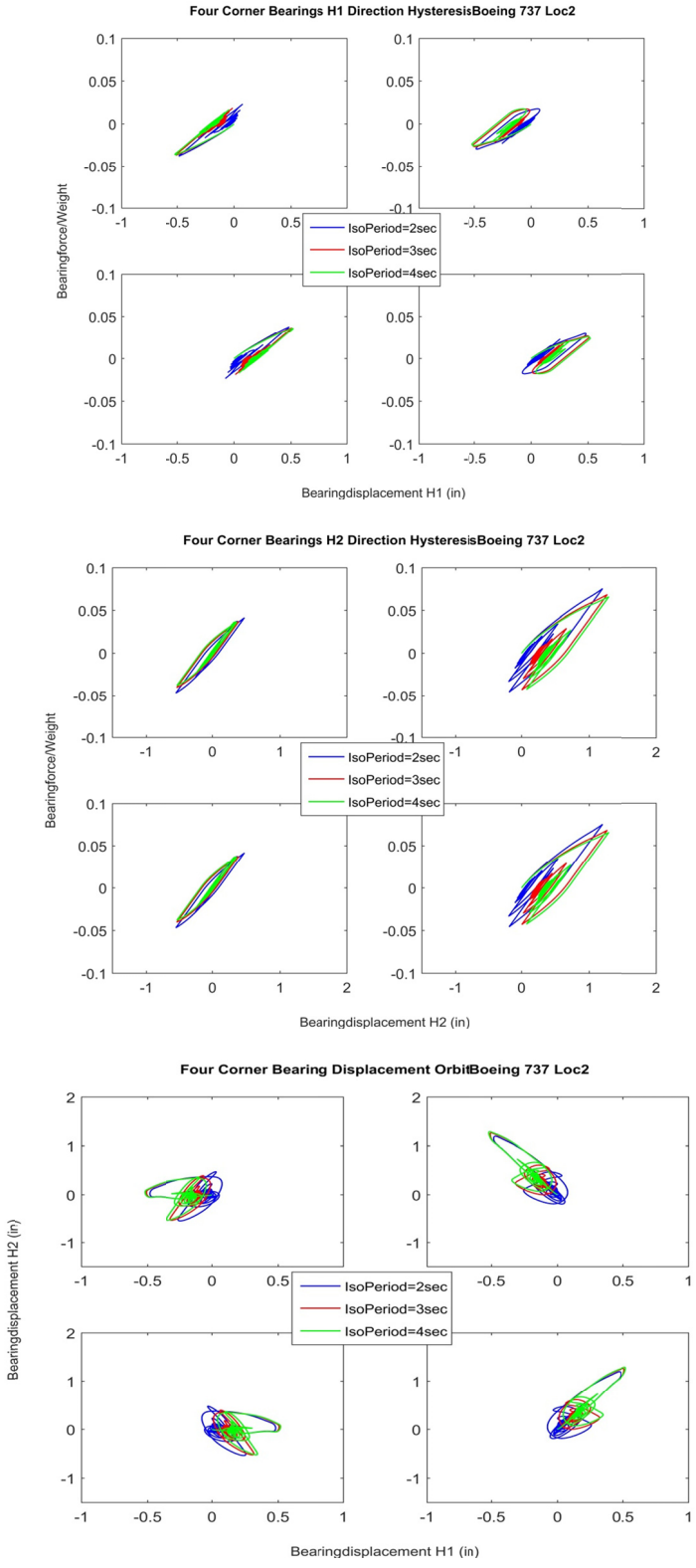

Figure 5.28 **Hysteresis loops and displacement orbits for bearings at the four corners of the base mat. Impact Scenario 2 (Boeing-737 at location 2): base-isolated cases with different T_{iso} ($K_{initial}$ = 10 $K_{postyield}$ and F_y = 0.1 W).**

5.4.2.3 Response of Auxiliary Building: Scenario 5

Impact Scenario 5 is discussed in this section. The impact location is the same as for Impact Scenario 2, but with the larger and faster Boeing-747 instead of the Boeing-737. As was observed for Impact Scenario 4, the impact of the larger and faster plane resulted in lateral displacements in some of the bearings in excess of 255 mm (10 in.) and forces far in excess of F_y.

The floor acceleration response spectra for the AUX are shown in Figure 5.29. The associated distribution of total accelerations with height is shown in Figure 5.30. The total accelerations were very similar to those computed for Impact Scenario 4. There is virtually no difference between the accelerations and acceleration spectra for the different T_{iso} values used in the analyses except in the lowest level shown at frequencies less than 2 Hz. At this location, a smaller post-yield period had a slightly larger response.

Response of floor peak acceleration is shown in Figure 5.30. Comparing the responses between Impact Scenario 5 and Impact Scenario 2, the amplification of responses due to the larger plane was similar when comparing Impact Scenario 4 to Impact Scenario 1. There was no difference in acceleration response of the AUX comparing Impact Scenarios 2 and 1 as long as the loading function and direction were the same. The floor acceleration response was the same for the AUX for all the normal impacts with the same loading function. The drift response is not shown because the response was similar to Impact Scenario 4 and the response value was small.

The rotation response of the AUX is shown in Figure 5.31. Compared to the rotation response of AUX under Impact Scenario 4, the response under Impact Scenario 5 is smaller. The response for the same case, which has a 3-sec isolation period and initial stiffness 10 times the post-yield stiffness, is around 0.18° for Impact Scenario 5 but around 0.23° for Scenario 4. The difference is due to the change in the distance of the loading location to the center-of-mass and stiffness, because these are not uniformly distributed along the H1 direction and the RCB is not centered in the layout of the AUX.

A comparison of responses with different isolation periods demonstrates that the difference shown in Figure 5.31 is more noticeable compared to the response shown in Figure 5.24 for Impact Scenario 2, which involved the impact of a smaller and slower plane. Since the loading impulse was larger for Impact Scenario 5, the post-yield stiffness was affected, resulting in different displacement demands of the bearings for different cases; therefore, the rotation of the base mat, which depends on the movement of the bearings, will be different. The post-yield period for smaller bearings will result in a smaller rotation response of the AUX.

5.4.2.4 Response of Reactor Containment Building: Scenario 5

The floor acceleration spectra for the RCB are shown in Figure 5.32. As demonstrated earlier, there is virtually no difference between base-isolated cases with different isolator post-yield periods. Comparing spectral acceleration values against the response spectra for Impact Scenario 4 in Figure 5.17, the values for Impact Scenario 5 are much larger. The peak amplitudes of the spectra were almost twice those when considering the Boeing-747 impacts at location 2 instead of location 1. As discussed previously, the floor accelerations of the AUX, which received the impact directly, were not sensitive to whether impact occurred at location 1 or 2. The RCB was sensitive to the location of the impact on the AUX due to the movement of the base mat.

The same conclusion can be drawn from the response of peak floor acceleration; see Figure 5.34. When compared to the peak floor acceleration due to Impact Scenario 4, the responses were larger.

The floor rotation of the RCB was the same as the floor rotation of the AUX. A smaller rotation was obtained compared to Impact Scenario 4 where the loading location was further from the center-of-mass. The bearing displacement orbit and the hysteresis loops for this loading case are shown in Figure 5.35. First, the displacement demand for the isolator was around 250 mm (10 in.) in the H2 direction and 120 mm (5 in.) in the H1 direction. The displacement of the bearing is similar to Impact Scenario 4. However, since the impact loading was at the right side of the AUX, the center of rotation was located at the left side of the impact location. The right two bearings experienced much larger displacements compared to the left two bearings since the distance to the center of rotation of the two right-side bearings was larger than the two left-side bearings.

The direction of rotation of the displacement orbit was counter-clockwise. It is clear that the displacement demand was affected by the isolation period as shown in the second plot in Figure 5.35. The displacement demand can be reduced to around 120 mm (5 in.) by using an isolation period of 2 sec instead of 4 sec. In general, the bearing displacement demand due to Boeing-747 impact was larger than the demand from seismic analysis under design-level earthquake. Therefore, when considering the design of the isolator, the displacement capacity might be controlled by aircraft impact loading.

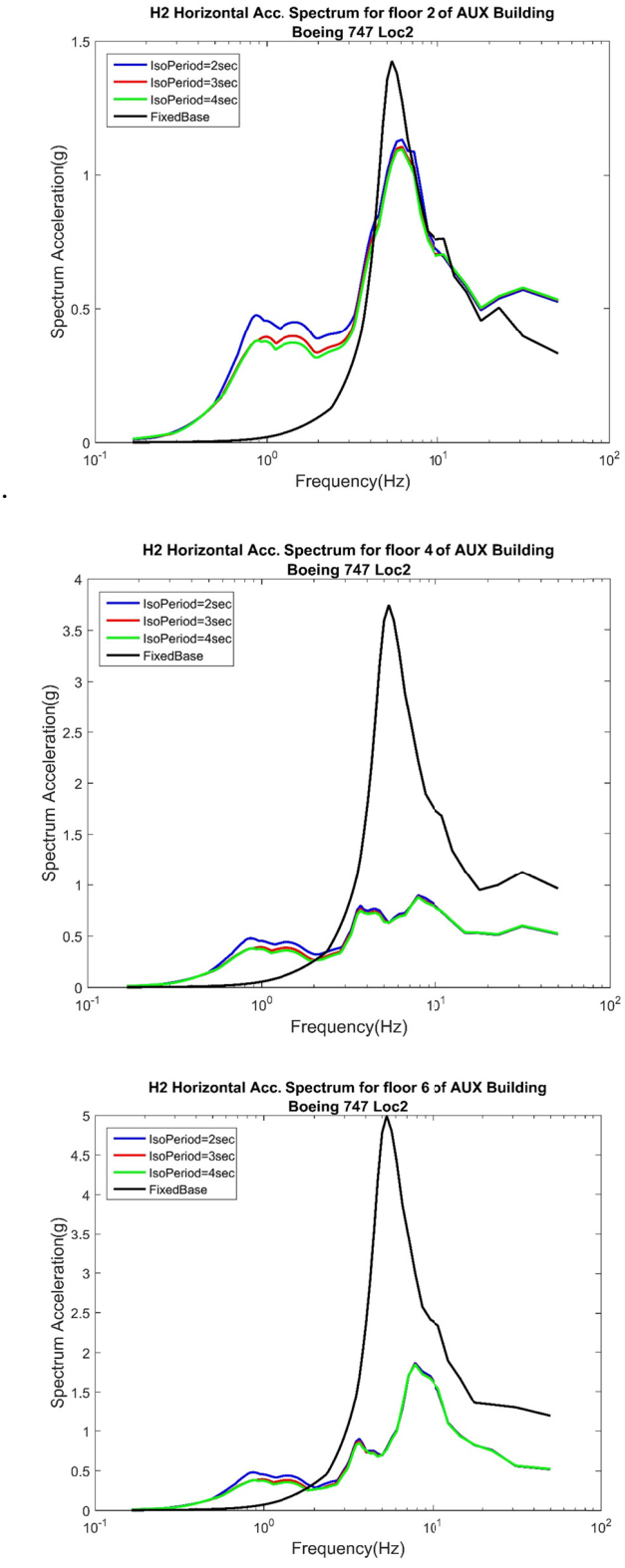

Figure 5.29 **Floor acceleration spectra for auxiliary building in the H2 direction. Impact Scenario 5 (Boeing-747 at location 2): fixed-base and base-isolated cases with different T_{iso} ($K_{initial}$ = 10 $K_{postyield}$ and F_y = 0.1 W).**

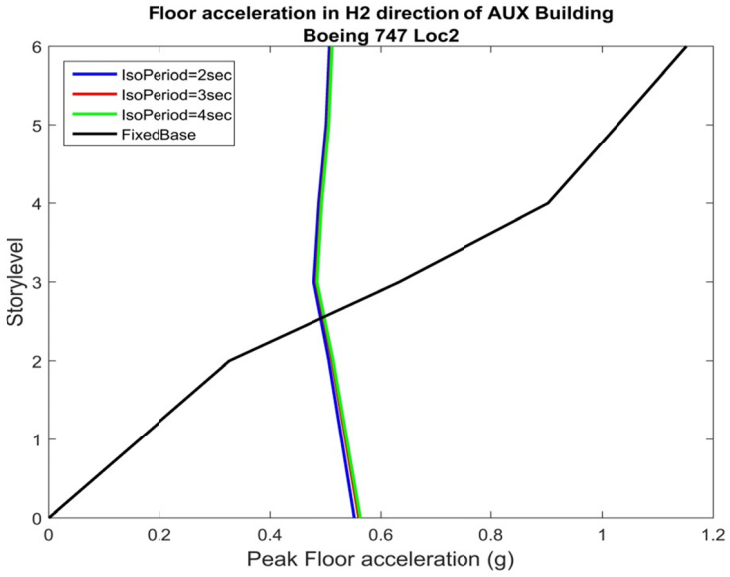

Figure 5.30 **Peak floor accelerations along height for the auxiliary building. Impact Scenario 5 (Boeing-747 at location 2): fixed-base and base-isolated cases with different T_{iso} ($K_{initial}$ = 10 $K_{postyield}$ and F_y = 0.1 W).**

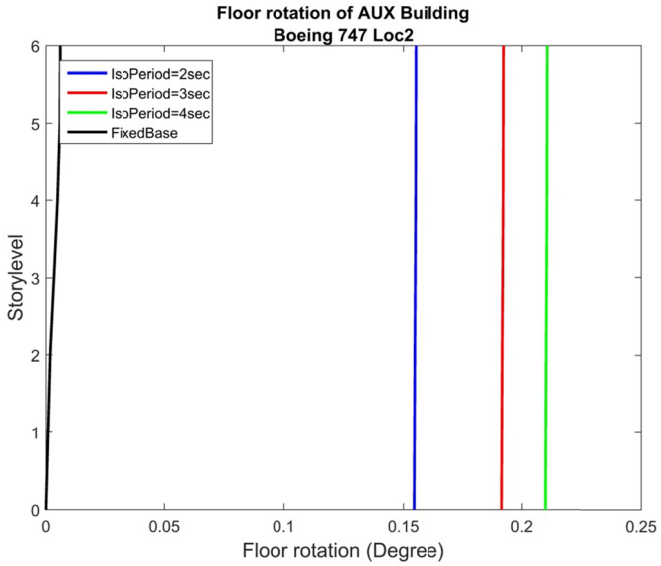

Figure 5.31 **Maximum floor rotations along height for the auxiliary building. Impact Scenario 5 (Boeing-747 at location 2): fixed-base and base-isolated cases with different T_{iso} ($K_{initial}$ = 10 $K_{postyield}$ and F_y = 0.1 W).**

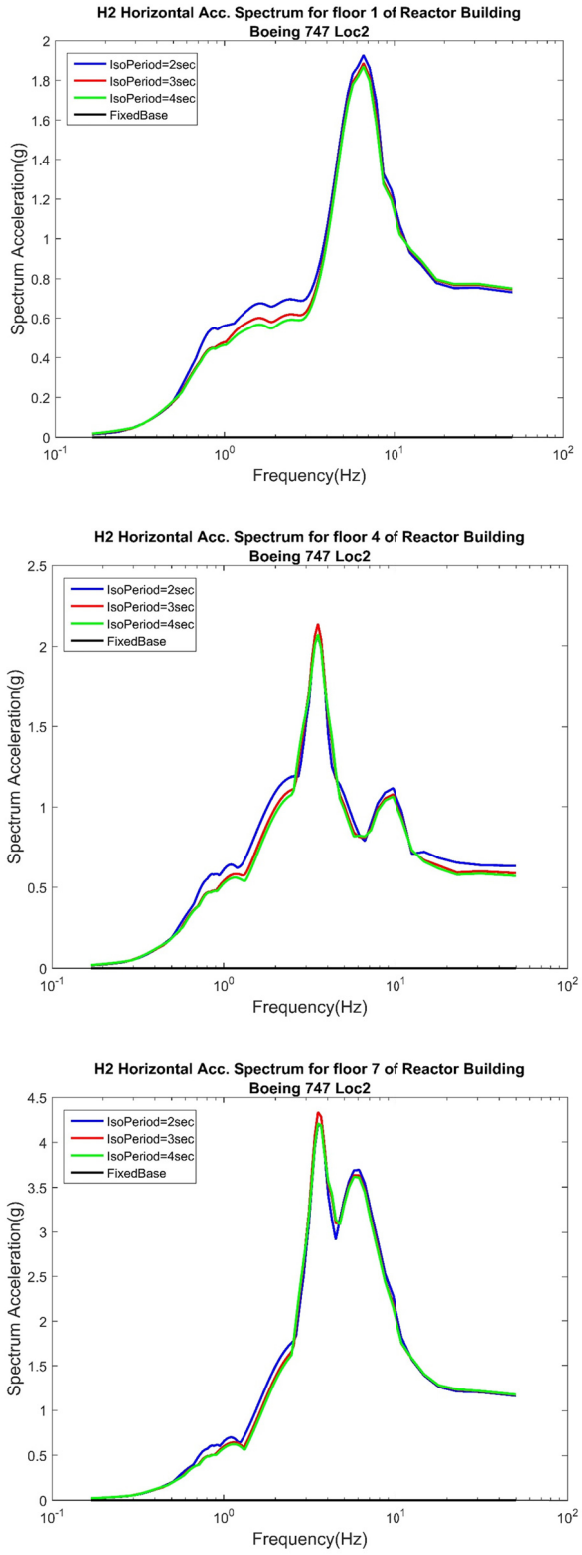

Figure 5.32 **Floor acceleration spectra for the reactor containment building in the H2 direction. Impact Scenario 5 (Boeing-747 at location 2): fixed-base and base-isolated cases with different T_{iso} ($K_{initial}$ = 10; $K_{postyield}$ and F_y = 0.1 W).**

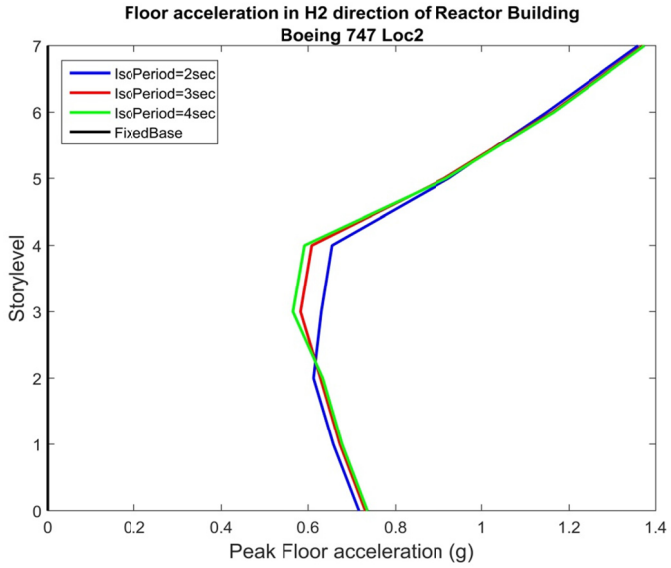

Figure 5.33 **Peak floor accelerations along height for the reactor containment building. Impact Scenario 5 (Boeing-747 at location 2): fixed-base and base-isolated cases with different T_{iso} ($K_{initial}$ = 10 $K_{postyield}$ and F_y = 0.1 W).**

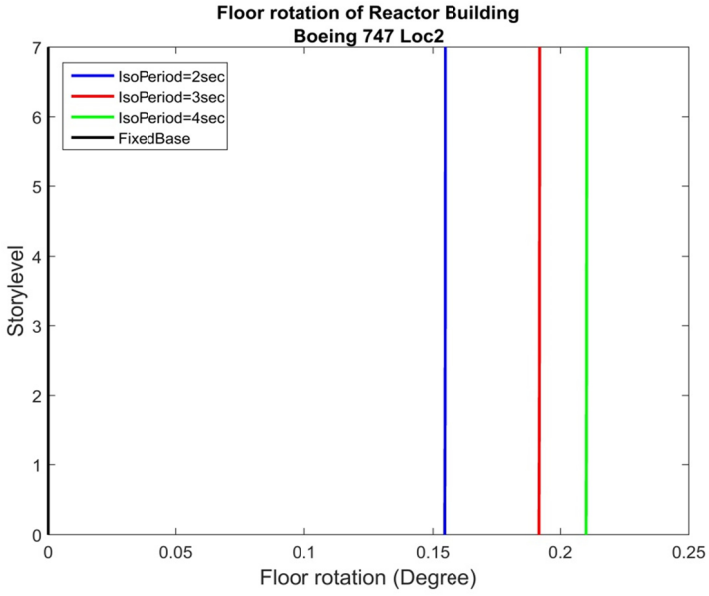

Figure 5.34 **Maximum floor rotations along height for the reactor containment building. Impact Scenario 5 (Boeing-747 at location 2): fixed-base and base-isolated cases with different T_{iso} ($K_{initial}$ = 10 $K_{postyield}$ and F_y = 0.1 W).**

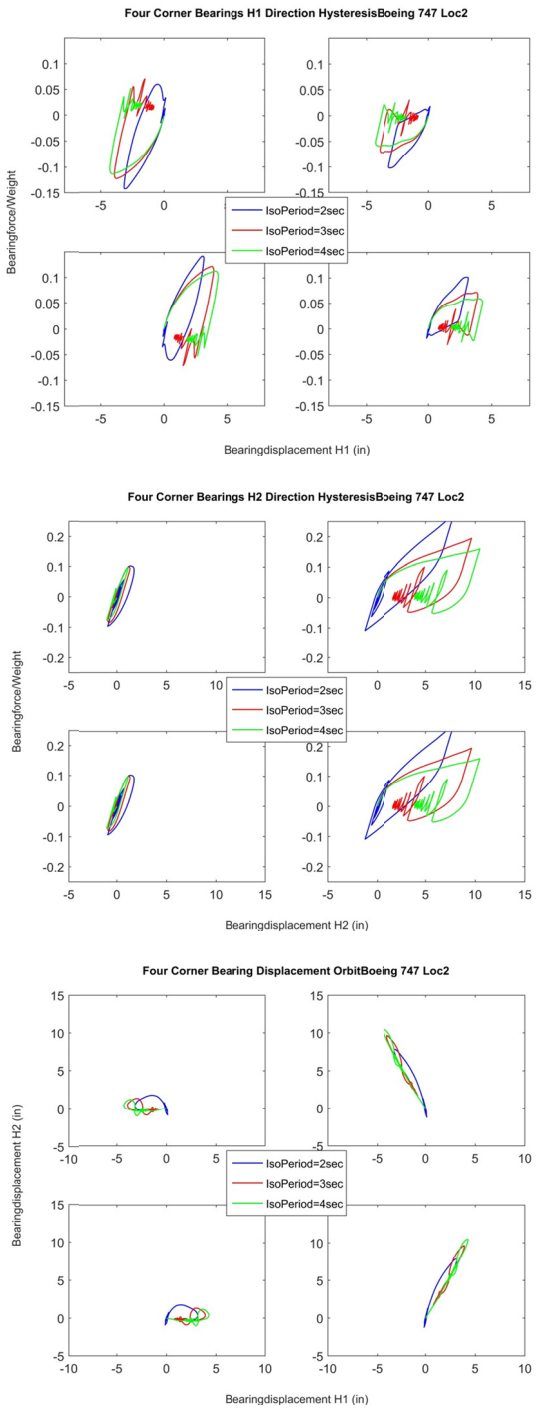

Figure 5.35 **Hysteresis loops and displacement orbits for bearings at the four corners of the base mat. Impact Scenario 5 (Boeing-747 at location 2); base-isolated cases with different T_{iso} ($K_{initial}$ = 10 $K_{postyield}$ and F_y = 0.1 W).**

5.4.2.5 Conclusions Regarding the Effect of Different T_{iso}

Varying T_{iso} did not significantly affect the acceleration response but slightly influenced the rotation of the base slab about a vertical axis during larger impact loading. A smaller T_{iso} resulted in smaller rotation response. The floor acceleration responses of the AUX for different loading locations were the same as long as the loading direction and function were the same. Under Impact Scenario 2 and 5, where the loading location was near to the center-of-mass, the system experienced smaller rotation of the isolation plane than for Impact Scenarios 1 and 4, where the impact location was relatively far from the center-of-mass.

- The floor acceleration response of the RCB was larger for Impact Scenario 5. Because there was less eccentricity of the impulse with respect to the center-of-mass, less of the energy of the impact was directed to the torsional response of the system and more was directed to translational movement of the system.
- Displacement demands on the isolators were similar when comparing Impact Scenarios 1 and 2, and 4 and 5. Under larger impact due to the Boeing-747, the displacement demand in the H1 and H2 directions were 120 mm (5 in.) and 250 mm (10 in.), respectively.
- The rotation of the base mat was clockwise for Impact Scenario 1 and counter-clockwise for Impact Scenario 2. The isolators near the loading location experienced larger displacement compared to the isolators far from the loading location.

5.4.3 Responses Considering Different F_y

In the previous two sections, the responses of Loading Scenarios 1 and 4 (corresponding to loading location 1) and responses of loading scenarios 2 and 5 (corresponding to loading location 2) were discussed. This section discusses loading scenarios 3 and 6 (corresponding to loading location 3). These loading cases correspond to:

Impact Scenario 3: Impact location 3 for Boeing-737

Impact Scenario 6: Impact location 3 for Boeing-747

Both of these scenarios were oriented in the longitudinal H1 direction of the PGSFR and acted through the center-of-mass of the system. Since the impact load was directed through the center-of-mass and the structure is symmetric in that direction, no torsional response was expected. For the lighter Boeing-737, very little response was expected for this excitation. Therefore, only Impact Scenario 6 will be discussed in detail.

5.4.3.1 Response of Auxiliary Building: Scenario 6

Since the force time history for Impact Scenario 6 is applied through the center-of-mass in the H1 direction, the acceleration response only occurred in the H1 direction. The amplitude of the computed floor spectrum and magnitudes of the total floor accelerations was very similar to the other two loading cases of the impact of a Boeing-747, which can be seen by comparing Figure 5.36 with Figure 5.13 and Figure 5.29, and Figure 5.34 with Figure 5.14 and Figure 5.30. The

reduction in response is larger in higher floors when using base isolation; the response of the fixed-base model was large.

- For bearings with different yield forces, the difference of the acceleration related response was not significant. The only difference in the floor spectrum was near the frequency of the isolation mode: the larger the bearing yield force, the larger the acceleration response.
- Floor peak accelerations are shown in Figure 5.37. The acceleration response of the AUX was nearly constant over height for the isolated structure and varied linearly with height for the fixed-base case. The amplitude of the acceleration was similar for Impact Scenarios 4 and 5 despite the location of the impacts being different.
- The drift response is not shown here as the values are small and similar to results presented earlier. The main difference was that due to the impact loads being applied in a plane of symmetry, no torsional response was observed.

5.4.3.2 Response of Reactor Containment Building: Scenario 6

The acceleration floor spectrum and floor accelerations for the RCB are shown in Figure 5.38 and Figure 5.39. Compared to the response of the AUX, the floor spectrum of the RCB is larger, almost twice the response values of AUX. Minor differences can be seen for isolators with different yield forces. Isolators with large yield strengths resulted in a slightly larger peak acceleration response. As shown in Figure 5.39, the difference between different bearing yield forces in terms of peak floor acceleration was negligible, and the amplitude of responses was larger than the peak floor acceleration of the AUX.

For the response of the corner isolators shown in Figure 5.40, only the H1 direction hysteresis is shown since there is no response in the H2 direction. For the bearing hysteresis in the H1 direction, all of the isolators exhibited the same behavior because they moved in phase. The displacement demand of the isolator depends on the bearing yield force; with a smaller yield force, the displacement demand will be larger. Overall the displacement demand was around 127 mm (5 in.), which is similar to the response determined from seismic analysis.

A comparison between the isolator displacement and the other loading cases including torsion effects shows that although the loading function is the same, the bearing displacement demand was significantly smaller without the torsional response. The bearing displacement orbit is shown in the second plot in Figure 5.40. Clearly, only translation in the H1 direction is recorded for the isolator movement since there is no torsion to introduce the movement in the H2 direction.

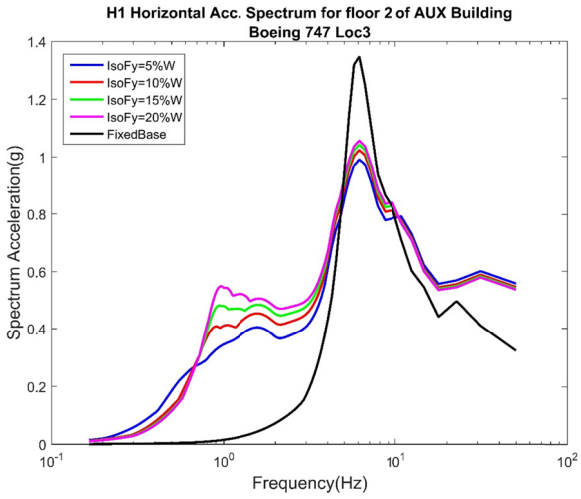

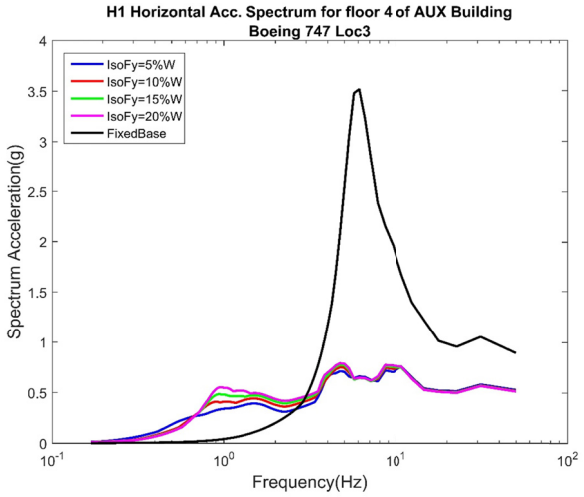

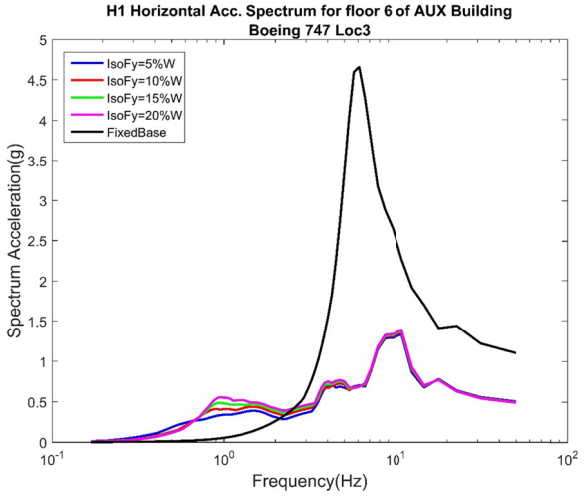

Figure 5.36 **Floor acceleration spectra for the auxiliary building in the H1 direction. Impact Scenario 6 (Boeing-747 at location 3): fixed-base and base-isolated cases with different F_y ($K_{initial}$ = 10 $K_{postyield}$ and T_{iso} = 3 sec).**

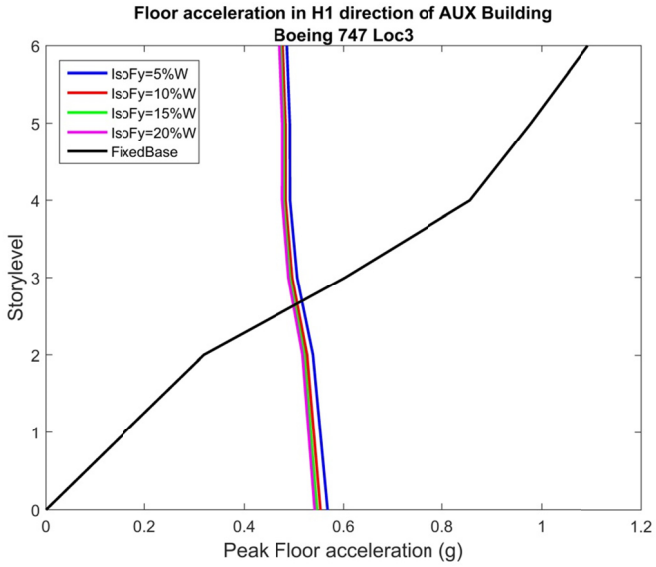

Figure 5.37 **Peak floor acceleration responses along height of the auxiliary building. Impact Scenario 6 (Boeing-747 at location 3): fixed-base and base-isolated cases with different F_y ($K_{initial}$ = 10 $K_{postyield}$ and T_{iso} = 3 sec).**

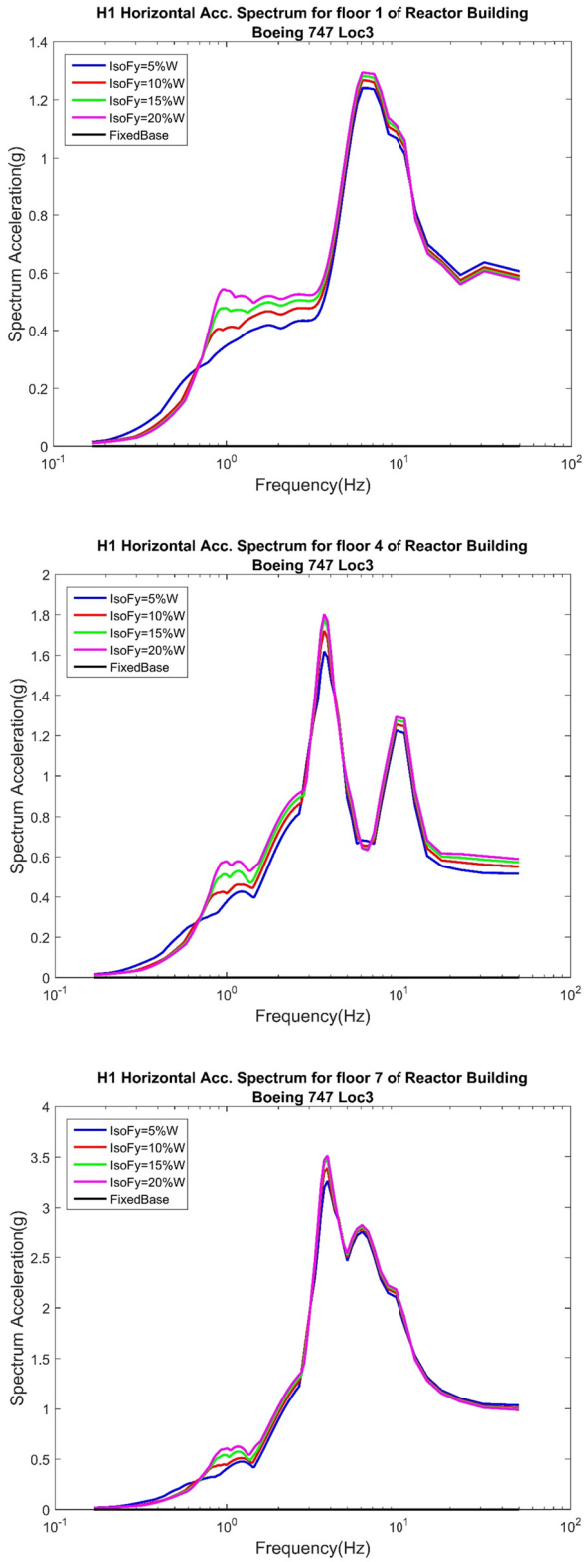

Figure 5.38 **Floor acceleration spectra for the reactor containment building in the H1 direction. Impact Scenario 6 (Boeing-747 at location 3): fixed-base and base-isolated cases with different F_y ($K_{initial}$ = 10 $K_{postyield}$ and T_{iso} = 3 sec).**

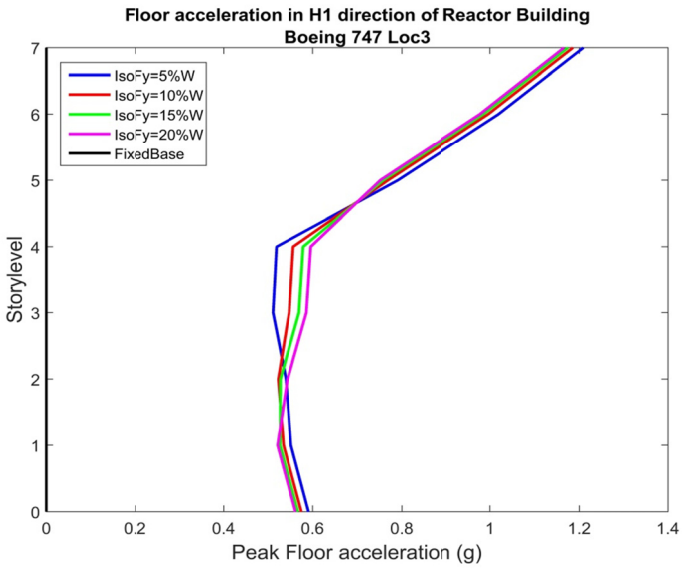

Figure 5.39 **Peak floor acceleration along height of the reactor containment building. Impact Scenario 6 (Boeing-747 at location 3): fixed-base and base-isolated cases with different F_y ($K_{initial}$ = 10 $K_{postyield}$ and T_{iso} = 3 sec).**

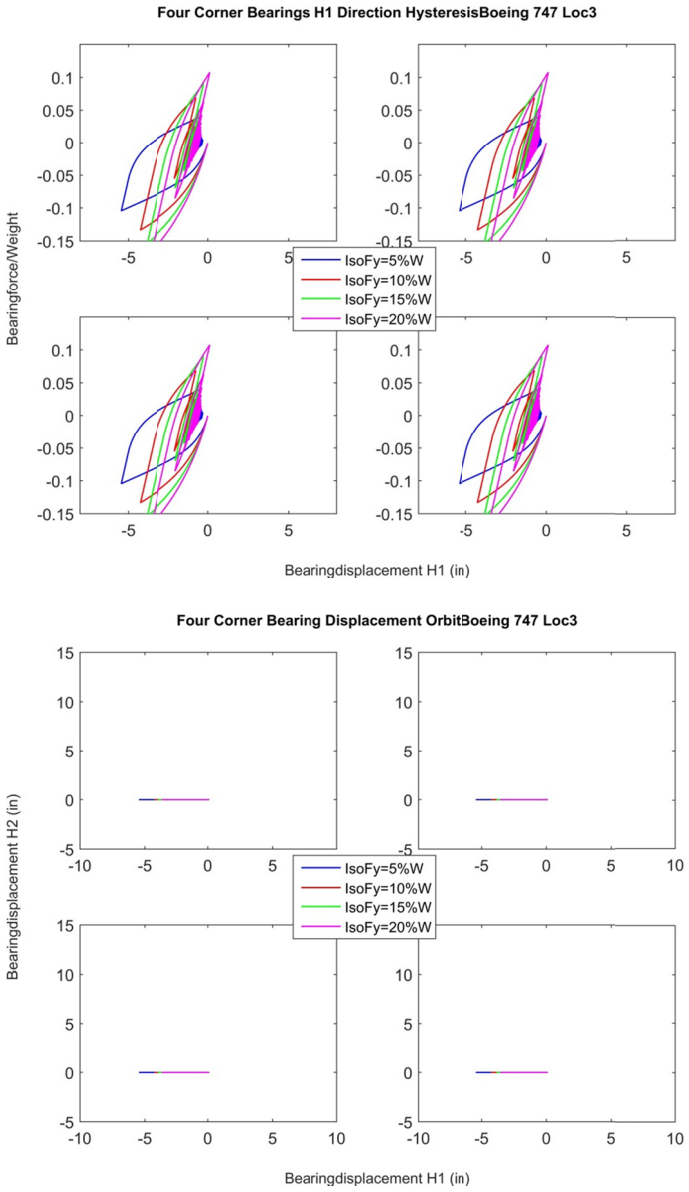

Figure 5.40 **Hysteretic loops and displacement orbits for the four corner bearings in the PGSFR. Impact Scenario 6 (Boeing-747 at location 3): fixed-base and base-isolated cases with different F_y ($K_{initial}$ = 10 $K_{postyield}$ and T_{iso} = 3 sec).**

5.4.3.3 Conclusions Regarding the Effect of Different F_y

This part of the parametric study considered the effect of different bearing yield strengths. Only Impact Scenario 6 was examined, where no torsional response developed.

- The floor acceleration spectrum for the AUX and the RCB were similar compared to the response under the other loading cases with the same loading function.
- The response of the RCB was larger than the AUX even without evidence of torsion.
- The dependence of response on different isolator yield forces was small for the acceleration response of the two buildings even though the smaller yield force of bearing resulted in larger bearing displacement demands. The peak bearing displacement demand was around 127 mm (5 in.). This is larger than that required to withstand the SSE.

5.5 SENSITIVITY OF RESPONSES TO IMPACT LOADING CONDITIONS

The response of isolated PGSFR due to aircraft impact under different loading conditions was investigated, with a particular focus on the response due to different aircraft speeds and different loading-function shapes.

5.5.1 Sensitivity of Responses to Change of Impact Velocity

First, the response of the base-isolated PGSFR model under aircraft impact of a Boeing-747-400 at different flying speeds was investigated and the results compared. For the different loading cases considered, the aircraft weight and length were kept the same but with different impact velocity; the cruising speeds were varied from 20% to 110%. Using the same scale method based on Riera's loading function, the force scale and time scale were calculated. The resulting loading force curves are shown in Figure 5.41 for all cases considered.

As shown in Figure 5.41, the plane lengths were the same, but because the speeds at impact were different for each case, the loading durations varied. Note that the loading function for aircraft impact of a Boeing-747 used previously assumed the speed was 100% of the cruising speed. The impact location considered in this part of analysis is location 1 shown in Figure 5.2. The response of the isolated PGSFR under each of the aircraft impact loading scenarios was determined and the maximum response shown for each case. The response was normalized by the absolute response value at 100% cruising speed. The vertical axis of the plot shows the ratio between the response at a specific impact velocity compared to the response of the standard case of impact at 100% of cruising speed. The horizontal axis indicates different impact velocities.

The response of maximum drift and rotation of the AUX and the RCB are shown in Figure 5.42 through Figure 5.43. Note that the increase of the response was between linear and quadratic, with a linear increase as the impact velocity increased. Note that the response investigated here in Figure 5.42 and Figure 5.43 is the response for the AUX and RCB. Since the dominant frequencies of this response are similar to the fundamental frequency of the building, ~10 Hz in the model, it cannot be treated as an impulse even though the loading duration due to

aircraft impact is short. The responses amplitudes are dependent on the amplitude of loading forces determined from structural dynamics. The scaling of the force increases in a quadratic pattern with linear increasing velocity; therefore, since the response is more sensitive to the amplitude of force, a quadratic increase pattern occurs.

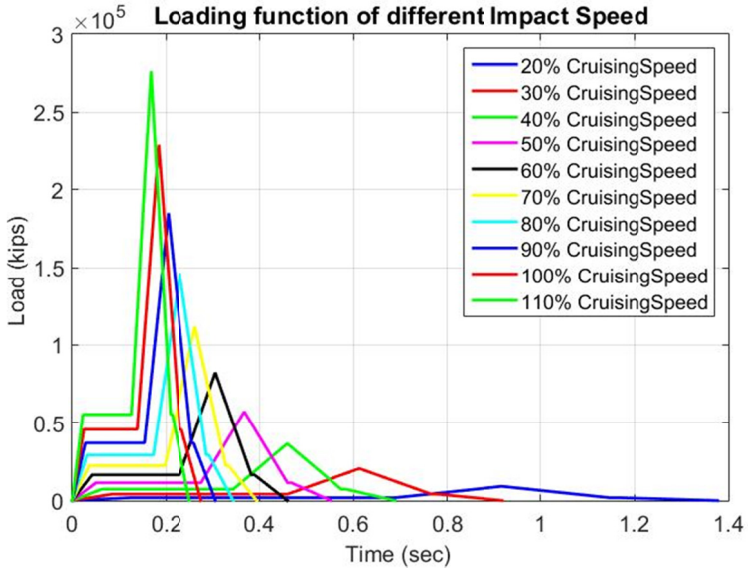

Figure 5.41 **Loading functions used for aircraft impact analysis due to Boeing-747-400 with different impact speeds.**

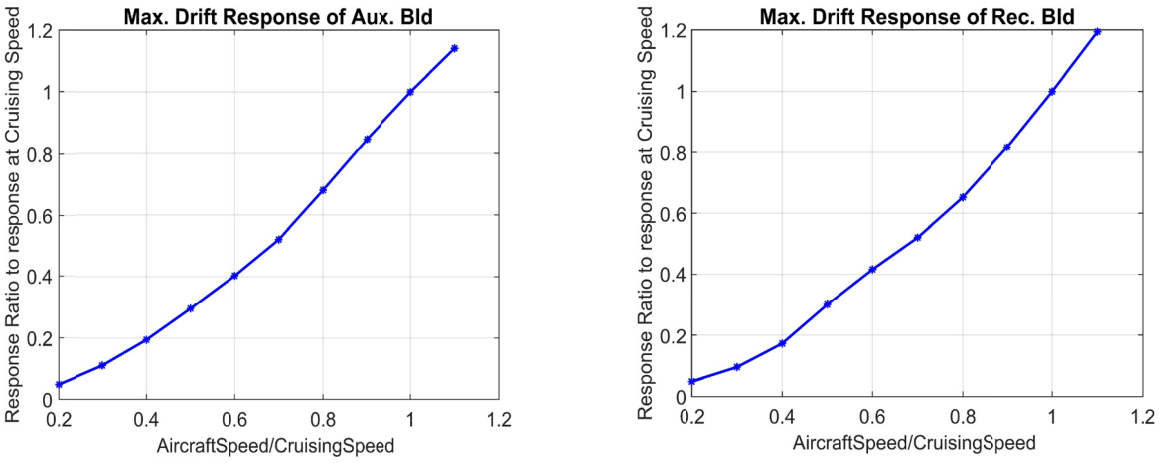

Figure 5.42 **Maximum drift ratios under different impact velocities of aircraft: (a) maximum drift response of the auxiliary building and (b) maximum drift response of the reactor containment building.**

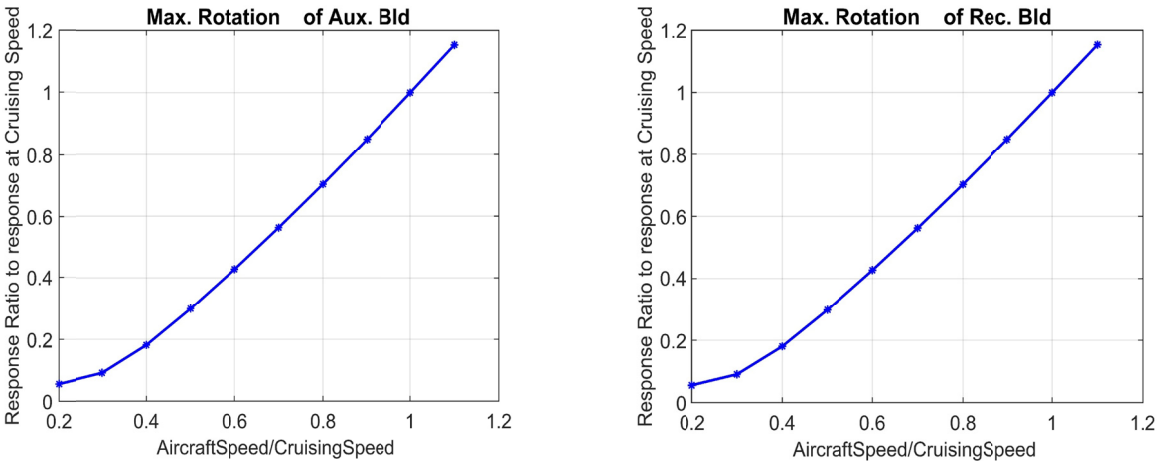

Figure 5.43 Maximum rotation responses under different impact velocities of aircraft: (a) maximum rotation response of the auxiliary building and (b) maximum rotation response of the reactor containment building.

The response of the maximum floor acceleration spectrum value of the RCB and the AUX for different frequency ranges are shown in Figure 5.44 and Figure 5.45. The top floor responses were considered here. From the results shown, the increase rate was different for the response at different frequency ranges. Peak floor acceleration around the isolation frequency range increased almost linearly; see the red line in Figure 5.44 and Figure 5.45. Note that the response at the frequency ranges of RCB and AUX fundamental frequency increased in a quadratic pattern.

The reason for the difference is the different relative scale between the response dominant frequency and the aircraft loading frequency or duration. Since the period is larger, at the isolation dominant period range the aircraft loading can be characterized as an impulse loading. Therefore, in this case, the response amplitude is sensitive to the amplitude of the loading momentum instead of the amplitude of loading force. In the scaling system used for generating loading functions for different impact speeds, the momentum scale is the same as the velocity scale. Therefore, it increases linearly with rising velocities, and the response, which is more sensitive to the momentum, shows a linearly increasing pattern.

The floor acceleration at the superstructure frequency range shows a quadratic increase pattern with linearly increasing velocity. Given that it cannot characterize the loading as an impulse because it is insensitive to the loading momentum, the response was scaled as the square of the velocity scale because of its sensitivity to the force amplitude; therefore, a quadratic increase pattern is expected and observed for the peak floor acceleration in the high-frequency range.

The isolator maximum displacement response is shown in Figure 5.45. The real response amplitude and the response amplitude ratio are plotted together in Figure 5.45. Note that the increase of the bearing displacement response was almost linear with increasing impact velocity since the response of the isolation displacement is sensitive to the isolation period, which is much larger compared to the loading duration of aircraft impact: this is consistent with the

previous conclusion. The response is more sensitive to the momentum of the loading, which increases linearly with increasing impact velocity.

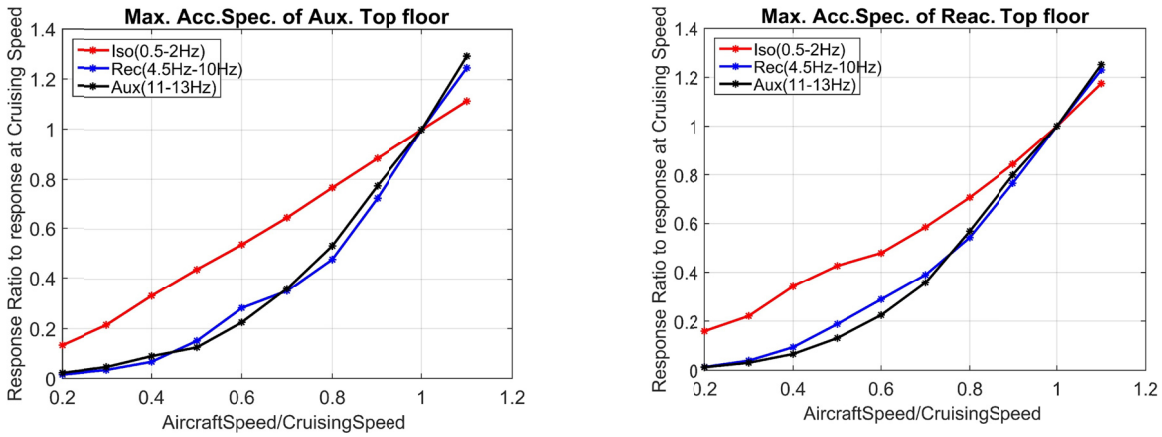

(a) (b)

Figure 5.44 Maximum top floor horizontal acceleration spectrum value for the reactor containment building and the auxiliary building under different impact velocities: (a) maximum top floor acceleration spectrum of the auxiliary building and (b) maximum top floor acceleration spectrum of the reactor containment building.

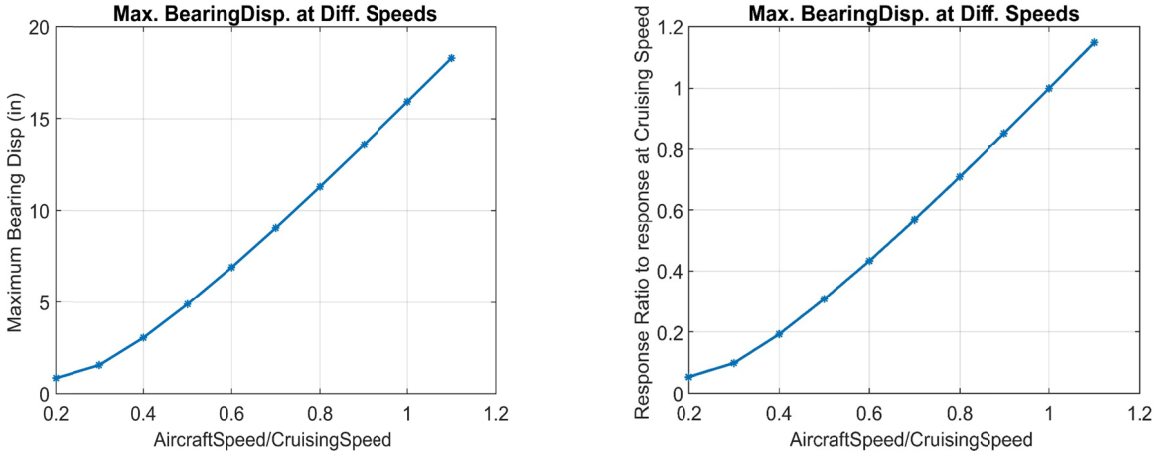

(a) (b)

Figure 5.45 Maximum isolator displacement responses at different impact velocities: (a) real displacement response amplitude and (b) normalized displacement amplitude relative to 100% cruising speed.

5.5.2 Sensitivity of Responses to Change of Loading-Function Shapes

This part of study investigated different loading-function shapes; see Figure 5.46. The loading functions were constructed so that they had the same total momentum. The original loading function for the Boeing-747 at cruising speed corresponded to loading shape number 4, represented by the red line in Figure 5.46. Then, with the same duration of loading, another two loading-function shapes—numbers 5 and 6—were constructed with rectangular and triangle loading force shapes, respectively. The areas underneath the force curve were the same compared to the original aircraft loading function, indicating that the momentum of these three loading shapes were the same. Note that the rectangular and triangle loading do not correspond to a real aircraft loading function; they are used in this part of study to examine the effect of loading shape on the response.

Besides the three loading functions described, another three loading functions were considered, which had the same loading shapes as the first three but twice the loading duration. Similarly, the force amplitudes were adjusted so that the momentums for these three loading functions remained the same as the original three.

The response of the isolated PGSFR under each of the scenarios was determined, and the maximum value of the responses discussed and compared for different loading-function shapes. First, the response of the maximum drift and rotation response of the AUX and the RCB were investigated as shown in Figure 5.47 and Figure 5.48. Note that the response characterized in these figures was the real response amplitude and not the normalized response ratio.

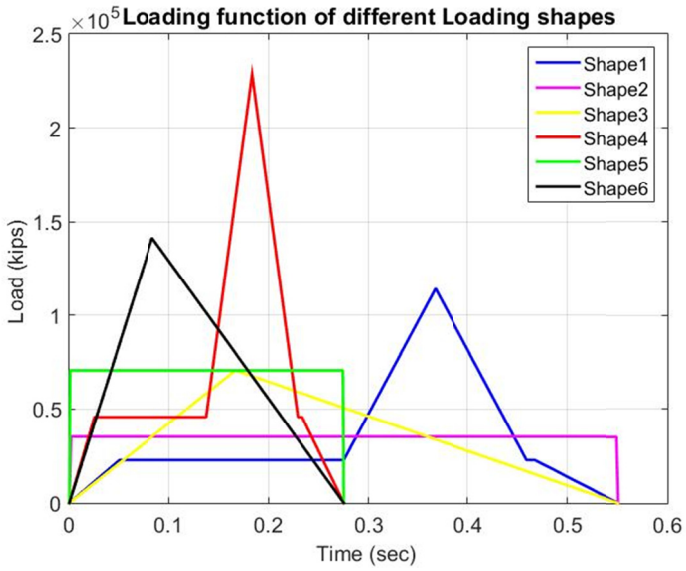

Figure 5.46 Different loading-function shapes considered in this section. All the loading functions had the same momentum value.

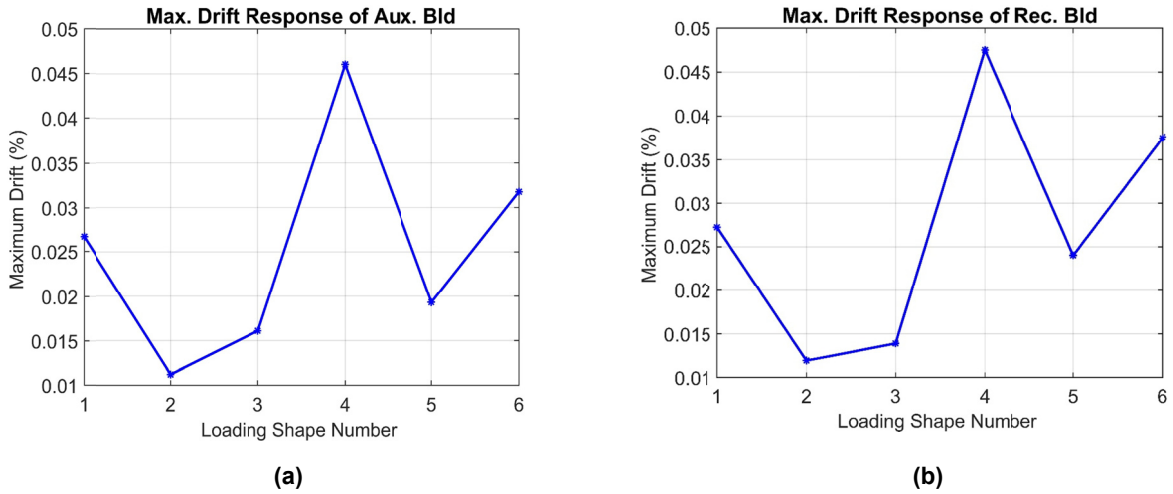

Figure 5.47 **Maximum drift response under different loading-function shapes: (a) maximum drift response of the auxiliary building and (b) maximum drift response of the reactor containment building.**

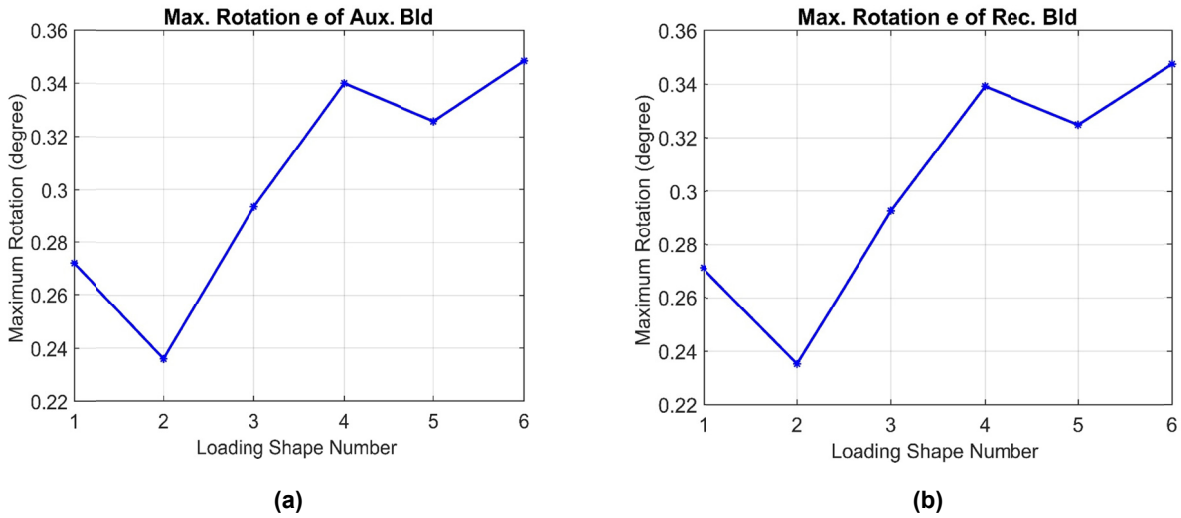

Figure 5.48 **Maximum rotation response under different loading-function shapes: (a) maximum rotation response of the auxiliary building and (b) maximum rotation response of the reactor containment building.**

The response shown in Figure 5.47 and Figure 5.48 indicates that although the loading momentums are the same for all cases, the responses are different for different loading functions. However, if we compare the relative response amplitude among the six loading scenarios and the relative loading force amplitude of the six loading functions, it is clear that the relative relations for these two are the same. For example, the maximum loading force for loading shape 4 was larger than loading shape 6, which had a triangular loading-function shape, and was larger than loading shape 5, which was rectangular in shape, and the response for loading scenario 6 was larger than Scenario 4, which was larger than loading Scenario 5. If the loading function has a

higher maximum loading force, then the response of the AUX and the RCB is larger. This is consistent with the previous conclusion, i.e., the responses of the AUX and the RCB are sensitive to the force amplitude. Although we had the same momentum for different loading-function shapes, because the force amplitudes were different, the responses in the high-frequency range were different.

The responses of the floor acceleration for the RCB and the AUX are shown in Figure 5.49. Per the previous part of the study of different impact velocities, the response at the isolation dominant period should be sensitive to the loading momentum, and the responses at the superstructure frequency range should be sensitive to the force amplitude. As shown in Figure 5.49, the floor acceleration response at the isolation period—represented by the red line—changed only slightly for different loading-function shapes since all the loading scenarios had the same loading momentum. However, for floor accelerations in the superstructure frequency range—represented by the blue and black lines—the responses varied considerably for different loading-function shapes. The relative response amplitudes for each loading shape was the same as the relative loading force amplitudes since the response at this high-frequency range is more sensitive to the loading force.

Finally, maximum isolator displacements are shown in Figure 5.50. It is clear that for loading shapes 4, 5, and 6, the amplitudes of the response are almost the same, while for the first three loading shapes the response is slightly different. Note that for loading shapes 1, 2, and 3, the loading duration is doubled and around 0.6 sec; the impulse effect is much smaller since the loading duration is approaching the effective fundamental period of the isolator. Therefore, the responses of the isolator displacement for these three loading scenarios tended to be more sensitive to the amplitude of force. For loading shapes 4, 5, and 6, the loading duration was twice as short; therefore, the loading was more like an impulse to the isolation system as the response for the isolator displacement is more sensitive to the loading momentum. Therefore, the response amplitudes of the maximum isolator displacement of loading scenarios 4, 5, and 6 were similar since the momentum of different loading shapes were the same.

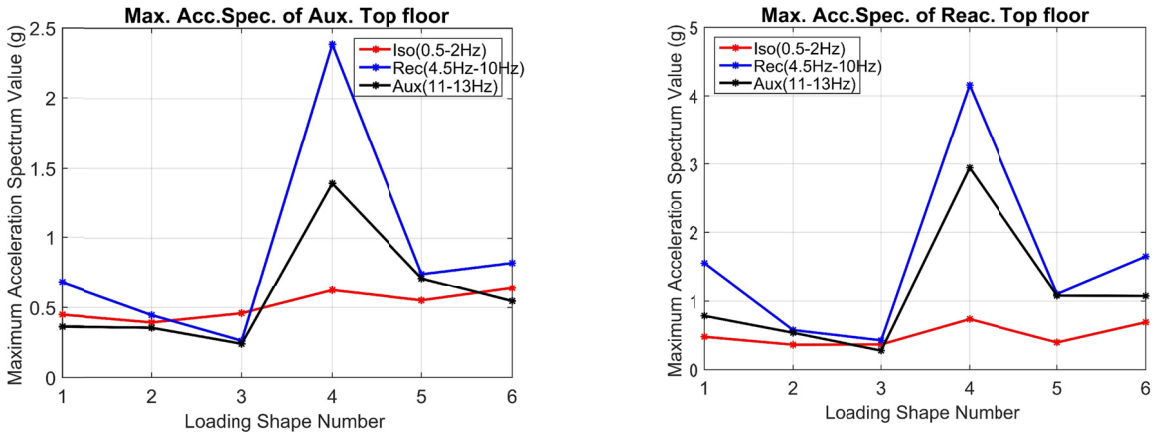

(a) (b)

Figure 5.49 Maximum top floor horizontal acceleration spectrum value for the reactor containment building and the auxiliary building under different loading-function shapes: (a) maximum top floor acceleration spectrum of the auxiliary building and (b) maximum top floor acceleration spectrum of the reactor containment building.

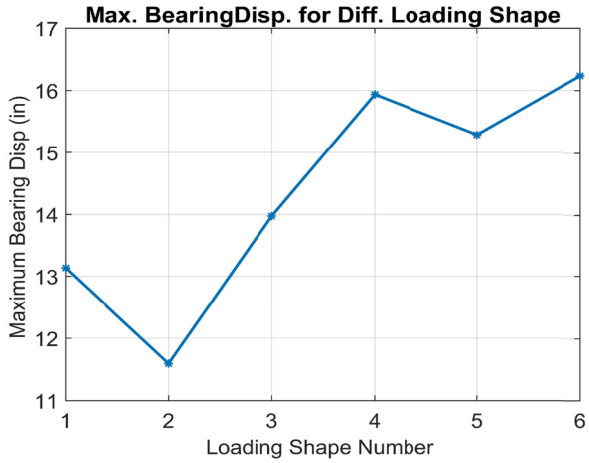

Figure 5.50 Maximum isolator displacement responses under different loading-function shapes.

5.5.3 Summary of the Sensitivity Study

For this part of analysis, the study focused on the maximum response of the isolated PGSFR under different aircraft impact loading conditions. The loading conditions for a Boeing-747-400 impacting at different speeds were considered together with different shapes of the loading functions.

Based on Riera's theory, if the impact velocity of the aircraft is linearly increasing, then the force amplitude of the resulting loading function should increase at a quadratic rate while the

total momentum of the loading increases at a linear rate. Since the loading duration is short, the response with the fundamental frequency around the isolation period, such as the total isolator displacement and the floor spectrum at the isolation dominant frequency range, will be sensitive to the momentum of the loading, and the loading can be treated as an impulse. However, the response with fundamental frequencies around the superstructure period, such as the responses of the RCB and the AUX above the isolation plane, amplitudes *are* sensitive to the maximum loading force since the loading *cannot* be treated as an impulse.

For the linearly increasing aircraft impact velocities, the isolator displacement and floor acceleration spectrum at the isolation period increased linearly, while the floor accelerations at the high-frequency range increased more or less at a quadratic rate. For different loading-function shapes with same loading momentum, the response of the isolator displacement and the floor acceleration spectrum at the isolation period range remained similar, while the amplitudes of the responses of auxiliary and RCB changed according to the maximum force amplitudes of the loading functions.

5.6 RESPONSE COMPARISON BETWEEN THE AIRCRAFT IMPACT ANALYSIS AND SEISMIC ANALYSIS

Responses under aircraft impact are compared in this section with results for seismic excitations under PGA 0.3*g* events. Comparisons were made in terms of the peak drift response, floor acceleration response, and the isolator deformation response. Both the fixed-base and the base-isolated cases were included in the comparison. For the base-isolated case, the fundamental parameter combinations used are: T_{iso} = 3 sec, F_y = 10% W, and $K_{initial}/K_{postyield}$ = 10. In this section, only aircraft impact load scenarios 1 and 4 (which correspond to a Boeing-737-900 impact and a Boeing-747-400 impact both in the H2 direction) were compared with the median response under seismic event for the PGA set at 0.3*g*.

For the fixed-base case where the aircraft impacts with the AUX, there was no effect on the RCB in the simplified model; the base was assumed to be completely rigid. The response of the AUX in the H2 direction under the Boeing-737 impact and the dynamic response under PGA 0.3*g* seismic excitation were compared. The drift responses for these conditions are shown in Figure 5.51, where the response under aircraft impact of a Boeing-737 was about one-third of that under a PGA of 0.3*g*.

In terms of the floor acceleration spectra, it is clear that the response under aircraft impact of Boeing-737 was small compared to the seismic event considered here, as shown in Figure 5.52. The shapes of the floor spectra are similar for the two loading cases, but the spectral ordinates for the AIA were smaller than for the seismic loading case. For the base-isolated case, the RCB drifts and floor spectra are compared in Figure 5.53 and Figure 5.54. Since aircraft impact on AUX also triggered a response of the RCB, one can see significant response in the RCB compared to the fixed-base case. Nonetheless, the overall response in the RCB under aircraft loading is smaller than for the seismic response (PGA 0.3*g*). For the AUX (Figure 5.55 and Figure 5.56), the story drifts near the floor where the aircraft impact occurred were slightly larger than the maximum drift response obtained from seismic condition. For the floor acceleration response in the high-frequency range, the aircraft impact loading was similar

compared to the seismic response. At the lower frequency range, the response was much smaller compared to the seismic response.

The largest isolator displacement for the aircraft impact loading is around 38 mm (1.5 in); for the seismic analysis, the median bearing displacement demand was 107 mm (4.2 in). Therefore, for the aircraft impact of the smaller-sized plane, the bearing size considered in the seismic design is adequate.

Aircraft load scenario 4 corresponds to the impact of a Boeing-747 in the H2 direction. The response to this impact is compared to the response to a seismic event having a PGA of 0.3*g*. Both fixed-base and base-isolated cases were considered. The maximum drift response is shown in Figure 5.57 for the fixed-base AUX. For the larger and faster aircraft, drift response was larger than the response to seismic excitation, although the overall drift response for both cases was relatively small.

For the floor acceleration response, the peak of the floor spectra lies around the AUX's fundamental frequency. The floor spectra for the AIA and seismic analyses are almost the same; however, because of the very short duration of the impact loading, the floor spectrum for the aircraft impact is much smaller in the low-frequency range than the seismic excitation; see Figure 5.58.

For the base-isolated cases, the RCB responses are compared in Figure 5.59 and Figure 5.60. Even if the aircraft does not directly impact the RCB, the drift response due to aircraft impact is still larger than for the seismic response. For the floor pseudo-acceleration response spectrum, the RCB has a smaller response due to aircraft impact than for seismic excitation in the low-frequency range (near the isolation period). The opposite is true in the higher frequency ranges; see Figure 5.60. For the AUX, aircraft impact also results in much higher floor acceleration responses in the higher frequency range but a smaller response at the lower frequency range; see Figure 5.62. The drift response due to the Boeing-747 aircraft impact is larger in comparison to the seismic response; see Figure 5.61.

The largest isolator displacement for the aircraft loading Case 4 is around 280 mm (11 in.), while the median bearing displacement demand for the seismic analysis is 107 mm (4.2 in.). Therefore, the demand from aircraft impact is much larger than the seismic demand. Thus, the design of the isolator is governed by the AIA for this specific case. Note: beyond DBE excitations might result in larger seismic isolator demands. These were not considered herein.

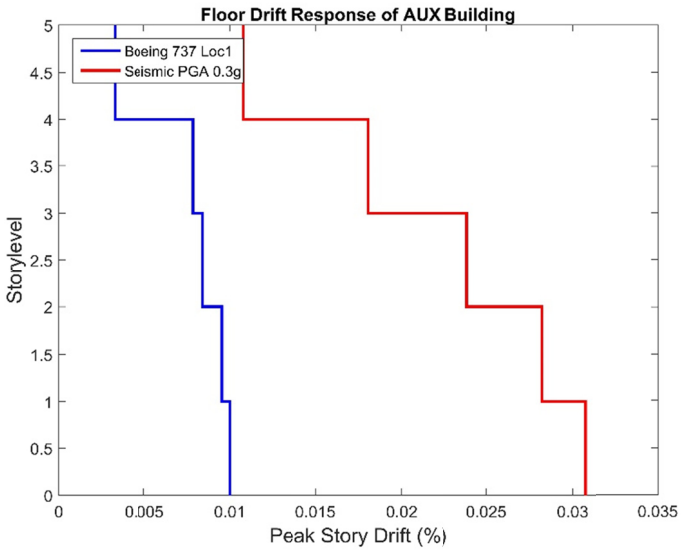

Figure 5.51 **Floor peak drift responses along height for the auxiliary building. Impact Scenario 1 (Boeing-737 at location 1) and seismic condition under the PGA 0.3*g* event; responses are for the fixed-base case.**

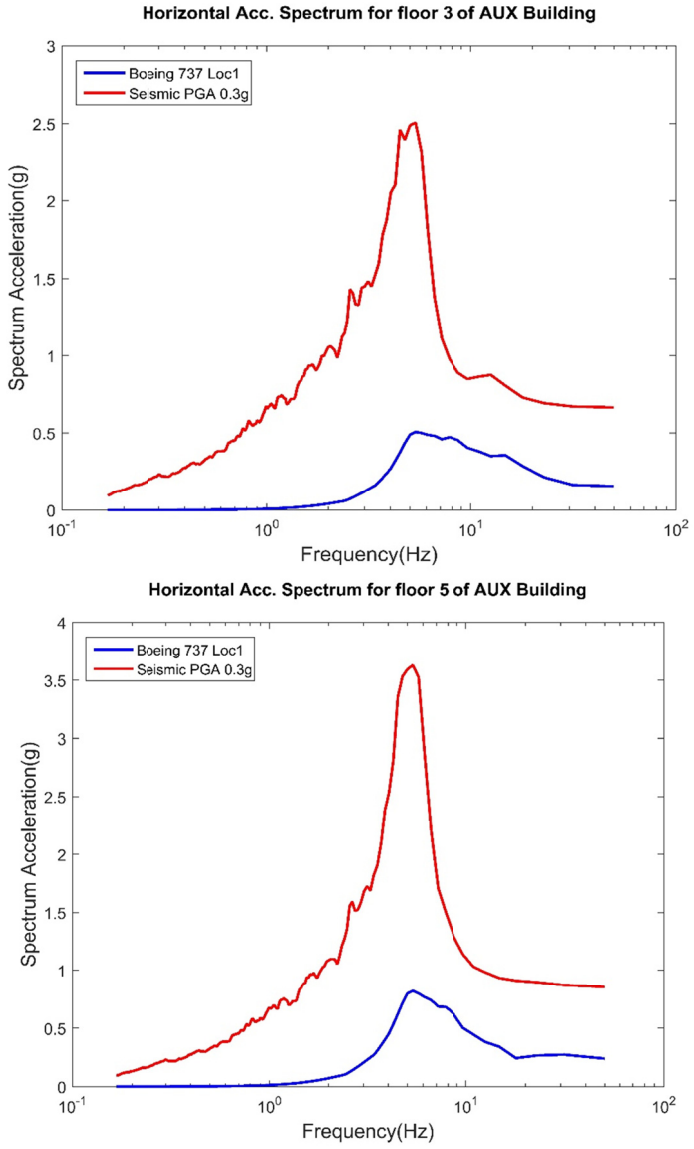

Figure 5.52 **Floor acceleration spectra for the auxiliary building. Impact Scenario 1 (Boeing-737 at Location 1) and seismic condition under PGA 0.3*g* event; responses are for the fixed-base case.**

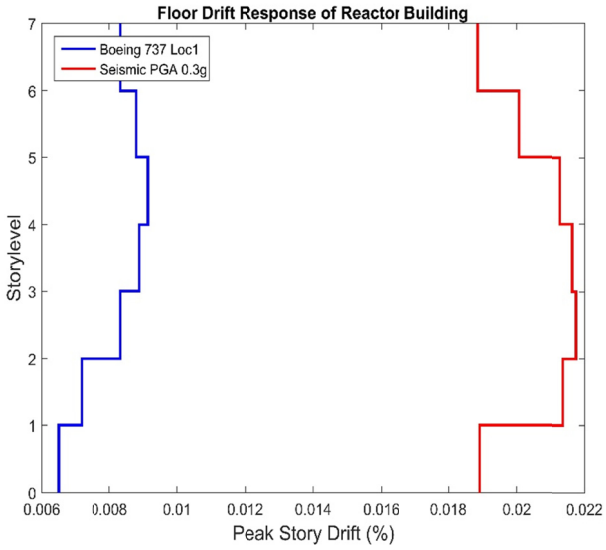

Figure 5.53 **Floor peak drift responses along height for the reactor containment building. Impact Scenario 1 (Boeing-737 at location 1) and seismic condition under PGA 0.3*g* event; responses are for the base-isolated case (F_y = 10% W, $K_{initial}$ = 10 $K_{postyield}$, and T_{iso} = 3 sec).**

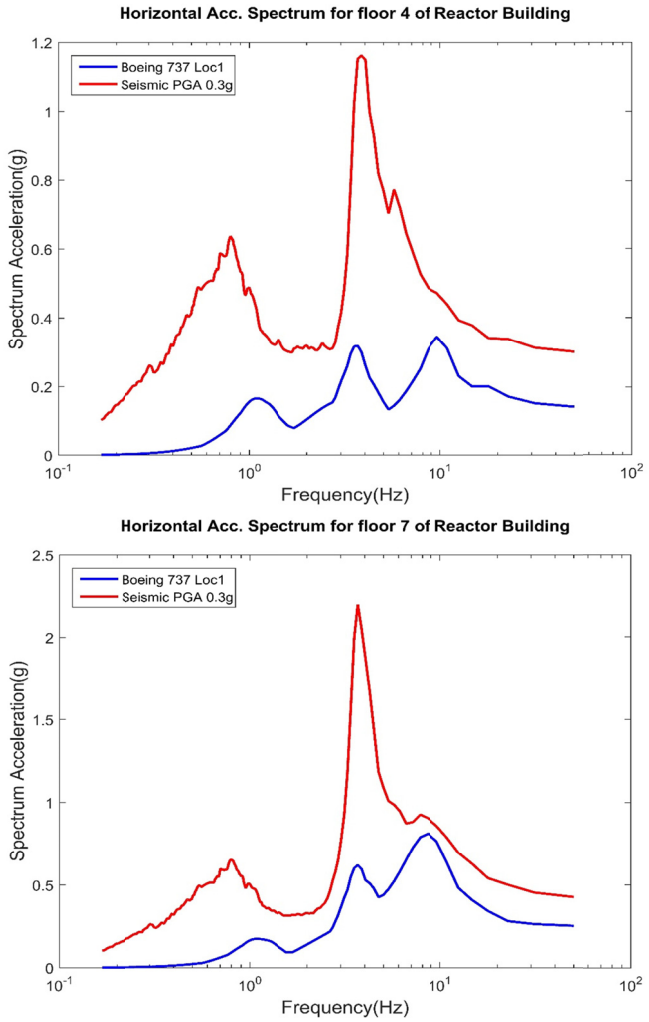

Figure 5.54 **Floor acceleration spectra for the reactor containment building. Impact Scenario 1 (Boeing-737 at location 1) and seismic condition under PGA 0.3*g* event; responses are for the base-isolated case (F_y = 10% W, $K_{initial}$ = 10 $K_{postyield}$, and T_{iso} = 3 sec).**

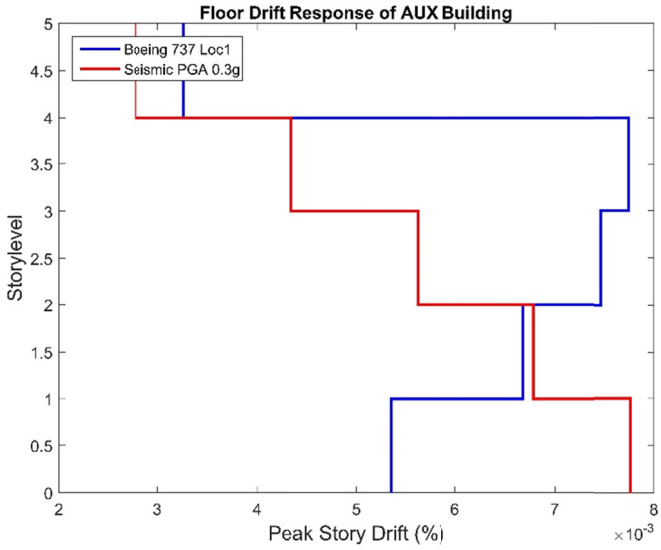

Figure 5.55 **Floor peak drift responses along height for the auxiliary building. Impact Scenario 1 (Boeing-737 at location 1) and seismic condition under PGA 0.3*g* event; responses are for the base-isolated case (F_y = 10% W, $K_{initial}$ = 10 $K_{postyield}$, and T_{iso} = 3 sec).**

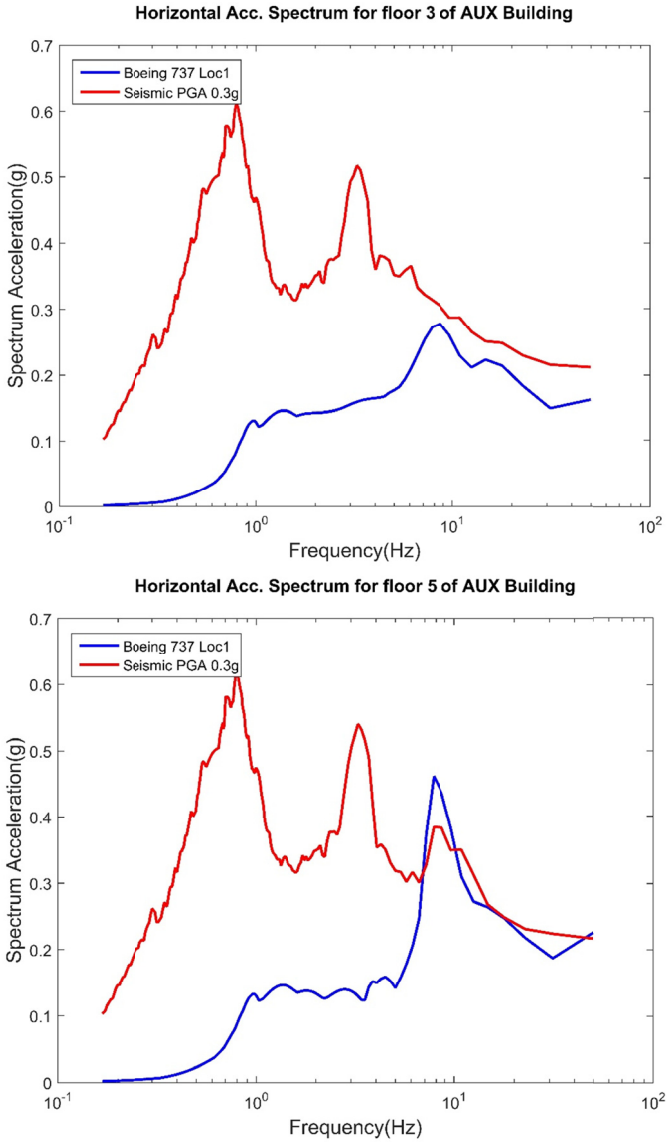

Figure 5.56 **Floor acceleration spectra for the auxiliary building. Impact Scenario 1 (Boeing-737 at location 1) and seismic condition under PGA 0.3*g* event; responses are for the base-isolated case (F_y = 10% W, $K_{initial}$ = 10 $K_{postyield}$, and T_{iso} = 3 sec).**

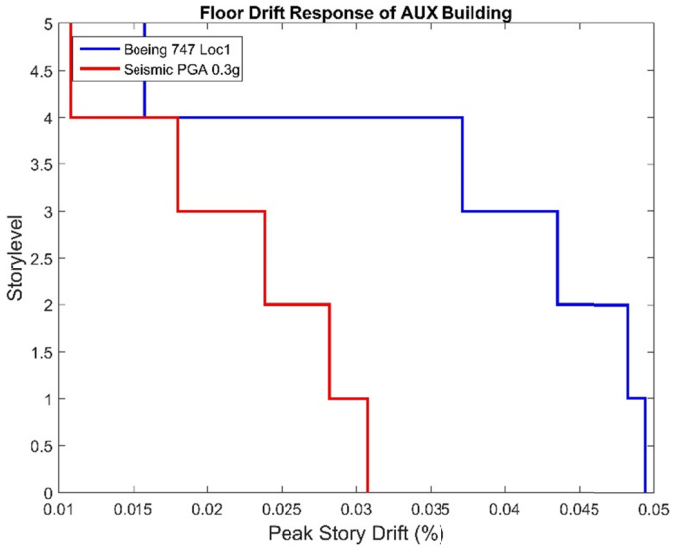

Figure 5.57 **Floor peak drift responses along height for the auxiliary building. Impact Scenario 4 (Boeing-747 at location 1) and seismic condition under PGA 0.3*g* event; responses are for the fixed-base case.**

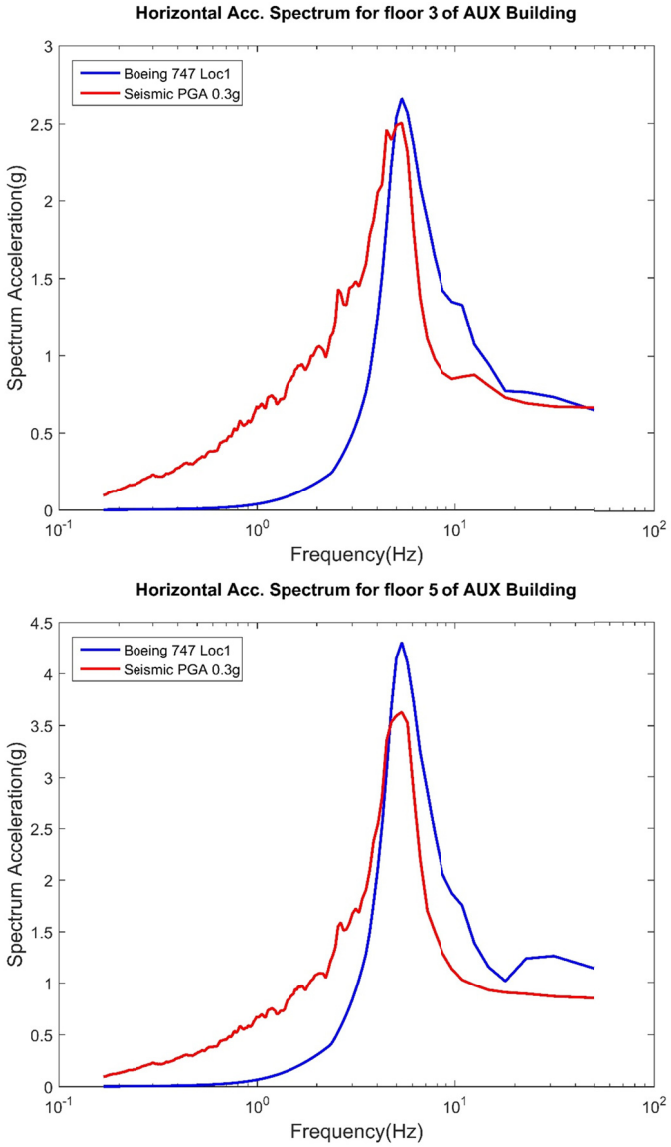

Figure 5.58 **Floor acceleration spectra for the auxiliary building. Impact Scenario 4 (Boeing-747 at location 1) and seismic condition under PGA 0.3*g* event; responses are for the fixed-base case.**

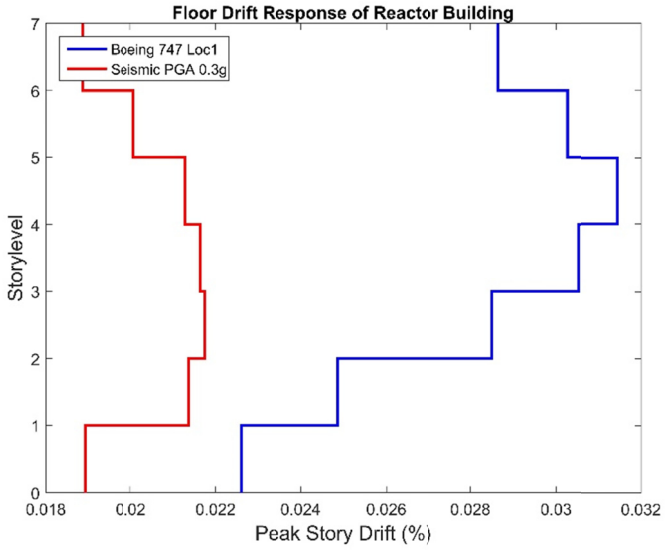

Figure 5.59 **Floor peak drift responses along height for the reactor containment building. Impact Scenario 4 (Boeing-747 at location 1) and seismic condition under PGA 0.3*g* event; responses are for the base-isolated case (F_y = 10% W, $K_{initial}$ = 10 $K_{postyield}$, and T_{iso} = 3 sec).**

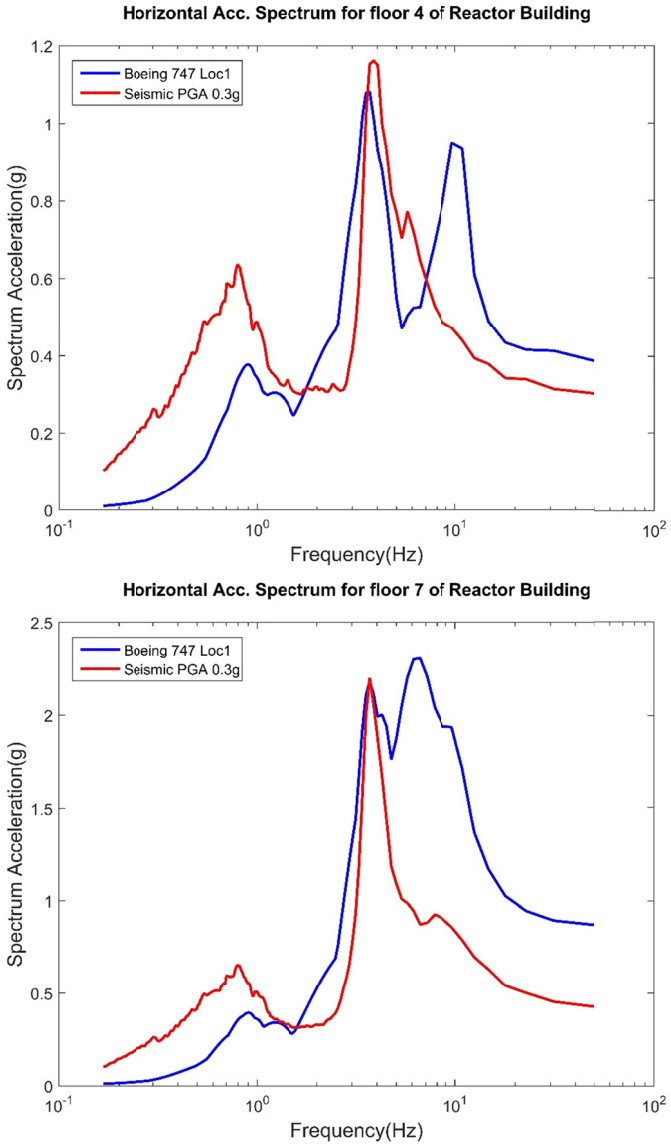

Figure 5.60 **Floor acceleration spectra for the reactor containment building. Impact Scenario 4 (Boeing-747 at location 1) and seismic condition under PGA 0.3*g* event; responses are for the base-isolated case (F_y = 10% W, $K_{initial}$ = 10 $K_{postyield}$, and T_{iso} = 3 sec).**

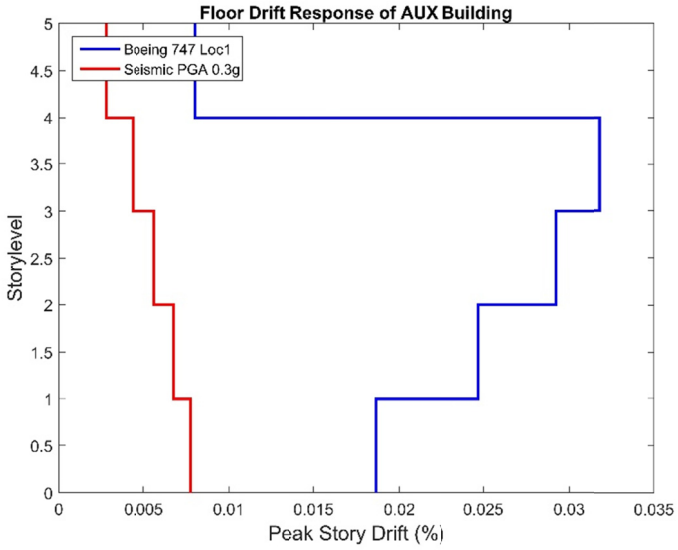

Figure 5.61 **Floor peak drift responses along height for the auxiliary building. Impact Scenario 4 (Boeing-747 at location 1) and seismic condition under PGA 0.3*g* event; responses are for the base-isolated case (F_y = 10% W, $K_{initial}$ = 10 $K_{postyield}$, and T_{iso} = 3 sec).**

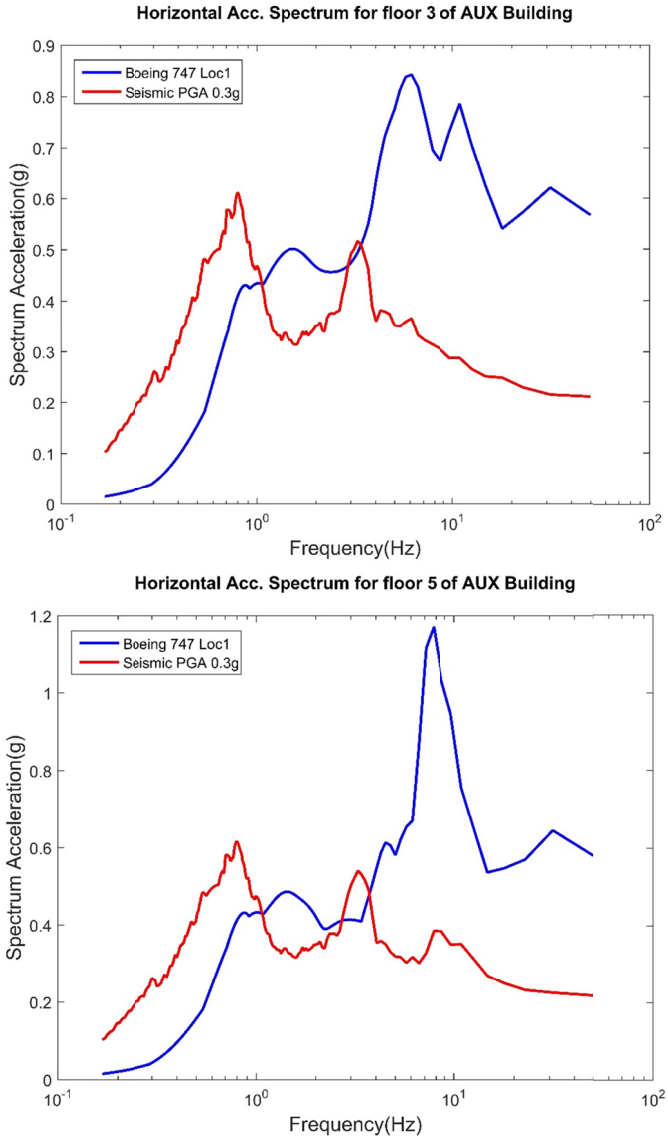

Figure 5.62 **Floor acceleration spectra for the auxiliary building. Impact Scenario 4 (Boeing-747 at location 1) and seismic condition under PGA 0.3*g* event; responses are for the base-isolated case (F_y = 10% W, $K_{initial}$ = 10 $K_{postyield}$, and T_{iso} = 3 sec).**

5.7 SUMMARY OF OBSERVATIONS AND CONCLUSIONS

In this chapter, a preliminary and simplified AIA was conducted using a fixed-base and base-isolated model of the PGSFR. Three impact locations were considered. At these locations two simplified force functions were imposed to simulate the impact of Boeing-737 and Boeing-747 planes flying at their cruising velocities. For the isolated condition, several different sets of isolation bearings were considered to explore the effect of a range of initial (elastic) bearing stiffnesses, post-yield stiffness, and the bearing yield strength. The numerical model consisted of two elastic, lumped-mass "stick" models representing the RCB and the surrounding AUX, where the RCB was idealized as being significantly offset from the center of the AUX. Detailed modeling at the location of impact was not included.

In terms of the global response of the PGSFR, the NPP is able to resist aircraft impact when the structure is seismically isolated. For the impact scenarios considered, peak bearing displacements ranged from 25 mm (1 in.) to about 300 mm (12 in.). While these beyond-design-basis events were beyond the demands posed by the postulated SSE, bearing technology exists to easily achieve these displacement demands. Moreover, current regulatory trends and considerations of subsequent siting of the PGSFR in locations of higher seismic hazard would suggest that bearing capacities greater than the median SSE demands should be provided.

The results illustrate some interesting behavior of the seismically isolated PGSFR when impacted by a large commercial aircraft. In terms of in-structure accelerations that might adversely affect sensitive equipment and components, it appears that for impact scenarios involving fast-moving heavy aircraft, the peak accelerations in the isolated AUX were significantly reduced in the upper levels and at levels where impact occurred. However, since the isolated structure tends to move as a rigid block, the lower levels in the plant also experienced roughly the same accelerations. For a conventional fixed-base facility, the floor accelerations tended to be high at the roof and zero at the base. In the isolated PGSFR, the accelerations in the AUX were nearly uniform over the height of the structure, being lower at the top and higher at the bottom compared to the fixed-base design. The isolation system was particularly effective in reducing the peaks in floor spectra that may occur near the fundamental frequency of the structure. The peaks of response spectra at upper floors of the AUX were reduced by factors up to and including five compared to the fixed-base structure.

Impact by lighter and slower moving aircraft resulted in behavior far more complex: the bearing displacements were generally quite low, and the bearings responded in what might be considered the nominal elastic range of behavior. Thus, the effectiveness of the isolation system was controlled by the initial elastic stiffness of the bearings. Nonetheless, the design of the system is likely to be controlled by the impact of heavy, fast-moving aircraft.

In the case of an idealized rigid foundation for the fixed-base PGSFR, a plane impacting the surrounding AUX did not result in any vibration of the RCB; however, because in the base-isolated PGSFR the AUX and RCB were supported on a common, seismically isolated, raft foundation, the RCB vibrated as a result of the aircraft impact with the AUX. In fact, the accelerations developed in the RCB were often significantly larger than in the AUX. This counterintuitive behavior seems to be a result of the dynamics of the current model of the RCB, which is characterized by high mass in its lower levels and a lighter and more flexible shell structure above the fourth level. As a result, the upper levels tended to amplify the acceleration

responses considerably in a manner reminiscent of a “penthouse” effect. Thus, some special design consideration may be desirable in the design of the RCB.

Drifts and other distortions of the structures above the mat level were relatively small. Significant internal forces may result, but at this point the general layouts and structural details of the PGSFR are not known well enough to justify more detailed analyses than presented herein. Note that the asymmetry of the PGSFR and the eccentricity of several of the impact scenarios resulted in substantial torsional response of the plant. These torsional movements doubled the isolator demands in some cases. Thus, various approaches for mitigating torsion by increasing the resistance of the isolation plane to torsional motion should be explored.

There is a disproportionate increase in the response of the fixed-base structure for increases in the aircraft’s weight or velocity. The isolated system was much more effective at mitigating these increases than the fixed-base structure. The isolation system was relatively effective in limiting the growth of accelerations, drifts, and other in-structure actions. That said, bearing displacements and torsional deformations may become quite large.

Some more specific observations and findings in this chapter are:

- The floor accelerations in the isolated PGSFR due to aircraft impact from Boeing-747 are similar to those resulting from the response under the design-level earthquake.
- There is a large difference in response between the impact from a Boeing-737 and a Boeing-747. The response to impact of the Boeing-747 was almost five times larger than the response to impact of the Boeing-737.
- Offset of the impact relative to the center-of-resistance of the PGSFR introduces torsional response. It is expected that the rotation for base-isolated case is on the order of 0.2°.

6 SUMMARY AND RECOMMENDATIONS FOR FUTURE RESEARCH

6.1 SUMMARY

This report presents the results of a preliminary investigation of the feasibility of seismically isolating the Prototype Gen-IV Sodium Cooled Fast Reactor (PGSFR) being designed by KEPCO Engineering and Construction Company, Inc. A series of analytical studies were carried out to assess the dynamic response of simplified models of the PGSFR to SSE-level seismic events and aircraft impacts.

The literature review in Chapter 2 discussed the work done to date that has been carried out globally to move various types of fast reactors from being theoretical concepts to commercial production facilities. The special features of fast reactors, which typically include complex equipment that is delicate and heavy, and operate at high temperatures, raise safety concerns in the event of an earthquake. For that reason, nearly all of the literature suggests that fast reactor facilities be seismically isolated.

Based on the literature, seismic isolation of these facilities is indeed feasible and desirable. However, there is no consensus currently on the best approach to seismically isolate these structures, and engineering details of how certain technical issues can be resolved for a particular plant design are not publicly available. Some designs propose isolation for the horizontal components of motion only. Other designs address the vertical components of ground motion through the use of isolator subassemblies that provide 3D isolation capabilities, or by providing separate mechanisms for horizontal and vertical isolation. There is no general agreement on the optimum type of isolator devices to be used or on the mechanical properties of the devices selected. Similarly, only a few studies have addressed regulatory concerns, including consideration of beyond-design-basis seismic events and aircraft impact.

Two relatively simple but comprehensive computational studies were undertaken to facilitate this assessment. Since few general arrangement details are currently available, the numerical models used in these studies were simplified to provide as much information as possible about the general effects of seismic isolation on the PGSFR. In keeping with the preliminary nature of this investigation, SSI effects were disregarded, the superstructure was assumed to remain elastic.

As reported in Chapter 3, a rigid body representative of the estimated weight of the PGSFR was used as part of a large parametric study that examined the effect of a wide variation

of isolator properties on seismic response. For strong and stiff structures supported on seismic isolators, the supported structure tends to respond as a rigid body. This approximation is reasonable for studies focused on the global response of the isolation system. As such, a wide range of bearing properties was investigated. These studies indicate that a wide range of seismic isolation systems is likely to be practicable for SSE-level events. Although isolator displacements for SSE events of the type considered do not require large displacement capacities and are capable of reducing seismic demands by a large amount, there are tradeoffs: weaker or softer isolators result in higher lateral displacements of the bearings, while stronger and stiffer bearings result in higher forces transmitted to the superstructure.

With that background, the second set of analyses was carried out (see Chapter 4) based on a refined, yet simplified numerical model of the PGSFR. The model consisted of traditional lumped-mass stick models for the RCB and AUX. These were developed based on current information available about the general layout of the PGSFR. The two models were in turn supported on a mat foundation. This foundation was supported on a distributed set of seismic isolators or rigidly attached to the ground (the fixed-base condition). Comparisons were made between the fixed-base model and models having an informed set of bearing modeling parameters based on the rigid body analyses of Chapter 3. These parameters represented the initial loading "elastic" stiffness, the effective yield strength, and post-yield stiffness of the bearing. Results were evaluated in terms of bearing response, the peak story drifts, peak total accelerations, floor response spectra, and peak floor level rotations about a vertical axis. Results were examined separately for the RCB and AUX.

It was found that including seismic isolation lowered substantially the seismic demands at the SSE level. The predicted demands on the seismic isolators were well within the capabilities of current isolator technologies. Story drifts and floor level accelerations were generally reduced, sometimes substantially, by the many isolation systems considered. Torsional response of the eccentric layout of the superstructure was significant. It was noted that the initial stiffness of the bearings was very important as recommended values aligned with the natural frequency of the supported structure. Fine-tuning of bearing properties, and perhaps modification of the plant layout, can optimize performance. Comparisons of floor response spectra (and other response parameters) for the isolated plant at the SSE-level excitation, with the fixed-base plant at the OBE level of excitation, indicated that in many cases isolation was able to achieve OBE-like performance when the plant was subjected to an earthquake three times larger than the OBE. Note: this was not always the case, and fine tuning of the isolation design is needed considering the specific SSCs of concern in the facility. The maximum responses for each case considered in the parametric analysis presented in Chapter 4 are summarized in Table 6.1.

Table 6.1(a) Summary of results of seismic analysis for different cases.*

Parameters considered			Max. drift (%)		Floor acceleration spectrum (Unit: *g*)					
					Reactor containment building					
					MF	MF	MF	TF	TF	TF
T_{iso} (sec)	$K_{initial}$/ $K_{posty.}$	F_y/W	Rec. Bld.	Aux. Bld.	Iso (0.5–2 Hz)	Rec (4.5–10 Hz)	Aux (11–13 Hz)	Iso (0.5–2 Hz)	Rec (4.5–10 Hz)	Aux (11–13Hz)
3	*5*	10%	0.022	0.008	0.57	0.81	0.42	0.58	1.16	0.72
3	*10*	10%	0.022	0.008	0.64	0.82	0.44	0.65	1.18	0.79
3	*100*	10%	0.026	0.009	0.75	0.85	0.57	0.90	1.31	1.03
2	10	10%	0.023	0.009	0.75	0.82	0.45	0.77	1.19	0.78
3	10	10%	0.022	0.008	0.64	0.82	0.44	0.65	1.18	0.79
4	10	10%	0.022	0.007	0.61	0.82	0.44	0.62	1.18	0.79
3	10	*5%*	0.019	0.006	0.35	0.79	0.41	0.36	1.15	0.74
3	10	*10%*	0.022	0.008	0.64	0.82	0.44	0.65	1.18	0.79
3	10	*15%*	0.022	0.009	0.82	0.83	0.46	0.84	1.20	0.81
3	10	*20%*	0.024	0.011	0.99	0.84	0.48	1.02	1.21	0.81
Fixed-base PGA 0.1*g*			0.009	0.010	0.37	0.61	0.36	0.40	1.13	0.45
Fixed-base PGA 0.3*g*			0.028	0.031	1.10	1.84	1.08	1.20	3.40	1.36

Table 6.1(b) Summary on results of seismic analysis for different cases [continuation of Table 6.1(a)].*

Parameters considered			Floor acceleration spectrum (Unit: *g*)									Bearing disp. [mm (in.)]
			Auxiliary building									
			BF	BF	BF	MF	MF	MF	TF	TF	TF	
T_{iso} (sec)	$K_{initial}$/ $K_{posty.}$	F_y/W	Iso (0.5–2 Hz)	Rec (4.5–10 Hz)	Aux (11–13 Hz)	Iso (0.5–2 Hz)	Rec (4.5–10 Hz)	Aux (11–13 Hz)	Iso (0.5–2 Hz)	Rec (4.5–10 Hz)	Aux (11–13 Hz)	
3	*5*	10%	0.56	0.51	0.30	0.56	0.38	0.29	0.56	0.39	0.35	151(5.96)
3	*10*	10%	0.61	0.52	0.31	0.61	0.37	0.29	0.62	0.38	0.35	107(4.20)
3	*100*	10%	0.64	0.76	0.49	0.69	0.42	0.37	0.72	0.57	0.44	65(2.56)
2	10	10%	0.72	0.53	0.33	0.72	0.39	0.30	0.73	0.42	0.34	101(3.99)
3	10	10%	0.61	0.52	0.31	0.61	0.37	0.29	0.62	0.38	0.35	107(4.20)
4	10	10%	0.59	0.51	0.32	0.59	0.37	0.29	0.59	0.39	0.35	113(4.47)
3	10	*5%*	0.35	0.50	0.29	0.36	0.36	0.27	0.36	0.38	0.34	133(5.23)
3	10	*10%*	0.61	0.52	0.31	0.61	0.37	0.29	0.62	0.38	0.35	107(4.20)
3	10	*15%*	0.79	0.53	0.32	0.78	0.39	0.30	0.79	0.42	0.35	97(3.84)
3	10	*20%*	0.95	0.55	0.34	0.93	0.40	0.31	0.95	0.44	0.37	92(3.61)
Fixed-base PGA 0.1*g*			0.33	0.39	0.31	0.35	0.84	0.29	0.36	1.21	0.34	NA
Fixed-base PGA 0.3*g*			1.00	1.18	0.92	1.06	2.51	0.88	1.09	3.63	1.03	NA

*MF = middle floor, TF = top floor, BF = base floor, Rec.Bld. = reactor containment building, Aux.Bld. = auxiliary building; Iso (0.5 Hz–2 Hz) = isolation frequency range, Rec (4.5 Hz–10 Hz) = reactor containment building frequency range; and Au (11 Hz–13 Hz) = auxiliary building frequency range.

Recommendations on selecting specific bearing properties were made based on the results for the seismic event level considered. For the initial bearing stiffness, a smaller value will reduce the horizontal floor acceleration spectrum at all frequency ranges. Smaller values of the post-yield stiffness and the bearing strength will reduce significantly the floor spectrum at the isolation predominate frequency range (0.5–2 Hz), but it will have little effect on the response at other frequency ranges; therefore, for seismic considerations, smaller initial stiffness, smaller bearing strength, and larger isolation period are desired as long as the resulting bearing displacement is acceptable. Since the seismic input considered in the study is fairly small, the selection of smaller parameters for the isolator will result in a reasonable bearing displacement demand.

An issue of recent regulatory concern has been the effect of aircraft impact. Few studies have been made of the effects of aircraft impact on any type of structures. While considerable work has been undertaken to analyze and design nuclear facilities to resist aircraft impact, it is prudent to carefully identify any special or new issues introduced by seismically isolating a nuclear facility such as the PGSFR. A series of numerical studies similar to those undertaken in Chapter 5 was done to assess the effect of aircraft impact on the seismically isolated PGSFR. In this preliminary study, two different planes and three impact locations were considered. As in Chapter 5, several combinations of bearing characteristics were considered, including one having different initial stiffness, yield strength, and post-yield tangent stiffness. As shown in Chapter 5, although the demands on the isolators due to the aircraft impact scenarios considered were modest, they were larger in some cases than seismic demands at the SSE level. Nonetheless, the bearing displacement demands predicted were well within the capabilities of modern bearings. Generally, no major problems were identified in this study.

Some interesting observations regarding aircraft impact on an isolated PGSFR include: (1) that for lighter, and slower moving aircraft, the response is likely to remain in the elastic range of isolator behavior, so that the initial elastic stiffness of the bearing is a more important consideration than it is for large seismic excitations; (2) the isolated plant moves as a nearly rigid body, so while the accelerations in the upper parts of the AUX are significantly reduced by isolation, accelerations in the lower part of the plant increased compared to the fixed-base PGSFR. In terms of aircraft impact, the RCB was largely shielded by the surrounding AUX and ideally would not vibrate at all if the impact occurred on the AUX. However, since the isolation system considered herein placed the RCB and AUX on a common isolated base mat, an aircraft striking the AUX would trigger strong vibrations in the RCB. Typically, the global responses of the superstructure are within the range developed under the SSE motions, so aircraft impact may not control the design. Further study is needed on this topic.

Another observation regarding aircraft impact is that off-center strikes may result in significant torsional global response of the plant. These deformations were seen to double the demands on some of the isolators. Thus, studies to assess methods to help the isolation layer resist torsional movement are desired. Although off-center aircraft impact by a heavy, fast moving aircraft was seen to lead to bearing displacements significantly larger than demands for the SSE, it is expected that aircraft impact bearing displacements may not control the design if procedures like those being considered by the U.S. NRC are followed that require isolation bearings to be able to withstand with high confidence a beyond-design-basis earthquakes without hitting a hard stop. Thus, it seems that the PGSFR concept lends itself to seismic isolation, but

continued investigations related to the specifics of the plant design and underlying technological basis are needed.

The responses for the different cases considered for the aircraft impact analyses in Chapter 5 are summarized in Table 6.2–Table 6.7. By comparing responses for different bearing properties, recommendations for bearing selection can be made relative to aircraft impact. Smaller initial stiffness, larger isolation period, and lower bearing strength will result in smaller floor acceleration spectrum for the AUX but will have little effect on the RCB—although large bearing displacement demand and rotational response will be expected. Since the bearing displacement demand under impact of a Boeing-747 considered herein is larger than the demand from seismic consideration, displacement capacity of isolator in design is controlled by aircraft impact response. In closing, in terms of either a seismic event or aircraft impact, as long as the resulting bearing displacement under the aircraft-impact evaluation is smaller than the allowable displacement capacity of bearing, a smaller initial stiffness, lower strength, and larger post-yield isolation period are recommended.

Table 6.2(a) Summary of results of aircraft impact analysis of Boeing-737 impact at location 1.*

Parameters considered			Max. drift (%)		Max. rotation (°)		Floor acceleration spectrum (Unit: *g*)					
							Reactor containment building					
							MF	MF	MF	TF	TF	TF
T_{iso} (sec)	$K_{initial}$/ $K_{posty.}$	F_y/W	Rec. Bld.	Aux. Bld.	Rec. Bld.	Aux. Bld.	Iso (0.5–2 Hz)	Rec (4.5–10 Hz)	Aux (11–13 Hz)	Iso (0.5–2 Hz)	Rec (4.5–10 Hz)	Aux (11–13Hz)
3	*5*	10%	0.009	0.008	0.044	0.045	0.14	0.34	0.30	0.14	0.81	0.64
3	*10*	10%	0.009	0.008	0.033	0.033	0.17	0.35	0.31	0.17	0.81	0.64
3	*100*	10%	0.012	0.009	0.010	0.010	0.18	0.42	0.38	0.25	0.94	0.70
2	10	10%	0.009	0.008	0.031	0.032	0.18	0.35	0.31	0.19	0.81	0.64
3	10	10%	0.009	0.008	0.033	0.033	0.17	0.35	0.31	0.17	0.81	0.64
4	10	10%	0.009	0.008	0.033	0.034	0.16	0.35	0.31	0.17	0.81	0.64
3	10	*5%*	0.009	0.008	0.038	0.038	0.13	0.34	0.31	0.14	0.81	0.64
3	10	*10%*	0.009	0.008	0.033	0.033	0.17	0.35	0.31	0.17	0.81	0.64
3	10	*15%*	0.009	0.008	0.031	0.032	0.19	0.35	0.31	0.20	0.81	0.64
3	10	*20%*	0.009	0.008	0.030	0.031	0.20	0.35	0.32	0.22	0.81	0.64
Fixed base			0.000	0.010	0.000	0.002	0.00	0.00	0.00	0.00	0.00	0.00

Table 6.2(b) Summary of results of aircraft impact analysis of Boeing-737 impact at location 1.*

Parameters considered			Floor acceleration spectrum (Unit: *g*)									Bearing disp. [mm (in.)]
			Auxiliary building									
			BF	BF	BF	MF	MF	MF	TF	TF	TF	
T_{iso} (sec)	$K_{initial}$/ $K_{posty.}$	F_y/W	Iso (0.5–2 Hz)	Rec (4.5–10 Hz)	Aux (11–13 Hz)	Iso (0.5–2 Hz)	Rec (4.5–10 Hz)	Aux (11–13 Hz)	Iso (0.5–2 Hz)	Rec (4.5–10 Hz)	Aux (11–13 Hz)	
3	*5*	10%	0.13	0.52	0.38	0.13	0.27	0.24	0.12	0.46	0.30	51(2.02)
3	*10*	10%	0.15	0.53	0.38	0.15	0.28	0.23	0.15	0.46	0.31	38(1.51)
3	*100*	10%	0.09	0.56	0.40	0.13	0.35	0.28	0.15	0.42	0.33	12(0.49)
2	10	10%	0.17	0.53	0.38	0.15	0.28	0.23	0.15	0.46	0.31	36(1.43)
3	10	10%	0.15	0.53	0.38	0.15	0.28	0.23	0.15	0.46	0.31	38(1.51)
4	10	10%	0.15	0.53	0.38	0.14	0.28	0.23	0.14	0.46	0.31	39(1.54)
3	10	*5%*	0.12	0.52	0.38	0.13	0.27	0.23	0.13	0.46	0.31	44(1.75)
3	10	*10%*	0.15	0.53	0.38	0.15	0.28	0.23	0.15	0.46	0.31	38(1.51)
3	10	*15%*	0.17	0.53	0.38	0.16	0.28	0.23	0.16	0.46	0.31	36(1.43)
3	10	*20%*	0.19	0.53	0.38	0.16	0.28	0.23	0.16	0.46	0.31	35(1.38)
Fixed base			0.00	0.00	0.00	0.04	0.51	0.38	0.07	0.82	0.45	NA

*MF = middle floor, TF = top floor, BF = base floor, Rec.Bld. = reactor containment building, Aux.Bld. = auxiliary building; Iso (0.5 Hz–2 Hz) = isolation frequency range, Rec (4.5 Hz–10 Hz) = reactor containment building frequency range; and Au (11 Hz–13 Hz) = auxiliary building frequency range.

Table 6.3(a) Summary of results of aircraft impact analysis of Boeing-737 impact at location 2.*

Parameters considered			Max. drift (%)		Max. rotation (°)		Floor acceleration spectrum (Unit: *g*)					
							Reactor containment building					
							MF	MF	MF	TF	TF	TF
T_{iso} (sec)	$K_{initial}$/ $K_{posty.}$	F_y/W	Rec. Bld.	Aux. Bld.	Rec. Bld.	Aux. Bld.	Iso (0.5–2 Hz)	Rec (4.5–10 Hz)	Aux (11–13 Hz)	Iso (0.5–2 Hz)	Rec (4.5–10 Hz)	Aux (11–13Hz)
3	*5*	10%	0.018	0.008	0.036	0.036	0.26	0.36	0.30	0.35	1.09	0.70
3	*10*	10%	0.019	0.008	0.025	0.025	0.28	0.38	0.32	0.38	1.10	0.72
3	*100*	10%	0.018	0.009	0.008	0.008	0.22	0.52	0.32	0.30	1.11	0.80
2	10	10%	0.019	0.008	0.024	0.024	0.29	0.39	0.33	0.39	1.11	0.73
3	10	10%	0.019	0.008	0.025	0.025	0.28	0.38	0.32	0.38	1.10	0.72
4	10	10%	0.019	0.008	0.025	0.026	0.28	0.38	0.32	0.37	1.10	0.72
3	10	*5%*	0.018	0.008	0.030	0.030	0.27	0.37	0.31	0.36	1.09	0.71
3	10	*10%*	0.019	0.008	0.025	0.025	0.28	0.38	0.32	0.38	1.10	0.72
3	10	*15%*	0.019	0.008	0.024	0.024	0.29	0.39	0.33	0.39	1.11	0.73
3	10	*20%*	0.020	0.008	0.023	0.023	0.30	0.39	0.33	0.39	1.12	0.73
Fixed base			0.000	0.010	0.000	0.002	0.00	0.00	0.00	0.00	0.00	0.00

Table 6.3(b) Summary of results of aircraft impact analysis of Boeing-737 impact at location 2.*

Parameters considered			Floor acceleration spectrum (Unit: *g*)									Bearing disp. [mm (in.)]
			Auxiliary building									
			BF	BF	BF	MF	MF	MF	TF	TF	TF	
T_{iso} (sec)	$K_{initial}$/ $K_{postyield.}$	F_y/W	Iso (0.5–2 Hz)	Rec (4.5–10 Hz)	Aux (11–13 Hz)	Iso (0.5–2 Hz)	Rec (4.5–10 Hz)	Aux (11–13 Hz)	Iso (0.5–2 Hz)	Rec (4.5–10 Hz)	Aux (11–13 Hz)	
3	*5*	10%	0.16	0.64	0.36	0.14	0.24	0.21	0.14	0.54	0.35	48(1.88)
3	*10*	10%	0.17	0.65	0.37	0.17	0.25	0.21	0.17	0.55	0.36	35(1.36)
3	*100*	10%	0.12	0.63	0.43	0.14	0.32	0.26	0.15	0.45	0.36	11(0.45)
2	10	10%	0.18	0.65	0.38	0.18	0.25	0.21	0.18	0.55	0.36	33(1.29)
3	10	10%	0.17	0.65	0.37	0.17	0.25	0.21	0.17	0.55	0.36	35(1.36)
4	10	10%	0.17	0.65	0.37	0.16	0.25	0.21	0.16	0.55	0.36	35(1.39)
3	10	*5%*	0.16	0.64	0.36	0.13	0.25	0.21	0.13	0.54	0.35	40(1.59)
3	10	*10%*	0.17	0.65	0.37	0.17	0.25	0.21	0.17	0.55	0.36	35(1.36)
3	10	*15%*	0.19	0.65	0.38	0.18	0.25	0.21	0.19	0.55	0.36	33(1.28)
3	10	*20%*	0.20	0.65	0.38	0.20	0.25	0.21	0.20	0.55	0.36	31(1.24)
Fixed base			0.00	0.00	0.00	0.04	0.51	0.38	0.07	0.82	0.45	NA

*MF = middle floor, TF = top floor, BF = base floor, Rec.Bld. = reactor b containment building, Aux.Bld. = auxiliary building; Iso (0.5 Hz–2 Hz) = isolation frequency range, Rec (4.5 Hz–10 Hz) = reactor containment building frequency range; and Au (11 Hz–13 Hz) = auxiliary building frequency range.

Table 6.4(a) Summary of results of aircraft impact analysis of Boeing-737 impact at location 3.*

Parameters considered			Max. drift (%)		Max. rotation (°)		Floor acceleration spectrum (Unit: *g*)					
							Reactor containment building					
							MF	MF	MF	TF	TF	TF
T_{iso} (sec)	$K_{initial}$/ $K_{postyield}$.	F_y/ W	Rec. Bld.	Aux. Bld.	Rec. Bld.	Aux. Bld.	Iso (0.5–2 Hz)	Rec (4.5–10 Hz)	Aux (11–13 Hz)	Iso (0.5–2 Hz)	Rec (4.5–10 Hz)	Aux (11–13Hz)
3	*5*	10%	0.011	0.006	0.000	0.000	0.18	0.44	0.41	0.24	0.94	0.73
3	*10*	10%	0.012	0.007	0.000	0.000	0.20	0.45	0.42	0.27	0.95	0.75
3	*100*	10%	0.013	0.007	0.000	0.000	0.18	0.48	0.38	0.25	0.93	0.75
2	10	10%	0.012	0.007	0.000	0.000	0.21	0.46	0.43	0.27	0.96	0.75
3	10	10%	0.012	0.007	0.000	0.000	0.20	0.45	0.42	0.27	0.95	0.75
4	10	10%	0.012	0.007	0.000	0.000	0.20	0.45	0.42	0.26	0.95	0.74
3	10	*5%*	0.012	0.006	0.000	0.000	0.19	0.45	0.41	0.25	0.95	0.74
3	10	*10%*	0.012	0.007	0.000	0.000	0.20	0.45	0.42	0.27	0.95	0.75
3	10	*15%*	0.012	0.007	0.000	0.000	0.21	0.46	0.43	0.27	0.96	0.75
3	10	*20%*	0.012	0.007	0.000	0.000	0.21	0.46	0.43	0.27	0.96	0.75
Fixed base			0.000	0.008	0.000	0.000	0.00	0.00	0.00	0.00	0.00	0.00

Table 6.4(b) Summary of results of aircraft impact analysis of Boeing-737 impact at location 3.*

Parameters considered			Floor acceleration spectrum (Unit: *g*)									Bearing disp. [mm (in.)]
			Auxiliary building									
			BF	BF	BF	MF	MF	MF	TF	TF	TF	
T_{iso} (sec)	$K_{initial}$/ $K_{postyield}$.	F_y/ W	Iso (0.5–2 Hz)	Rec (4.5–10 Hz)	Aux (11–13 Hz)	Iso (0.5–2 Hz)	Rec (4.5–10 Hz)	Aux (11–13 Hz)	Iso (0.5–2 Hz)	Rec (4.5–10 Hz)	Aux (11–13 Hz)	
3	*5*	10%	0.14	0.52	0.40	0.14	0.26	0.22	0.14	0.43	0.32	21(0.84)
3	*10*	10%	0.16	0.53	0.41	0.16	0.27	0.23	0.16	0.44	0.33	16(0.61)
3	*100*	10%	0.10	0.49	0.42	0.13	0.33	0.29	0.14	0.38	0.34	5(0.20)
2	10	10%	0.17	0.53	0.41	0.18	0.27	0.23	0.18	0.44	0.33	15(0.59)
3	10	10%	0.16	0.53	0.41	0.16	0.27	0.23	0.16	0.44	0.33	16(0.61)
4	10	10%	0.15	0.53	0.41	0.16	0.27	0.23	0.16	0.44	0.33	16(0.62)
3	10	*5%*	0.12	0.53	0.40	0.12	0.26	0.22	0.12	0.43	0.32	18(0.69)
3	10	*10%*	0.16	0.53	0.41	0.16	0.27	0.23	0.16	0.44	0.33	16(0.61)
3	10	*15%*	0.18	0.53	0.41	0.18	0.27	0.23	0.18	0.44	0.33	15(0.59)
3	10	*20%*	0.19	0.53	0.41	0.20	0.27	0.23	0.20	0.44	0.33	15(0.57)
Fixed base			0.00	0.00	0.00	0.03	0.55	0.39	0.06	0.87	0.51	NA

*MF = middle floor, TF = top floor, BF = base floor, Rec.Bld. = reactor containment building, Aux.Bld. = auxiliary building; Iso (0.5 Hz–2 Hz) = isolation frequency range, Rec (4.5 Hz–10 Hz) = reactor containment building frequency range; and Au (11 Hz–13 Hz) = auxiliary building frequency range.

Table 6.5(a) Summary of results of aircraft impact analysis of Boeing-747 impact at location 1.*

Parameters considered			Max. drift (%)		Max. rotation (°)		Floor acceleration spectrum (Unit: *g*)					
							Reactor containment building					
							MF	MF	MF	TF	TF	TF
T_{iso} (sec)	$K_{initial}$/ $K_{postyield}$.	F_y/ W	Rec. Bld.	Aux. Bld.	Rec. Bld.	Aux. Bld.	Iso (0.5–2 Hz)	Rec (4.5–10 Hz)	Aux (11–13 Hz)	Iso (0.5–2 Hz)	Rec (4.5–10 Hz)	Aux (11–13Hz)
3	*5*	10%	0.032	0.031	0.285	0.285	0.38	0.94	0.93	0.51	2.31	1.71
3	*10*	10%	0.031	0.032	0.239	0.240	0.38	0.95	0.94	0.53	2.31	1.72
3	*100*	10%	0.030	0.032	0.157	0.157	0.42	0.97	0.93	0.56	2.23	1.64
2	10	10%	0.031	0.032	0.197	0.198	0.47	0.97	0.95	0.56	2.31	1.72
3	10	10%	0.031	0.032	0.239	0.240	0.38	0.95	0.94	0.53	2.31	1.72
4	10	10%	0.032	0.032	0.264	0.265	0.37	0.94	0.93	0.52	2.30	1.71
3	10	*5%*	0.032	0.031	0.308	0.308	0.36	0.94	0.92	0.51	2.31	1.71
3	10	*10%*	0.031	0.032	0.239	0.240	0.38	0.95	0.94	0.53	2.31	1.72
3	10	*15%*	0.031	0.032	0.210	0.211	0.50	0.96	0.95	0.55	2.31	1.72
3	10	*20%*	0.031	0.032	0.192	0.193	0.58	0.97	0.96	0.62	2.31	1.72
Fixed Base			0.000	0.049	0.000	0.006	0.00	0.00	0.00	0.00	0.00	0.00

Table 6.5(b) Summary of results of aircraft impact analysis of Boeing-747 impact at location 1.*

Parameters considered			Floor acceleration spectrum (Unit: *g*)									Bearing disp. [mm (in.)]
			Auxiliary building									
			BF	BF	BF	MF	MF	MF	TF	TF	TF	
T_{iso} (sec)	$K_{initial}$/ $K_{postyield}$.	F_y/ W	Iso (0.5–2 Hz)	Rec (4.5–10 Hz)	Aux (11–13 Hz)	Iso (0.5–2 Hz)	Rec (4.5–10 Hz)	Aux (11–13 Hz)	Iso (0.5–2 Hz)	Rec (4.5–10 Hz)	Aux (11–13 Hz)	
3	*5*	10%	0.37	1.40	1.03	0.50	0.82	0.80	0.48	1.17	0.77	337(13.27)
3	*10*	10%	0.36	1.42	1.03	0.50	0.84	0.79	0.49	1.17	0.76	288(11.32)
3	*100*	10%	0.30	1.38	1.00	0.45	0.87	0.78	0.44	1.11	0.73	195(7.69)
2	10	10%	0.44	1.43	1.03	0.57	0.88	0.78	0.55	1.22	0.80	233(9.18)
3	10	10%	0.36	1.42	1.03	0.50	0.84	0.79	0.49	1.17	0.76	288(11.32)
4	10	10%	0.35	1.40	1.03	0.47	0.83	0.79	0.45	1.15	0.76	319(12.54)
3	10	*5%*	0.24	1.39	1.03	0.46	0.81	0.80	0.45	1.15	0.78	366(14.40)
3	10	*10%*	0.36	1.42	1.03	0.50	0.84	0.79	0.49	1.17	0.76	288(11.32)
3	10	*15%*	0.47	1.43	1.03	0.53	0.87	0.78	0.52	1.20	0.78	251(9.87)
3	10	20%	0.354	1.44	1.03	0.57	0.89	0.77	0.56	1.21	0.80	229(9.01)
Fixed base			0.00	0.00	0.00	0.18	2.66	1.33	0.31	4.31	1.75	NA

*MF = middle floor, TF = top floor, BF = base floor, Rec.Bld. = reactor containment building, Aux.Bld. = auxiliary building; Iso (0.5 Hz–2 Hz) = isolation frequency range, Rec (4.5 Hz–10 Hz) = reactor containment building frequency range; and Au (11 Hz–13 Hz) = auxiliary building frequency range.

Table 6.6(a) Summary of results of aircraft impact analysis of Boeing-747 impact at location 2.*

Parameters considered			Max. drift (%)		Max. rotation (°)		Floor acceleration spectrum (Unit: *g*)					
							Reactor containment building					
							MF	MF	MF	TF	TF	TF
T_{iso} (sec)	$K_{initial}$/ $K_{postyield}$	F_y/W	Rec. Bld.	Aux. Bld.	Rec. Bld.	Aux. Bld.	Iso (0.5–2 Hz)	Rec (4.5–10 Hz)	Aux (11–13 Hz)	Iso (0.5–2 Hz)	Rec (4.5–10 Hz)	Aux (11–13Hz)
3	*5*	10%	0.032	0.031	0.285	0.285	0.38	0.94	0.93	0.51	2.31	1.71
3	*10*	10%	0.031	0.032	0.239	0.240	0.38	0.95	0.94	0.53	2.31	1.72
3	*100*	10%	0.030	0.032	0.157	0.157	0.42	0.97	0.93	0.56	2.23	1.64
2	10	10%	0.031	0.032	0.197	0.198	0.47	0.97	0.95	0.56	2.31	1.72
3	10	10%	0.031	0.032	0.239	0.240	0.38	0.95	0.94	0.53	2.31	1.72
4	10	10%	0.032	0.032	0.264	0.265	0.37	0.94	0.93	0.52	2.30	1.71
3	10	*5%*	0.032	0.031	0.308	0.308	0.36	0.94	0.92	0.51	2.31	1.71
3	10	*10%*	0.031	0.032	0.239	0.240	0.38	0.95	0.94	0.53	2.31	1.72
3	10	*15%*	0.031	0.032	0.210	0.211	0.50	0.96	0.95	0.55	2.31	1.72
3	10	*20%*	0.031	0.032	0.192	0.193	0.58	0.97	0.96	0.62	2.31	1.72
Fixed Base			0.000	0.049	0.000	0.006	0.00	0.00	0.00	0.00	0.00	0.00

Table 6.6(b) Summary of results of aircraft impact analysis of Boeing-747 impact at location 2.*

Parameters considered			Floor acceleration spectrum (Unit: *g*)									Bearing disp. [mm (in.)]
			Auxiliary building									
			BF	BF	BF	MF	MF	MF	TF	TF	TF	
T_{iso} (sec)	$K_{initial}$/ $K_{postyield}$	F_y/W	Iso (0.5–2 Hz)	Rec (4.5–10 Hz)	Aux (11–13 Hz)	Iso (0.5–2 Hz)	Rec (4.5–10 Hz)	Aux (11–13 Hz)	Iso (0.5–2 Hz)	Rec (4.5–10 Hz)	Aux (11–13 Hz)	
3	***5***	**10%**	0.61	1.91	1.02	0.40	0.79	0.72	0.40	1.28	0.83	310(12.20)
3	***10***	**10%**	0.60	1.89	1.04	0.39	0.82	0.71	0.39	1.27	0.81	264(10.40)
3	***100***	**10%**	0.52	1.76	1.04	0.37	0.87	0.70	0.35	1.16	0.81	177(6.98)
2	**10**	**10%**	0.68	1.93	1.07	0.48	0.84	0.71	0.48	1.29	0.83	215(8.45)
3	**10**	**10%**	0.60	1.89	1.04	0.39	0.82	0.71	0.39	1.27	0.81	264(10.40)
4	**10**	**10%**	0.57	1.87	1.02	0.38	0.81	0.71	0.38	1.26	0.82	287(11.32)
3	**10**	***5%***	0.56	1.87	1.02	0.35	0.79	0.72	0.34	1.27	0.84	332(13.08)
3	**10**	***10%***	0.60	1.89	1.04	0.39	0.82	0.71	0.39	1.27	0.81	264(10.40)
3	**10**	***15%***	0.64	1.90	1.06	0.49	0.83	0.71	0.49	1.27	0.82	232(9.11)
3	**10**	***20%***	0.66	1.91	1.08	0.57	0.85	0.70	0.57	1.28	0.83	209(8.25)
Fixed Base			0.00	0.00	0.00	0.18	2.66	1.33	0.31	4.31	1.75	NA

*MF = middle floor, TF = top floor, BF = base floor, Rec.Bld. = reactor containment building, Aux.Bld. = auxiliary building; Iso (0.5 Hz–2 Hz) = isolation frequency range, Rec (4.5 Hz–10 Hz) = reactor containment building frequency range; and Au (11 Hz–13 Hz) = auxiliary building frequency range.

Table 6.7(a) Summary of results of aircraft impact analysis of Boeing-747 impact at location 3.*

Parameters considered			Max. drift (%)		Max. rotation (°)		Floor acceleration spectrum (Unit: *g*)					
							Reactor containment building					
							MF	MF	MF	TF	TF	TF
T_{iso} (sec)	$K_{initial}$/ $K_{postyield}$	F_y/ W	Rec. Bld.	Aux. Bld.	Rec. Bld.	Aux. Bld.	Iso (0.5–2 Hz)	Rec (4.5–10 Hz)	Aux (11–13 Hz)	Iso (0.5–2 Hz)	Rec (4.5–10 Hz)	Aux (11–13Hz)
3	*5*	10%	0.038	0.024	0.000	0.000	0.71	1.24	1.23	0.95	2.78	1.84
3	*10*	10%	0.040	0.025	0.000	0.000	0.72	1.26	1.25	0.96	2.79	1.87
3	*100*	10%	0.040	0.026	0.000	0.000	0.64	1.29	1.24	0.86	2.80	1.85
2	10	10%	0.042	0.025	0.000	0.000	0.78	1.29	1.28	1.02	2.82	1.90
3	10	10%	0.040	0.025	0.000	0.000	0.72	1.26	1.25	0.96	2.79	1.87
4	10	10%	0.039	0.025	0.000	0.000	0.70	1.25	1.24	0.94	2.78	1.86
3	10	*5%*	0.038	0.024	0.000	0.000	0.67	1.23	1.21	0.90	2.76	1.83
3	10	*10%*	0.040	0.025	0.000	0.000	0.72	1.26	1.25	0.96	2.79	1.87
3	10	*15%*	0.041	0.025	0.000	0.000	0.76	1.28	1.27	1.00	2.81	1.89
3	10	*20%*	0.043	0.025	0.000	0.000	0.79	1.29	1.29	1.03	2.83	1.91
Fixed Base			0.000	0.041	0.000	0.000	0.00	0.00	0.00	0.00	0.00	0.00

Table 6.7(b) Summary of results of aircraft impact analysis of Boeing-747 impact at location 3.*

Parameters considered			Floor acceleration spectrum (Unit: *g*)									Bearing disp. [mm (in.)]
			Auxiliary building									
			BF	BF	BF	MF	MF	MF	TF	TF	TF	
T_{iso} (sec)	$K_{initial}$/ $K_{postyield}$	F_y/ W	Iso (0.5–2 Hz)	Rec (4.5–10 Hz)	Aux (11–13 Hz)	Iso (0.5–2 Hz)	Rec (4.5–10 Hz)	Aux (11–13 Hz)	Iso (0.5–2 Hz)	Rec (4.5–10 Hz)	Aux (11–13 Hz)	
3	*5*	10%	0.46	1.25	1.02	0.44	0.80	0.76	0.43	0.95	0.86	133(5.22)
3	*10*	10%	0.47	1.27	1.04	0.45	0.81	0.74	0.44	0.96	0.88	108(4.26)
3	*100*	10%	0.42	1.29	1.08	0.42	0.85	0.70	0.41	1.00	0.90	59(2.32)
2	10	10%	0.52	1.29	1.05	0.50	0.85	0.74	0.49	0.99	0.90	95(3.74)
3	10	10%	0.47	1.27	1.04	0.45	0.81	0.74	0.44	0.96	0.88	108(4.26)
4	10	10%	0.45	1.26	1.03	0.43	0.81	0.74	0.42	0.95	0.87	114(4.49)
3	10	*5%*	0.42	1.24	1.01	0.40	0.78	0.75	0.39	0.94	0.85	138(5.44)
3	10	*10%*	0.47	1.27	1.04	0.45	0.81	0.74	0.44	0.96	0.88	108(4.26)
3	10	*15%*	0.50	1.28	1.05	0.48	0.83	0.74	0.49	0.98	0.89	98(3.84)
3	10	*20%*	0.54	1.29	1.06	0.55	0.85	0.73	0.56	0.99	0.91	91(3.58)
Fixed Base			0.00	0.00	0.00	0.14	2.51	1.27	0.24	4.04	1.81	NA

*MF = middle floor, TF = top floor, BF = base floor, Rec.Bld. = reactor containment building, Aux.Bld. = auxiliary building; Iso (0.5 Hz–2 Hz) = isolation frequency range, Rec (4.5 Hz–10 Hz) = reactor containment building frequency range; and Au (11 Hz–13 Hz) = auxiliary building frequency range..

6.2 RECOMMENDATIONS FOR FUTURE RESEARCH

To design a cost-effective and efficient design for the PGSFR with the desired margin of safety, additional research and development is needed. Both simple and more refined studies are recommended. An extension of the simple studies presented herein will help identify optimal isolation strategies in terms of geometry, location, type of isolation system, etc., for the PGSFR. More refined studies and analytical models will help fine tune design strategies and develop simplified design and analysis methods. More detailed performance-based design studies can identify the economic as well as performance benefits of various design alternatives, and formal probabilistic risk assessments would be useful in obtaining licensing approval from regulatory agencies. Some specific recommendations are offered below for future research.

The studies presented herein and nearly all of the literature on fast reactors has been based on rigid-base conditions without consideration of soil. This is likely conservative in terms of the demands on the isolation system and response of the superstructure. But as shown previously in studies by the UC Berkeley research team, embedment and SSI can substantially reduce the demands on a fixed-base and seismically isolated plant. Thus, SSI for many sites of interest may reduce the demands sufficiently that seismic isolation may not be necessary. However, when considering a beyond-design-basis event, seismic isolation is likely still quite beneficial. Prior studies have shown that the sensitivities of response to soil conditions are greatly reduced by using seismic isolation. This is an important motivation for using seismic isolation when the plant design is being considered at many sites with different seismic hazard and soil conditions. Given the sensitivity of the PGSFR to seismic motions, SSI analyses should be an integral part of any research plan.

Because many of the systems and components used in a sodium-cooled fast reactor have not been tested under earthquake or other dynamic conditions, analyses and tests to develop data that can be used validate analytical models and develop fragility models may be desirable, in particular, assessing the dynamic behavior of thin walled vessels and piping systems at elevated temperatures.

Currently, little information is available about the expected performance of various SSCs and suitable acceptance criteria. This report presented comparisons between the response of a fixed-base plant versus a comparable base-isolated plant to several different scenarios. Although such results are useful, this approach is very limited since the facility is in its preliminary design phase. That said, incorporating isolation in the design phase can be used to avoid problems and issues that may be difficult to overcome with a fixed-base plant.

Thus, work to identify quantitative performance goals and acceptance criteria are essential. In the U.S., non-nuclear buildings designed according to performance-based design procedures permitted by current building codes need to develop a basis of design. Such a document would be useful in developing efficient and effective isolation strategies for the PGSFR. This effort might simply be a review of the seismic design component of a Preliminary Safety Information Document (PSID).

6.2.1 Seismic Hazard Characterization

These preliminary studies have been based on a large set of three-component ground-motion records spectrally matched to the US NRC RegGuide 1.60 spectrum anchored to a PGA of 0.3*g*. Although these studies provided useful information, it is not clear whether this is the appropriate SSE spectrum for use with the PGSFR; several other earthquake conditions should be evaluated, i.e., as a licensing strategy is developed, a particular SSE spectrum for design may be developed. This might result in a different spectral shape, one that is more appropriate for anticipated locations of the PGSFR or anchored at a different PGA.

Similarly, other spectra representative of different hazard levels should be considered. Two other levels should be considered as a minimum. The first of these would be for a beyond-design-basis seismic event. The U.S. NRC is developing guidance on the selection of extended ground-motion response spectra for defining such events, but Korea and other countries where the PGSFR might be located may require different definitions. The U.S. NRC is likely to require a probabilistic estimate of the peak bearing displacement; therefore, studies using spectrum compatible motions and appropriately selected motions considering the median target spectrum and the expected dispersion of spectral ordinates about the median should be studied to quantify bearing displacement capacities.

Although seismic isolation is very effective for high levels of seismic excitation, strong and stiff isolators may not be very effective at lower levels of excitation. Thus, studies may be warranted that consider earthquake excitations representative of an OBE. These are not likely to affect the safety of the NPP, but studies based on these motions might help avoid the need to stop a plant for inspection; i.e., the OBE event might be raised if floor spectra and stresses in components and systems are small enough.

For all hazard levels, it is likely that the vertical component of motion is very important. These motions will be critical in assessing the need for vertical isolation of the PGSFR. The traditional U.S. NRC RegGuide 1.60 anchors the vertical target spectrum to two-thirds of the horizontal spectrum. Recent research at PEER and elsewhere indicates that the two-thirds value is perhaps too conservative for many sites located at moderate to long distances from many earthquakes. Thus, some studies of selecting and modifying ground motions to represent the vertical component of motion are desired.

6.2.2 Aircraft Impact Characterization and Parametric Studies

This report described two simplified models that were developed to simulate force time histories representative of impacts by Boeing-737 and 747 aircraft. These models were adapted considering dynamic similitude considerations based on a much lighter and slower Boeing-707 developed by Riera [1968]. The variation observed in parametric studies and importance of this loading scenario suggests that improved force time histories are needed. In particular, the Boeing-747 aircraft considered in this study is not the largest plane flying today, and our assumption of the plane flying at its cruising velocity is not the most conservative assumption. Aircraft impact models are available from various regulatory agencies and industry associations, and the models used should be consistent with those standards. Understandably, these models are not publicly available.

In addition, Riera's models are based on a number of simplifying assumptions. For this study, one of the key assumptions was the rigidity of the structure being struck by the aircraft. With an isolated structure, this assumption is no longer entirely valid. Some literature exists related to the use uncoupled analyses based on determining a force time history resulting from an aircraft impacting a rigid surface and the response of a stiff system to that force time history; however, the adequacy of this uncoupled analysis for a stiff nuclear facility on isolators is not well studied. Thus, validity of the Riera approach compared to more realistic coupled FE and other analyses that consider the physical impact of the plane with an isolated structure would be desirable.

Because of the movement of the structure during the impact of the aircraft, it may be desirable to conduct local penetration and perforation analysis for the region of impact. The duration of load on the structure and the energy absorption by the isolation system may alter the local damage condition expected for a fixed-base plant.

Parallel efforts with those outlined above would be useful to extend the work begun in this report. This would include as appropriate studies related to:

- The accuracy of the Riera force model when isolator movement is significant.
- Examine rate dependency effects on bearings since the rate of movement associated with aircraft impact may be much higher than considered for seismic loading. There may be a need for additional testing to identify appropriate bearing properties.
- Any beneficial effects associated with energy dissipation due to SSI and local damage at the impact location.
- Practical methods of estimating twist about a vertical axis and methods to avoid large torsional movements in the case of off-center impacts. This might include placing stronger LRBs around the perimeter of the structure, and more flexible or NR bearings in the center of the structure. Similarly, various types of dampers can be place on the perimeter. In some instances, pantograph mechanisms have been used (in Japan) to reduce torsional response of the isolation layer. Friction pendulum bearings have been shown to be particularly good at reducing torsional motion of the isolation layer. From the results presented herein, it would seem that reducing the mass and stiffness eccentricities of the superstructure would help reduce but not eliminate these motions as well.
- Configuration studies to develop countermeasures to mitigate the effects of aircraft impact, e.g., structural design configurations of the draft chimney, addition of sacrificial elements, and strengthening or toughening of components, etc.

6.2.3 Improved Numerical Modeling of PGSFR

As noted at the beginning of this section, it is desirable to carry out both simplified and refined analysis of the PGSFR. Simplified models can be useful for various conceptual, schematic, or

preliminary design studies. Thus, the models used in this study should be validated based on other more refined models used by KEPCO E&C's engineering staff and improved where needed. In particular, some anomalies noted in this study should be addressed. For example, the top levels of the RCB were seen to amplify greatly accelerations and floor spectrum, especially in the case of aircraft impact. The models may be inadequate or the mechanical properties of these regions of the structure may promote "penthouse" resonance behavior, and design modifications or different isolator properties could be used to mitigate these types of responses. Simplified modes that allow rapid modeling of various issues are desired. Thus, the current lumped mass, the stick models used herein should be refined.

Recent trends in seismic analysis of nuclear facilities focus on the use of more realistic FE models as they produce realistic predictions of response and provide much more information about the local dynamic behavior of the structure. As such, it would be useful to develop one or more detailed FE models of the PGSFR to assess differences between the simplified "stick" and FE models. The models should be able to account for cracking of concrete elements, thermal effects, and various heavy equipment items attached to the structure. In such models, issues of modeling viscous damping, especially in isolated configurations, require study.

6.2.4 Improved Modeling of Isolation Bearings and Isolation Systems

Current work by KEPCO, UC Berkeley, and other engineers aims at improving the cogency of numerical models for isolation bearings. These models tend to be simple and are used for large numbers of runs by engineering designers. To assess the adequacy of these simplified design models, and to develop research data to substantiate the behavior of a nuclear facility under severe loading conditions, more refined models are needed. For the PGSFR project, only the types of bearings relevant to the project need to be assessed and improved when necessary.

This work should include a range of activities, including:

- Calibrate models currently available or newly developed with the appropriate experimental data considering various ranges of behavior (small as well as large deformations). For many of the analyses undertaken in this project, the bearing displacement demands were quite small compared to typical cases, and it is not certain that the behavior exhibited by isolators in these analyses were as realistic as desired.
- Because of the sensitivity of isolation bearings to axial load and of sodium-cooled fast reactors and associated components and equipment to vertical excitations, it is desirable to assess and improve the modeling capabilities of isolators of interest to combined horizontal and vertical loading, especially to vertical excitations and transient vertical loads. As noted in previous tests, isolators are highly nonlinear and somewhat inelastic under vertical loading. Similarly, geometric nonlinearities serve to couple horizontal and vertical responses of the supported system when vertical loads are applied. These models will be important for seismic and aircraft impact analyses.

- For all types of elastomeric bearings, analytical models should be evaluated to assure that they represent the behavior of the bearings as they approach their stability limits under vertical loading.
- Assess and improve the rate dependency of models, especially with regards to loading rates associated with aircraft impact.
- Assess and improve as necessary the ability of bearings to represent behavior under elevated temperatures related to the energy dissipated during inelastic cyclic loading.
- Modeling of hardening behavior in LRBs and other bearings. The hardening that occurs in many elastomeric bearings and friction pendulum bearings as they approach their displacement capacity may be an effective method of slowing the superstructure prior to impact with a hard-stop mechanism. This needs to be modeled accurately to assess its stopping capabilities but also the forces and accelerations transmitted by the bearing up into the superstructure.
- Modeling of hard and/or soft stops. The U.S. NRC is considering requiring hard stops for NPPs. Currently these are not required for conventional building structures. A hard stop can transfer a substantial load to the structure, resulting in local damage at the impact location but also transferring significant forces and accelerations to the superstructure. Thus, realistic modeling of effective hard stops or softer stops that more gradually slow a structure prior to impact is a priority.
- Consideration of special models for bearings that allow vertical isolation. Special efforts are needed to model elastomeric bearings where thicker rubber sheets are used to decrease the vertical stiffness of the bearing, thereby providing a form of vertical isolation to the supported structure. Since most fast reactors have considered the use of vertical isolation, realistic numerical models are needed.
- Consider hybrid systems that provide isolation in vertical direction. As noted in the literature survey, many different types of systems have attempted to provide both vertical and horizontal isolation. In some cases, a hybrid approach is taken where conventional isolation bearings are used to provide isolation in the horizontal direction, and isolation in the vertical direction is achieved by a set of hydraulic, air or metallic springs (and dampers). The ability to model such hybrid systems may be useful in studies that consider vertical isolation.
- Develop methods to model systems that can restrain rocking motions of vertically isolated structures. Unless it is possible to isolate a structure or component from the elevation of its center-of-mass, a vertically isolated structure may have significant rocking motion. To allow vertical and horizontal movement of the isolated structure and prevent rocking motion requires complex mechanical or hydraulic anti-rocking systems. Very few

efforts have been made to model such systems, and additional work will be needed if this type of system is used.

- Conduct a test program to confirm models. Quasi-static, hybrid, and shaking table tests may be useful to validate numerical models used and demonstrate the effectiveness of any new isolation concepts developed.

6.2.5 Parametric Investigations for Isolation Systems

Even in cases like those considered here, where seismic isolation is only provided to protect against horizontal components of motion, additional research and development studies are desirable. For instance:

- Studies to assess the implications of different isolator layouts and different numbers of isolators on cost and performance.
- Studies comparing simple and refined isolator models in order to develop an understanding of the importance of different bearing properties on system performance, and to develop useful design simplifications and guides.
- Studies comparing simplified lump-mass stick models to various FE models having different resolution and properties.
- Studies assessing the effect of various ground motion, isolator, and structural characteristics on the vertical response of the PGSFR based on refined FE models.
- Studies that examine differences in seismic performance under OBE, SSE, and beyond design-basis events and other levels of hazard. From the perspective of evolving regulatory requirements, information on the dispersion of responses under beyond design-basis events is needed.
- Studies to investigate the effects of soft or hard stops and different gap sizes. The focus would be to develop economical and effective methods of achieving safety goals, i.e., can a larger gap be more cost-effective than using a soft or hard stop?
- Studies that fine tune bearing design or alter the properties of the structure to best match performance criteria.

Ideally, these studies will be undertaken in such a way that SSI effects can be assessed and compared to fixed-base cases. Soil–structure interaction, including embedment effects, may have a significant effect on the response of heavy and stiff structures.

Studies similar to those reported herein are needed for three-dimensional isolation systems, but additional studies are needed related to:

- Use of softer vertical elastomeric bearings.
- Use of separate systems that isolate the whole plant, but use hybrid bearings or a separate system for horizontal and vertical isolation.

- The effect of hard and soft stops on systems with vertical isolation. A sudden stop may cause the structure to pitch suddenly, resulting in tension or uplift in the bearings.

In some designs, although a complete horizontal isolation system is provided for the entire plant, portions of the plant are isolated. In other designs, only localized isolation is provided in a fixed-base NPP. These may be quite useful strategies for the PGSFR. Thus, additional studies should explore:

- Horizontal isolation of whole structure plus local vertical isolation.
- A fixed-base plant with local horizontal or horizontal and vertical isolation of equipment and a small region of plant.

6.3 General Recommendations

A wide variety of risk-based and performance oriented studies will help to identify what aspects of the structural design contribute most to the response and its uncertainties, and the economic tradeoffs associated with alternative designs. Thus, research related to several topics is recommended.

- Sensitivity analyses to identify parameters used in modeling the isolated and fixed-base system that most influence performance and uncertainties to aid in devising design strategies for improving performance.
- Cost-benefit analysis: the expert panel strongly advised conducting a simplified cost-benefit study early in the project. Investigations of expected construction and repair costs, and downtime associated with post-event inspection, design, permitting, and repair. To provide a basis for comparison, it would be ideal to repeat the parametric studies done above for cases where the structure is assumed to be fixed to the ground.

In addition to considerable expertise related to seismic, structural, and geotechnical engineering, the development of the PGSFR may benefit from advice and research related to nuclear and safety engineering.

Several other types of studies may be useful, including:

- Development of step-by-step design and analysis examples, workshops and short courses, and videos to help train design engineers about seismic isolation, computational modeling and nonlinear analysis, performance-based design, etc.
- Simplified design-oriented studies to seismically isolate emergency operations buildings and other structures associated with the PGSFR power station.

REFERENCES

Abbas H., Paul D.K., Godbole P.N., Nayak G.C. (1996). Aircraft crash upon outer containment of nuclear power plant, *Nucl. Eng. Des.,* 160: 13–50.

Aiken I.D., Kelly J.M., Tajirian F.F. (1989). Mechanics of low shape factor elastomeric seismic isolation bearings, *Report No. UCB/EERC-89/13*, Earthquake Engineering Research Center, University of California, Berkeley, CA.

Andonov A., Apostolov K., Stefanov D., Kostov M. (2010). Parametric study on the floor response spectra and the damage potential of aircraft impact induced vibratory loading, *J. Disaster Res.*, 5(4): 417–425.

Aoto K., Uto N., Sakamoto Y., Ito T., Toda M., Kotake S. (2012). Design study and R&D progress on Japan Sodium-Cooled Fast Reactor, *Nucl. Sci. Tech.*, 48(4): 463–471.

Arros J., Doumbalski N. (2007). Analysis of aircraft impact to concrete structures, *Nucl. Eng. Des*., 237 (12): 1241–1249.

Berglund C.R., Tippets E.F., Salerno N.L. (1988). PRISM: A safe, economic, and testable liquid-metal fast breeder reactor plant, *ANS Topic Meeting on Safety of Next Generation Power Reactors,* Seattle, WA.

Bignon P.G., Riera J.D. (1980). Verification of methods of analysis for soft missile impact problems, *Nucl. Eng. Des.,* 60: 311–326.

Blandford E., Keldrauk E., Laufer M., Mieler M., Wei J., Stojadinovic B., Peterson P.F. (2009). Advanced seismic base isolation methods for modular reactors, *Report UCBTH-09-004*, Departments of Civil and Environmental Engineering and Nuclear Engineering, University of California, Berkeley, CA, 132 pgs.

Chadmail J.F. (1985). Equivalent loading due to airplane impact taking into account the nonlinearities of impacted reinforced concrete buildings, *Nucl. Eng. Des.,* 85: 47–57.

De Grandis S., Forni M., De Bruyn D., Cardini S. (2011). Seismic isolation of Gen IV lead-cooled reactors, *Proceedings, SMiRT 21*, New Delhi, India.

Derham C.J., Kelly J.M., Thomas A.G. (1985). Nonlinear natural rubber bearings for seismic isolation, *Nucl. Eng. Des.,* 84(3): 417–428.

European Utilities (2012). European Utility Requirements (EUR) for LWR Nuclear Power Plants, Volume 2, Generic Nuclear Island requirement.

Etoh M., Kamishima Y., Okamura S., Watanabe O., Ohyama K., Kotake S., Negishi K., Kamide H., Sakamoto Y. (2009). Conceptual design study of JSFR (2), *Proceedings*, *FR09*, Kyoto, Japan.

Forni M., De Grandis S. (2012). Seismic-initiated events risk mitigation in lead-cooled reactors: the SILER Project, *Proceedings, 15th World Conference on Earthquake Engineering*, Lisbon, Portugal.

Forni M., Poggianti A., Dusi A. (2012). Seismic isolation of nuclear power plants, *Proceedings, 15th World Conference on Earthquake Engineering*, Lisbon, Portugal.

Gibert R.J., Martelli A. (1989). Seismic analysis of liquid metal fast breeder reactors, *Report, International Atomic Energy Agency*, Vienna, Austria.

Gluekler E.L., Tajirian F.F., Kelly J.M. (1988) Seismic isolation for a modular liquid metal reactor concept (PRISM), *In: IANS Topical Meetings on Safety of Next Generation Power Reactors,* Seattle, WA.

Gyorey G.L., Hardy R.W., Magee P.M. (1992). Safety and licensing of the PRISM liquid metal cooled reactor, *Nucl. Eng. Des*., (2): 181–189.

Hahn D., Kim Y., Lee C., Kim S., Lee S., Lee Y., Kim B., Jeong H. (2007). Conceptual design of the sodium-cooled fast reactor Kalimer-600, *Nucl. Eng. Tech.*, 39(3): 193–206.

Hahn D., Min J.B. Kim I.Y., Kim C.Y., Cho M. (1995). *Technical Committee Meeting on Conceptual Designs of Advanced Fast Reactors*, Kalpakkam, India.

Hara H., Hosoya T., Negishi K., Kotake S., Suzuki L. (2009). Conceptual design study of JSFR (4), *Proceedings*, *FR09*, Kyoto, Japan.

Ichikawa K., Shimoji K., Xu Y., Tsujita Y., Sato M., Sakai T., Kotake S. (2009). Conceptual design study of JSFR (3), *Proceedings*, *FR09*, Kyoto, Japan.

Inaba S., Anabukl T., Shirai K., Yabana S., Kitamura S. (2009). Shaking table tests with large test specimens of seismically isolated FBR plants, Part 2: Damage test of reinforced concrete wall structure. *Proceedings, ASME Pressure Vessels and Piping Division Conference (PVP 2009)*, PVP2009-77603, Prague, Czech Republic.

JEAG (2000). *Design Guideline of Seismic Isolation Systems for Nuclear Power Plants*, Japan Electric Association, *JEAG 4614-2000* (in Japanese).

Jeon S., Jin B.M., Kim Y.J. (2012). Assessment of the fire resistance of a nuclear power plant subjected to a large commercial aircraft crash, *Nucl. Eng. Des.*, 247: 11–22.

Jiang H., Chorzepa M.G. (2014). Aircraft impact analysis of nuclear safety-related concrete structures: A review, *Eng. Fail. Anal.*, 46: 118–133.

Johnson A.R., Golan S., Guenther E. (1988). SAFR, an economic, inherently safe liquid metal reactor, *Nucl. Eng. Des.*, 109(1-2): 87–95.

Kageyama M., Somaki T., Hino H., Umeki, K. (2002). Development of cable reinforced 3-dimensional base isolation air spring, *Proceedings, ASME 2002 Pressure Vessels and Piping Division Conference (PVP 2002)*, Vancouver, B.C., Canada.

Kajii S., Sawa N., Kunitake N., Umeki, K. (2002) Three dimensional seismic isolation system using hydraulic cylinder, *Proceedings, ASME 2002 Pressure Vessels and Piping Division Conference (PVP 2002)*, Vancouver, B.C., Canada.

Kammerer A.M., Whittaker A.S., Constantinou M.C. (2013). *Technical Considerations for Seismic Isolation of Nuclear Facilities (DRAFT)*. Office Nuclear Regulatory Research Division of Engineering, U.S. Nuclear Regulatory Commission, Washington, D.C.

Kashiwazaki A., Shimada T., Fujiwaka T., Umeki K. (2000a). Feasibility tests on a three-dimensional base isolation system incorporating hydraulic mechanism, *Proceedings, ASME 2002 Pressure Vessels and Piping Division Conference (PVP 2002)*, Vancouver, B.C., Canada.

Kato A. Moro S. Morishita M., Fujita T., Midorikawa S. (2003). A development program of three-dimensional seismic isolation for advanced reactor systems in Japan, *Proceedings*, *SMiRT 17*, Prague, Czech Republic.

Kato M., Watanabe Y., Kato A. (1991). Study on the seismic base-isolated reactor building for demonstration FBR Plant in Japan, *Proceedings, SMiRT 11*, Tokyo, Japan.

Kato M., Watanabe Y., Kato A., Suhara J., Shirahana K., Fukushima Y., Murazumi Y., Yoneda G. (1995a). Design study of the seismic-isolated reactor building of demonstration FBR plant in Japan, *Proceedings, SMiRT 13*, Porto Alegre, Brazil.

Kato M., Watanabe Y., Kato A., Tomora H., Shirahama K., Somaki T. (1995b). Study on ultimate behavior and fragility of seismic isolated FBR plant in Japan, *Proceedings, SMiRT 13*, Porto Alegre, Brazil.

Kelly J.M., Aiken I.D., Tajirian F.F. (1990). Mechanics of high shape factor elastomeric seismic isolation bearings, *Report No. UCB/EERC-90/01*, Earthquake Engineering Research Center, University of California, Berkeley, CA.

Kelly J.M., Aiken I.D., Clark P.W. (1997). Experimental testing of reduced-scale seismic isolation bearings for nuclear application, seismic isolation, passive energy dissipation and active control of seismic vibration of structures, *Proceedings, International Post-SMiRT Conference Seminar*, Taormina, Sicily, Italy.

Kelly J.M., Konstantinidis D. (2011). *Mechanics of Rubber Bearings for Seismic and Vibration Isolation*, John Wiley & Sons, Ltd., Chichester, U.K., 240 pgs.

Kitamura S., Morishita M., Yabana S., Hirata K., Umeki K. (2009). Shaking table tests with large test specimens of seismically isolated FBR plants Part 1: response behavior of test specimen under design ground motions, *Proceedings, ASME Pressure Vessels and Piping Division Conference*, Prague, Czech Republic, PVP2009-77614.

Kulak F.R., Yoo B. (2003). Effects of aircraft impact on a seismically isolated reactor building, *Proceedings, SMiRT 17*, Prague, Czech Republic, Paper WHJKP01-4, 6 pgs.

Kwant W., Boardman C.E. (1992) PRISM-liquid metal cooled reactor plant design and performance, *Nucl. Eng. Des.*, 136(1-2): 111–120.

Lee K.L., Han S.E., Hong J.W. (2013). Analysis of impact of large commercial aircraft on a prestressed containment building, *Nucl. Eng. Des.*, 265: 431–449.

Lu X., Lin K., Cen C., Xu Z., Lin L. (2015). Comparing different fidelity models for the impact analysis of large commercial aircrafts on a containment building, *J. Eng. Failure Anal.*, 57: 254–269.

Mazda T., Shiojiri H., Oka Y., Fujita T., Seki M. (1989). Testing on large-scale seismic isolation elements, *Proceedings, SMIRT-10,* Vol. K2, Anaheim, CA.

Naeim F., Kelly J.M. (1999). *Design of Seismic Isolated Structures: From Theory to Practice*, John Wiley & Sons, Inc., Chichester, U.K., 304 pgs.

Nakamura K., Ogiso S., Suzuk M., Umeki K. (2000). Development of double metal bellows air pressure spring with lead rubber bearing type 3-dimensional seismic isolator, ASME, *Proceedings, Pressure Vessels and Piping Conference*, Seismic Engineering, Vol. 1, New York, NY.

Noh S.H., Kim H.U. (2012). Aircraft impact assessment for a base-isolated nuclear power plant structure, *World Congress on Advances in Civil, Environmental, and Materials Research (ACEM' 12)*, Seoul, Korea, pp 1092–1095.

NEI (2009) *NEI 07-13: Methodology for Performing Aircraft Impact Assessments for New Plant Designs* (rev.7), Nuclear Energy Institute, Washington D.C

Ogura M., Okubo Y., Ito T., Toda M., Kobayashi S., Ohki S., Okubo T., Mizuno T., Kotake S. (2009). Conceptual design study of JSFR (1)-Overview and core concept, *FR09*, Kyoto, Japan.

Okamura S., Kamishima Y., Negishi K., Sakamoto Y., Kitamura S., Kotake S. (2011). Seismic isolation design for JSFR, *Nucl. Sci. Tech.*, 48(4): 688–692.

Oldenkamp R.D., Brunings J.E., Hren R. (1988). Update-Sodium Fast Reactor (SAFR) concept, *Proceedings, American Power Conference*, Vol.50, 1988.

Riera J.D. (1968). On the stress analysis of structures subjected to aircraft impact forces, *Nucl. Eng. Des.*, 8(4): 415–426.

Riera J.D. (1980). A critical reappraisal of nuclear power plant safety against accidental aircraft impact, *Nucl. Eng. Des.*, 57: 193–206.

Riera J.D. (1982). An approach to evaluate the design load time history for normal engine impact taking into account the crash-velocity distribution, *Nucl. Eng. Des.*, 71: 311–316.

Riera J.D. (1989). Penetration, scabbing and perforation of concrete structures hit by solid missiles, *Nucl. Eng. Des.*, 115: 121–131.

Riera J.D., Zorn N., Schueller G. (1982). An approach to evaluate the design load time history for normal engine impact taking into account the crash-velocity distribution, *Nucl. Eng. Des.*, 71: 311–316.

Sadique M.R., Iqbal M.A., Bhargava P. (2013). Nuclear containment structure subjected to commercial and fighter aircraft crash, *Nucl. Eng. Des.*, 260: 30–46.

Salerno L.N., Berglund R.C., Gyorey G.L., Tippets E.F., Tschamper M.P. (1988). PRISM concept, Modular LMR reactors, *Nucl. Eng. Des.*, 109(1-2): 79–86.

Sawada Y., Shiojiri H., Kurihara C., Maeno Y., Aoyagi S., Shimizu H., Goto T., Shibata, H., Fujita T., Kitagawa Y., Shigeta M., Takabayashi K. (1989). Seismic isolation test program, *Transactions, 10th International Conference on Structural Mechanics in Reactor Technology*, Los Angeles, CA

Schellenberg A., Baker J., Mahin S.A., Sitar N. (2014). Investigation of seismic isolation technology applied to the APR 1400 nuclear power plant: Selection of ground motions, Vol. 2, *Project Report to KEPCO E&C*, Pacific Earthquake Engineering Research Center, University of California, Berkeley, CA.

Shiojiri H. (1991). CRIEPI test program for seismic isolation of the FBR, *Nuclear Engineering and Design*, 127: 393–407.

Shiojiri H., Mazada T., Kasai H., Kanda J.N., Kubo T., Madokoro M., Shimomura T., Kawamura Y., Nojima O., Kawai N. (1989) Comparison of seismic isolation concepts for FBR, *Proceedings, SMiRT 10*, Anaheim, CA.

Siefert A., Henkel F.O. (2014). Nonlinear analysis of commercial aircraft impact on a reactor building—comparison between integral and decoupled crash simulation, *Nucl. Eng. Des.*, 269: 130–135.

Sugano T., Tsubota H., Kasai Y., Koshika N., Orui S., von Riesemann W.A., Bickel D.C., Parks M. (1993a). Full-scale aircraft impact test for evaluation of impact force, *Nucl. Eng. Des.*, 140(3): 373–385.

Sugano T., Tsubota, H., Kasai Y., Koshika N., Ohnuma H., von Riesemann W.A., Bickel D.C. Parks M.B. (1993b). Local damage to reinforced concrete structures caused by impact of aircraft engine missiles: Part 1. Test program, method and results, *Nucl. Eng. Des.*, 140: 387–405.

Suhara J., Tamura T., Okada Y., Umeki K. (2000). Development of three dimensional seismic isolation device with laminated rubber bearing and rolling seal type air spring, ASME, *Proceedings, Pressure Vessels and Piping Conference*, Seismic Engineering, Vol. 1, New York, NY.

Tajirian F.F., Gluekler E.L., Chen W.P., Canoga P., Kelly J.M. (1992). Qualification of high damping seismic isolation bearings for the ALMR, *International Working Group on Fast Reactors*, Vienna, Austria, pp 164–176.

Tajirian F.F., Kelly J.M. (1988). Testing of seismic isolation bearings for advanced liquid metal reactor PRISM, ASME, *Proceedings, Seismic, Shock, and Vibration Isolation*, PVP 147: 95–99, Pittsburg, PA.

Tajirian F.F., Kelly J.M., Aiken I.D. (1990). Seismic isolation for advanced nuclear power stations, *Earthq. Spectra*, 6(2): 371–401.

Tajirian F.F., Patel M.R. (1993). Response of seismic isolated facilities, a parametric study of the ALMR, *Proceedings, SMiRT 12*, Stuttgart, Germany.

Tajirian F.F., Schrag M.R. (1987). Conceptual design of seismic isolation for the PRISM liquid metal reactor, *Proceedings, SMiRT 9*, Lausanne, Switzerland.

Tang Y., Grandy C., Seidensticker R. (2011). Seismic isolation for advanced fast reactors, *Nucl. Tech.*, 173: 135–152.

Ueta M., Inagaki T., Shibata Y., Tarutani K., Okada K. (1995). The development of demonstration fast breeder reactor (DFBR), *Proceedings, SMiRT 13*, Porto Alegre, Brazil.

U.S. NRC (2014). *Regulatory Guide 1.208, A Performance-Based Approach to Define the Site-Specific Earthquake Ground Motion*, U.S. Nuclear Regulatory Commission, Washington, DC.

Watanabe Y., Kato A., Somaki T., Umeki K., Sato N. (2000b). Shaking table test and analysis on base isolated FBR plant model with high damping rubber bearing, *Proceedings, 12th World Conference on Earthquake Engineering*, Auckland, New Zealand.

Wilt T., Chowdhury A., Cox P.A. (2011). Response of reinforced concrete structures to aircraft crash impact, *Contract NRC−02−07−006*, SouthWest Research Institute, San Antonio, TX.

Wong J., Zhou Z., Mahin S.A. (2013) Seismic isolation of nuclear power plants, *EPRI Report 3002000561*, Palo Alto, CA.

Yabana S., Kanazawa K., Nagata S., Kitamura S., Sano T. (2009). Shaking table tests with large test specimens of seismically isolated FBR Plants. Part 3: Ultimate behavior of upper structure and rubber bearings, *Proceedings, 2009 ASME Pressure Vessels and Piping Division Conference (PVP 2009)*, PVP2009-77229, Prague, Czech.

Yoo B., Kulak F.R. (2002), Application of seismic isolation to the Star-LM Reactor, *Proceedings, ICONE 10*, Arlington, VA.

Yoo B., Lee J.-H., Koo G.-H. (1995). Effects of high damping rubber bearing on seismic response of superstructure in base isolated system, *Proceedings, SMiRT 13*, Porto Alegre, Brazil

Yoo B., Lee J.-H., Koo G.-H. (1997). Study of reduced-scale model test results of high damping and lead laminated rubber bearings for liquid metal reactor, *KAERI/TR-539/95* (in Korean).

Yoo B., Lee J.-H., Koo G.-H., Lee H.-Y., Kim, J.-B. (2000) Seismic base isolation technologies for Korea advanced liquid metal reactor, *Nucl. Eng. Des.*, 199: 125–142.

PEER REPORTS

PEER reports are available as a free PDF download from https://peer.berkeley.edu/peer-reports. Printed hard copies of PEER reports can be ordered directly from our printer by following the instructions also available at https://peer.berkeley.edu/peer-reports. For other related questions about the PEER Report Series, contact the Pacific Earthquake Engineering Research Center, 325 Davis Hall; Mail Code 1792, Berkeley, CA 94720. Tel.: (510) 642-3437; and Email: peer_center@berkeley.edu.

PEER 2017/10 *Development of Time Histories for IEEE693 Testing and Analysis (including Seismically Isolated Equipment).* Shakhzod M. Takhirov, Eric Fujisaki, Leon Kempner, Michael Riley, and Brian Low. December 2017.

PEER 2017/09 *""R" Package for Computation of Earthquake Ground-Motion Response Spectra.* Pengfei Wang, Jonathan P. Stewart, Yousef Bozorgnia, David M. Boore, and Tadahiro Kishida. December 2017.

PEER 2017/08 *Influence of Kinematic SSI on Foundation Input Motions for Bridges on Deep Foundations*. Benjamin J. Turner, Scott J. Brandenberg, and Jonathan P. Stewart. November 2017.

PEER 2017/07 *A Nonlinear Kinetic Model for Multi-Stage Friction Pendulum Systems*. Paul L. Drazin and Sanjay Govindjee, September 2017.

PEER 2017/06 *Guidelines for Performance-Based Seismic Design of Tall Buildings, Version 2.02*. TBI Working Group led by co-chairs Ron Hamburger and Jack Moehle: Jack Baker, Jonathan Bray, C.B. Crouse, Greg Deierlein, John Hooper, Marshall Lew, Joe Maffei, Stephen Mahin, James Malley, Farzad Naeim, Jonathan Stewart, and John Wallace. May 2017.

PEER 2017/05 *Recommendations for Ergodic Nonlinear Site Amplification in Central and Eastern North America*. Youssef M.A. Hashash, Joseph A. Harmon, Okan Ilhan, Grace A. Parker, and Jonathan P. Stewart. March 2017.

PEER 2017/04 *Expert Panel Recommendations for Ergodic Site Amplification in Central and Eastern North America*. Jonathan P. Stewart, Grace A Parker, Joseph P. Harmon, Gail M. Atkinson, David M. Boore, Robert B. Darragh, Walter J. Silva, and Youssef M.A. Hashash. March 2017.

PEER 2017/03 *NGA-East Ground-Motion Models for the U.S. Geological Survey National Seismic Hazard Maps*. Christine A. Goulet, Yousef Bozorgnia, Nicolas Kuehn, Linda Al Atik, Robert R. Youngs, Robert W. Graves, and Gail M. Atkinson. March 2017.

PEER 2017/02 *U.S.–New Zealand–Japan Workshop: Liquefaction-Induced Ground Movements Effects, University of California, Berkeley, California, 2–4 November 2016.* Jonathan D. Bray, Ross W. Boulanger, Misko Cubrinovski, Kohji Tokimatsu, Steven L. Kramer, Thomas O'Rourke, Ellen Rathje, Russell A. Green, Peter K. Robinson, and Christine Z. Beyzaei. March 2017.

PEER 2017/01 *2016 PEER Annual Report*. Khalid M. Mosalam, Amarnath Kasalanati, and Grace Kang. March 2017.

PEER 2016/10 *Performance-Based Robust Nonlinear Seismic Analysis with Application to Reinforced Concrete Bridge Systems*. Xiao Ling and Khalid M. Mosalam. December 2016.

PEER 2016/08 *Resilience of Critical Structures, Infrastructure, and Communities***.** Gian Paolo Cimellaro, Ali Zamani-Noori, Omar Kamouh, Vesna Terzic, and Stephen A. Mahin. December 2016.

PEER 2016/07 *Hybrid Simulation Theory for a Classical Nonlinear Dynamical System*. Paul L. Drazin and Sanjay Govindjee. September 2016.

PEER 2016/06 *California Earthquake Early Warning System Benefit Study*. Laurie A. Johnson, Sharyl Rabinovici, Grace S. Kang, and Stephen A. Mahin. July 2016.

PEER 2016/05 *Ground-Motion Prediction Equations for Arias Intensity Consistent with the NGA-West2 Ground-Motion Models.* Charlotte Abrahamson, Hao-Jun Michael Shi, and Brian Yang. July 2016.

PEER 2016/04 *The M_W 6.0 South Napa Earthquake of August 24, 2014: A Wake-Up Call for Renewed Investment in Seismic Resilience Across California.* Prepared for the California Seismic Safety Commission, Laurie A. Johnson and Stephen A. Mahin. May 2016.

PEER 2016/03 *Simulation Confidence in Tsunami-Driven Overland Flow.* Patrick Lynett. May 2016.

PEER 2016/02 *Semi-Automated Procedure for Windowing time Series and Computing Fourier Amplitude Spectra for the NGA-West2 Database.* Tadahiro Kishida, Olga-Joan Ktenidou, Robert B. Darragh, and Walter J. Silva. May 2016.

PEER 2016/01 *A Methodology for the Estimation of Kappa (κ) from Large Datasets: Example Application to Rock Sites in the NGA-East Database and Implications on Design Motions.* Olga-Joan Ktenidou, Norman A. Abrahamson, Robert B. Darragh, and Walter J. Silva. April 2016.

PEER 2015/13 *Self-Centering Precast Concrete Dual-Steel-Shell Columns for Accelerated Bridge Construction: Seismic Performance, Analysis, and Design*. Gabriele Guerrini, José I. Restrepo, Athanassios Vervelidis, and Milena Massari. December 2015.

PEER 2015/12 *Shear-Flexure Interaction Modeling for Reinforced Concrete Structural Walls and Columns under Reversed Cyclic Loading*. Kristijan Kolozvari, Kutay Orakcal, and John Wallace. December 2015.

PEER 2015/11 *Selection and Scaling of Ground Motions for Nonlinear Response History Analysis of Buildings in Performance-Based Earthquake Engineering*. N. Simon Kwong and Anil K. Chopra. December 2015.

PEER 2015/10 *Structural Behavior of Column-Bent Cap Beam-Box Girder Systems in Reinforced Concrete Bridges Subjected to Gravity and Seismic Loads. Part II: Hybrid Simulation and Post-Test Analysis*. Mohamed A. Moustafa and Khalid M. Mosalam. November 2015.

PEER 2015/09 *Structural Behavior of Column-Bent Cap Beam-Box Girder Systems in Reinforced Concrete Bridges Subjected to Gravity and Seismic Loads. Part I: Pre-Test Analysis and Quasi-Static Experiments*. Mohamed A. Moustafa and Khalid M. Mosalam. September 2015.

PEER 2015/08 *NGA-East: Adjustments to Median Ground-Motion Models for Center and Eastern North America*. August 2015.

PEER 2015/07 *NGA-East: Ground-Motion Standard-Deviation Models for Central and Eastern North America*. Linda Al Atik. June 2015.

PEER 2015/06 *Adjusting Ground-Motion Intensity Measures to a Reference Site for which V_{S30} = 3000 m/sec*. David M. Boore. May 2015.

PEER 2015/05 *Hybrid Simulation of Seismic Isolation Systems Applied to an APR-1400 Nuclear Power Plant.* Andreas H. Schellenberg, Alireza Sarebanha, Matthew J. Schoettler, Gilberto Mosqueda, Gianmario Benzoni, and Stephen A. Mahin. April 2015.

PEER 2015/04 *NGA-East: Median Ground-Motion Models for the Central and Eastern North America Region*. April 2015.

PEER 2015/03 *Single Series Solution for the Rectangular Fiber-Reinforced Elastomeric Isolator Compression Modulus*. James M. Kelly and Niel C. Van Engelen. March 2015.

PEER 2015/02 *A Full-Scale, Single-Column Bridge Bent Tested by Shake-Table Excitation.* Matthew J. Schoettler, José I. Restrepo, Gabriele Guerrini, David E. Duck, and Francesco Carrea. March 2015.

PEER 2015/01 *Concrete Column Blind Prediction Contest 2010: Outcomes and Observations.* Vesna Terzic, Matthew J. Schoettler, José I. Restrepo, and Stephen A Mahin. March 2015.

PEER 2014/20 *Stochastic Modeling and Simulation of Near-Fault Ground Motions for Performance-Based Earthquake Engineering*. Mayssa Dabaghi and Armen Der Kiureghian. December 2014.

PEER 2014/19 *Seismic Response of a Hybrid Fiber-Reinforced Concrete Bridge Column Detailed for Accelerated Bridge Construction*. Wilson Nguyen, William Trono, Marios Panagiotou, and Claudia P. Ostertag. December 2014.

PEER 2014/18 *Three-Dimensional Beam-Truss Model for Reinforced Concrete Walls and Slabs Subjected to Cyclic Static or Dynamic Loading*. Yuan Lu, Marios Panagiotou, and Ioannis Koutromanos. December 2014.

PEER 2014/17 *PEER NGA-East Database*. Christine A. Goulet, Tadahiro Kishida, Timothy D. Ancheta, Chris H. Cramer, Robert B. Darragh, Walter J. Silva, Youssef M.A. Hashash, Joseph Harmon, Jonathan P. Stewart, Katie E. Wooddell, and Robert R. Youngs. October 2014.

PEER 2014/16 *Guidelines for Performing Hazard-Consistent One-Dimensional Ground Response Analysis for Ground Motion Prediction*. Jonathan P. Stewart, Kioumars Afshari, and Youssef M.A. Hashash. October 2014.

PEER 2014/15 *NGA-East Regionalization Report: Comparison of Four Crustal Regions within Central and Eastern North America using Waveform Modeling and 5%-Damped Pseudo-Spectral Acceleration Response*. Jennifer Dreiling, Marius P. Isken, Walter D. Mooney, Martin C. Chapman, and Richard W. Godbee. October 2014.

PEER 2014/14 *Scaling Relations between Seismic Moment and Rupture Area of Earthquakes in Stable Continental Regions*. Paul Somerville. August 2014.

PEER 2014/13 *PEER Preliminary Notes and Observations on the August 24, 2014, South Napa Earthquake*. Grace S. Kang and Stephen A. Mahin, Editors. September 2014.

PEER 2014/12 *Reference-Rock Site Conditions for Central and Eastern North America: Part II – Attenuation (Kappa) Definition*. Kenneth W. Campbell, Youssef M.A. Hashash, Byungmin Kim, Albert R. Kottke, Ellen M. Rathje, Walter J. Silva, and Jonathan P. Stewart. August 2014.

PEER 2014/11 *Reference-Rock Site Conditions for Central and Eastern North America: Part I - Velocity Definition*. Youssef M.A. Hashash, Albert R. Kottke, Jonathan P. Stewart, Kenneth W. Campbell, Byungmin Kim, Ellen M. Rathje, Walter J. Silva, Sissy Nikolaou, and Cheryl Moss. August 2014.

PEER 2014/10 *Evaluation of Collapse and Non-Collapse of Parallel Bridges Affected by Liquefaction and Lateral Spreading*. Benjamin Turner, Scott J. Brandenberg, and Jonathan P. Stewart. August 2014.

PEER 2014/09 *PEER Arizona Strong-Motion Database and GMPEs Evaluation*. Tadahiro Kishida, Robert E. Kayen, Olga-Joan Ktenidou, Walter J. Silva, Robert B. Darragh, and Jennie Watson-Lamprey. June 2014.

PEER 2014/08 *Unbonded Pretensioned Bridge Columns with Rocking Detail*. Jeffrey A. Schaefer, Bryan Kennedy, Marc O. Eberhard, and John F. Stanton. June 2014.

PEER 2014/07 *Northridge 20 Symposium Summary Report: Impacts, Outcomes, and Next Steps*. May 2014.

PEER 2014/06 *Report of the Tenth Planning Meeting of NEES/E-Defense Collaborative Research on Earthquake Engineering*. December 2013.

PEER 2014/05 *Seismic Velocity Site Characterization of Thirty-One Chilean Seismometer Stations by Spectral Analysis of Surface Wave Dispersion*. Robert Kayen, Brad D. Carkin, Skye Corbet, Camilo Pinilla, Allan Ng, Edward Gorbis, and Christine Truong. April 2014.

PEER 2014/04 Effect of Vertical Acceleration on Shear Strength of Reinforced Concrete Columns. Hyerin Lee and Khalid M. Mosalam. April 2014.

PEER 2014/03 *Retest of Thirty-Year-Old Neoprene Isolation Bearings.* James M. Kelly and Niel C. Van Engelen. March 2014.

PEER 2014/02 *Theoretical Development of Hybrid Simulation Applied to Plate Structures.* Ahmed A. Bakhaty, Khalid M. Mosalam, and Sanjay Govindjee. January 2014.

PEER 2014/01 *Performance-Based Seismic Assessment of Skewed Bridges.* Peyman Kaviani, Farzin Zareian, and Ertugrul Taciroglu. January 2014.

PEER 2013/26 *Urban Earthquake Engineerin*g. Proceedings of the U.S.-Iran Seismic Workshop. December 2013.

PEER 2013/25 *Earthquake Engineering for Resilient Communities: 2013 PEER Internship Program Research Report Collection.* Heidi Tremayne (Editor), Stephen A. Mahin (Editor), Jorge Archbold Monterossa, Matt Brosman, Shelly Dean, Katherine deLaveaga, Curtis Fong, Donovan Holder, Rakeeb Khan, Elizabeth Jachens, David Lam, Daniela Martinez Lopez, Mara Minner, Geffen Oren, Julia Pavicic, Melissa Quinonez, Lorena Rodriguez, Sean Salazar, Kelli Slaven, Vivian Steyert, Jenny Taing, and Salvador Tena. December 2013.

PEER 2013/24 *NGA-West2 Ground Motion Prediction Equations for Vertical Ground Motions*. September 2013.

PEER 2013/23 *Coordinated Planning and Preparedness for Fire Following Major Earthquakes*. Charles Scawthorn. November 2013.

PEER 2013/22 *GEM-PEER Task 3 Project: Selection of a Global Set of Ground Motion Prediction Equations.* Jonathan P. Stewart, John Douglas, Mohammad B. Javanbarg, Carola Di Alessandro, Yousef Bozorgnia, Norman A. Abrahamson, David M. Boore, Kenneth W. Campbell, Elise Delavaud, Mustafa Erdik, and Peter J. Stafford. December 2013.

PEER 2013/21 *Seismic Design and Performance of Bridges with Columns on Rocking Foundations*. Grigorios Antonellis and Marios Panagiotou. September 2013.

PEER 2013/20 *Experimental and Analytical Studies on the Seismic Behavior of Conventional and Hybrid Braced Frames*. Jiun-Wei Lai and Stephen A. Mahin. September 2013.

PEER 2013/19 *Toward Resilient Communities: A Performance-Based Engineering Framework for Design and Evaluation of the Built Environment.* Michael William Mieler, Bozidar Stojadinovic, Robert J. Budnitz, Stephen A. Mahin, and Mary C. Comerio. September 2013.

PEER 2013/18 *Identification of Site Parameters that Improve Predictions of Site Amplification*. Ellen M. Rathje and Sara Navidi. July 2013.

PEER 2013/17 *Response Spectrum Analysis of Concrete Gravity Dams Including Dam-Water-Foundation Interaction*. Arnkjell Løkke and Anil K. Chopra. July 2013.

PEER 2013/16 *Effect of Hoop Reinforcement Spacing on the Cyclic Response of Large Reinforced Concrete Special Moment Frame Beams.* Marios Panagiotou, Tea Visnjic, Grigorios Antonellis, Panagiotis Galanis, and Jack P. Moehle. June 2013.

PEER 2013/15 *A Probabilistic Framework to Include the Effects of Near-Fault Directivity in Seismic Hazard Assessment.* Shrey Kumar Shahi, Jack W. Baker. October 2013.

PEER 2013/14 *Hanging-Wall Scaling using Finite-Fault Simulations.* Jennifer L. Donahue and Norman A. Abrahamson. September 2013.

PEER 2013/13 *Semi-Empirical Nonlinear Site Amplification and its Application in NEHRP Site Factors*. Jonathan P. Stewart and Emel Seyhan. November 2013.

PEER 2013/12 *Nonlinear Horizontal Site Response for the NGA-West2 Project.* Ronnie Kamai, Norman A. Abramson, Walter J. Silva. May 2013.

PEER 2013/11 *Epistemic Uncertainty for NGA-West2 Models.* Linda Al Atik and Robert R. Youngs. May 2013.

PEER 2013/10 *NGA-West 2 Models for Ground-Motion Directionality.* Shrey K. Shahi and Jack W. Baker. May 2013.

PEER 2013/09 *Final Report of the NGA-West2 Directivity Working Group.* Paul Spudich, Jeffrey R. Bayless, Jack W. Baker, Brian S.J. Chiou, Badie Rowshandel, Shrey Shahi, and Paul Somerville. May 2013.

PEER 2013/08 *NGA-West2 Model for Estimating Average Horizontal Values of Pseudo-Absolute Spectral Accelerations Generated by Crustal Earthquakes*. I. M. Idriss. May 2013.

PEER 2013/07 *Update of the Chiou and Youngs NGA Ground Motion Model for Average Horizontal Component of Peak Ground Motion and Response Spectra*. Brian Chiou and Robert Youngs. May 2013.

PEER 2013/06 *NGA-West2 Campbell-Bozorgnia Ground Motion Model for the Horizontal Components of PGA, PGV, and 5%-Damped Elastic Pseudo-Acceleration Response Spectra for Periods Ranging from 0.01 to 10 sec.* Kenneth W. Campbell and Yousef Bozorgnia. May 2013.

PEER 2013/05 *NGA-West 2 Equations for Predicting Response Spectral Accelerations for Shallow Crustal Earthquakes*. David M. Boore, Jonathan P. Stewart, Emel Seyhan, and Gail M. Atkinson. May 2013.

PEER 2013/04 *Update of the AS08 Ground-Motion Prediction Equations Based on the NGA-West2 Data Set*. Norman Abrahamson, Walter Silva, and Ronnie Kamai. May 2013.

PEER 2013/03 *PEER NGA-West2 Database.* Timothy D. Ancheta, Robert B. Darragh, Jonathan P. Stewart, Emel Seyhan, Walter J. Silva, Brian S.J. Chiou, Katie E. Wooddell, Robert W. Graves, Albert R. Kottke, David M. Boore, Tadahiro Kishida, and Jennifer L. Donahue. May 2013.

PEER 2013/02 *Hybrid Simulation of the Seismic Response of Squat Reinforced Concrete Shear Walls*. Catherine A. Whyte and Bozidar Stojadinovic. May 2013.

PEER 2013/01 *Housing Recovery in Chile: A Qualitative Mid-program Review*. Mary C. Comerio. February 2013.

PEER 2012/08 *Guidelines for Estimation of Shear Wave Velocity.* Bernard R. Wair, Jason T. DeJong, and Thomas Shantz. December 2012.

PEER 2012/07 *Earthquake Engineering for Resilient Communities: 2012 PEER Internship Program Research Report Collection.* Heidi Tremayne (Editor), Stephen A. Mahin (Editor), Collin Anderson, Dustin Cook, Michael Erceg, Carlos Esparza, Jose Jimenez, Dorian Krausz, Andrew Lo, Stephanie Lopez, Nicole McCurdy, Paul Shipman, Alexander Strum, Eduardo Vega. December 2012.

PEER 2012/06 *Fragilities for Precarious Rocks at Yucca Mountain.* Matthew D. Purvance, Rasool Anooshehpoor, and James N. Brune. December 2012.

PEER 2012/05 *Development of Simplified Analysis Procedure for Piles in Laterally Spreading Layered Soils.* Christopher R. McGann, Pedro Arduino, and Peter Mackenzie–Helnwein. December 2012.

PEER 2012/04 *Unbonded Pre-Tensioned Columns for Bridges in Seismic Regions.* Phillip M. Davis, Todd M. Janes, Marc O. Eberhard, and John F. Stanton. December 2012.

PEER 2012/03 *Experimental and Analytical Studies on Reinforced Concrete Buildings with Seismically Vulnerable Beam-Column Joints*. Sangjoon Park and Khalid M. Mosalam. October 2012.

PEER 2012/02 *Seismic Performance of Reinforced Concrete Bridges Allowed to Uplift during Multi-Directional Excitation*. Andres Oscar Espinoza and Stephen A. Mahin. July 2012.

PEER 2012/01 *Spectral Damping Scaling Factors for Shallow Crustal Earthquakes in Active Tectonic Regions.* Sanaz Rezaeian, Yousef Bozorgnia, I. M. Idriss, Kenneth Campbell, Norman Abrahamson, and Walter Silva. July 2012.

PEER 2011/10 *Earthquake Engineering for Resilient Communities: 2011 PEER Internship Program Research Report Collection*. Heidi Faison and Stephen A. Mahin, Editors. December 2011.

PEER 2011/09 *Calibration of Semi-Stochastic Procedure for Simulating High-Frequency Ground Motions*. Jonathan P. Stewart, Emel Seyhan, and Robert W. Graves. December 2011.

PEER 2011/08 *Water Supply in regard to Fire Following Earthquake*. Charles Scawthorn. November 2011.

PEER 2011/07 *Seismic Risk Management in Urban Areas*. Proceedings of a U.S.-Iran-Turkey Seismic Workshop. September 2011.

PEER 2011/06 *The Use of Base Isolation Systems to Achieve Complex Seismic Performance Objectives*. Troy A. Morgan and Stephen A. Mahin. July 2011.

PEER 2011/05 *Case Studies of the Seismic Performance of Tall Buildings Designed by Alternative Means.* Task 12 Report for the Tall Buildings Initiative. Jack Moehle, Yousef Bozorgnia, Nirmal Jayaram, Pierson Jones, Mohsen Rahnama, Nilesh Shome, Zeynep Tuna, John Wallace, Tony Yang, and Farzin Zareian. July 2011.

PEER 2011/04 *Recommended Design Practice for Pile Foundations in Laterally Spreading Ground.* Scott A. Ashford, Ross W. Boulanger, and Scott J. Brandenberg. June 2011.

PEER 2011/03 *New Ground Motion Selection Procedures and Selected Motions for the PEER Transportation Research Program*. Jack W. Baker, Ting Lin, Shrey K. Shahi, and Nirmal Jayaram. March 2011.

PEER 2011/02 *A Bayesian Network Methodology for Infrastructure Seismic Risk Assessment and Decision Support*. Michelle T. Bensi, Armen Der Kiureghian, and Daniel Straub. March 2011.

PEER 2011/01 *Demand Fragility Surfaces for Bridges in Liquefied and Laterally Spreading Ground.* Scott J. Brandenberg, Jian Zhang, Pirooz Kashighandi, Yili Huo, and Minxing Zhao. March 2011.

PEER 2010/05 *Guidelines for Performance-Based Seismic Design of Tall Buildings.* Developed by the Tall Buildings Initiative. November 2010.

PEER 2010/04 *Application Guide for the Design of Flexible and Rigid Bus Connections between Substation Equipment Subjected to Earthquakes.* Jean-Bernard Dastous and Armen Der Kiureghian. September 2010.

PEER 2010/03 *Shear Wave Velocity as a Statistical Function of Standard Penetration Test Resistance and Vertical Effective Stress at Caltrans Bridge Sites.* Scott J. Brandenberg, Naresh Bellana, and Thomas Shantz. June 2010.

PEER 2010/02 *Stochastic Modeling and Simulation of Ground Motions for Performance-Based Earthquake Engineering.* Sanaz Rezaeian and Armen Der Kiureghian. June 2010.

PEER 2010/01 *Structural Response and Cost Characterization of Bridge Construction Using Seismic Performance Enhancement Strategies.* Ady Aviram, Božidar Stojadinović, Gustavo J. Parra-Montesinos, and Kevin R. Mackie. March 2010.

PEER 2009/03 *The Integration of Experimental and Simulation Data in the Study of Reinforced Concrete Bridge Systems Including Soil-Foundation-Structure Interaction.* Matthew Dryden and Gregory L. Fenves. November 2009.

PEER 2009/02 *Improving Earthquake Mitigation through Innovations and Applications in Seismic Science, Engineering, Communication, and Response*. Proceedings of a U.S.-Iran Seismic Workshop. October 2009.

PEER 2009/01 *Evaluation of Ground Motion Selection and Modification Methods: Predicting Median Interstory Drift Response of Buildings*. Curt B. Haselton, Editor. June 2009.

PEER 2008/10 *Technical Manual for Strata.* Albert R. Kottke and Ellen M. Rathje. February 2009.

PEER 2008/09 *NGA Model for Average Horizontal Component of Peak Ground Motion and Response Spectra.* Brian S.-J. Chiou and Robert R. Youngs. November 2008.

PEER 2008/08 *Toward Earthquake-Resistant Design of Concentrically Braced Steel Structures*. Patxi Uriz and Stephen A. Mahin. November 2008.

PEER 2008/07 *Using OpenSees for Performance-Based Evaluation of Bridges on Liquefiable Soils*. Stephen L. Kramer, Pedro Arduino, and HyungSuk Shin. November 2008.

PEER 2008/06 *Shaking Table Tests and Numerical Investigation of Self-Centering Reinforced Concrete Bridge Columns*. Hyung IL Jeong, Junichi Sakai, and Stephen A. Mahin. September 2008.

PEER 2008/05 *Performance-Based Earthquake Engineering Design Evaluation Procedure for Bridge Foundations Undergoing Liquefaction-Induced Lateral Ground Displacement*. Christian A. Ledezma and Jonathan D. Bray. August 2008.

PEER 2008/04 *Benchmarking of Nonlinear Geotechnical Ground Response Analysis Procedures.* Jonathan P. Stewart, Annie On-Lei Kwok, Youssef M. A. Hashash, Neven Matasovic, Robert Pyke, Zhiliang Wang, and Zhaohui Yang. August 2008.

PEER 2008/03 *Guidelines for Nonlinear Analysis of Bridge Structures in California*. Ady Aviram, Kevin R. Mackie, and Božidar Stojadinović. August 2008.

PEER 2008/02 *Treatment of Uncertainties in Seismic-Risk Analysis of Transportation Systems*. Evangelos Stergiou and Anne S. Kiremidjian. July 2008.

PEER 2008/01 *Seismic Performance Objectives for Tall Buildings.* William T. Holmes, Charles Kircher, William Petak, and Nabih Youssef. August 2008.

PEER 2007/12 *An Assessment to Benchmark the Seismic Performance of a Code-Conforming Reinforced Concrete Moment-Frame Building.* Curt Haselton, Christine A. Goulet, Judith Mitrani-Reiser, James L. Beck, Gregory G. Deierlein, Keith A. Porter, Jonathan P. Stewart, and Ertugrul Taciroglu. August 2008.

PEER 2007/11 *Bar Buckling in Reinforced Concrete Bridge Columns.* Wayne A. Brown, Dawn E. Lehman, and John F. Stanton. February 2008.

PEER 2007/10 *Computational Modeling of Progressive Collapse in Reinforced Concrete Frame Structures*. Mohamed M. Talaat and Khalid M. Mosalam. May 2008.

PEER 2007/09 *Integrated Probabilistic Performance-Based Evaluation of Benchmark Reinforced Concrete Bridges*. Kevin R. Mackie, John-Michael Wong, and Božidar Stojadinović. January 2008.

PEER 2007/08 *Assessing Seismic Collapse Safety of Modern Reinforced Concrete Moment-Frame Buildings*. Curt B. Haselton and Gregory G. Deierlein. February 2008.

PEER 2007/07 *Performance Modeling Strategies for Modern Reinforced Concrete Bridge Columns*. Michael P. Berry and Marc O. Eberhard. April 2008.

PEER 2007/06 *Development of Improved Procedures for Seismic Design of Buried and Partially Buried Structures*. Linda Al Atik and Nicholas Sitar. June 2007.

PEER 2007/05 *Uncertainty and Correlation in Seismic Risk Assessment of Transportation Systems*. Renee G. Lee and Anne S. Kiremidjian. July 2007.

PEER 2007/04 *Numerical Models for Analysis and Performance-Based Design of Shallow Foundations Subjected to Seismic Loading.* Sivapalan Gajan, Tara C. Hutchinson, Bruce L. Kutter, Prishati Raychowdhury, José A. Ugalde, and Jonathan P. Stewart. May 2008.

PEER 2007/03 *Beam-Column Element Model Calibrated for Predicting Flexural Response Leading to Global Collapse of RC Frame Buildings*. Curt B. Haselton, Abbie B. Liel, Sarah Taylor Lange, and Gregory G. Deierlein. May 2008.

PEER 2007/02 *Campbell-Bozorgnia NGA Ground Motion Relations for the Geometric Mean Horizontal Component of Peak and Spectral Ground Motion Parameters*. Kenneth W. Campbell and Yousef Bozorgnia. May 2007.

PEER 2007/01 *Boore-Atkinson NGA Ground Motion Relations for the Geometric Mean Horizontal Component of Peak and Spectral Ground Motion Parameters*. David M. Boore and Gail M. Atkinson. May 2007.

PEER 2006/12 Societal Implications of Performance-Based Earthquake Engineering. Peter J. May. May 2007.

PEER 2006/11 *Probabilistic Seismic Demand Analysis Using Advanced Ground Motion Intensity Measures, Attenuation Relationships, and Near-Fault Effects*. Polsak Tothong and C. Allin Cornell. March 2007.

PEER 2006/10 *Application of the PEER PBEE Methodology to the I-880 Viaduct*. Sashi Kunnath. February 2007.

PEER 2006/09 *Quantifying Economic Losses from Travel Forgone Following a Large Metropolitan Earthquake*. James Moore, Sungbin Cho, Yue Yue Fan, and Stuart Werner. November 2006.

PEER 2006/08 *Vector-Valued Ground Motion Intensity Measures for Probabilistic Seismic Demand Analysis*. Jack W. Baker and C. Allin Cornell. October 2006.

PEER 2006/07 *Analytical Modeling of Reinforced Concrete Walls for Predicting Flexural and Coupled–Shear-Flexural Responses*. Kutay Orakcal, Leonardo M. Massone, and John W. Wallace. October 2006.

PEER 2006/06 *Nonlinear Analysis of a Soil-Drilled Pier System under Static and Dynamic Axial Loading*. Gang Wang and Nicholas Sitar. November 2006.

PEER 2006/05 *Advanced Seismic Assessment Guidelines.* Paolo Bazzurro, C. Allin Cornell, Charles Menun, Maziar Motahari, and Nicolas Luco. September 2006.

PEER 2006/04 *Probabilistic Seismic Evaluation of Reinforced Concrete Structural Components and Systems*. Tae Hyung Lee and Khalid M. Mosalam. August 2006.

PEER 2006/03 *Performance of Lifelines Subjected to Lateral Spreading.* Scott A. Ashford and Teerawut Juirnarongrit. July 2006.

PEER 2006/02 *Pacific Earthquake Engineering Research Center Highway Demonstration Project.* Anne Kiremidjian, James Moore, Yue Yue Fan, Nesrin Basoz, Ozgur Yazali, and Meredith Williams. April 2006.

PEER 2006/01 *Bracing Berkeley. A Guide to Seismic Safety on the UC Berkeley Campus.* Mary C. Comerio, Stephen Tobriner, and Ariane Fehrenkamp. January 2006.

PEER 2005/17 *Earthquake Simulation Tests on Reducing Residual Displacements of Reinforced Concrete Bridges.* Junichi Sakai, Stephen A Mahin, and Andres Espinoza. December 2005.

PEER 2005/16 *Seismic Response and Reliability of Electrical Substation Equipment and Systems.* Junho Song, Armen Der Kiureghian, and Jerome L. Sackman. April 2006.

PEER 2005/15 *CPT-Based Probabilistic Assessment of Seismic Soil Liquefaction Initiation.* R. E. S. Moss, R. B. Seed, R. E. Kayen, J. P. Stewart, and A. Der Kiureghian. April 2006.

PEER 2005/14 *Workshop on Modeling of Nonlinear Cyclic Load-Deformation Behavior of Shallow Foundations.* Bruce L. Kutter, Geoffrey Martin, Tara Hutchinson, Chad Harden, Sivapalan Gajan, and Justin Phalen. March 2006.

PEER 2005/13 *Stochastic Characterization and Decision Bases under Time-Dependent Aftershock Risk in Performance-Based Earthquake Engineering*. Gee Liek Yeo and C. Allin Cornell. July 2005.

PEER 2005/12 *PEER Testbed Study on a Laboratory Building: Exercising Seismic Performance Assessment.* Mary C. Comerio, Editor. November 2005.

PEER 2005/11 *Van Nuys Hotel Building Testbed Report: Exercising Seismic Performance Assessment.* Helmut Krawinkler, Editor. October 2005.

PEER 2005/10 *First NEES/E-Defense Workshop on Collapse Simulation of Reinforced Concrete Building Structures.* September 2005.

PEER 2005/09 *Test Applications of Advanced Seismic Assessment Guidelines.* Joe Maffei, Karl Telleen, Danya Mohr, William Holmes, and Yuki Nakayama. August 2006.

PEER 2005/08 *Damage Accumulation in Lightly Confined Reinforced Concrete Bridge Columns.* R. Tyler Ranf, Jared M. Nelson, Zach Price, Marc O. Eberhard, and John F. Stanton. April 2006.

PEER 2005/07 *Experimental and Analytical Studies on the Seismic Response of Freestanding and Anchored Laboratory Equipment.* Dimitrios Konstantinidis and Nicos Makris. January 2005.

PEER 2005/06 *Global Collapse of Frame Structures under Seismic Excitations*. Luis F. Ibarra and Helmut Krawinkler. September 2005.

PEER 2005//05 *Performance Characterization of Bench- and Shelf-Mounted Equipment.* Samit Ray Chaudhuri and Tara C. Hutchinson. May 2006.

PEER 2005/04 *Numerical Modeling of the Nonlinear Cyclic Response of Shallow Foundations.* Chad Harden, Tara Hutchinson, Geoffrey R. Martin, and Bruce L. Kutter. August 2005.

PEER 2005/03 *A Taxonomy of Building Components for Performance-Based Earthquake Engineering*. Keith A. Porter. September 2005.

PEER 2005/02 *Fragility Basis for California Highway Overpass Bridge Seismic Decision Making*. Kevin R. Mackie and Božidar Stojadinović. June 2005.

PEER 2005/01 *Empirical Characterization of Site Conditions on Strong Ground Motion.* Jonathan P. Stewart, Yoojoong Choi, and Robert W. Graves. June 2005.

PEER 2004/09 *Electrical Substation Equipment Interaction: Experimental Rigid Conductor Studies.* Christopher Stearns and André Filiatrault. February 2005.

PEER 2004/08 *Seismic Qualification and Fragility Testing of Line Break 550-kV Disconnect Switches.* Shakhzod M. Takhirov, Gregory L. Fenves, and Eric Fujisaki. January 2005.

PEER 2004/07 *Ground Motions for Earthquake Simulator Qualification of Electrical Substation Equipment.* Shakhzod M. Takhirov, Gregory L. Fenves, Eric Fujisaki, and Don Clyde. January 2005.

PEER 2004/06 *Performance-Based Regulation and Regulatory Regimes.* Peter J. May and Chris Koski. September 2004.

PEER 2004/05 *Performance-Based Seismic Design Concepts and Implementation: Proceedings of an International Workshop.* Peter Fajfar and Helmut Krawinkler, Editors. September 2004.

PEER 2004/04 *Seismic Performance of an Instrumented Tilt-up Wall Building*. James C. Anderson and Vitelmo V. Bertero. July 2004.

PEER 2004/03 *Evaluation and Application of Concrete Tilt-up Assessment Methodologies.* Timothy Graf and James O. Malley. October 2004.

PEER 2004/02 *Analytical Investigations of New Methods for Reducing Residual Displacements of Reinforced Concrete Bridge Columns.* Junichi Sakai and Stephen A. Mahin. August 2004.

PEER 2004/01 *Seismic Performance of Masonry Buildings and Design Implications.* Kerri Anne Taeko Tokoro, James C. Anderson, and Vitelmo V. Bertero. February 2004.

PEER 2003/18 *Performance Models for Flexural Damage in Reinforced Concrete Columns.* Michael Berry and Marc Eberhard. August 2003.

PEER 2003/17 *Predicting Earthquake Damage in Older Reinforced Concrete Beam-Column Joints.* Catherine Pagni and Laura Lowes. October 2004.

PEER 2003/16 *Seismic Demands for Performance-Based Design of Bridges.* Kevin Mackie and Božidar Stojadinović. August 2003.

PEER 2003/15 *Seismic Demands for Nondeteriorating Frame Structures and Their Dependence on Ground Motions.* Ricardo Antonio Medina and Helmut Krawinkler. May 2004.

PEER 2003/14 *Finite Element Reliability and Sensitivity Methods for Performance-Based Earthquake Engineering*. Terje Haukaas and Armen Der Kiureghian. April 2004.

PEER 2003/13 *Effects of Connection Hysteretic Degradation on the Seismic Behavior of Steel Moment-Resisting Frames.* Janise E. Rodgers and Stephen A. Mahin. March 2004.

PEER 2003/12 *Implementation Manual for the Seismic Protection of Laboratory Contents: Format and Case Studies*. William T. Holmes and Mary C. Comerio. October 2003.

PEER 2003/11 *Fifth U.S.-Japan Workshop on Performance-Based Earthquake Engineering Methodology for Reinforced Concrete Building Structures*. February 2004.

PEER 2003/10 *A Beam-Column Joint Model for Simulating the Earthquake Response of Reinforced Concrete Frames.* Laura N. Lowes, Nilanjan Mitra, and Arash Altoontash. February 2004.

PEER 2003/09 *Sequencing Repairs after an Earthquake: An Economic Approach.* Marco Casari and Simon J. Wilkie. April 2004.

PEER 2003/08 *A Technical Framework for Probability-Based Demand and Capacity Factor Design (DCFD) Seismic Formats*. Fatemeh Jalayer and C. Allin Cornell. November 2003.

PEER 2003/07 *Uncertainty Specification and Propagation for Loss Estimation Using FOSM Methods.* Jack W. Baker and C. Allin Cornell. September 2003.

PEER 2003/06 *Performance of Circular Reinforced Concrete Bridge Columns under Bidirectional Earthquake Loading*. Mahmoud M. Hachem, Stephen A. Mahin, and Jack P. Moehle. February 2003.

PEER 2003/05 *Response Assessment for Building-Specific Loss Estimation.* Eduardo Miranda and Shahram Taghavi. September 2003.

PEER 2003/04 *Experimental Assessment of Columns with Short Lap Splices Subjected to Cyclic Loads*. Murat Melek, John W. Wallace, and Joel Conte. April 2003.

PEER 2003/03 *Probabilistic Response Assessment for Building-Specific Loss Estimation*. Eduardo Miranda and Hesameddin Aslani. September 2003.

PEER 2003/02 *Software Framework for Collaborative Development of Nonlinear Dynamic Analysis Program*. Jun Peng and Kincho H. Law. September 2003.

PEER 2003/01 *Shake Table Tests and Analytical Studies on the Gravity Load Collapse of Reinforced Concrete Frames.* Kenneth John Elwood and Jack P. Moehle. November 2003.

PEER 2002/24 *Performance of Beam to Column Bridge Joints Subjected to a Large Velocity Pulse.* Natalie Gibson, André Filiatrault, and Scott A. Ashford. April 2002.

PEER 2002/23 *Effects of Large Velocity Pulses on Reinforced Concrete Bridge Columns.* Greg L. Orozco and Scott A. Ashford. April 2002.

PEER 2002/22 *Characterization of Large Velocity Pulses for Laboratory Testing.* Kenneth E. Cox and Scott A. Ashford. April 2002.

PEER 2002/21 *Fourth U.S.-Japan Workshop on Performance-Based Earthquake Engineering Methodology for Reinforced Concrete Building Structures*. December 2002.

PEER 2002/20 *Barriers to Adoption and Implementation of PBEE Innovations.* Peter J. May. August 2002.

PEER 2002/19 *Economic-Engineered Integrated Models for Earthquakes: Socioeconomic Impacts.* Peter Gordon, James E. Moore II, and Harry W. Richardson. July 2002.

PEER 2002/18 *Assessment of Reinforced Concrete Building Exterior Joints with Substandard Details.* Chris P. Pantelides, Jon Hansen, Justin Nadauld, and Lawrence D. Reaveley. May 2002.

PEER 2002/17 *Structural Characterization and Seismic Response Analysis of a Highway Overcrossing Equipped with Elastomeric Bearings and Fluid Dampers: A Case Study*. Nicos Makris and Jian Zhang. November 2002.

PEER 2002/16 *Estimation of Uncertainty in Geotechnical Properties for Performance-Based Earthquake Engineering*. Allen L. Jones, Steven L. Kramer, and Pedro Arduino. December 2002.

PEER 2002/15 *Seismic Behavior of Bridge Columns Subjected to Various Loading Patterns*. Asadollah Esmaeily-Gh. and Yan Xiao. December 2002.

PEER 2002/14 *Inelastic Seismic Response of Extended Pile Shaft Supported Bridge Structures.* T.C. Hutchinson, R.W. Boulanger, Y.H. Chai, and I.M. Idriss. December 2002.

PEER 2002/13 *Probabilistic Models and Fragility Estimates for Bridge Components and Systems.* Paolo Gardoni, Armen Der Kiureghian, and Khalid M. Mosalam. June 2002.

PEER 2002/12 *Effects of Fault Dip and Slip Rake on Near-Source Ground Motions: Why Chi-Chi Was a Relatively Mild M7.6 Earthquake*. Brad T. Aagaard, John F. Hall, and Thomas H. Heaton. December 2002.

PEER 2002/11 *Analytical and Experimental Study of Fiber-Reinforced Strip Isolators*. James M. Kelly and Shakhzod M. Takhirov. September 2002.

PEER 2002/10 *Centrifuge Modeling of Settlement and Lateral Spreading with Comparisons to Numerical Analyses***.** Sivapalan Gajan and Bruce L. Kutter. January 2003.

PEER 2002/09 *Documentation and Analysis of Field Case Histories of Seismic Compression during the 1994 Northridge, California, Earthquake*. Jonathan P. Stewart, Patrick M. Smith, Daniel H. Whang, and Jonathan D. Bray. October 2002.

PEER 2002/08 *Component Testing, Stability Analysis and Characterization of Buckling-Restrained Unbonded Braces™.* Cameron Black, Nicos Makris, and Ian Aiken. September 2002.

PEER 2002/07 *Seismic Performance of Pile-Wharf Connections.* Charles W. Roeder, Robert Graff, Jennifer Soderstrom, and Jun Han Yoo. December 2001.

PEER 2002/06 *The Use of Benefit-Cost Analysis for Evaluation of Performance-Based Earthquake Engineering Decisions*. Richard O. Zerbe and Anthony Falit-Baiamonte. September 2001.

PEER 2002/05 *Guidelines, Specifications, and Seismic Performance Characterization of Nonstructural Building Components and Equipment*. André Filiatrault, Constantin Christopoulos, and Christopher Stearns. September 2001.

PEER 2002/04 *Consortium of Organizations for Strong-Motion Observation Systems and the Pacific Earthquake Engineering Research Center Lifelines Program: Invited Workshop on Archiving and Web Dissemination of Geotechnical Data, 4–5 October 2001*. September 2002.

PEER 2002/03 *Investigation of Sensitivity of Building Loss Estimates to Major Uncertain Variables for the Van Nuys Testbed*. Keith A. Porter, James L. Beck, and Rustem V. Shaikhutdinov. August 2002.

PEER 2002/02 *The Third U.S.-Japan Workshop on Performance-Based Earthquake Engineering Methodology for Reinforced Concrete Building Structures*. July 2002.

PEER 2002/01 *Nonstructural Loss Estimation: The UC Berkeley Case Study.* Mary C. Comerio and John C. Stallmeyer. December 2001.

PEER 2001/16 *Statistics of SDF-System Estimate of Roof Displacement for Pushover Analysis of Buildings.* Anil K. Chopra, Rakesh K. Goel, and Chatpan Chintanapakdee. December 2001.

PEER 2001/15 *Damage to Bridges during the 2001 Nisqually Earthquake.* R. Tyler Ranf, Marc O. Eberhard, and Michael P. Berry. November 2001.

PEER 2001/14 *Rocking Response of Equipment Anchored to a Base Foundation.* Nicos Makris and Cameron J. Black. September 2001.

PEER 2001/13 *Modeling Soil Liquefaction Hazards for Performance-Based Earthquake Engineering*. Steven L. Kramer and Ahmed-W. Elgamal. February 2001.

PEER 2001/12 *Development of Geotechnical Capabilities in OpenSees*. Boris Jeremić. September 2001.

PEER 2001/11 *Analytical and Experimental Study of Fiber-Reinforced Elastomeric Isolators*. James M. Kelly and Shakhzod M. Takhirov. September 2001.

PEER 2001/10 *Amplification Factors for Spectral Acceleration in Active Regions.* Jonathan P. Stewart, Andrew H. Liu, Yoojoong Choi, and Mehmet B. Baturay. December 2001.

PEER 2001/09 *Ground Motion Evaluation Procedures for Performance-Based Design.* Jonathan P. Stewart, Shyh-Jeng Chiou, Jonathan D. Bray, Robert W. Graves, Paul G. Somerville, and Norman A. Abrahamson. September 2001.

PEER 2001/08 *Experimental and Computational Evaluation of Reinforced Concrete Bridge Beam-Column Connections for Seismic Performance*. Clay J. Naito, Jack P. Moehle, and Khalid M. Mosalam. November 2001.

PEER 2001/07 *The Rocking Spectrum and the Shortcomings of Design Guidelines.* Nicos Makris and Dimitrios Konstantinidis. August 2001.

PEER 2001/06 *Development of an Electrical Substation Equipment Performance Database for Evaluation of Equipment Fragilities*. Thalia Agnanos. April 1999.

PEER 2001/05 *Stiffness Analysis of Fiber-Reinforced Elastomeric Isolators.* Hsiang-Chuan Tsai and James M. Kelly. May 2001.

PEER 2001/04 *Organizational and Societal Considerations for Performance-Based Earthquake Engineering*. Peter J. May. April 2001.

PEER 2001/03 *A Modal Pushover Analysis Procedure to Estimate Seismic Demands for Buildings: Theory and Preliminary Evaluation*. Anil K. Chopra and Rakesh K. Goel. January 2001.

PEER 2001/02 *Seismic Response Analysis of Highway Overcrossings Including Soil-Structure Interaction*. Jian Zhang and Nicos Makris. March 2001.

PEER 2001/01 *Experimental Study of Large Seismic Steel Beam-to-Column Connections.* Egor P. Popov and Shakhzod M. Takhirov. November 2000.

PEER 2000/10 *The Second U.S.-Japan Workshop on Performance-Based Earthquake Engineering Methodology for Reinforced Concrete Building Structures*. March 2000.

PEER 2000/09 *Structural Engineering Reconnaissance of the August 17, 1999 Earthquake: Kocaeli (Izmit), Turkey.* Halil Sezen, Kenneth J. Elwood, Andrew S. Whittaker, Khalid Mosalam, John J. Wallace, and John F. Stanton. December 2000.

PEER 2000/08 *Behavior of Reinforced Concrete Bridge Columns Having Varying Aspect Ratios and Varying Lengths of Confinement*. Anthony J. Calderone, Dawn E. Lehman, and Jack P. Moehle. January 2001.

PEER 2000/07 *Cover-Plate and Flange-Plate Reinforced Steel Moment-Resisting Connections.* Taejin Kim, Andrew S. Whittaker, Amir S. Gilani, Vitelmo V. Bertero, and Shakhzod M. Takhirov. September 2000.

PEER 2000/06 *Seismic Evaluation and Analysis of 230-kV Disconnect Switches.* Amir S. J. Gilani, Andrew S. Whittaker, Gregory L. Fenves, Chun-Hao Chen, Henry Ho, and Eric Fujisaki. July 2000.

PEER 2000/05 *Performance-Based Evaluation of Exterior Reinforced Concrete Building Joints for Seismic Excitation*. Chandra Clyde, Chris P. Pantelides, and Lawrence D. Reaveley. July 2000.

PEER 2000/04 *An Evaluation of Seismic Energy Demand: An Attenuation Approach*. Chung-Che Chou and Chia-Ming Uang. July 1999.

PEER 2000/03 *Framing Earthquake Retrofitting Decisions: The Case of Hillside Homes in Los Angeles.* Detlof von Winterfeldt, Nels Roselund, and Alicia Kitsuse. March 2000.

PEER 2000/02 *U.S.-Japan Workshop on the Effects of Near-Field Earthquake Shaking*. Andrew Whittaker, Editor. July 2000.

PEER 2000/01 *Further Studies on Seismic Interaction in Interconnected Electrical Substation Equipment.* Armen Der Kiureghian, Kee-Jeung Hong, and Jerome L. Sackman. November 1999.

PEER 1999/14 *Seismic Evaluation and Retrofit of 230-kV Porcelain Transformer Bushings*. Amir S. Gilani, Andrew S. Whittaker, Gregory L. Fenves, and Eric Fujisaki. December 1999.

PEER 1999/13 *Building Vulnerability Studies: Modeling and Evaluation of Tilt-up and Steel Reinforced Concrete Buildings*. John W. Wallace, Jonathan P. Stewart, and Andrew S. Whittaker, Editors. December 1999.

PEER 1999/12 *Rehabilitation of Nonductile RC Frame Building Using Encasement Plates and Energy-Dissipating Devices*. Mehrdad Sasani, Vitelmo V. Bertero, James C. Anderson. December 1999.

PEER 1999/11 *Performance Evaluation Database for Concrete Bridge Components and Systems under Simulated Seismic Loads*. Yael D. Hose and Frieder Seible. November 1999.

PEER 1999/10 *U.S.-Japan Workshop on Performance-Based Earthquake Engineering Methodology for Reinforced Concrete Building Structures*. December 1999.

PEER 1999/09 *Performance Improvement of Long Period Building Structures Subjected to Severe Pulse-Type Ground Motions*. James C. Anderson, Vitelmo V. Bertero, and Raul Bertero. October 1999.

PEER 1999/08 *Envelopes for Seismic Response Vectors.* Charles Menun and Armen Der Kiureghian. July 1999.

PEER 1999/07 *Documentation of Strengths and Weaknesses of Current Computer Analysis Methods for Seismic Performance of Reinforced Concrete Members*. William F. Cofer. November 1999.

PEER 1999/06 *Rocking Response and Overturning of Anchored Equipment under Seismic Excitations*. Nicos Makris and Jian Zhang. November 1999.

PEER 1999/05 *Seismic Evaluation of 550 kV Porcelain Transformer Bushings.* Amir S. Gilani, Andrew S. Whittaker, Gregory L. Fenves, and Eric Fujisaki. October 1999.

PEER 1999/04 *Adoption and Enforcement of Earthquake Risk-Reduction Measures.* Peter J. May, Raymond J. Burby, T. Jens Feeley, and Robert Wood. August 1999.

PEER 1999/03 *Task 3 Characterization of Site Response General Site Categories*. Adrian Rodriguez-Marek, Jonathan D. Bray and Norman Abrahamson. February 1999.

PEER 1999/02 *Capacity-Demand-Diagram Methods for Estimating Seismic Deformation of Inelastic Structures: SDF Systems*. Anil K. Chopra and Rakesh Goel. April 1999.

PEER 1999/01 *Interaction in Interconnected Electrical Substation Equipment Subjected to Earthquake Ground Motions*. Armen Der Kiureghian, Jerome L. Sackman, and Kee-Jeung Hong. February 1999.

PEER 1998/08 *Behavior and Failure Analysis of a Multiple-Frame Highway Bridge in the 1994 Northridge Earthquake*. Gregory L. Fenves and Michael Ellery. December 1998.

PEER 1998/07 *Empirical Evaluation of Inertial Soil-Structure Interaction Effects.* Jonathan P. Stewart, Raymond B. Seed, and Gregory L. Fenves. November 1998.

PEER 1998/06 *Effect of Damping Mechanisms on the Response of Seismic Isolated Structures*. Nicos Makris and Shih-Po Chang. November 1998.

PEER 1998/05 *Rocking Response and Overturning of Equipment under Horizontal Pulse-Type Motions*. Nicos Makris and Yiannis Roussos. October 1998.

PEER 1998/04 *Pacific Earthquake Engineering Research Invitational Workshop Proceedings, May 14–15, 1998: Defining the Links between Planning, Policy Analysis, Economics and Earthquake Engineering*. Mary Comerio and Peter Gordon. September 1998.

PEER 1998/03 *Repair/Upgrade Procedures for Welded Beam to Column Connections*. James C. Anderson and Xiaojing Duan. May 1998.

PEER 1998/02 *Seismic Evaluation of 196 kV Porcelain Transformer Bushings.* Amir S. Gilani, Juan W. Chavez, Gregory L. Fenves, and Andrew S. Whittaker. May 1998.

PEER 1998/01 *Seismic Performance of Well-Confined Concrete Bridge Columns.* Dawn E. Lehman and Jack P. Moehle. December 2000.

PEER REPORTS: ONE HUNDRED SERIES

PEER 2012/103 *Performance-Based Seismic Demand Assessment of Concentrically Braced Steel Frame Buildings.* Chui-Hsin Chen and Stephen A. Mahin. December 2012.

PEER 2012/102 *Procedure to Restart an Interrupted Hybrid Simulation: Addendum to PEER Report 2010/103.* Vesna Terzic and Bozidar Stojadinovic. October 2012.

PEER 2012/101 *Mechanics of Fiber Reinforced Bearings.* James M. Kelly and Andrea Calabrese. February 2012.

PEER 2011/107 *Nonlinear Site Response and Seismic Compression at Vertical Array Strongly Shaken by 2007 Niigata-ken Chuetsu-oki Earthquake.* Eric Yee, Jonathan P. Stewart, and Kohji Tokimatsu. December 2011.

PEER 2011/106 *Self Compacting Hybrid Fiber Reinforced Concrete Composites for Bridge Columns.* Pardeep Kumar, Gabriel Jen, William Trono, Marios Panagiotou, and Claudia Ostertag. September 2011.

PEER 2011/105 *Stochastic Dynamic Analysis of Bridges Subjected to Spacially Varying Ground Motions.* Katerina Konakli and Armen Der Kiureghian. August 2011.

PEER 2011/104 *Design and Instrumentation of the 2010 E-Defense Four-Story Reinforced Concrete and Post-Tensioned Concrete Buildings.* Takuya Nagae, Kenichi Tahara, Taizo Matsumori, Hitoshi Shiohara, Toshimi Kabeyasawa, Susumu Kono, Minehiro Nishiyama (Japanese Research Team) and John Wallace, Wassim Ghannoum, Jack Moehle, Richard Sause, Wesley Keller, Zeynep Tuna (U.S. Research Team). June 2011.

PEER 2011/103 *In-Situ Monitoring of the Force Output of Fluid Dampers: Experimental Investigation.* Dimitrios Konstantinidis, James M. Kelly, and Nicos Makris. April 2011.

PEER 2011/102 *Ground-Motion Prediction Equations 1964–2010.* John Douglas. April 2011.

PEER 2011/101 *Report of the Eighth Planning Meeting of NEES/E-Defense Collaborative Research on Earthquake Engineering.* Convened by the Hyogo Earthquake Engineering Research Center (NIED), NEES Consortium, Inc. February 2011.

PEER 2010/111 *Modeling and Acceptance Criteria for Seismic Design and Analysis of Tall Buildings.* Task 7 Report for the Tall Buildings Initiative - Published jointly by the Applied Technology Council. October 2010.

PEER 2010/110 *Seismic Performance Assessment and Probabilistic Repair Cost Analysis of Precast Concrete Cladding Systems for Multistory Buildlings.* Jeffrey P. Hunt and Božidar Stojadinovic. November 2010.

PEER 2010/109 *Report of the Seventh Joint Planning Meeting of NEES/E-Defense Collaboration on Earthquake Engineering. Held at the E-Defense, Miki, and Shin-Kobe, Japan, September 18–19, 2009.* August 2010.

PEER 2010/108 *Probabilistic Tsunami Hazard in California.* Hong Kie Thio, Paul Somerville, and Jascha Polet, preparers. October 2010.

PEER 2010/107 *Performance and Reliability of Exposed Column Base Plate Connections for Steel Moment-Resisting Frames.* Ady Aviram, Božidar Stojadinovic, and Armen Der Kiureghian. August 2010.

PEER 2010/106 *Verification of Probabilistic Seismic Hazard Analysis Computer Programs.* Patricia Thomas, Ivan Wong, and Norman Abrahamson. May 2010.

PEER 2010/105 *Structural Engineering Reconnaissance of the April 6, 2009, Abruzzo, Italy, Earthquake, and Lessons Learned.* M. Selim Günay and Khalid M. Mosalam. April 2010.

PEER 2010/104 *Simulating the Inelastic Seismic Behavior of Steel Braced Frames, Including the Effects of Low-Cycle Fatigue.* Yuli Huang and Stephen A. Mahin. April 2010.

PEER 2010/103 *Post-Earthquake Traffic Capacity of Modern Bridges in California.* Vesna Terzic and Božidar Stojadinović. March 2010.

PEER 2010/102 *Analysis of Cumulative Absolute Velocity (CAV) and JMA Instrumental Seismic Intensity (I_{JMA}) Using the PEER–NGA Strong Motion Database.* Kenneth W. Campbell and Yousef Bozorgnia. February 2010.

PEER 2010/101 *Rocking Response of Bridges on Shallow Foundations.* Jose A. Ugalde, Bruce L. Kutter, and Boris Jeremic. April 2010.

PEER 2009/109 *Simulation and Performance-Based Earthquake Engineering Assessment of Self-Centering Post-Tensioned Concrete Bridge Systems.* Won K. Lee and Sarah L. Billington. December 2009.

PEER 2009/108 *PEER Lifelines Geotechnical Virtual Data Center.* J. Carl Stepp, Daniel J. Ponti, Loren L. Turner, Jennifer N. Swift, Sean Devlin, Yang Zhu, Jean Benoit, and John Bobbitt. September 2009.

PEER 2009/107 *Experimental and Computational Evaluation of Current and Innovative In-Span Hinge Details in Reinforced Concrete Box-Girder Bridges: Part 2: Post-Test Analysis and Design Recommendations.* Matias A. Hube and Khalid M. Mosalam. December 2009.

PEER 2009/106 *Shear Strength Models of Exterior Beam-Column Joints without Transverse Reinforcement.* Sangjoon Park and Khalid M. Mosalam. November 2009.

PEER 2009/105 *Reduced Uncertainty of Ground Motion Prediction Equations through Bayesian Variance Analysis.* Robb Eric S. Moss. November 2009.

PEER 2009/104 *Advanced Implementation of Hybrid Simulation.* Andreas H. Schellenberg, Stephen A. Mahin, Gregory L. Fenves. November 2009.

PEER 2009/103 *Performance Evaluation of Innovative Steel Braced Frames.* T. Y. Yang, Jack P. Moehle, and Božidar Stojadinovic. August 2009.

PEER 2009/102 *Reinvestigation of Liquefaction and Nonliquefaction Case Histories from the 1976 Tangshan Earthquake.* Robb Eric Moss, Robert E. Kayen, Liyuan Tong, Songyu Liu, Guojun Cai, and Jiaer Wu. August 2009.

PEER 2009/101 *Report of the First Joint Planning Meeting for the Second Phase of NEES/E-Defense Collaborative Research on Earthquake Engineering.* Stephen A. Mahin et al. July 2009.

PEER 2008/104 *Experimental and Analytical Study of the Seismic Performance of Retaining Structures.* Linda Al Atik and Nicholas Sitar. January 2009.

PEER 2008/103 *Experimental and Computational Evaluation of Current and Innovative In-Span Hinge Details in Reinforced Concrete Box-Girder Bridges. Part 1: Experimental Findings and Pre-Test Analysis.* Matias A. Hube and Khalid M. Mosalam. January 2009.

PEER 2008/102 *Modeling of Unreinforced Masonry Infill Walls Considering In-Plane and Out-of-Plane Interaction.* Stephen Kadysiewski and Khalid M. Mosalam. January 2009.

PEER 2008/101 *Seismic Performance Objectives for Tall Buildings.* William T. Holmes, Charles Kircher, William Petak, and Nabih Youssef. August 2008.

PEER 2007/101 *Generalized Hybrid Simulation Framework for Structural Systems Subjected to Seismic Loading*. Tarek Elkhoraibi and Khalid M. Mosalam. July 2007.

PEER 2007/100 *Seismic Evaluation of Reinforced Concrete Buildings Including Effects of Masonry Infill Walls*. Alidad Hashemi and Khalid M. Mosalam. July 2007.

The Pacific Earthquake Engineering Research Center (PEER) is a multi-institutional research and education center with headquarters at the University of California, Berkeley. Investigators from over 20 universities, several consulting companies, and researchers at various state and federal government agencies contribute to research programs focused on performance-based earthquake engineering.

These research programs aim to identify and reduce the risks from major earthquakes to life safety and to the economy by including research in a wide variety of disciplines including structural and geotechnical engineering, geology/seismology, lifelines, transportation, architecture, economics, risk management, and public policy.

PEER is supported by federal, state, local, and regional agencies, together with industry partners.

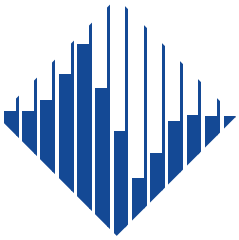

PEER Core Institutions

University of California, Berkeley (Lead Institution)
California Institute of Technology
Oregon State University
Stanford University
University of California, Davis
University of California, Irvine
University of California, Los Angeles
University of California, San Diego
University of Nevada, Reno
University of Southern California
University of Washington

PEER reports can be ordered at https://peer.berkeley.edu/peer-reports or by contacting

Pacific Earthquake Engineering Research Center
University of California, Berkeley
325 Davis Hall, Mail Code 1792
Berkeley, CA 94720-1792
Tel: 510-642-3437
Email: peer_center@berkeley.edu

ISSN 1547-0587X